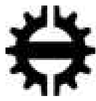
TAMPEREEN TEKNILLINEN YLIOPISTO
TAMPERE UNIVERSITY OF TECHNOLOGY

IRINA SAFONOVA

CHARACTERIZATION OF THE DOPED SILICON DIOXIDE AND ITS IMPLICATIONS ON THE RESISTIVE SWITCHING PHENOMENA IN THE ELECTROCHEMICAL METALLIZATION CELLS

Master's thesis

Examiners:

Professor Donald Lupo

Professor Veli-Tapani Kuokkala

TIIVISTELMÄ

IRINA SAFONOVA: Characterization of the doped silicon dioxide and its implications on the resistive switching phenomena in the electrochemical metallization cells
Tampereen teknillinen yliopisto
Diplomityö, 67 sivua, 10 liiteitä, 152 liitesivua
Syyskuu 2017
Materiaalitekniikan tutkinto-ohjelma
Pääaine: Elektroniset materialit
Sivuaine: Elektroniikka
Tarkastajat: professori Donald Lupo (Elektroniikan ja tietotekniikan laboratorio) ja professori Veli-Tapani Kuokkala (Materiaaliopin laboratorio)

Avainsanat: resistiivinen kytkentä, sähkökemiallinen muistisolu, piidioksidi, douppaus, kynnysjännitekytkentä, negatiivinen differentiaaliresistanssi

Tässä diplomityössä verrattiin seostettujen ja seostamattomien piidioksidipohjaisten ECM muistisolujen resistiivistä käyttäytymistä. Lähes 270 ohutkalvonäytettä (5nm - 50nm) valmistettiin CT1000-sputterointilaitteistolla RWTH Aachenin yliopistossa Saksassa. Substraattina ohutkalvojen kasvatuksessa käytettiin platinaa, titaaninitridiä ja safiiria. Kasvatusmateriaaleina käytettiin eri tavoin doupattuja kohtioita. Douppauksen tavoitteena oli parantaa ECM muistisolujen kytkentäkäyttäytymistä.

ECM muistisoluille tehtiin sekä sähköinen että fysikaalinen karakterisointi. Ohutkalvojen fysikaalisessa karakterisoinnissa käytetiin pyyhkäisyelektronimikroskooppia (SEM*),* röntgensäteen kokonaisheijastavuutta, röntgendiffraktiota sekä energia-dispersiivisen röntgenspektroskopian menetelmiä. Sähköinen karakterisointi tehtiin koeasemalla, joka on varustettu valomikroskoopilla ja Keithley- sähkömittarilla. Tulokset analysoitiin käyttäen EDA statistiikan periaatetta.

Analysoitujen tulosten perusteella kahdella ei-seostetulla näytteellä havaittiin odottamaton haihtuvan muistin kynnyskytkentä. Mittausdata testattiin myös graafisesti Schottky- tai Frenkel-Poole emission osoittamiseksi. Tulosten sovituksen perustella kumpikaan sähköjohtavuusmekanismi ei ole dominoivia.

ABSTRACT

IRINA SAFONOVA: Characterization of the doped silicon dioxide and its implications on the resistive switching phenomena in the electrochemical metallization cells
Tampere University of Technology
Master of Science Thesis, 67 pages, 10 Appendixes with 152 pages
September 2017
Master's Degree Material Science
Major: Electronic materials
Minor. Electronics
Examiners: Professor Donald Lupo (Laboratory of Electronics and Communications Engineering) and professor Veli-Tapani Kuokkala (Laboratory of Material Science)

Keywords: Resistive switching, electrochemical metallization cell, silicon dioxide, doping, threshold switching, negative differential resistance

In this Master's thesis, the switching behavior of the doped and undoped SiO2-based memory cells was compared. The aim of doping was to enhance the switching behavior of the ECM memory cells. About 270 samples were sputtered using the CT1000 cluster deposition tool in the IWE2 of RWTH Aachen University. For the deposition of the thin films, the platinum, titanium nitride and Al2O3 substrates were used. The deposition was performed by using three differently doped targets.

The physical characterization of the thin films was done using SEM, XRR, XRD, and EDX. Electroforming and electric characterization of the fabricated memory cells were made in the probe station with the light microscope and the Keithley electrometer. The results of the physical and electrical characterization were analyzed using the principle of Exploratory Data Analysis (EDA). The analysis of the result shows that two undoped samples on the platinum substrate and some doped samples exhibit the unexpected volatile threshold switching of metallic and semiconductive origin, respectively. Linear fitting of the measurement data in a logarithmic scale suggests that Schottky- and Frenkel- Poole conduction mechanisms are not dominant.

PREFACE

First, I am thankful Prof. Dr. Rainer Waser from RWTH Aachen University (Germany) for the opportunity to prepare this master thesis at the Institute of Materials Science for Electrical Engineering N2, for suggesting the topic and for the financial support.

I am indebted to Michael Lübben for comprehensive technical support and fruitful discussions during this project. I express my gratitude for Dr. Ilia Valov (Forschungszentrum Jülich, Peter Grünberg Institute (PGI)) and Dr. Christian Neumann (Heraeus) for conceptualizing the idea of this research project.

I thank Dr. Ilia Valov for supervising my master thesis. I appreciate the high quality of testing materials supplied by Heraeus Group. I thank Gisella Wasse for helping with getting SEM pictures and EDX. I also thank the lab technician Daliborka Erdogja for fabrication of the active electrode.

I am very grateful to Univ. Prof. Dr. Udo Schwalke (TU Darmstadt) for his passion at SiO2.

I thank all lecturers, professors, teaching assistants and personnel of the Tampere University of Technology for what they have taught me. Also, I sincerely thank the Tampere University of Technology for the provision of a student license of Matlab software, and MATLAB Academy for comprehensive courses enabling the processing of measurement data.

Additionally, I am thankful professor Veli-Tapani Kuokkala for his useful suggestions for improving this text. Finally, I thank professor Donald Lupo for valuable comments related to the theoretical interpretation of obtained experimental results, which allowed me to focus on the most important experimental findings.

Tampere, 28.09.2017

Irina Safonova

CONTENT

1. INTRODUCTION ... 1
1.1 Foreword ... 1
1.2 Memory ... 2
1.3 Resistive RRAMs (ReRAM or RRAM) ... 4
1.3.1 Electrochemical metallization cell (ECM) ... 6
2. THEORETICAL BACKGROUND ... 11
2.1 Resistive switching ... 11
2.1.1 The switching polarity ... 11
2.1.2 Current compliance ... 11
2.1.3 Electroforming ... 12
2.1.4 The threshold switching ... 13
2.1.5 Negative differential resistance (NDR) ... 16
2.2 Structure and morphology of SiO2 ... 17
2.3 Doping ... 20
2.3.1 Doping of SiO2 ... 21
2.4 Other methods for improving resistive switching ... 25
2.5 Conduction mechanism ... 26
2.5.1 Preface ... 26
2.5.2 Schottky emission ... 26
2.5.3 Poole- Frenkel Emission ... 27
3. THE RESULTS AND ANALYSIS ... 29
3.1 Structural and morphological characterization ... 29
3.1.1 XRR ... 29
3.2 Electrical characterization ... 34
3.2.1 Electroforming ... 39
3.2.2 I-V characteristics ... 50
3.2.3 The R-V characteristics ... 61
3.2.4 The threshold switching ... 61
4. CONCLUSIONS ... 68
REFERENCES ... 69

LIST OF FIGURES

Figure 1. Schematics of possible defects in a silica networks (Revesz 1965). 22
Figure 2. The comparison of the deposition rates of the samples sputtered using the TD0 and TD1 targets 30
Figure 3. The comparison of the deposition rate of the samples sputtered using the TD0 and TD2 targets 31
Figure 4. The thickness of the samples deposited using the TD0 and TD2 targets obtained by the fitting of the measured curves 32
Figure 5. The density of the samples deposited using the TD0 and TD2 targets obtained by the fitting of the measured curves 33
Figure 6. The roughness of the samples deposited using the TD0 and TD2 targets obtained by the fitting of the measured curves 34
Figure 7. The I-V curve of the 5nm-thick sample deposited using the TD0 target on the Pt substrate at 100C, electroformed with 3V and the current compliance of 10^{-8} A. 40
Figure 8. The overview of the electroforming data for the cell size of 100µmx100µm for the samples deposited using the TD0 target on the platinum substrate 40
Figure 9. The overview of the electroforming data for the cell size of 100µmx100µm for samples deposited using the TD0 target on Pt substrate 41
Figure 10. The yield % of the electroforming data of the samples deposited using the TD0 target on platinum substrate 41
Figure 11. The overview of the electroforming data of the samples deposited using the TD0 target on the TiN substrate 42
Figure 12. The yield % of the electroforming data of the samples deposited using the TD0 target on the TiN substrate 43
Figure 13. The I-V and R-V curves of the 50nm-thick layer of SiO2 deposited using the TD1 target on the TiN substrate at 100C during the electroforming 44
Figure 14. The electroforming curve of the 30nm-thick SiO2 layer deposited using the TD1 target on the TiN substrate at 150C. 45
Figure 15. The overview of the electroforming data for the cell size of 100µmx100µm for the samples deposited using the TD1 target on the TiN substrate 45
Figure 16. The overview of the electroforming data for the cell size of 50µmx50µm for the samples deposited using the TD1 target on the TiN substrate 46
Figure 17. The yield % of the electroforming data of the samples deposited using the TD1 target on the TiN substrate 46
Figure 18. The I-V and R-V curves of the 30nm-thick layer of SiO2 deposited using the TD2 target on the TiN substrate at 150C during the electroforming 47

Figure 19. The overview of the electroforming data for the cell size of 100µmx100µm for the samples deposited using the TD2 target on platinum substrate ... *48*
Figure 20. The overview of the electroforming data for the cell size of 50µmx50µm for the samples deposited using the TD2 target on the platinum substrate ... *48*
Figure 21. The yield % of the electroforming data of the samples deposited using the TD2-target on the platinum substrate ... *49*
Figure 22. The current-voltage characteristics of the 30-nm-thick sample deposited using the TD0 target on the platinum substrate at 100C and biased with 10^{-5}*A and +1V/-1V.* ... *51*
Figure 23. The current- voltage characteristics of the 30-nm-thick sample deposited using the TD0 target on the platinum substrate at 100C and biased with 10^{-4}*A of the current compliance* ... *52*
Figure 24.The I-V and R-V curves related to the memory cell deposited on the platinum substrate at 150C with the threshold-like behavior and biased with the current compliance of 10^{-2}*A and symmetric +1V/-1Vvoltage bias* ... *53*
Figure 25. The I-V and R-V curves of the memory cell deposited on the platinum substrate at 150C with the threshold-like behavior and biased with the current compliance of 0.1A ... *53*
Figure 26. The I-V and R-V characteristics of the memory cell deposited on the platinum substrate at 150C with the threshold-like behavior and biased with the current compliance of 1mA ... *54*
Figure 27. The I-V and R-V characteristics related to the memory cell deposited on the platinum substrate at 150C biased with the current compliance of 1mA and the voltage of+1.5V/-1.5V. ... *55*
Figure 28. The current- voltage characteristics of the 30-nm-thick sample deposited using the TD1 target on the TiN substrate at 100C and biased with the positive current compliance of 10^{-4}*A and the negative compliance of* $4\cdot10^{-5}$*A at the voltage +0.6V/-0.6V* ... *57*
Figure 29. The current- voltage characteristics of the 30-nm-thick sample deposited using the TD1 target on the TiN substrate at 100C and biased with the positive current compliance of $2\cdot10^{-4}$*A and the negative current compliance of* $0.5\cdot10^{-4}$*A with the voltage +0.8V/-0.6V.* ... *57*
Figure 30. The current- voltage characteristics of the 30-nm-thick sample deposited using the TD1 target on the TiN substrate at 100C and biased with the negative current compliance of $2.5\cdot10^{-5}$*A at the voltage 0V/-0.8V.* ... *58*
Figure 31. The current-voltage characteristics of the 50-nm-thick sample deposited using the TD2 target on the Pt substrate at 100C and biased with the positive and negative current compliance of 10^{-6}*A at the voltage +3/-5V.* ... *60*

Figure 32. The current- voltage characteristics of the 50-nm-thick sample deposited using the TD2 target on the platinum substrate at 100C and biased with the positive and negative current compliance of 10^{-6}A at the voltage +2/-5V. *60*
Figure 33. The ZY view of I-V curves of the samples deposited using the TD0 target on the platinum substrate at RT showing the threshold-like switching behavior *61*
Figure 34. The ZY view of the I-V curves of the samples deposited using the TD0 target on the platinum substrate at RT showing the threshold-like switching behavior *62*
Figure 35. The ZY view of the I-V curves of the samples deposited using the TD0 target on the platinum substrate at RT showing the threshold-like switching behavior *62*
Figure 36. The test for the Schottky emission: the ZY view of log(J)-sqrt(E) of the sample deposited on the platinum substrate at RT *63*
Figure 37. The test for the Frenkel-Poole emission: the ZY view of log(J)-sqrt(E) of the sample deposited on the platinum substrate at RT *64*
Figure 38. The part of the current-voltage characteristics of the samples deposited using the TD0 target on the platinum substrate at 150C showing the threshold-like switching behavior *65*
Figure 39. The part of I-V curves of the samples deposited using the TD0 target on the platinum substrate at 150C showing the threshold-like switching behavior *65*
Figure 40. The test for the Schottky emission: the ln(J) – sqrt(E) of the sample deposited using the TD0 target on the platinum substrate at 150C. *66*
Figure 41. The test for the Frenkel-Poole emission: the ZY view of the log(J)-sqrt(E) of the sample deposited on the platinum substrate at 150C *67*

LIST OF ABBREVIATIONS AND SYMBOLS

1D	1 Diode
1S1R1	1 Selector 1 Resistor
1T1M	1 Transistor 1 Memory cell
1Th	1 Threshold device
1Th1M	1 Threshold device 1 Memory cell
AC	Alternating Current
AE	Active Electrode
AFM	Atomic force microscope
ANOVA	Analysis of Variance
BSE	Back-scattered electrons
CBRAM	Conductive Bridge Random Access Memory
CC-NDR	Current-Controlled Negative Differential Resistance
CF	Conducting Filament
CT1000	Cluster deposition tool
DRAM	Dynamic Random-Access Memory
D1	One dopant used in the TD1 target
D2	Two dopants used in the TD2 targets
E	Extreme value in boxplot
ECM	Electrochemical metallization cell
EDA	Exploratory data analysis
EDX	Energy Dispersive X-ray Spectroscopy
FTTR	Field triggered thermal runaway
H	Hinges in boxplot
HP	Hewlett-Packard
HRS	High Resistive State
IMT	Insulator –Metal Transition
IoE	Internet of Everything
loci	Lissajous figure
log	natural logarithm in MATLAB
LRS	Low Resistive State
MEM	Metal-Electrolyte-Metal
Memristor	Memory resistor
MIEC	a mixed ionic electronic conducting material
MIM	Metal – Insulator- Metal
MIT	Metal-Insulator Transition
MS	Memory Switching
MtM	More than Moore
NCs	Nanocrystals
N-NDR	Voltage-controlled Negative differential resistance
OE	ohmic counter electrode
OFF	High Resistance State
ON	Low Resistance State
PC	Personal Computer

PF	Poole –Frenkel conduction
PMC device	Programmable Metallization Cell device
PVD	Physical Vapor Deposition
q	Charge
RBS	Rutherford backscattering spectroscopy
ReRAM	Redox based Resistive Switching Random Access Memory
RESET	Transition from LRS to HRS
RF	Radio – frequency
RRAM	Resistive Switching Random Access Memory
RT	Room Temperature
RWTH Aachen	Rheinisch-Westfälische Technische Hochschule Aachen
SEM	Scanning Electron Microscopy
SET	Transition from HRS to LRS
S-NDR	Current-controlled Negative differential resistance
TCM	Thermochemical memory
TD0	extremely pure SiO2-target
TD1	the SiO2 target doped with D1
TD2	the SiO2 target doped with D2
TS	Threshold Switching
VCM	Valence Change Mechanism
VRS	Volatile Resistance state
XRD	X-ray Diffraction
XRR	X-Ray Reflection
φ	magnetic flux
ε	Electromotive force

Author's contribution

The collaboration project with the Heraeus Group was performed under the guidance of Univ. Prof. Dr. Rainer Waser from the Institute of Materials Science for Electrical Engineering N2 at the RWTH Aachen University. Dr. Ilia Valov made the direct supervising of the Master's Thesis, while Ph.D. student Michael Lüebben performed my laboratory and other technical orientation. In addition, the latter maintained the functionality of the electrical part of the sputtering equipment. Univ.Prof. Dr. Rainer Waser and Dr.-In. Ulrich Böttger made the general supervising of the project. Furthermore, Heraeus Group supplied the high-end materials for testing and financed the project.

Moreover, the lab technician Daliborka Erdogja made the metallization layer of an active electrode (AE) from Cu by the electron beam. Gisela Wasse took the SEM images together with the EDX, whereas I prepared the samples, and chose the image regions and chemical elements for detection. All retained technical works, which include samples' sputtering, XRD (X-ray diffraction) measurements and analysis, XRR (X-ray reflectivity), electrical measurements, characterization and choosing the appropriate testing method were facilitated by me.

1. INTRODUCTION

1.1 Foreword

The theme of this Master's thesis is 'Characterization of the doped silicon dioxide and its implication on the resistive switching phenomena in the electrochemical metallization cells.' The ECM or the electrochemical metallization cell is one of the emerging resistive random-access memories (RRAM), which can perhaps replace the Flash technology someday. The ECM has different names, such as a conductive bridging RAM (CBRAM) (Axon Technologies Corp.), a programmable metallization cell memory (Kozicki et al. 2005), a 'gapless-type atomic switch' (Tsuruoka et al. 2012), and an electrolytic resistance memory (Aratani et al. 2007).

The experimental part of this work was performed in the laboratories of RWTH Aachen, while the interpretation of the obtained results was made and the theoretical part of the thesis was written after returning to Finland. In this thesis, the switching behavior of the doped and the pure SiO2 –based memory cells was studied. Originally, the aim of the doping of SiO2 was to improve the switching behavior. However, the experimental results reveal that both doped and pure SiO2 samples exhibit the unexpected switching behavior.

Approximately, the 270 thin film samples with thickness between 5nm and 50nm were sputtered using the TD0, TD1 and TD2 targets on the platinum, TiN, and Al2O3 substrates. The TD0-target contains the extremely pure SiO2, whereas the TD1-target contains one doping element and TD2-target contains two dopants.

Next, I focused on the concepts of the memory in general, the emerging RRAM memories, the ECM memory cells and the memristors. The definition of all these basic concepts would be necessary, if one would like to interpret the switching behavior of the ECM memory cell.

The additional concepts were introduced in Appendixes 1-9. Appendix 1introduces the concept of the memristor in more details. In Appendix 2, the alternative explanation of the moisture effect on the resistive switching in the SiO2-based RAM is done using the Pourbaix diagram. In Appendix 3, the review of the doping of other oxides is introduced. Appendix 4 introduces the research methodology, the results of the materials characterization and the fabrication. Appendix 5 introduces the comparison of the related statistics. Appendixes 6-9 introduce the additional figures with explanations related to electroforming (Appendix 6), current-voltage characteristics (Appendix 7), resistance (Appendix 8), threshold switching (Appendix 9), as well as quantum size effect and Coulomb blockade Appendix (10).

1.2 Memory

More than Moore and Internet of Everything. The fast development of the transistor-based memories allowed the creation of portable computers, cellular phones, and digital cameras. This development already goes beyond Moore's law toward the era of "More than Moore (MtM)", beginning with the "Internet of Things" toward "Internet of Everything (IoE) "(ITRS 2015).

The MtM means the integrating of complex systems in one chip or package, advanced ICs for the flat panel displays (FPD), the micro electro mechanical systems MEMS, sensors, and radio components. Moreover, the Internet of Things allows the direct integration of computer-based systems and a physical world, whereas IoE is nothing else than a distributed computer access, to the remote memories or Data Centers, to a variety of sensors and actuators via Internet (ITRS 2015).

With the fast development, every new generation of ICs has more and more transistors. The transistors are working at higher and higher frequencies. This leads to more power being emitted. This excess power needs to be dissipated. The fundamental limit of the power dissipation in ICs is approaching the maximum fundamental limit (ITRS 2015). Therefore, alternative technology solutions are being sought.

The memory cell in general. The memory device consists of small building blocks known as memory cells. The memory cell has at least two stable states representing 1 and 0 in the digital logic. The traditional memory cell needs three operating terminals. First, the selector device which chooses a memory cell to read or write on. Second, the control terminal that specifies the read or write function. Third, the terminal which supplies an electrical signal for writing by setting the cell to 1 or 0. The output signal of the third terminal is used for reading the memory state (Stallings 2000).

Volatile and non-volatile memories. Memories can be classified as *the volatile* as well as *non-volatile types*. The volatile RAMs (random access memories) consists of static (SRAM) and dynamic (DRAM) types, whereas read-only memories (ROM) are of non-volatile type (Stallings 2000; Muller et al. 2012).

RAM memory is volatile because the data would be lost if the power would be interrupted. As a result, the RAM can be used only for the temporary storage of data (Stallings 2000). The *non-volatile* ROM memory does not consume power for maintaining a memory bit. Data in ROM can be read, but it is impossible to rewrite it. The data in ROM is stored once during the chip fabrication. The programmable ROM can be written electrically and it is possible to write on it after the chip fabrication (Stallings 2000)

DRAM. A *dynamic* RAM consists of memory cells, which store data as a charge in capacitors. Usually, the DRAM cells consist of one capacitor and one transistor. This

memory cell is used for the storage of one bit of information. In the memory cell, the transistor works as an open and closed switch. The charged or discharged capacitor represents a binary 1 or 0 respectively. However, the capacitor tends to lose charge over time; therefore, the charge in the capacitor needs periodic refreshing. The DRAM is an analog device because the capacitor can store any amount of charge within the given range. The interpretation of 1 or 0 is made using threshold value of voltage (Stallings 2000).

SRAM. A *static* RAM uses flip-flop logic gates and the same logic as in processors; therefore, it is a digital device. The SRAM just like the DRAM can hold data if it has power. The SRAM's memory cells have four transistors connected in a pattern for producing stable logic states. Additionally, unlike the DRAM, the data in SRAM needs not to be refreshed (Stallings 2000).

ROM memories. Another type of memories is the *read-mostly memory*, where the read function can be done more frequent than the write function. This group consists of EPROM, EEPROM and Flash memories. The EPROM memory is an *optically* erasable programmable read-only memory. The erasing occurs by 20 minutes exposure of chip to the UV radiation through the window on the packaging.

EPROM, EEPROM, and Flash memories. The data holds in EPROM indefinitely and the erasing can be made many times. The EEPROM is an *electrically* erasable programmable read-only memory, which is more expensive and less dense than EPROM memories. In EEPROM, the reading time is much shorter than writing time. In the *Flash* memory, the data is erased electrically and quickly. It is possible to erase just the blocks of the data; however, single bits cannot be erased. Like EPROM, it uses only one transistor per bit of data, and, therefore, it is very dense (Stallings 2000).

Flash memory. The development of a cellular phone, for example, required a high-volume non-volatile solid-state memory with fast code execution. In addition, the memory should be large enough to store the whole program, the application and user data. First, the NOR and later the NAND flash memories fulfilled the need for smartphones, MP3 music players, and digital cameras. NAND is dominating in the market (95%) (Lee 2011). The flash memory is used as a reference for all emerging electrically erasable non-volatile memories.

The requirement for emerging memory concepts. It is expected that only one emerging technology can be adopted as a replacement for the mass memory storage such as NAND flash. The new entrant should deliver most features in order to be adopted in an industrial scale. The memory speed, scalability, power consumption, endurance, and density need to be better than in a flash memory. However, if the entrant can be better only on a limited scale, then this technology can be suitable for the niche applications only (Meena et al. 2014).

The emerging resistive RAMs. The RRAM including the memristor-based RAMs can revolutionize the consumer electronics and personal computing. RRAM is a simple bistable device with two terminals. It can switch between two or more resistive states by voltage pulses. Data retention and endurance, as well as reliability, may be the most critical issues in the RRAM development. Samsung and IBM companies involve actively in research with RRAMs (Meena et al. 2014).

1.3 Resistive RRAMs (ReRAM or RRAM)

Introduction. The emerging resistive RAM memories are today at different stages of technology development. Some of the prototypical devices are compatible with CMOS technology and even have better performance than Flash memories (Muller et al. 2012).

These devices are based on a generic *MIM* structure (Metal-Insulator-Metal). *M* stands for metals or the electron conducting non-metals (Waser & Aono 2007b). The electrode materials can be the same or different. If different electrode materials are used, then the bottom electrode needs to be inert (Pt, W or TiN), whereas the top active electrode is Cu or Ag.

The *I* can represent an insulator or an ion conducting material (Waser & Aono 2007b) or a *solid-state electrolyte* (Lu et al. 2012). Various oxides, sulfides, selenides, tellurides as well as amorphous Si, the mixture of oxides and chalcogenides, and even organic compounds can be used (Waser & Aono 2007a; Lu et al. 2012). These materials change their resistive states under the influence of an electric stimuli. The various thermal and electrical effects together with the ion migration can explain the resistance switching. Moreover, the redox reaction can couple with the ion migration in the same device (Waser & Aono 2007b).

Terminology and general remarks. Many different concepts of emerging memories are recently investigated. Also, different classification and terminology may be used for the description of RRAMs (Waser et al. 2009; Muller et al. 2012). One can mention, for example, MRAM (magnetoresistive memory), PCM (phase change memory), RRAM (resistive RAMs) including the oxide RAM (OxRAM) or valence change memories (VCM), TCM (Ielmini et al. 2011) and CBRAM (ECM) (Waser et al. 2009; Muller et al. 2012).

Usually, oxides are used in the ECM devices as well as in OxRAM or in VCM. Some memory types such as ECM or VCM historically can have a lot of different names and definitions. Moreover, the same oxides such as NiOx can appear in multiple categories (PCM and OxRAM) or the same oxide materials can be in VCM and ECM categories (Lu et al. 2012; Valov & Waser 2013; Celano 2016).

Furthermore, in principle, the same basic effect can be described using completely different terminology. In addition, the same memory cell can exhibit many types of behaviors. There are various definitions of two-terminal emerging devices, some define it as memristors and while others don't.

PCM (Phase Change Memories). At the moment, PCM types of memories are at the most mature stage of development. Such a cell uses the chalcogenide materials, which exhibit a reversible transition between two phases of different resistivity, therefore they were named as phase change memories. The amorphous phase can be denoted as "0" and crystalline phase as "1" in digital logic. The reset (or erasing) current is in the order of 100µA for GeSb with OFF/ON resistance >10^4. PCM memory reads and writes faster with lower power than NOR or NAND Flash memories (Muller et al. 2012).

Thermochemical memory (TCM). Another example of emerging devices is thermochemical memories with the unipolar type of switching. In prototypical Pt/NiO/Pt structure, the thermally induced local change in stoichiometry together with redox reactions causes a variation of the local conductivity. TCM type of behavior was observed in NiO, Al2O3, Nb-oxide, SiO, TiO2, HfO2, Fe2O3 and CoO- based devices. Joule heating causes the change of resistance after applying voltage bias. The resulting current in semiconductive NiO would be thermally activated and further heating would increase the current too. As a result, a thermal runaway can occur leading to thermal-induced dielectric breakdown (Ielmini et al. 2011). As it can be seen, the same oxides are used in VCM and ECM memory cells. In addition, the thermally induced local change in stoichiometry (Ielmini et al. 2011) can mean the presence of oxygen vacancies (Waser & Aono 2007) or simply cation-rich region in the oxide.

The valence change memory (VCM). The VCM is a valence change memory, where anion is assumed to migrate when voltage is applied. VCM consists of high and low work function electrodes with an oxide in between. The VCM cells base on the creation of 'mixed ionic-electronic conducting filaments', which are oxygen-deficient (Valov et al. 2013). In tested ReRAMs, in both VCM and ECM cell, the measured electrochemical potential indicates the presence of an emf and nano-size battery effect (Valov et al. 2013).

However, in the typical VCM cells (TaOx, HfOx, and TiOx) not only oxygen vacancies but also the metal cations are mobile and contribute to conduction. Moreover, the device can change the switching mode from VCM to ECM due to the intermediate layer of amorphous carbon (Wedig et al. 2016). According to Dr. Valov Ilia, 'it is not always possible to strictly distinguish between ECM and VCM cells. Rather, both switching mechanisms can be found in one and the same cell' (Valov).

The electrochemical metallization cell (ECM). Generally, the ECM is defined as a memory cell, whose functionality is based on cation migration. It uses Cu or Ag as an active electrode. In addition, the ECM cell has an inert counter electrode at the bottom

and *a solid electrolyte* between the opposite electrodes. The material of the positively biased active electrode when dissolving causes the metal deposition on the opposite electrode. Growing the metallic filament connects the electrodes. This short-circuits the cell and turns it into the ON state, whereas applying a negative bias switches the cell OFF (Valov & Waser 2013; Valov et al. 2013).

However, the ECM category includes materials with a quite different behavior. For example, one can consider the ECM cells based on the GeS or SiO2. The 50nm-thick Ag -electrode would completely be dissolved in 50nm-thick GeS-matrix without any treatment within two weeks, however, the Ag does not do the same in SiO2 (Cho et al. 2012). This implies that, even without applied bias, the GeS matrix behaves as an intrinsic *solid electrolyte* in the same way as the *liquid electrolyte* in the electrochemical cell. The GeS matrix dissolves the inserted metal electrode, but SiO2 does not.

In this work, SiO2- based ECM cell with Cu-electrode was studied. Therefore, the resistive behavior of SiO2 and copper transport in SiO2 in ICs would be also relevant in the interpretation of ECM switching behavior. In ICs, SiO2 is thought as an insulator, but in the literature devoted to RRAMs, it can be also defined as the *solid electrolyte* (Lu et al. 2012) or cation-transporting material (Valov & Waser 2013; Valov et al. 2013).

In addition, similar effects of the growth of the metallic dendrites inside an insulator were investigated in the printed circuit boards (PCB) (Zhou et al. 2013), ceramic capacitors (Preu et al. 2014), and MOS capacitors (Willis & Lang 2004), where the effect was explained as an electrochemical migration of metal in the presence of moisture.

1.3.1 Electrochemical metallization cell (ECM)

The chemical reaction in ECM in general. Generally, the dissolution of the active electrode in ECM memory cells is described by the equation $Me \rightarrow Me^{z+} + ze^{-}$ (1), whereas the electrodeposition at the opposite inert electrode as $Me^{z+} + ze^{-} \rightarrow Me$ (2). The Me is metal, z is the valence state and the number of electrons. The materials, which are usually used for active electrodes, are Ag, Cu. The usual material choice for the inert electrode is Pt or W (Lu et al. 2012).

Dissolution of Cu into SiO2. Nevertheless, as it was previously mentioned, Ag does not dissolve into SiO2, as it does in the GeS-based ECM cells. For example, Ag dissolves directly into GeS even without any treatment, but Ag stays metallic when it is deposited on SiO2 (Cho et al. 2012). Also, in the impure or contamination-free environment, the Cu cannot dissociate into ions $Cu \rightarrow Cu^{z+} + ze^{-}$ even under the influence of the electric field (He & Lu 2012).

However, Cu can reduce the SiO2 in the presence of residual moisture and contamination due to the oxygen-containing species. If the oxide of copper exists at the Cu and SiO2

interface, then, under the influence of electric or thermal stress, copper ions may be created and released into the SiO2 (He & Lu 2012).

Moreover, the metallic species can migrate into the dielectric material by diffusion or drift. The diffusion can occur due to the concentration gradient and the drift is due to the electric field (He & Lu 2012). Copper transport in the oxide is controlled by both temperature and applied voltage. In copper oxide, the copper ions and copper neutrals are present (Raghavan et al. 1995). The nanoscale metallic inclusions in dielectric material can dynamically change their position, size, and shape when the voltage bias is applied. The clusters of metals may be thought as the BPEs (bipolar electrodes), which may be dissolved, nucleated, and redeposited at any other location. The competitive electrochemical reactions can occur on both polarized sides (Yang et al. 2014).

Therefore, the creation of the Cu ions in SiO2 is more complicated than the general chemical reaction (1) of ECM cells can suggest. For thermal diffusion, the metal atoms should overcome the barriers between metallic bonding and the interface layers. At the interface between the dielectric and metal, the metal would oxidize creating a polarized dipole. If an electric field is applied, the dipole would be distorted, which then increases the probability of breakage of the metal-oxygen (Me-O) bonds. Only after breakage of the Me-O bonds, the metallic ions can be generated (He & Lu 2012). The injection of the copper ions into the dielectric material generates a charge build-up, which then limits the ionic current (Raghavan et al. 1995).

The experiments with MOS capacitor show the presence of the significant ionic copper diffusion into SiO2 in the samples, which were oxidized in the ambient or in the pure oxygen. However, the vacuum treated samples do not show any sign of copper diffusion. Therefore, the oxidized copper electrode suggested being responsible for the transport of the copper ions through the oxide. The copper diffuses only if the oxidized copper is present. The Cu can oxidize via moisture of the ambient gases (Willis & Lang 2004). These results are consistent with tests made by Tsuruoka (Tsuruoka et al. 2012) and Tappertzhofen (Tappertzhofen et al. 2013) with SiO2-based ECM memory cell with Cu as the active electrode. The switching in the SiO2 depends on the water partial pressure pH_2O, because without the water uptake, the SiO2-based memory cell does not switch in the vacuum, but Ta2O5 does.

The effect of moisture in ECM memory cells. Tsuruoka et.al has put forward that, at the interface between electrode and oxide, copper ions are created as the result of the chemical oxidation with the help of the residual water. The chemical oxidation in the ECM memory cell is affected by the moisture from an ambient environment as well as the presence of oxygen in the oxide or residual water. The sputtered SiO2 having the nanoporous structure absorbs the moisture, but due to the smaller isoelectric point, SiO2 absorbs water in less extent than T2O5. In addition, SiO2 desorbs water in the vacuum easily due to the

weak hydrogen bonds between the silanol groups. Cu ions may migrate through the network of the hydrogen bonds at the grain boundaries (Tsuruoka et al. 2012).

The electroforming and the switching in the Cu/SiO2/Pt memory cell depend on the pH2O pressure. Unlike Ta2O5, the SiO2-based cells failed to switch with decreasing the pH2O pressure. In the vacuum, rather the dielectric breakdown of SiO2 occurs without creating of the metallic filament (Tsuruoka et al. 2012). At approximately 600 K, the Cu/Ta2O5/Pt cell made the transition from non-volatile switching to volatile, but the Cu/SiO2/Pt cell showed only the non-volatile switching mode (Tsuruoka et al. 2012).

Tappertzhofen et al. proposed that the moisture from the ambient environment can penetrate from the lateral side of the ECM cell. The moisture is responsible for the filament creation and the transition of resistance in the SiO2-based ECM cells. He suggested that not only the positive bias at the top electrode but also the counter reaction at the opposite bottom electrode is needed for maintaining the charge electroneutrality. According to Tappertzhofen, the top electrode is active whereas the bottom electrode is inert. The resistive switching and the electrochemical oxidation of the active electrode would be blocked if the charge transfer reaction at the inert electrode failed. The following reactions at the top electrode $Cu \rightarrow Cu^{2+} + 2e^{-}$ and at the bottom Pt electrode $\frac{1}{2}O_2 + H_2O + 2e^{-} \rightarrow 2OH^{-}$ are supposed to occur (Tappertzhofen et al. 2013).

Effect of density and porosity. According to Tsuruoka et al., the Ta2O5-based devices may be electroformed, however, the Pt/Ta2O5/Pt cell at higher voltage bias than Cu/Ta2O5/Pt cell. The Cu/Ta2O5/Pt structure displays the bipolar switching, but the Pt/Ta2O5/Pt mostly does not switch. The disconnection of opposite electrodes or RESET seems to be due to the oxidation of Cu atoms assisted by the Joule heating and the Cu-ions diffusion under a concentration gradient. The disconnecting of the electrodes can also occur at a positive bias, however, repetitive switching needs both positive and negative bias (Tsuruoka et al. 2010).

In Cu/Ta2O5/Pt cell, the enhancing of the redox current and the reduction of the electroforming voltage were achieved with a decrease in the density of the Ta2O5 film. The density of Ta2O5 increases as RF power increases. Water absorbed into the Ta2O5 layer from the ambient atmosphere may react according to the equation $2H_2O + 2e^{-} \rightarrow 2OH^{-} + H_2$ at the Ta2O5/Pt interface. The Ta2O5 films were fabricated by electron beam deposition and by RF sputtering at 30W and 200W.All samples had different densities despite the almost similar Ta/O ratio. The films with different densities showed different switching behavior. The films with the highest densities had only an electronic current without ionic current contribution. The decrease in density caused the appearance of current peaks in the cyclic voltammetry (CV) attributed to the redox reactions. The peak of the ionic current would be larger than the electronic current at low voltage for the layer with the lowest density. Therefore, the decreasing the film density would enhance the redox reaction (Tsuruoka et al. 2015).

The size of the grains in the nanoporous amorphous thin films may be only a few nanometers. The absorbed water molecules would create a network of the hydrogen bonds at the Ta-O dangling bonds and grain boundaries. At a positive bias, the metal would oxidize at the anode and ions would migrate toward the opposite electrode. At the cathode, the cell electroneutrality would be maintained by the reduction of water molecules to OH^{-}ions. The emf in the cell would depend on the concentration of the hydroxide and metal ions. The dense films absorb very little water therefore, the limited redox reactions create a very small ionic current. Decreasing of the film density allows the incorporation of more water molecules into the Ta2O5 film. This enhances the redox reaction at both interfaces and increases the ionic current. In addition, the electroforming voltage decreases with the decrease in the density of the layer (Tsuruoka et al. 2015).

Electroforming. First, the electroforming as a soft electric breakdown is needed for the initiation of resistive switching in the insulator, where the total charge controls the process of electroforming. As a result, the bipolar switching occurs between the virtual anode and the cathode with the creation of the conductive path due to local redox reactions (Waser & Aono 2007).

Switching polarity. Switching may be unipolar or bipolar. The symmetric or unipolar switching is not dependent on the bias polarity. In unipolar switching, the change in resistance level from ON to OFF would require a higher voltage and current than in the opposite direction, during the transition from the OFF to the ON state. Thermally induced resistive switching exhibits a unipolar characteristic with the conductive filament affected by Joule heating. The filament consists of the electrode metal or suboxides. The unipolar switching needs the higher level of used compliance current. Switching is asymmetric or bipolar when the transition between switching states takes place at different polarity. Usually, the memory cells with bipolar behavior need asymmetry: the different polarity of voltage during the electroforming or electrodes from different materials (Waser & Aono 2007).

Circuit elements: diode and transistor, ReRAMs and memristor. A transistor, which is a shortage for transresistance, is the three-terminal device that amplifies and switches the electrical signal. On the other hand, a diode is a two-terminal element which rectifies the current. Rectification means that the diode has low electric resistance when current flows in one direction whereas it has high resistance in the opposite direction. Because of rectification, switching, and amplifying of electronic signals, the transistors and diodes had a huge technological impact in circuit design. However, in general, they are not considered as fundamental circuit elements such as a resistor, conductor, and inductor.

In 2008, Strukov et. al announced that the TiO2 based switching memory elements are memristors (memory resistors) (Strukov et al. 2008). 1971, Leon Chua has suggested that memristor is the fourth circuit element which is fundamental (Chua 1971). Based on the mathematical symmetry Leon Chua had suggested that in addition to a resistor,

inductor, and a capacitor as basic circuit elements, the fourth fundamental circuit element should exist and he had named it a memristor, which comes from the shortening of the words memory resistor (Chua 1971). The concept of the memristor is introduced in more detail in Appendix 1.

According to Leon Chua, all non-volatile memory devices with 2 terminals irrespective of their physical mechanisms or the used materials are memristors, because they are based on resistance switching, and they all have a loop with pinched hysteresis in 1st and 3rd part of the current –voltage characteristics (Chua 2011). Therefore, it is worth seeing what kind of circuit element the ECM memory cell is. Is it the current or voltage- controlled device, the passive or active circuit element? If the ECM memory cell is an electrochemical cell, then the question is to define what kind of electrochemical cell it is.

The Pourbaix diagram. However, the alternative explanation of the moisture effect on the resistance switching in the SiO2-based electrochemical metallization cell may be done based on the Pourbaix diagram. The explanation is introduced separately in Appendix 2.

2. THEORETICAL BACKGROUND

2.1 Resistive switching

2.1.1 The switching polarity

The unipolar type of resistive switching. *The unipolar* resistive switching means that the transition between the OFF and the ON states occurs under the same voltage polarity (Schindler 2009; van den Hurk 2016). Typically, the writing voltage is higher than the erasing voltage (Schindler 2009; van den Hurk 2016), but the write current is lower than the erase current (Schindler 2009). The writing and erasing are usually from the upper µA to mA (Schindler 2009). The high erase currents in the unipolar memory cells indicate the dominance of the thermal effect. Nevertheless, the unipolar and bipolar switching can occur in the same type of the memory cell (Schindler 2009).

The bipolar switching. The *bipolar switching* implies that the writing and erasing occur under opposite polarities (Schindler 2009; Tappertzhofen 2014; van den Hurk 2016). Usually, the bipolar switching occurs at much lower current than unipolar switching. Additionally, the asymmetry due to the different electrodes or electroforming needs to be in cells with a bipolar type of switching (Schindler 2009).

Polarity and memory cells. Typically, *ECM* and *VCM* memory cells show the bipolar type of switching, whereas the *TCM* (Thermo-Chemical Memory) cells exhibit the unipolar type of switching (Tappertzhofen 2014; van den Hurk 2016). The TCM and VCM memory cells are affected by processes in the insulator or *electrolyte*, whereas the ECM behavior depends on the choice of electrode materials (van den Hurk 2016). The Cu-SiO2 memory cells exhibit the bipolar switching (Schindler 2009).

2.1.2 Current compliance

Current compliance. A current compliance during writing is typically used to control the low resistance ON state (Schindler 2009; Tappertzhofen 2014; van den Hurk 2016). Very small current creates weak filaments, which results in the unstable ON state, whereas high current creates strong filaments, which can't be dissolved. The high current compliance can induce the unipolar switching. Repetitive switching can cause a strengthening of the filament, which after several hundred cycles can only be erased by much higher currents. After this hard erasing, the bipolar switching can be possible again (Schindler 2009).

2.1.3 Electroforming

The electroforming in general. The electroforming is usually defined as an irreversible change in conductivity of a thin film at a high electric field. After the electroforming, the switching and memory effects together with the negative differential resistance are found in amorphous and microcrystalline binary inorganic insulators (Dearnaley et al. 1970).

The electroforming resembles the dielectric breakdown in amorphous or microcrystalline insulators. The dielectric breakdown is based on an electron avalanche and is a function of temperature and film thickness (Dearnaley et al. 1970).

The gaseous fluorine from fluorides and oxygen from oxides develop during the electroforming. The created bubbles then can merge and spoil the region between metal and insulator. The electroforming voltage is sensitive to the anode materials, while cathode material seems not to affect the electroforming. The electroforming is sensitive to the atmosphere. During the electroforming, the oxygen vacancies are injected into the dielectrics. These vacancies increase the conduction locally in the insulator layer. The electrode dependence on the electroforming voltage is due to the anode reactivity (Dearnaley et al. 1970).

The insulators (oxides and fluorides) containing the reactive anions can be most readily electroformed. In addition, it seems to be easier to electroform the non-stoichiometric insulators. Oxygen can reverse the forming process. The electroformed MIM device displays the negative differential resistance of N-type (Dearnaley et al. 1970).

The voltage dependence on the dielectric constant. In oxides, the voltage for the maximum current was found to be dependent on the dielectric constant. The voltage would be smaller, when the dielectric constant of oxide is higher (Dearnaley et al. 1970). The dielectric breakdown strength of an insulator and dielectric constant are related to each other. The time-dependent dielectric breakdown increases with increase in dielectric constants (McPherson et al. 2003). Therefore, it can be stated that differences between the electroforming (switching) behavior of different oxides, for example, can relate directly to the dissimilar value of dielectric constant of oxides used in RRAMs.

Electroforming in EMC sells. For the repetitive resistive switching, EMC memory cell needs an electroforming cycle. The electroforming imposes asymmetry on the system. The Pt/SiO2/Pt device, for example, did not show any breakdown up to seven volts; therefore, the required asymmetry can be introduced by using the inert and oxidizable electrodes in the MIM structure. Electroforming can also be thought as a current-limited dielectric breakdown (Schindler 2009).

The voltage during switching is typically lower than during electroforming. The difference in voltage can be due to the existence of the partly dissolved filament from the previous cycle (Schindler 2009). Typically, the electroforming voltage is a function of the

layer thickness, whereas the SET voltage does not depend on the device geometry (Tappertzhofen 2014).

The film density affects the electroforming characteristics but not switching voltage. The film density increases after annealing which causes a consequent increase in the forming voltage. The denser films make the ion motion more difficult, and a higher electric field is necessary to create a conductive path (Schindler 2009).

In addition, the electroforming can be explained via the creation of a conductive path through the cracks in the oxide layer. These cracks might occur because of an electrodeposit growing from the inert electrode. The electrodeposits then can cause mechanical stress and cracks, making further filament growth to take place. However, the switching voltage shows a rather high variability in a single sample (Schindler 2009; Tappertzhofen 2014).

The electroforming voltage depends on the temperature when the voltage drops at 120°C. At higher temperatures, the increased mobility of ions may explain this voltage drop. The OFF state in ECM cell was stable up to 120°C, but the ON resistance was completely lost at temperatures >50°C (Schindler 2009).

2.1.4 The threshold switching

Preface. The chalcogenide glasses, niobium and vanadium oxides often display the threshold switching tightly bounded with the S-type of negative differential resistance. It means that during switching both effects show up simultaneously. Nevertheless, other oxides can display the threshold switching (TS) and negative differential resistance separately (NDR) at specific bias. In addition, the explanations of the observed effects together with the conduction mechanisms are usually the materials- or the oxide type- specific. First, the threshold switching behavior in chalcogenides, niobium and vanadium oxides would be reviewed, and then the TS effect would be explained for other oxides, amorphous Si, and SiO2.

The TS in chalcogenides. The chalcogenide- based devices display the reversible transition between the crystalline and the amorphous phase, which was named as Ovonic memory switching (OMS). The switching without such transition would be ovonic threshold switching (OTS) (Redaelli et al. 2008). The amorphous phase of the Ge-Sb-Te-based memory cell exhibits simultaneously the threshold switching and the S-type of the negative differential conductance (Redaelli et al. 2008). The threshold switching (OTS) in the chalcogenide glasses controls the operating voltage and the switching kinetics (Ielmini 2008).

The threshold switching is supposed to be the pure electronic effect (Redaelli et al. 2008; Le Gallo et al. 2016; Zalden et al. 2016; Pandey & Manivannan 2016) because the switching is faster than the crystallization can occur (Zalden et al. 2016). In addition, the transition to amorphous from a crystalline state is faster than from amorphous to the crystallized phase (Pandey & Manivannan 2016).

In chalcogenides, *the non-inform electric field,* as well as *a non-equilibrium population* of the high-mobility shallow traps in the band gap, may explain the TS switching in these glasses (Ielmini & Zhang 2007). Additionally, the TS can exist due to an *unstable transport of electrons* at a high electric field. In a forbidden gap of chalcogenide glasses, the concentration of the trap states is high. Consequently, the Fermi level would be in the central part of the band gap implying a high resistivity of the disordered glass structure. Therefore, the trap states would control the conductivity of the chalcogenide glasses (Ielmini 2008).

Moreover, the TS conduction in the chalcogenides may be attributed to *the Poole –Frenkel* conduction as a result of the deep traps in the band of the amorphous semiconductor (Ielmini & Zhang 2007), *the thermally induced Poole-Frenkel (P-F)* conduction or *the field –induced small polaron hopping* (Ielmini 2008).

Furthermore, the switching in the phase-change materials is explained by *the Joule-heating –induced* (Le Gallo et al. 2016) *thermal feedback* or by *a Joule heating-based thermal model* (Zalden et al. 2016).

Finally, therefore, the range of the explanation of the TS in chalcogenides varies from the pure electronic to just a thermal effect due to the Joule heating.

Niobium oxides. The threshold switching (TS) in the NbO2- based structures (Kim et al. 2013; Slesazeck et al. 2015) can be explained with (Kim et al. 2013) and without the influence of the metal- insulator transition (Slesazeck et al. 2015). The different switching type (TS or MS) is associated to the different Nb and O ratio because the TS switching is found in NbO2, whereas the MS in Nb2O5 (Kim et al. 2013).

The TS may be attributed to the temperature- activated and trap-assisted *Frenkel-Poole* like (P-F)conduction mechanism (Slesazeck et al. 2015), the electric field –triggered *Joule heating*- induced metal-insulator transition (IMT) or changes in electronic structure (Wang et al. 2016) as well as the *field- triggered thermal runaway (FTTR)* (Funck et al. 2016a). In the FTTP model, the temperature dependence is smaller than in the IMT model. In addition, the FTTR is based on an intrinsic hopping of polarons together with lowering the barrier similar to the P-F conduction (Funck et al. 2016a).

Vanadium oxides. The V2O5-ZnO-SrO-FeO structure exhibits the threshold switching which is explained as being due to the absence of the structural reorganization in the glass. Unlike the TS switching, the memory switching (MS) requires the structural change in

the rigid cross-linked glassy networks. (Ahmed 2013). The large variability of the switching voltage during the TS in the ViO2-based memory cell is attributed to the Joule heating (Lee et al. 2013).

Other oxide structures. The *Co-doped polycrystalline LBFCO* ceramics exhibits threshold switching (TS) at elevated temperatures and the memory switching (MS) at room temperature. The dopant increases the leakage current and concentration of the oxygen vacancies (Wang et al. 2012). *The ZnO/GaN heterostructure* exhibits the threshold switching (TS), which is assumed to be due to the traps of electrons at the oxygen vacancies and other deep level defects, which act as the trap centers. The threshold voltage decreases with increasing the concentration of the Mn dopants (Zhou et al. 2014).

The Ag-Cu2O structure exhibits the bi-directional threshold switching due to the unstable Ag-filament, which can spontaneously rupture in the Cu2O layer. The bi-directional behavior was achieved by engineering of a multilayer stack of Cu2O/Ag: Cu2O/Cu2O (Song et al. 2015). The MS and TS switching coexist in *the AlOx-based* crossbar RRAM. The current compliance controls the transition between the MS and TS switching mode. Threshold switching is explained being due to an electron transport through the oxygen vacancies acting as a point defect. The F-N tunneling can explain the conduction in the LRS state (Banerjee et al. 2015).

Silicon, zirconium oxide and silicon dioxide. The *hydrogen- treated Ag-amorphous Si –* based device exhibits threshold switching because such treatment enhances the dissolution of the Ag filament. Reducing the stability of the metallic filament is beneficial for obtaining the threshold switching at higher level of current compliance (Yoo et al. 2015).

The current compliance in the *Ag/SiO2/Pt memory cell* controls the switching mode because the volatile TS and non-volatile MS switching can coexist in the same memory cell. The MS switching is associated with the creation and electrochemical dissolution of the continuous conducting filament (CF), whereas the TS switching operates with the discontinuous CF between isolated Ag crystals. The tunneling barrier exists between nanocrystals (Sun et al. 2014).

Both *Cu/ZrO2/Pt* and *Ag/ZrO2/Pt* memories exhibit a threshold switching (TS), which is explained being due to the moisture absorption. The absorbed water molecules would create the networks of hydrogen and enhance the anodic oxidation and the Ag- ion migration. Moreover, the TS behavior in the electron beam evaporated and sputtered Ta2O5-based device is related to the different porosity level and the moisture uptake from the ambient environment. In addition, the absorbed moisture may influence the electromotive force, under the influence of which the spontaneous dissolution of the metallic filament would be driven during TS switching (Du et al. 2016).

2.1.5 Negative differential resistance (NDR)

Preface. The systems having the S-type negative differential resistance would be intrinsically unstable (Hudgens 2012). In the current-voltage characteristic, the region of the negative differential resistance is unstable (Zhang et al. 2015).

The TS effect can be used for the selector applications in ReRAMs and as the electric oscillator. These oscillators do not require any inductive elements or transistors as in the conventional ones. The region of NDR in the current-voltage curve was attributed to the oscillations. Such a device displays the sporadic, relaxation, and damped oscillations. The oscillations depend on the series resistance as well as on the applied voltage. The oscillation frequency can be adjusted by the load resistance or the source voltage (Liu et al. 2016).

NDR in different materials systems. Many material systems were frequently reported having the intrinsic negative differential resistance (NDR) such as *chalcogenides* displaying the current- controlled S-type NDR (Redaelli et al. 2008; Hudgens 2012). Nevertheless, the NDR was often reported in the materials having a specific chemical group like the nitroamine in the self-assembled monolayers (SAMs) (Chen et al. 2003) as well as the dopant concentration (up to 2.5%) and the geometrical restriction of the conductive filament in the *V2O5-ZnO-SrO-FeO* glass (Ahmed 2013).

Moreover, the creation of new oxygen-deficient oxide phase such as *AlOx* at the interface of the Al/Pr0.7Ca0.3MnO3 (Li et al. 2009), new sub-oxide in the TiO2-x/TaOx-based structure (Yang et al. 2012) as well as a new suboxide phase at the interface of Ti/HfOx (Chen et al. 2010) were connected to the NDR effect. In addition, the high-density state of the defects in the boundaries of the ZnO- nanorods was attributed to the NDR effect too (Chuang et al. 2014).

Trapping of electrons. In addition, the electron trapping or detrapping by the oxygen vacancies in the TiO2-based devices (Du et al. 2012; Zervos et al. 2015) as well as Ag nanocrystals in Ag/SiO2/Pt structure (Sun et al. 2014), for example, were related to the NDR effect. Nevertheless, the entire switching in the Al/TiOx /TiO2 /Al cell and the Cu/BaTiO3/Ag device were attributed to the oxygen vacancies trapping electrons (Kim & Choi 2009).

Tunneling. Moreover, the NDR was explained by the different tunneling effects. For example, the graphene-based multi-junction heterostructure shows the room-temperature NDR explained by *the resonant tunneling between two separated quantum states* (Lin et al. 2015). Additionally, deviating from the ideal step function for the NDR in transition metal oxides was explained by "*the quantum mechanical tunneling of electrons"* between

discontinious parts of the filament. Furthermore, the NDR is explained as the Joule heating- assisted transition from order to disorder in the conductive filament (Jeong et al. 2006).

The moisture effect. In many cases, the moisture from the ambient environment is not negligible for the NDR effect. The nearly identical NDR effect was observed in TiO2, Al2O3 and the banana skins in the presence of the ambient moisture. The water- inducing tunneling, the water absorption and decomposition can explain the NDR in these materials. The TiO2 and Al2O3 are intrinsic NDR materials, but the SiO2 and banana skin are not (Li et al. 2014).

2.2 Structure and morphology of SiO2

The glass structure of SiO2. The glasses are supercooled liquids, which form the extended non-periodic three-dimensional networks. The networks are not completely random, but all states are not equally probable. One can imagine the glass as a unit cell of infinite size comprising of an infinite number of atoms (Zachariasen 1932). The covalently bonded amorphous oxide has mainly the short-range order, but at longer ranges, the order is missing. Moreover, the comparatively ordered networks and rings are connected by surface states or dangling bonds (Dearnaley et al. 1970). The silicon dioxide has the SiO4 tetrahedra as single units, which is formed by joining SiO_4^{-4} in circles, chains, planes, and 3D structures (Galasso 2016).

The chemical composition of the glass structure can be written as A_mB_nO, where B is the glass-forming and A are other cations, n and m represent the non- integer number of atoms per each oxygen. The value of n of about 0.5 is the most advantageous for the glass structure. B- cations may surround the tetrahedra or triangles of oxygen. The glass should contain the glass-forming cations as Si+4, for example, or cations able for replacing B cations isomorphously. For example, Al2O3 cannot form glass, but Al+3 can replace Si+4 isomorphously (Zachariasen 1932).

For valence balancing, statistically distributed cations and holes need to be added to the network. The cation size in the hole determines the dimensions of holes. The repulsive potential between cations A and B should be negligible. Therefore, the distance between the cations B and cations A must be large. A- cations need to be large and have a small charge (Zachariasen 1932).

The cations A are usually alkali ions. The cations B are usually more tightly bound to the atoms of oxygen than the alkali cations A. Therefore, increasing the temperature of some migrating atoms A can occur without a significant breakage of the vitreous network. Univalent cations should migrate easier than the divalent ones. In addition, with the same charge, the smaller cations migrate easier than large ones. The electric conductivity of

glass, therefore, should be electrolytic and be a function of temperature (Zachariasen 1932).

Chemical defects in SiO2. The oxygen interstitials are the intrinsic defect with the highest concentration of the equilibrated alfa-quartz and silica, where the compensation of charge can be between the *negative interstitials of oxygen* and positive holes in the valence band. The defect concentration is the partial oxygen pressure and temperature dependent. The negative interstitials should be dominant at the high temperature and low pressure, while at the high-pressure and low-temperature the neutral defect should dominate. Due to the low concentration, the contribution of the negative oxygen interstitials to the ionic conductivity is negligible, however, if Fermi level due to the impurities, for example, raises, then the negative interstitials would make a substantial contribution to the ionic conductivity (Roma & Limoge 2004).

In the SiO2 glasses, the most common defects are *the oxygen vacancies*. In addition, the dangling bonds due to the modifier ions and strained Si-O bonds are formed. Two types of the paramagnetic dangling bond type defects dominate: the dangling bonds of oxygen and silicon. The oxygen dangling bonds are related to the non-bridging oxygen hole center. Induced by radiation, the interstitial atoms of oxygen are in the pyroxy mode (Si-O-O-Si), which interact with the dangling bonds of oxygen. The hydrogen doping reduces the defect concentration, however, produces new hydroxyl groups which are precursors and promote the generation of the oxygen vacancies (Skuja et al. 2005).

In the lattice, at the low temperatures, the interstitial states are empty and the normal states are fully occupied. With the increase in the temperature, the 'self-interstitial-vacancy pairs' are created due to the intrinsic thermal disorder. Therefore, the combined sub-lattices are partly occupied (Kilner 2000). The results of the emf and conductance measurements in the solid-state electrochemical cells based at the high impurity amorphous SiO2 suggest that the doubly charged oxygen interstitials as the native defects are mainly responsible for the ionic conduction at the elevated temperatures (Mills & Kroger 1973).

SiO2 as a dielectric material. The insulating materials should have a combination of the good dielectric properties together with the thermal and mechanical stability. The chemical structure of material affects its structural stability, which associates with a high density of the strong atomic bonds. Moreover, the strongest and the densest bonds are usually the most polarizable as in the case of SiO2, for example. The SiO2 has the relatively high dielectric constant (k=4). The decrease in density due to creating a porous strucuture causes decrease in the dielectric constant and polarizability, however, at the expense of the thermomechanical properties. In addition, increasing the porosity over 30% causes the percolation and interconnection of the porous network. Consequently, the local trapping of the impurities and moisture can cause the crack formation or increase in a dielectric constant (Ho et al. 2003). In addition, SiO2 is not only an insulator but also, at the

elevated temperature, a wide-gap semiconductor working as an active layer for the semiconductor devices (Han et al. 2010).

The incorporation of the lighter atoms or less polarizable bonds decreases *the dielectric constant*. The polarization in materials consists of the electronic, atomic, and orientational components. SiO2 has a large nuclear component due to the strong atomic polarization. The orientational polarization in the thin films arises due to the absorbed moisture. The water molecules have dipole moments, which are large and permanent. Therefore, water absorbed from ambient environment affects directly on the dielectric constant of materials (Ho et al. 2003).

At a temperature between 200 and 400°C, *charge storage* was identified under metal contact in the Si/SiO2/Metal structure. Development of charges can be a result of nonelectrical processes, the formation of double-layer or electrode discharge. The electrolytic rectification at the silicon-oxide boundary caused the unidirectionality of ohmic conduction and the asymmetry with the high differential capacitance at the silicon-oxide interface (Yamin 1965).

Microstructural defects. The concentration and the arrangement of defects such as pores, grain boundaries, dislocations, and impurities affect the physical properties of the material (Tuller & Bishop 2011).

*The dielectric breakdown of SiO2***.** The dielectric breakdown strength of the thermally grown SiO2 depends on how it was measured. Artifacts, thickness of metallurgical contact, oxide thickness, capacitor area, applied bias voltage, instrument impedance, and time constant have an influence on the breakdown properties of oxide. The breakdown characteristics of the thermally grown SiO2 films on the Si substrate are weakly affected by the dopant concentration in the silicon wafer, oxide thickness, metallization, measuring temperature or the oxidation ambient (Osburn & Ormond 1972b). The dielectric strength of the sputtered SiO2 is $0.5 \cdot 10^9\ V/m$ (Bartzsch et al. 2009).

SiO2 as the electrolyte. In MOS (metal-oxide-semiconductor) devices, silicon dioxide should be considered as a solid ***electrolyte*** rather than an insulator (Revesz 1965). Ionic solids may be *solid electrolytes* having pure ion-conducting or mixed conducting ionic-electronic behavior (Maier 2005).

An electrochemical cell consisting of two metal electrodes separated by *electrolyte* can dissolve and conduct ions. At the nanoscale thin films, the normally dielectric materials may act as *an electrolyte*. The thin films may exhibit quantization of the energy and electronic conductance as well as the effect of Coulomb blockade. Metallic ions (Ag, Ni, and Cu) may be electrochemically dissolved into SiO2 (Valov & Lu 2016).

Conductivities in pure SiO2. Not only predominantly *ionic*, *electronic* but also *mixed ionic-electronic behavior* was found in amorphous silicon dioxide films at elevated temperatures, where, ionic conduction was attributed to doubly charged oxygen interstitial (Mills & Kroger 1973). *The electronic transport* in an amorphous insulator SiO2 is described to be diffusive with Brownian-like motion involving carrier trapping rather than scattering (Wager 2017).

Impurities in SiO2. Below 450C, the conductivities of the thermally grown silicon dioxide were independent of temperature and attributed to *impurities* inside insulator. Above 450C, the dc conductivity of SiO2 increased with increase in temperature. In the temperature range between 500C and 960C, ionic as well as electronic conduction type was identified; the ionic conduction was attributed to the transport of oxygen ions (Srivastava et al. 1985).

The mobile ionic charges *(impurities of alkali ions or H+)* in the SiO2 can cause an unwanted instability of the electrical parameters in devices, which can be eliminated using the ultra-clean processing. Under applied field, decreasing of ionic conductivity with time can be attributed to the limited supply of ions, which cannot be freely injected into the oxide. Therefore, space charges will build up. Removing the external field causes ions to move back to equilibrium state causing the effect of a hysteresis (Bentarzi 2011).

According to ab initio modeling, the strained Si–O bonds may be broken by *H atoms* in amorphous silicon dioxide (a-SiO2) networks. The created dangling bonds are attributed to a 3-coordinated Si atom with an unpaired electron (El-Sayed et al. 2015).

2.3 Doping

Introduction. In the next section, the concept of the doping of SiO2 will be introduced. In addition, the doping of other oxides will be separately represented in Appendix 3.The aim was to determine the possible effects, which can be observed during the doping. In our case, the concentration of the doping elements is expected to be less in the memory cells than in the doped targets. Moreover, the available analytic techniques could not reliably measure the very low concentration of the doping elements. Therefore, the focus was mainly on the electrical characterization of the ECM cells to observe the possible differences due to doping.

Doping in general. Doping in *semiconductors i*ntroduces electrons or holes whereas doping in *ionic crystals* creates excess cation or anion vacancies (Sunandana 2015).

The ionic conductivity can be optimized by a specific structure or compound as well as materials modifications. The homogeneous doping with aliovalent ions causes the dissolution of dopant in the matrix and affects the ions concentration. The local electrical neutrality is required for the homogeneous doping. On the other hand, heterogeneous doping

means the adding of another phase where the deviation from local electrical neutrality may occur (Maier 1995).

2.3.1 Doping of SiO2

The doping of SiO2. *In acceptor* doped silica *(like B),* a decrease in O_i'' and increase in $h^\bullet$ as well as an increase in $V_O^{\bullet\bullet}$ and a decrease in e' would be observed. According to Kroger and Vink's notation, $h^\bullet$, e', $V_O^{\bullet\bullet}$ and O_i'' refer to ionized holes, electrons, oxygen vacancies and oxygen interstitials. A superscript dot refers to a positive charge and dash to a negative charge. Doping with *donors* would have the opposite effect (Mills & Kroger 1973). However, doping here means the introduction of *donors or acceptors*, which replace the Si in silica networks. These acceptors and donors work as network formers in silica. On the other hand, the introduction of metallic cations in silica does not imply such a replacement as shown in Figure 1. These cations work as network modifiers.

Figure 1 shows 2D- schematics of possible defects in SiO2 (Revesz 1965). It can be seen that cations (Me+ or Me++), which are added in silica glass, take the place of interstitials in silica networks and work as network modifiers. Using the schematics shown in Figure 1, it can be suggested that adding cations (Me+ or Me++) would affect directly the concentration of dangling bonds (or non-bridging bonds) in silica. Due to charge neutrality, adding of Me+ would require the creation of the non-bridging oxygen interstitial and non-bridging oxygen. Adding of Me++ would requre the creation of individual non-bridging oxygen vacancy and one non-bridging oxygen. It can be suggested that introduction of non-bridging bonds due to network modifiers would create the porous nanostructure in SiO2.

Therefore, both the substitution of Si in silica networks and the introduction of cations would affect the nanostructure of SiO2. Moreover, it should also affect the switching properties of silica. Not only the dopant concentration or its form (atom or ion) but also valency and even exact position as a network modifier or former would affect the switching properties of silica.

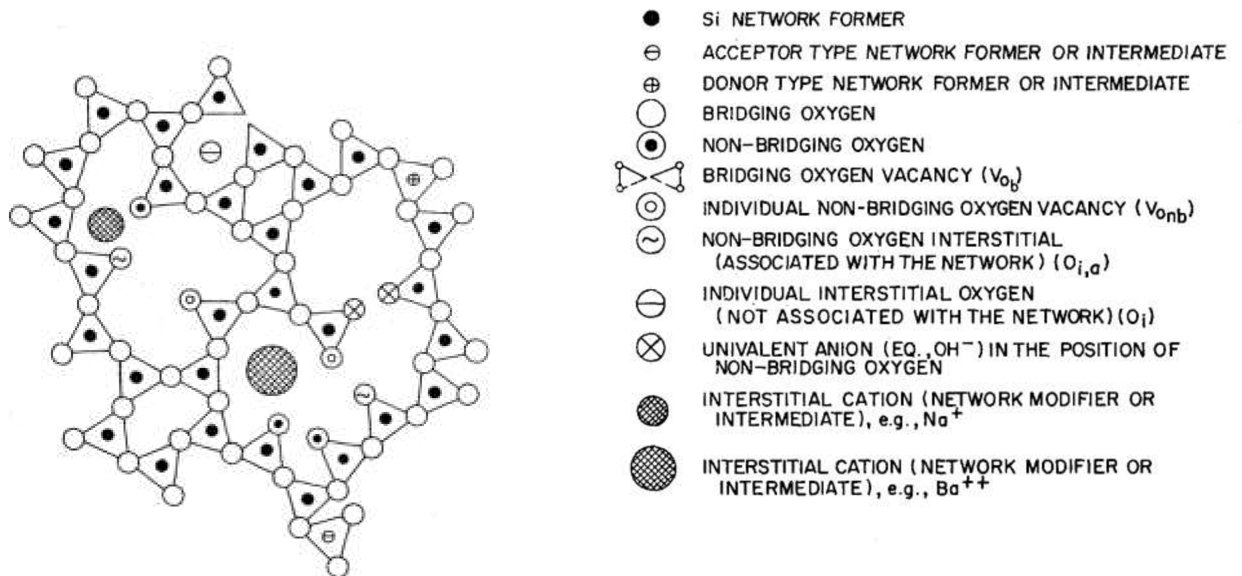

Figure 1. *Schematics of possible defects in a silica networks (Revesz 1965).*

The doping of SiO2 by Al. The doping of SiO2 with Al could have a different influence on the electrical properties silica. The Al ion can be interstitial in silica; it can *replace Si* in a lattice or be as a different secondary phase in silica. The replacement of Si+4 by Al3+ (or Me+++) in the silica network (Zachariasen 1932) is possible. However, Al can be introduced in silica in other forms without direct replacing of Si in the silica network.

In amorphous silica, inhibition of both the network and interstitial diffusion of oxygen was attributed to the small concentration of Al-dopants. However, these dopants did not replace Si in SiO2. The impurities in the silica network generate non-bridging O working as an easier path to oxygen transport. The six-membered rings of silica chains can pass the oxygen through. This controls the interstitial diffusion of oxygen. The Al-doped silica needs twice as high activation energy for diffusion than pure silica (Wang et al. 2006).

According to the ab initio calculations, Al_{Si} and P_{Si} would be the best choice for p- and n-type doping of SiO2 (Han et al. 2010). Moreover, the solubility of Er^{3+} in SiO2 has been enhanced when silica was co-doped by Al and P. The Al-doping increases the entropy of mixing (Saitoh et al. 2006; Yang et al. 2008), whereas doping by P influences the enthalpy (Saitoh et al. 2006).

Furthermore, Al-doped buried SiO2 was used for creating of holes as the majority charge carriers in a nearby layer of Si. Due to that, the acceptor states below the valence band edge of Si were created (Konig et al. 2017). This technique resembles the heterogeneous doping techniques using for the doping of ionic solids.

The substitution of Al^{3+} for Si^{4+} in the natural and synthetic porous zeolites creates the useful defects. The metallic cations or protons, for example, balance the charge to achieve

the overall neutrality in the solid. The holes as the charge carriers can hop between nearby oxygen and behave as a 'small bound polaron' (To et al. 2005).

Using the modified DFT+U (density functional theory, the electronic and atomic structure of the SiO2 doped with Al were modelled with the localized hole state created above the valence band. The Al-doped SiO2 has a hole, which would be shared by the four atoms of oxygen, however, one elongated Al-O bond would be structurally distorted (Saitoh et al. 2006; Yang et al. 2008).

According to the first principle calculations, the sharp DOS (the electronic density of state) peaks are found in the Al2O3- doped SiO2. In the networks of –[Al-O-Al]– bonds, this corresponds to the unsaturated 2p orbitals of the oxygen (Yang et al. 2008).

The Al-doping of SiGe –rich SiO2 enhances photoluminescence intensity in comparison to the samples without Al. However, the deterioration of photoluminescence was observed at a concentration level of 6×10^{14} cm^{-2} because the Al impurity generated a deep trap level in the band gap of the GeSi –nanoparticles (Zhong et al. 2011).

Trivalent defects in Si can be made by other means than using the doping technique. For example, in MOS (metal-oxide-semiconductor) devices, trivalent silicon can be obtained during oxide reduction using hydrogen or metal. Such a defect may act as the surface state with donor function. When an electric field is applied, migrating ions of metal may cause asymmetry in I-V characteristic, transient, and hysteresis effects. The uniformity of the defect distribution depends on oxidation (Revesz 1965).

Based on simulations and experimental results, the Al-doped silica may exhibit many possible effects, depending on the exact position of Al in glass networks. The replacement of Si by Al in silica causes the increase in oxygen vacancies. Also, Al interstitial would generate non-bringing oxygen, which can accelerate the network diffusion of oxygen. The presence of non-bridging oxygen would suggest also the more open porous nanostructure of silica doped with interstitial of Al. Increase in porosity could be identified by means of XRR, for example, or the measurement of dielectric constant.

The doping of SiO2 by Cu. The study of the Cu-doped SiO2 film shows that Cu remains in the elemental form after the diffusion for the annealing conditions used.Therefore, Cu does not react with the SiO2 (Thermadam et al. 2010). The electrical characterization of the Cu-SiO2 memory cell shows that also multi-bit storage is possible in a single cell. The material characterization suggests that Cu is present in the insulator as free atoms. In addition, the creation of the stress-induced voids in the insulator is the possible driving force of the Cu diffusion in oxide (Puthenthermadam 2011).

A SiO2 based PCM makes the transition from threshold switching to bipolar resistive switching after thermal doping with Cu. The suppression of Cu diffusion and/or the elimination emf due to moisture in the porous SiO2 matrix can explain the enhancement of

filament stability in a doped sample however with a larger cycle-to-cycle variation (Chen et al. 2016).

In the Cu- or Al-doped SiO2 memory cells, the conductive filament consists of many discrete Ag –particles. The low mobility of ions, as well as the low rate of redox reactions, can explain the granular structure of the conductive filament in the SiO2. It is estimated that diffusion coefficient of cations in nanoscale SiO2 is higher than bulk materials. The improvement of the retention in low resistive states can be made by reducing the diffusion, by doping of SiO2 with ions of metals as well as by increasing the oxide density. Nevertheless, the excessive doping could cause the degradation of off-state resistance. Too dense SiO2 slows down the switching speed and causes the cells to stack in LRS (Chen et al. 2017a).

The doping of SiO2 by Ni. The Ni-doping SiO2 was used in the Pt/Ni: SiO2 /TiN –based ReRAM device. The two separate targets of N and SiO2 were used for the sputtering of the doped SiO2. According to FTIR (Fourier transform infrared spectroscopy), the stretched Ni-O and O-H bonds were found (Tsai et al. 2012b).

In addition, the control sample with the structure of Pt/SiO2 /TiN was fabricated, which does not, however, shows the switching or electroforming behavior even at 30V with a current of 10^{-7}A. On the other hand, the Ni-doped sample switches with a relatively high current compliance of 0.01A and voltage bias +3V/-2V (Tsai et al. 2012b). The Frenkel-Poole and ohmic type of conduction were identified in the different regions of the same I-V curve. However, the temperature dependent tests for the differentiation of Poole-Frenkel and Schottky emissions were not mentioned. On the other hand, the cyclic endurance at 85C was evaluated. Moreover, it is possible that the same level of current compliance needs to be used in the control sample for the evaluation the doping effect.

The doping of SiO2 by Zr and C. The Pt/Zr: SiOx/ TiN and Pt/Zr: SiOx/C: SiOx/TiN device structures were investigated with compliance current of 1mA and voltage of +1V/-1.5V. Frenkel-Poole, ohmic type, and hopping conduction mechanisms were identified (Zhang et al. 2013).

The doping of SiO2 by Sn. The Pt/Sn: SiOx /TiN device structure was investigated using the supercritical CO2 to cross-link the dangling bonds. After treatment, the ohmic conduction was replaced by hopping (Tsai et al. 2012a).

The doping of SiO2 by ZnO. The ITO/ZnO: SiO2/ZnOx /TiN –based device was studied with the current compliance of 1mA and voltage bias +0.6V/-0.6V. The Indium –Tin-oxide (ITO) was used to create a concentration gradient of oxygen (Huang et al. 2014).

The doping of SiO2 by other elements. At the slight levels of doping, the resistivity of polycrystalline Si films does not depend on dopant concentration. However, in the heavily

doped regions, resistivity is a function of dopant concentration, which can be explained by dopant segregation in the grain boundaries (Fripp 1975).

Decrease in the amount of strained Si-O bonds was achieved by *doping of silica by F.* This has influence on optical properties of silica (Skuja et al. 2005), such as the radiation toughness and the vacuum-ultraviolet optical transmission. Co-doping by F enhances the rare earth ions' solubility in the silica glass melt (Funabiki et al. 2012). In addition, doping by F decreases the dielectric constant of SiO2 from 4 to 2.6 (Lim et al. 1999).

The doping by N results in the formation of a SiO_xN_y thin film with two separate phases of SiO2 and Si_3N_4 (Toyoda et al. 2003).

SiOx can be used as the sole active material in the memory cell, with switching occurring due to the creation and modification of Si nanocrystals (NCs) inside SiOx (Yao et al. 2010).

A Ti/In2O3: SiO2/Pt device exhibits the bipolar switching behavior, which is explained to be due to a high quality of the fabricated interface between the switching layer and top electrode, as well as migration of oxygen ions (Hsieh et al. 2014).

There is a correlation between the solubility limit of the impurity atoms in the non-stoichiometric materials and ionic radii of the impurity atoms. The solubility limit increases with the increased concentration of the charged and neutral cation vacancies (Rogacheva 2008).

2.4 Other methods for improving resistive switching

The doping, *varying oxygen* content or *annealing* after the deposition can modify the functional layer. Moreover, using a *buffer layer* or *changing the electrode* can improve the interface between the functional layer and electrode. The formation of the oxygen vacancies in the functional layer occurs when the metal electrode oxidizes. In summary, ECM needs the specific electrodes. However, in the VCM, the TiN or Ti electrode works as the reservoirs of oxygen and thus can deliver enough nonlattice oxygen vacancies and form filaments (Lian et al. 2011).

As for VCM, *the buffer layer* is typically a metal oxide or the oxidizing metal. In ECM, doping with Ag or Cu impurities can raise the concentration of the mobile cations. Whereas in VCM, more oxygen vacancies are created after doping with Li and Ti. These dopants have a higher absorption of oxygen than other impurities. The doping of tetravalent metal oxides by trivalent elements like Al, for example, would lower the energy for generating the vacancies of the oxygen. It would also facilitate creating the filaments along the doping locations (Lian et al. 2011).

2.5 Conduction mechanism

2.5.1 Preface

Conduction in insulators usually shows a clear temperature dependence. The common conduction mechanisms are Schottky emission, the Poole-Frenkel emission, the hopping conduction, as well as the space-charge-limited current (SCLC) (Dearnaley et al. 1970) and ionic conduction (Lim & Ismail 2015).

The Schottky emission is an emission of thermally excited electrons over the energy barrier into the conduction band of the insulator. This mechanism usually occurs at a high temperature in oxides (Lim & Ismail 2015). The Poole-Frenkel emission is the emission of electrons, which are excited by the electric field and trapped by immobile positive charge into the conduction band of insulator (Dearnaley et al. 1970).

The hopping conduction can be divided on the nearest neighbor hopping (NNH) and the Mott variable-range hopping (VRH). In the NNH mechanism, the electrons trapped in the insulator can hop into another trap location which is located a quite near. The trapping center can be defects in the oxide, for example. Unlike in NNH, the electrons in VRH can hope to the trap location, which is far away, but with relatively low energy. The SCLC is conduction mechanism limited by space charge and controlled by traps. This mechanism has $I \propto V$ (ohmic), $I \propto V^2$(Child's law), as well as a steep increase at the high field, regions (Lim & Ismail 2015).

2.5.2 Schottky emission

In Schottky emission, current density has dependency on both E (the electric field) and T (temperature). At a constant temperature, $\ln(J) \propto E^{1/2}$ is a straight line (Lim & Ismail 2015). Owing to the fact, that Schottky emission is the conducting mechanism, limited by the electrode, the current- voltage characteristics of the memory cell with different electrode material tend to be asymmetric, which can be employed for differentiating the Schottky emission from other mechanisms, limited by the bulk properties (Lim & Ismail 2015).

A sufficient linear relationship in the plot of $ln(J)$ and $\sqrt{V}$ indicates that the Schottky emission in Al/VO_x/Cu dominates as a conduction mechanism on highly resistive states. However, on low resistive states, the ohmic conduction is supposed to be dominant

$$J = \frac{4\pi q m^*(kT)^2}{h^3} \exp\left[\frac{-q\left(\phi_B - \sqrt{\frac{qE}{4\pi\varepsilon}}\right)}{kT}\right]$$ (Lim & Ismail 2015).

The derivation for plotting is made below.

$$\ln J = \ln\left(\frac{4\pi q m^*(kT)^2}{h^3}\cdot e^{\left[\frac{-q\left(\phi_B-\sqrt{\frac{qE}{4\pi\varepsilon}}\right)}{kT}\right]}\right)$$

$$= \underbrace{\ln\frac{4\pi q m^*(kT)^2}{h^3}}_{constant} + \ln\left(e^{\left[\frac{-q\left(\phi_B-\sqrt{\frac{qE}{4\pi\varepsilon}}\right)}{kT}\right]}\right) =$$

$$= \underbrace{\ln\frac{4\pi q m^*(kT)^2}{h^3}}_{constant} + \left[\frac{-q\left(\phi_B-\sqrt{\frac{qE}{4\pi\varepsilon}}\right)}{kT}\right]\cdot\underbrace{\ln e}_{1}$$

$$\ln J = A + \frac{-q\left(\phi_B-\sqrt{\frac{qE}{4\pi\varepsilon}}\right)}{kT} = A - \frac{q\cdot\phi_B}{kT} + \frac{1}{kT}\cdot\sqrt{\frac{qE}{4\pi\varepsilon}}$$

$$= \underbrace{\underbrace{\ln\frac{4\pi q m^*(kT)^2}{h^3}}_{constant} - \underbrace{\frac{q\cdot\phi_B}{kT}}_{constant}}_{B} + \underbrace{\underbrace{\frac{1}{kT}\cdot\sqrt{\frac{q}{4\pi\varepsilon}}}_{constant}}_{C}\cdot\sqrt{E}$$

$$\ln J = B + C\cdot\sqrt{E}$$

In the equation, A^*, J, m^*, m_0 , $T,$ k are the effective Richardson constant, current density, the effective electron mass , as well as free electron mass, the absolute temperature, and Boltzmann's constant, respectively. In addition, $q\cdot\phi_B$, q, E, h, ε_0, ε are the Schottky barrier height, the electronic charge, the electric field, Planck's constant, as well as the vacuum permittivity, and the dynamic dielectric constant, correspondently (Lim & Ismail 2015).

2.5.3 Poole- Frenkel Emission

The conduction mechanism dominated by Poole-Frenkel emission should have the linear fit if the current-voltage characteristic is drawn using $\ln(J/E)$ $vs.$ $(E^{1/2}/T)$ scale, based on the equation $J_{PF} = q\cdot\mu\cdot N_C\cdot E\cdot\exp\left[\frac{-q(\phi_T-\sqrt{qE/\pi\varepsilon}}{kT}\right]$ (Lim & Ismail 2015).

The derivation for the plotting

$$\ln J_{PF} = \ln\left(q\cdot\mu\cdot N_C\cdot E\cdot\exp\left[\frac{-q(\phi_T-\sqrt{qE/\pi\varepsilon}}{kT}\right]\right)$$

$$\ln J_{PF} = \underbrace{\ln q \cdot \mu \cdot N_C}_{A} + \ln E - \underbrace{\frac{q \cdot \phi_T}{k}}_{B} + \underbrace{\frac{\sqrt{q/\pi\varepsilon}}{k}}_{C} \cdot \frac{\sqrt{E}}{T}$$

$$\ln J_{PF} = \underbrace{A - B}_{D} + \ln E + C \cdot \frac{\sqrt{E}}{T}$$

$$\ln J_{PF} = \ln E + C \cdot \frac{\sqrt{E}}{T} + D$$

$$\ln \frac{J}{E} = C \frac{\sqrt{E}}{T} + D$$

Usually, the linear relationship in the $\ln(J/E)\ vs.\ (E^{1/2}/T)$plot identifies the P-F emission. The extra fitting of the temperature dependency in the plot $\ln \frac{J}{T^2} \propto 1/T$ as well as the current-voltage-characteristics can help to differentiate the Poole-Frenkel from the Schottky emission (Lim & Ismail 2015).

3. THE RESULTS AND ANALYSIS

The research methodology, as well as overall results of the materials characterization by the SEM, EDX, XRR, and XRD, are introduced in Appendix 4. Additionally, the general information of the fabrication of the ECM memory cell can be found in Appendix 3. The description and comparison of the relevant statistics methods such as the exploratory data analysis (EDA) and analysis of variance (ANOVA) are introduced in Appendix 5.

3.1 Structural and morphological characterization

Here, only the summarized results of XRR analysis are presented. The focus is on the existing trends and variability of the results.

3.1.1 XRR

Figure 2 presents the deposition rates of the TD0 and TD1 targets drawn versus the RF power. Since the fitted straight lines have different slopes, the deposition rate of the doped TD1 target is higher than for the undoped TD0 target. In addition, the linear correlation between the deposition rate and the power is shown: the higher the RF power, the higher the deposition rate. Moreover, the deposition rate relates in a straightforward manner to the thickness of the deposited layer.

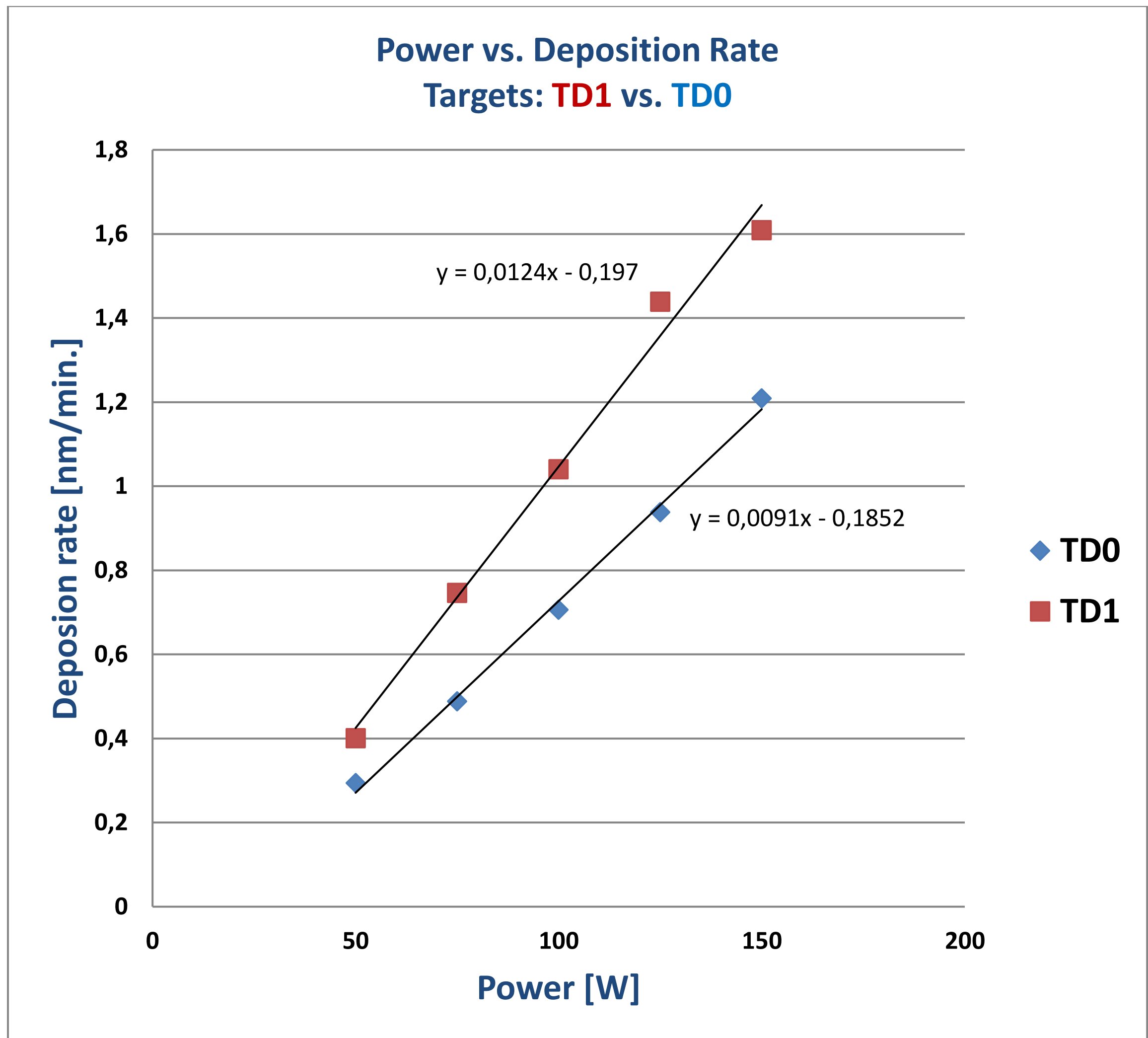

Figure 2. *The comparison of the deposition rates of the samples sputtered using the TD0 and TD1 targets*

In Figure 3, the deposition rate of TD0 and TD2 targets is shown as a function of temperature. The results suggest that there are no essential differences between the behaviors of these two targets except for the slight deviation from a straight line. The deposition rate is almost independent of the deposition temperature in the range between RT to 300C.

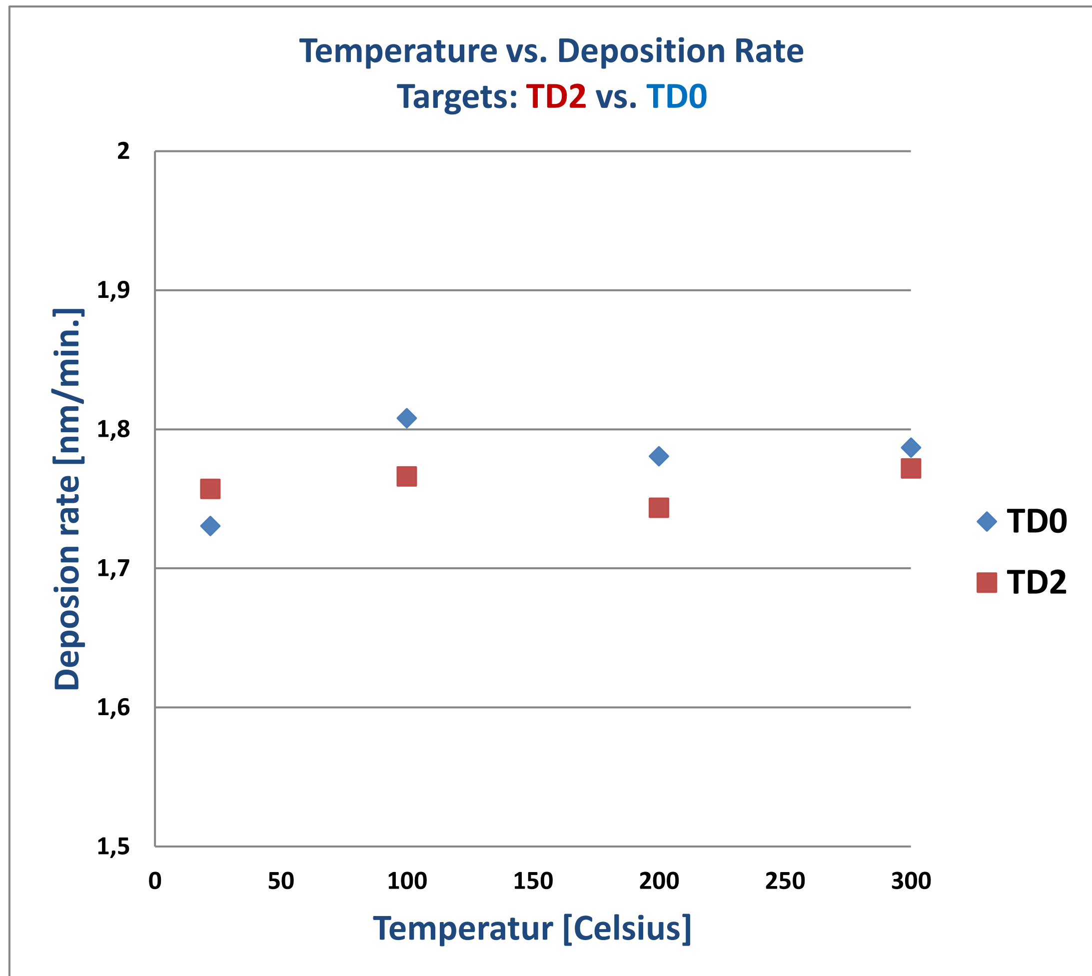

Figure 3. *The comparison of the deposition rate of the samples sputtered using the TD0 and TD2 targets*

Figure 4 compares the thickness of the samples sputtered using the TD0 and TD2 targets. The numerical values are obtained by extracting data from simulated curves, which are fitted to the real XRR measurements. The results are arranged according to the used target and temperature. With some scattering of the results, the thickness changes a little when the temperature increases.

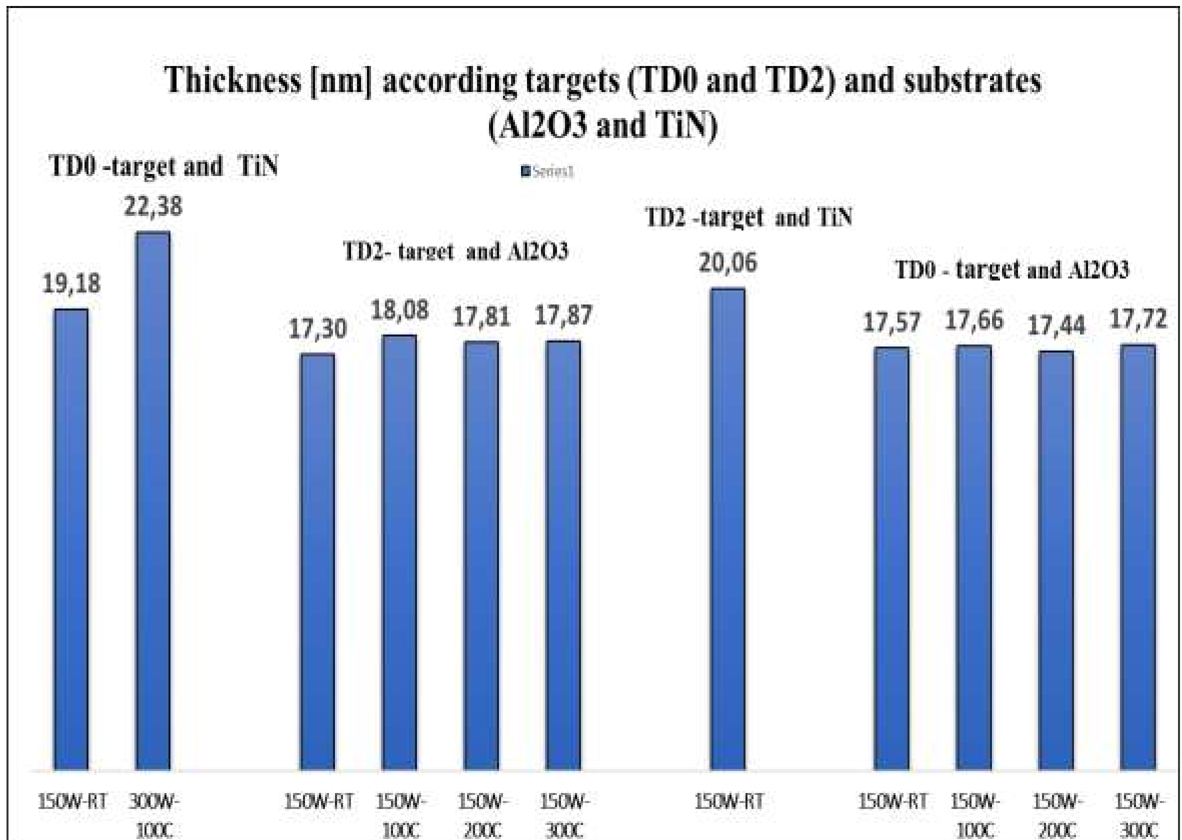

Figure 4. *The thickness of the samples deposited using the TD0 and TD2 targets obtained by the fitting of the measured curves*

In Figure 5, the densities obtained from the XRR curves fitting for the TD0 and TD2 targets are compared. If one excludes the maximum values for TD0 and TD2 2,36g/cm3 and 2,54g/cm3, there are no large differences in the fitted densities for the Al2O3 substrate.

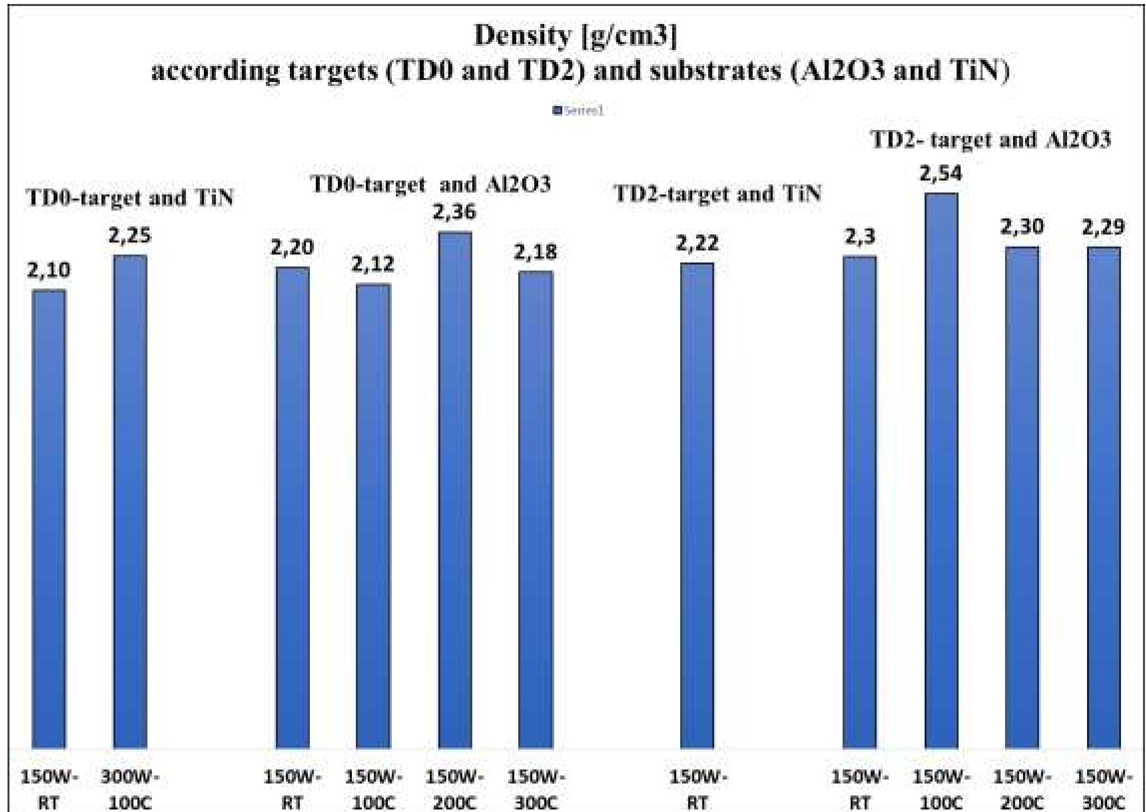

Figure 5. *The density of the samples deposited using the TD0 and TD2 targets obtained by the fitting of the measured curves*

In Figure 6, the roughness of the samples deposited with the TD0 and TD2 targets is compared. Unlike the thickness and the density, the roughness of the samples is sensitive to the deposition temperature. The higher the deposition temperature, the lower the roughness is. Additionally, the TiN and Al2O3 substrates show a different level of roughness (0,88nm vs. 1,78nm).

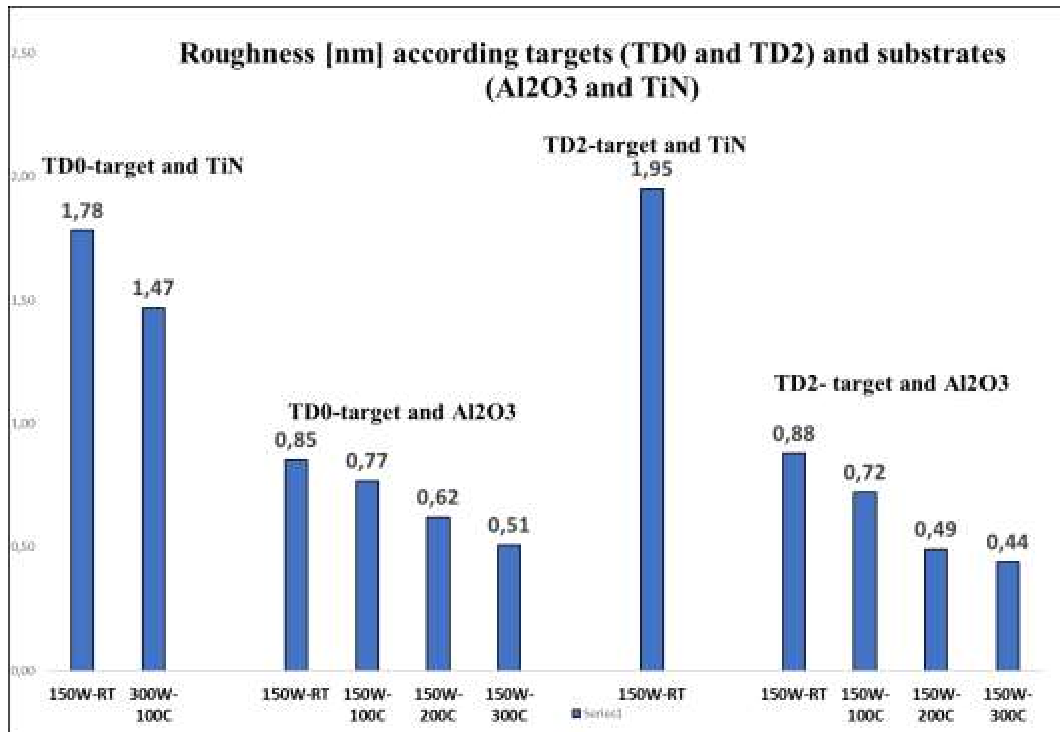

Figure 6. *The roughness of the samples deposited using the TD0 and TD2 targets obtained by the fitting of the measured curves*

3.2 Electrical characterization

Preface. For initiating the resistive switching in the ECM and VCM memory cells, the electroforming stage is usually needed. This means that the positive or sometimes negative bias applies to the insulating oxide. Typically, the switching voltage is much less than the electroforming voltage. During the electroforming, the conductive filament or conductive path is supposed to be created inside the insulating layer depending on the type of memory cells. In some cases, the doping with Cu, for example, can eliminate the need for the electroforming (Liu et al. 2009).

The electroforming was reported being linearly dependent on the thickness between 4nm and 22nm. It was proposed that both the electroforming and switching depend on the valence state and ion diameter. Additionally, increase in density causes increase in electroforming voltage in thin films. The choice of the material for the bottom electrode did not have an impact on the switching behavior (Schindler 2009).

Effect of doping. The insulators can be defined as wide gap semiconductors. The aim of the addition of doping elements is to modify the optical, electrical, or electronic properties of materials suitable for the specific application.

The resistive switching in ReRAMs, however, introduces the contradictive requirement for the used material. For example, in the OFF state, the material must be resistive whereas ,in the ON state, it must be conductive. The ON state has usually ohmic behavior if the metallic filament or dendrites connect the opposite electrodes in the ECM cell.

At first approximation, the ON and OFF states depend on a level of applied current compliance. However, the history of the thermal treatment with a consequent degree of crystallization, as well as other fabrication conditions, affects directly the OFF resistance of the amorphous oxide. The amorphous and crystalline phases of the same material usually have different conductivity while the crystalline phase is more conductive than a resistive amorphous phase. This is exploited in the TCM memory cells, for example. The OFF state in the oxides can be considered dependent on the degree of the oxidation and stoichiometry of oxide.

The attempts to improve the resistive OFF or the conductive ON state immediately affect the ON or OFF state.

The resistivity ρ of the materials with ohmic type of conduction such as metal is constant and resistance can be changed by varying the geometric parameters such as length l or area A:

$$R = \rho \frac{l}{A} = \frac{U}{I}$$

In addition, $R = R_{ref}\left[1 + \alpha\left(T - T_{ref}\right)\right]$, where R_{ref} and T_{ref} are usually given at 20C, α is the temperature coefficient. The temperature coefficient α is positive for the metals and negative for the semiconductors. It means that the resistance of the metals increases, when temperature increases. However, the resistance of the semiconductors decreases, when temperature increases.

The introduction of the transition metal ions as the metallic phase into the host oxide matrices is considered as an extrinsic method for modifying the conductivity of the oxide. In this case, the assumption is made that SiO2, for example, is completely passive and does not participate in the resistive switching.

The choice of the fabrication techniques depends on the desired position of the doping elements inside the host material. The form in which the dopant elements should be introduced and the ultimate function of the dopant depend on the application.

A classic example of the fabrication technique is the doping of Si by the ion implantation. The high energetic ions are shot through the layer of the amorphous SiO2 to ensure the random distribution of the dopant inside the crystalline Si. Following this, annealing of the Si wafer at approximately 1100C is done to ensure that ions replace the Si in the host

Si network and the damage is recovered during the recrystallization (Williams & Poate 2014).

The replacing of Si in SiO2 can be made using the chemical elements from group III or V of the periodic table. The use of aliovalent dopants from group III in place of Si in the amorphous SiO2 creates the oxygen vacancies $X_2O_3 \Rightarrow 2X'_{Si} + 3O_O^{x} + V_O^{\bullet\bullet}$, where X is any element of group III. Typically, the transition metal ions are not considered to replace Si in SiO2. However, the formation of the structure of the transition metal silicate or even silicide is theoretically possible depending on the fabrication conditions. The introduction of the transition metal ions to the host SiO2 is usually considered as the introduction of the metallic phase. Nevertheless, the oxidation during the fabrication of the originally metallic phase is also reported.

Effect of thickness. First, the increase in the electroforming voltage with the increase in thickness was observed only in the part of the samples deposited on the platinum substrate. This can relate to the missing data due to zero yield because that part of samples was not possible to electroform due to the high conductivity. The large ohmic conductivity after applying the positive bias means that memory cell conducts but does not switch with the hysteresis.

Second, the part of the samples deposited on the platinum substrate was electroformed at a very high average voltage of 14-16V, which means that the samples were originally very resistive. The high electroforming voltage creates a very strong metallic filament, which cannot easily be dissolved after the application of negative bias.

Third, the samples deposited on the TiN substrate show completely different electroforming behavior with the increase of electroforming voltage between 5nm and 20nm and a decrease of it with an increase in layer thickness between 20nm and 50nm.The same trend was observed for both sizes of the memory cells deposited on the TiN substrate.

The observed trends relating to the dependence of the electroforming voltage on the thickness can be observed just by chance. However, the reasonable explanation can be made based on the materials' properties and the history of the thermal treatment. It will be explained in more detail in the next section.

Effect of the substrate. Sometimes, the doped samples exhibited a high level of the electroforming voltage. It can indicate that there were not enough doping elements or the distribution of the dopants was not homogeneous.

Based on the electroforming data for samples deposited on the TiN substrate, the change of substrate had a more pronounced effect than expected effect due to adding of doping element. This effect related to change of deposition substrate was attributed to differences in morphology, nanostructure, and conductivity of substrate as shown in more details in Appendix 4.

Preface. The ECM memory cell is typically defined as a device, where the switching of resistance occurs to be due to both creation as well as dissolution of the metallic filament or dendrites inside the passive insulator. After the application of positive voltage, Cu or Ag from the active electrode dissolves or oxidizes. Then, after application of the electric field, the cations would move towards the opposite electrode where the ions are reduced.

The reduced cations form the metallic filament, which grows towards the cathode from the anode. The ECM memory cells switch to the ON state when the metallic filament connects the opposite electrodes. The switching to the OFF state occurs after applying the negative bias to the active electrode. There, metallic filaments dissolve and the ECM cell makes the transition to the OFF state. The assumption is that in this type of memory cells, the insulator, for example, SiO2, does not participate in switching. The ECM usually uses asymmetric, mostly, metallic electrodes. As the passive insulator in the ECM, the SiO2 and the other chalcogenide glasses are usually used.

In VCM cells, the mobility of the oxygen vacancies is higher than that of the metallic cations. Moreover, these oxygen vacancies are assumed to be responsible for resistive switching in VCM cell, where they create a conductive path in the ON state. However, the impact of metallic cations on the overall conductivity is not negligible (Wedig et al. 2016). The VCM cell can use the same or different electrodes. The active material layers in the VCM memory cells are usually the high-k materials such as TiO2, Ta2O5, and ZrO2. In principle, the actual differences between ECM and VCM memory cells, in addition to using the less dissolvable active electrode, lies on the differences in the dielectric constant or relative permittivity of the insulators. However, the exact nature of the conductive path in VCM or the filament in ECM memory cells is still under discussion.

Moreover, there are a lot of modifications of the ECM and VCM memory cells, which cannot be straightforwardly defined as of the certain types. For example, the different metallic and non-metallic conductive electrodes are also implemented. Some of the non-metallic electrodes such as TiN can be used as the bottom or top electrodes as well as polysilicon. The doped polysilicon instead of metallic electrodes can be used not only for amorphous silicon ReRAMs but also for SiOx based memory cells with symmetric or even asymmetric structure of the memory stacks. Furthermore, the sputtered SiO2- based memory cells are more likely to have the SiOx rather than the stoichiometric SiO2 structure. In addition, the evolution of the oxygen during the switching of the SiOx- based memory cells implies that Si nanocrystals or Si-rich regions in SiOx can exist in the silicon dioxide memory cells. Therefore, strictly speaking, the assumption behind the ECM memory cells that SiO2 or SiOx would be passive during the switching and only the cations without any exceptions can have an impact on overall conductivity in the memory cells is not completely justified. If the SiO2 can participate in the resistive switching, then there are even fewer differences between ECM and VCM memory cells. Recently, it was reported that the cations participate in the overall conductivity of the VCM cells

because the overall conductivity is usually higher when it is only due to the movements of the oxygen vacancies.

The switching tests. The tests for the switching of the memory cells were intended to find if the doped samples can be switched or not with any kind of hysteresis. The purpose was not to find optimal switching condition for each target or each memory cell, but only to compare the doped and pure SiO2 memory cells.

First, the memory cell cannot switch, if it cannot be electroformed. In this case, for example, the cell is short-circuited immediately after applying voltage. It means that the OFF or resistive state is not well defined therefore allowing the memory cell to conduct. The conductive path can be unintentionally created during fabrication. Assuming the doped ECM memory cell already has a conductive path or metallic filament after fabrication, first negative bias can be employed for the dissolution of the metallic filament. This method can be a success only if disconnecting of the opposite electrode is possible and that the metallic filament is not too strong.

In addition, the ECM memory cell usually cannot switch if the electroforming is made with very high voltage. Typically, such behavior was seen in the samples deposited on the platinum substrate. Such memory cells do not switch because the filament or the conductive path created was too strong. In addition, sometimes, the cell can stick on either the ON or OFF state, after which the repetitive switching is not possible. In addition, if the OFF/ON ratio is very low, then the ON and OFF states will be difficult to separate from each other. Therefore, for successful switching, many conditions need to be met.

The testing techniques. There were a lot of difficulties with the electrical characterization of the ECM cell. First, this type of cell was tested in the laboratory many years ago. Second, the memory cells were fabricated using completely different techniques or more powerful deposition tools. Third, the doping of amorphous oxides had not been tested before in this laboratory. Additionally, the tool for analysis in nanoscales was not available. Different processing equipment usually create different structures of the layer, which makes it difficult to compare with already published results.

In addition, it was known that the behavior of the ECM cell is very unstable, varying, and difficult to control. Unlike ECM, the VCM usually has the repetitive and more stable switching behavior.

It was reported previously that electroforming is needed for the pure samples. For a Cu-doped sample, strong electroforming is not usually required. However, the exact concentration of doping elements is not always revealed, therefore it was difficult to make the comparison between different experimental results.

3.2.1 Electroforming

Table 1 shows the overview of samples tested for the electroforming. Altogether, 20 samples and 708 cells were studied. The variable parameters were

- the layer thickness between 5nm and 50nm,
- the cell sizes: 50µmx50µm and 100µmx100µm,
- the used targets: TD0, TD1, TD2,
- the substrates: platinum and TiN,
- the limiting current compliance between 10^{-14} A and 1A,
- the voltage from -20V to +20V.

Categories		Samples		Cells	
Substrates	TiN	5	20	180	708
	Pt	15		528	
Targets	TD0	4	20	132	708
	TD1	11		411	
	TD2	5		165	
			20 samples		**708 cells**

Table 1. The overview of samples tested for the electroforming

The additional figures related to electroforming with the explanations introduced in Appendix 6.

Next, the electroforming data were analyzed for each target separately.

3.2.1.1 *Electroforming of the samples deposited using the TD0 target*

3.2.1.1.1 Platinum substrate

The aim of the electroforming tests for the samples deposited using the TD0 target was to obtain the reference data for the comparison with the doped samples deposited using the TD1 and TD2 targets.

Figure 7 shows an example of the electroforming curve of the 5nm-thick samples deposited using the TD0 target on the Pt substrate at 100C.

Figure 8 and Figure 9 show the overview of the electroforming data for both cells sizes of samples deposited using the TD0 target on the Pt substrate. Figure 10 shows the corresponding yield of the data of the samples shown in Figure 8 and Figure 9.

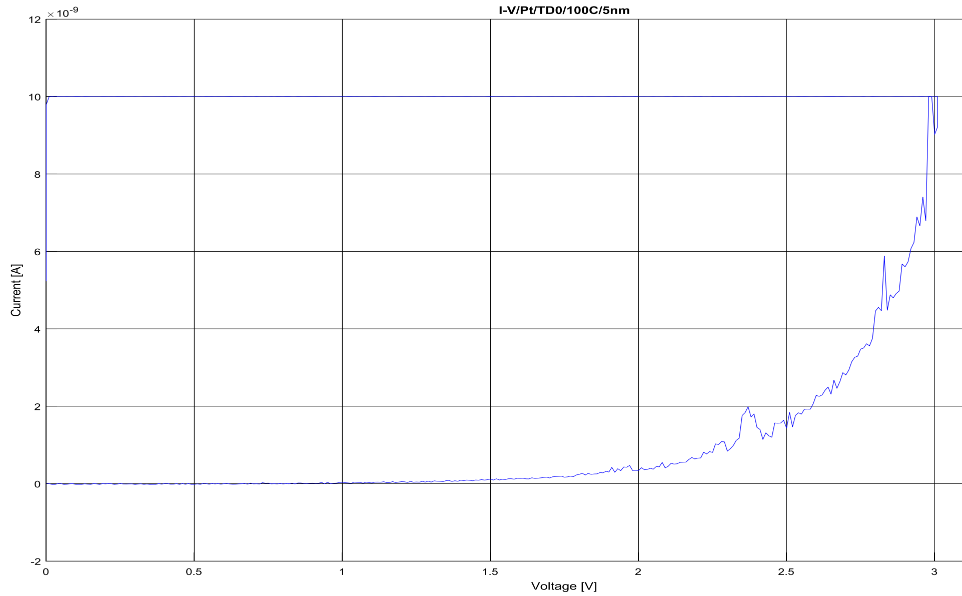

Figure 7. *The I-V curve of the 5nm-thick sample deposited using the TD0 target on the Pt substrate at 100C, electroformed with 3V and the current compliance of* 10^{-8} *A.*

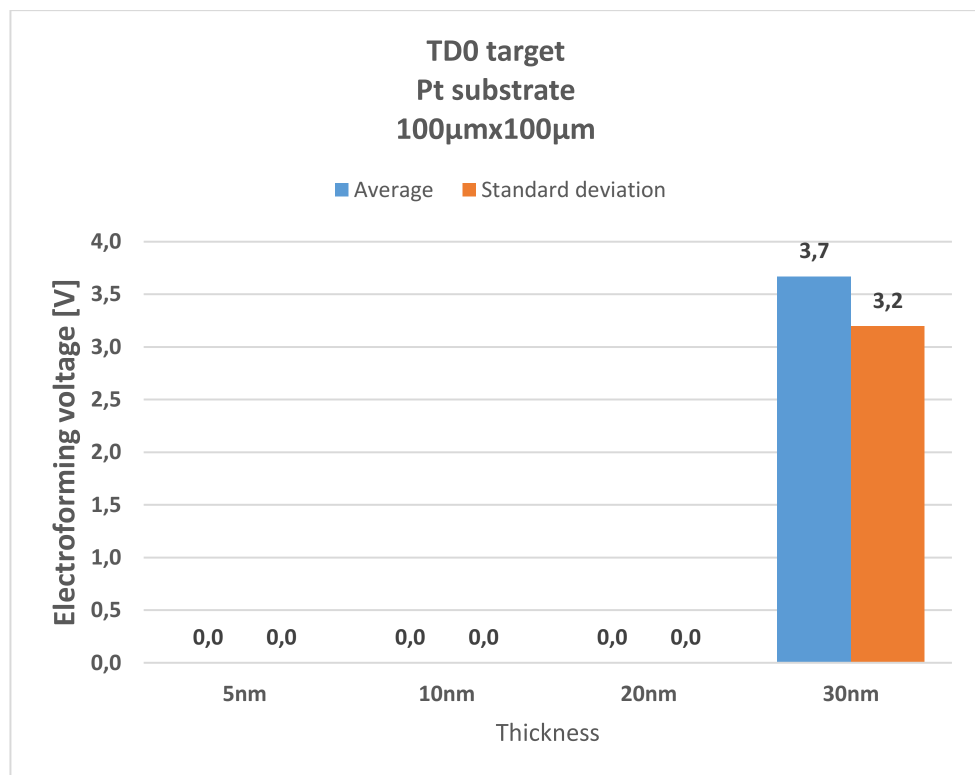

Figure 8. *The overview of the electroforming data for the cell size of 100µmx100µm for the samples deposited using the TD0 target on the platinum substrate*

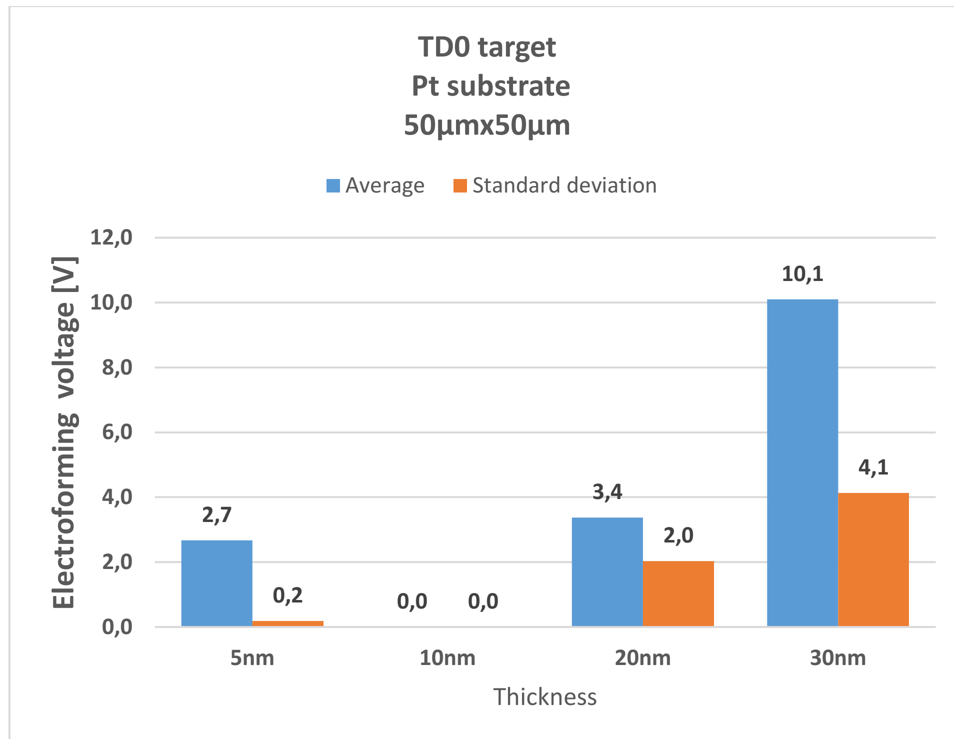

Figure 9. *The overview of the electroforming data for the cell size of 100µmx100µm for samples deposited using the TD0 target on Pt substrate*

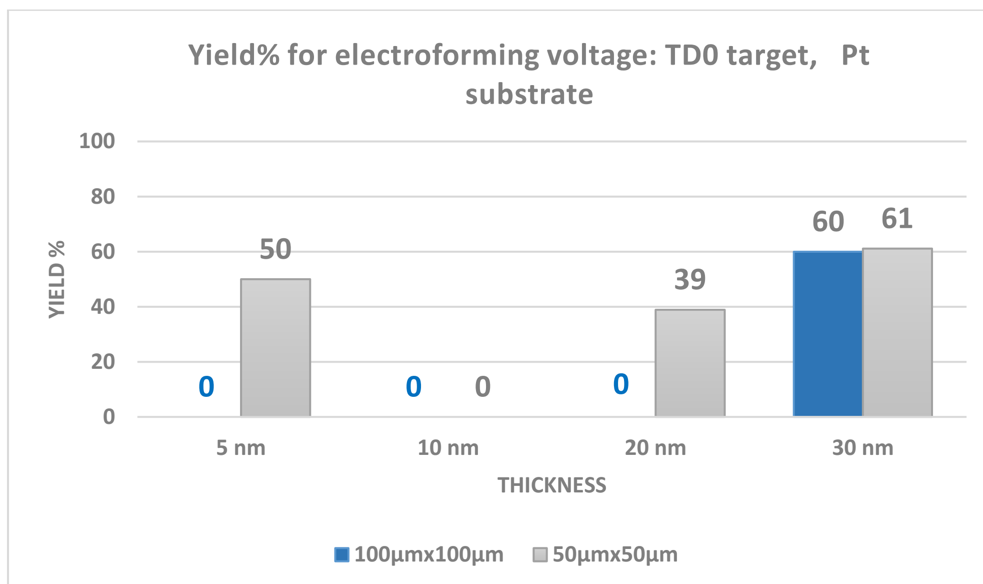

Figure 10. *The yield % of the electroforming data of the samples deposited using the TD0 target on platinum substrate*

Summary. Despite the significant efforts and used time, it was impossible to obtain enough reference data for the samples deposited using the TD0 target on the platinum substrate. It can be seen that the electroforming yield of the samples is extremely low, which is additionally coupled with missing data.

there is a lot of missing data. Many cells simply failed the electroforming test, because they were too conductive directly after applying the voltage bias.

In addition, the rest of the obtained data shows rather the large and non-uniform standard deviation indicating that the data is not normally distributed. It means that the average and standard deviation would describe the obtained data badly. Moreover, the non-normal distribution of data accompanied with low yield indicates that the comparison of data with other samples would be difficult. As can be seen in Appendix 6, the attempt to display data using median with helps of box plots did not reveal obvious trends as a result of specific treatment or parameter.

Figure 34 shows the overview of the electroforming data of samples deposited using the TD0 target on the TiN substrate. The corresponding yield of this data can be seen in Figure 12.

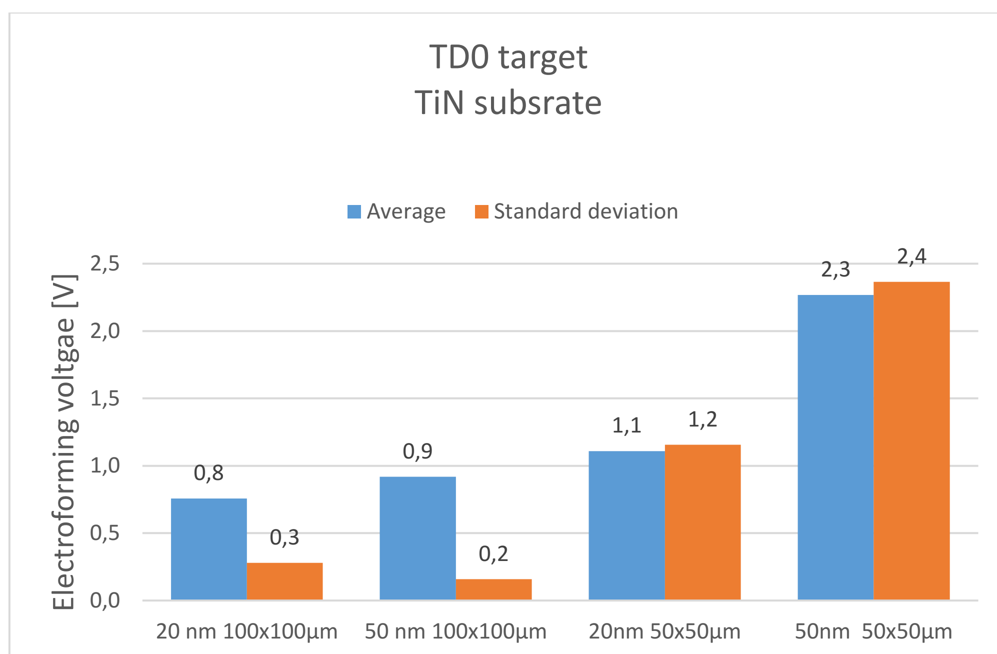

Figure 11. *The overview of the electroforming data of the samples deposited using the TD0 target on the TiN substrate*

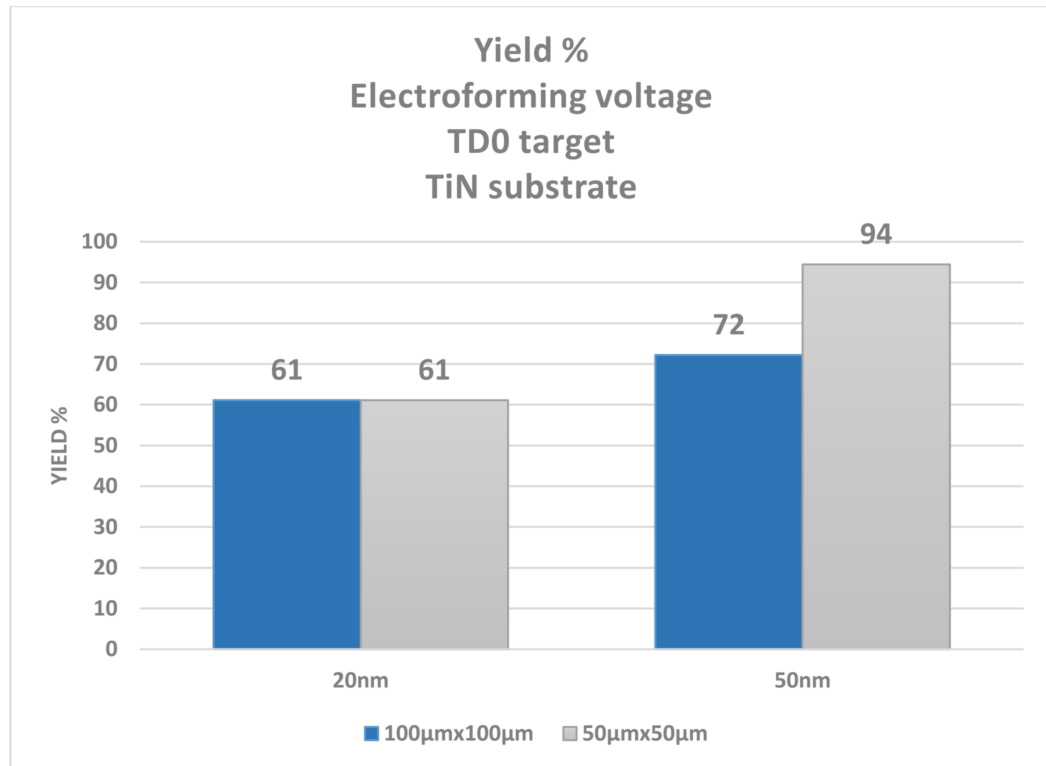

Figure 12. *The yield % of the electroforming data of the samples deposited using the TD0 target on the TiN substrate*

Summary. The electroforming yield of the 20 nm- and 50nm –thick specimens sputtered on the TiN substrate is higher than for the specimens deposited using the same target on the platinum substrate. However, a direct comparison of the samples deposited on the platinum and TiN substrates is not possible because the 50nm-thick sample on the platinum substrate cannot be fabricated due to the malfunction of the sputtering device. In addition, the 20nm- thick sample deposited on the Pt substrate has only data for 50µmx50µm size. Nevertheless, the comparison of the cells with a size of 100µmx100µm indicated that the electroforming yield was higher for the samples on the TiN substrate (39% vs. 61%).

In addition, the observed trend of increase in electroforming voltage with the thickness of the samples needs to be ignored due to the fact that standard deviation is too high. Moreover, the data is not clustered near the average value and therefore the data is not normally distributed. Moreover, the standard deviation for 50 nm-thick cells is higher than the average; therefore, the data is non-normally distributed.

3.2.1.2 *Electroforming of samples deposited using the TD1 target*

Figure 13 shows the electroforming curve of the 50nm-thick SiO2's layer deposited using the TD1 target on the TiN substrate at 100C. The electroformed voltage was less than

1V with the current compliance of 10^{-6}A. In addition, the memory cell was already OFF at 0,1V. This cell shows the unipolar behavior, which seems to be different than that in the PCM or TCM unipolar memory cells due to the absence of the large current.

Figure 14 shows the electroforming curve of the 30nm-thick SiO2 layer deposited using the TD1 target on the TiN substrate at 150C. The memory cell was electroformed at 9V with the current compliance of 10^{-6}A. However, the memory cell shows the filament instability in the middle and at the end of the current-voltage curve. This also means that the memory cell is OFF at the end of the cycle again. Such behavior resembles the unipolar type of switching, however without using the extreme parameters. In addition, the transition from the OFF to ON state in a resistance-voltage curve in Figure 14 is not abrupt. On the logarithmic scale, this resembles the straight line indicating the current and voltage to have the near exponential dependence from each other.

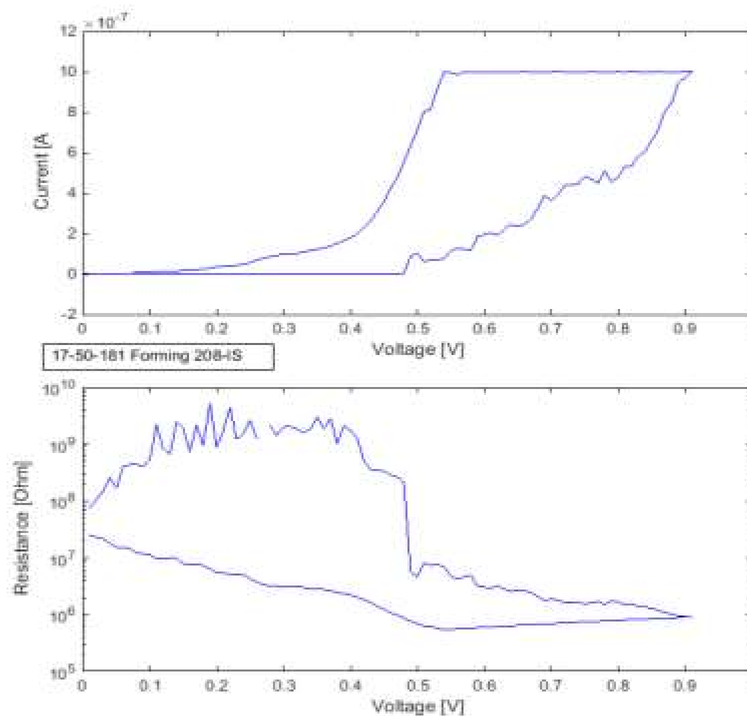

Figure 13. *The I-V and R-V curves of the 50nm-thick layer of SiO2 deposited using the TD1 target on the TiN substrate at 100C during the electroforming*

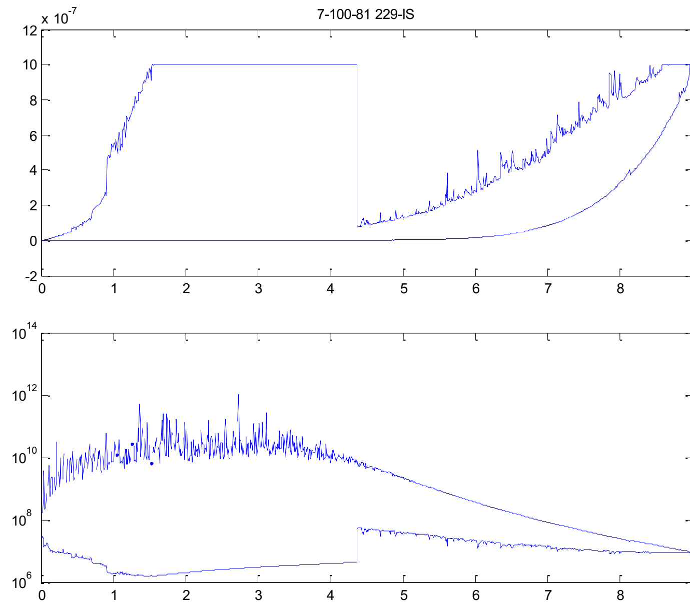

Figure 14. *The electroforming curve of the 30nm-thick SiO2 layer deposited using the TD1 target on the TiN substrate at 150C.*

Figure 15 and

Figure ***16*** shows the overview of the electroforming data for the samples deposited using the TD1 target on the TiN substrate. The corresponding yield in Figure 17 except for the 5nm sample was relatively high. In addition, the electroforming voltage is proportional to the sample thickness between 5nm and 20nm. However, the trend was surprisingly opposite between 20nm and 50nm. Both cell sizes showed the same trend with good overall yield.

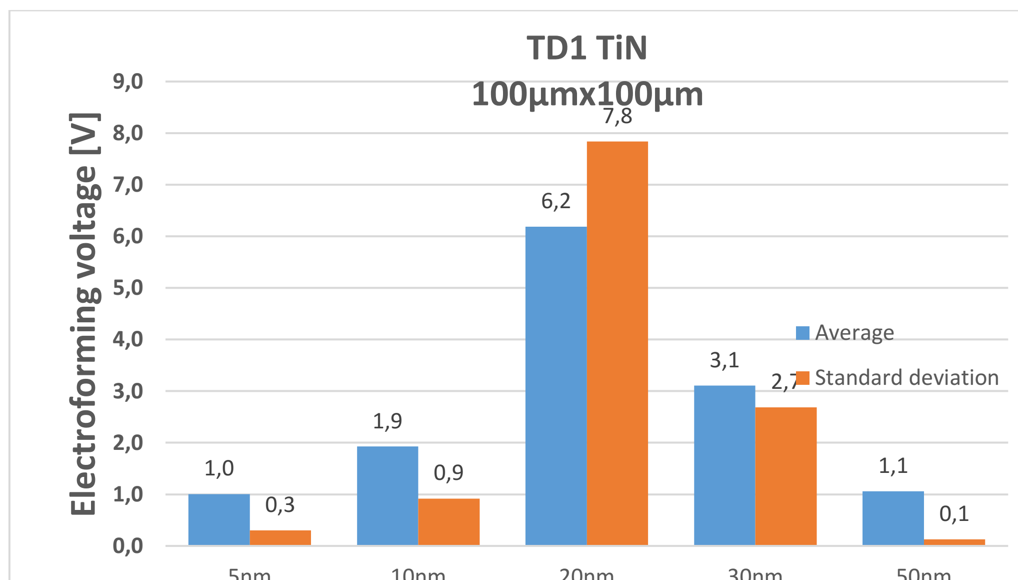

Figure 15. *The overview of the electroforming data for the cell size of 100µmx100µm for the samples deposited using the TD1 target on the TiN substrate*

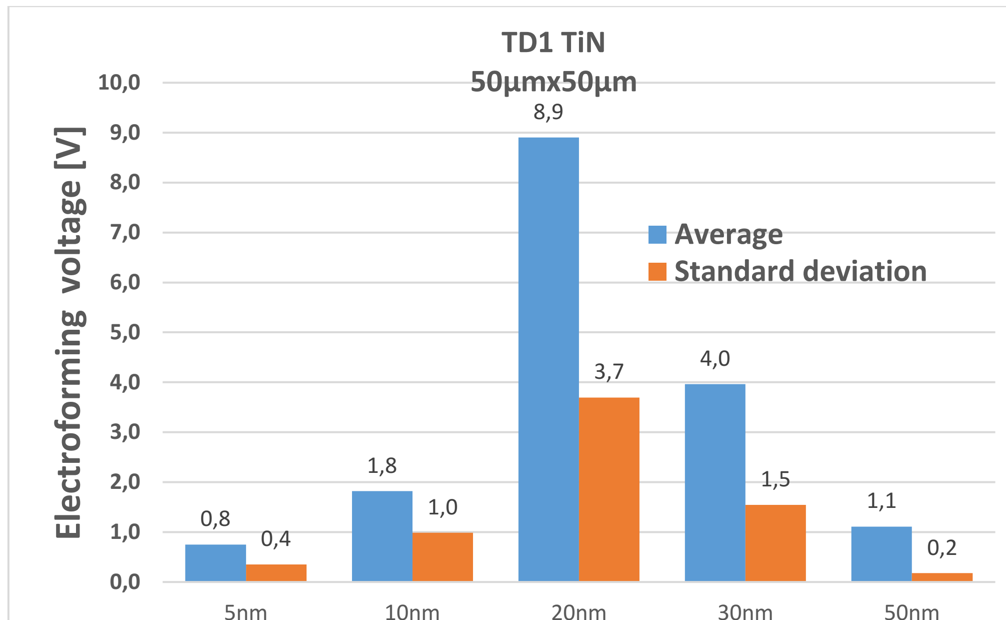

Figure 16. *The overview of the electroforming data for the cell size of 50µmx50µm for the samples deposited using the TD1 target on the TiN substrate*

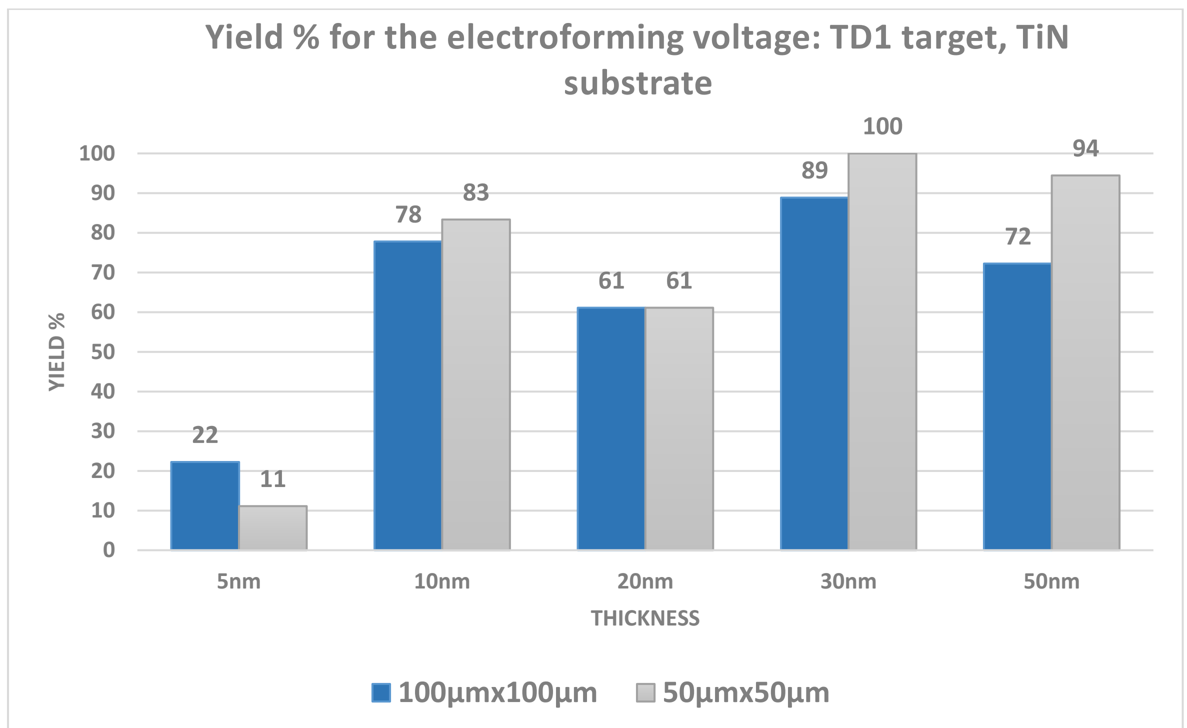

Figure 17. *The yield % of the electroforming data of the samples deposited using the TD1 target on the TiN substrate*

Summary. The electroforming yield for sample deposited using the TD1 target on the TIN substrate is relatively high except for the 5nm-thick sample. For the data to be normally distributed the size of standard deviation needs to be 1 sigma or in the order of 34.1%. However, the calculated standard deviation of the overall data seemed to be distributed non-normally. In one case, the standard deviation was even higher than calculated

average value. This fact indicated that the data was rather distorted, scattered and obviously not clustered around an average value.

3.2.1.3 *Electroforming of the samples deposited using the TD2 target*

Figure 18 shows the electroforming curve of the sample deposited using a TD2 target on the TiN substrate at 7V with the current compliance of 10^{-6}A. The shape of the curve indicates the clear metallic type of behavior with a sharp change of resistance from OFF to ON state.

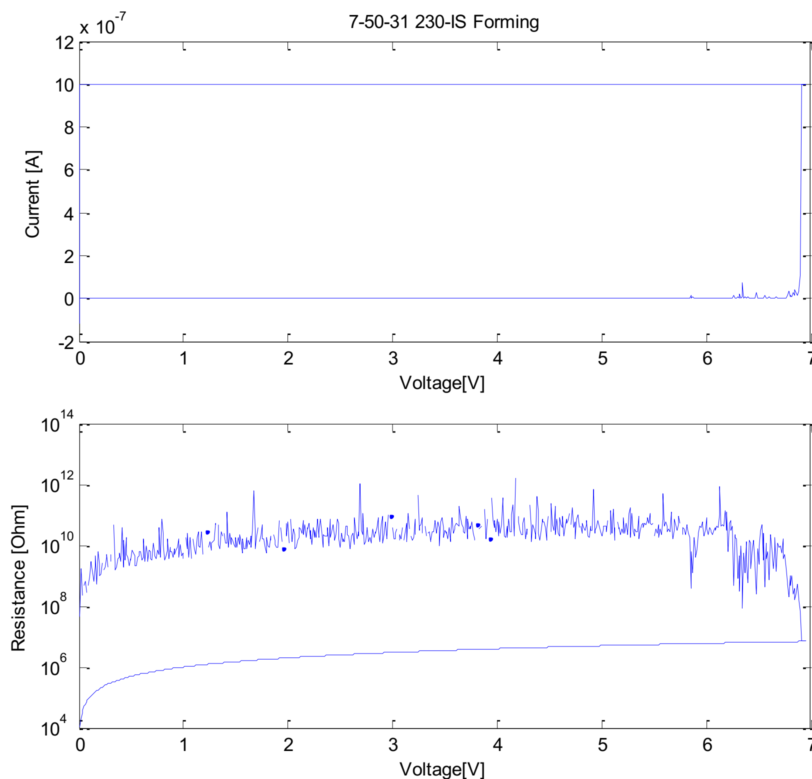

Figure 18. *The I-V and R-V curves of the 30nm-thick layer of SiO2 deposited using the TD2 target on the TiN substrate at 150C during the electroforming*

Figure 19 and Figure 20 show the overview of the electroforming data for the samples deposited using a TD2 target on the platinum substrate. The corresponding yield is shown in Figure 21. Again, some cells were too conductive and therefore they could not be electroformed which can be seen from the zero yield.

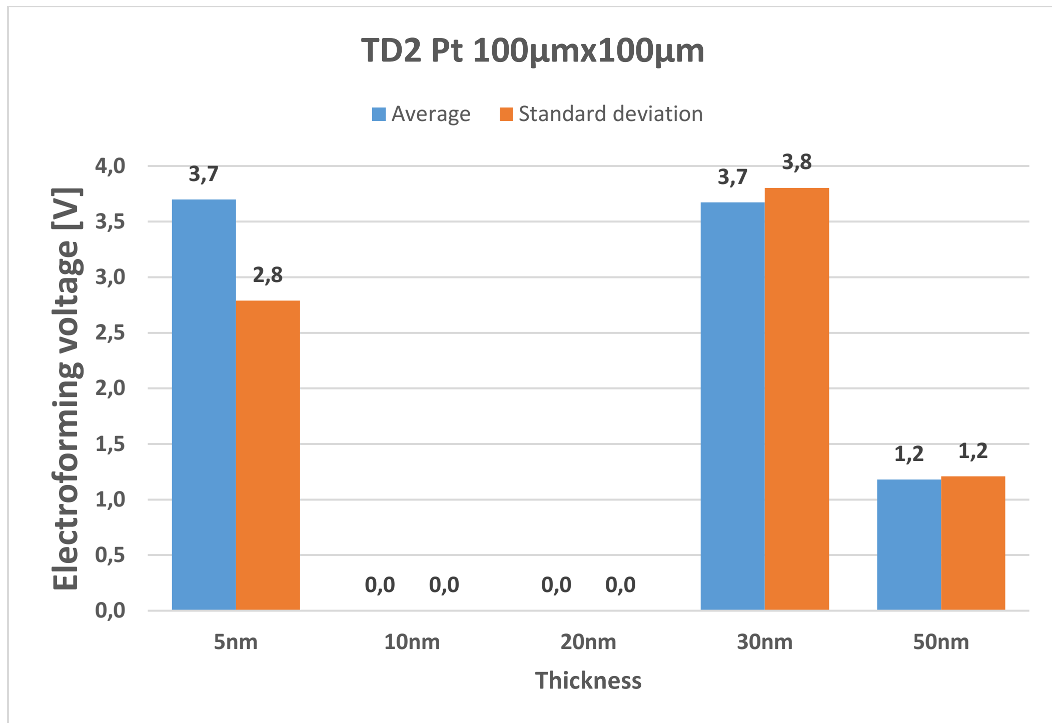

Figure 19. *The overview of the electroforming data for the cell size of 100µmx100µm for the samples deposited using the TD2 target on platinum substrate*

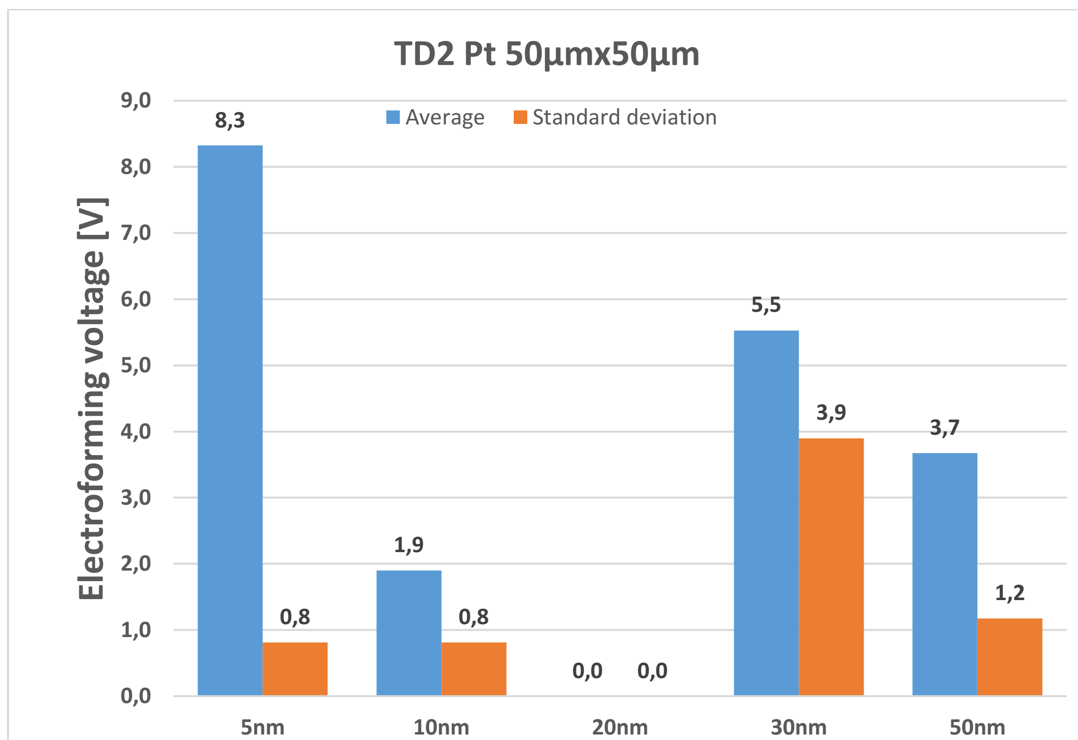

Figure 20. *The overview of the electroforming data for the cell size of 50µmx50µm for the samples deposited using the TD2 target on the platinum substrate*

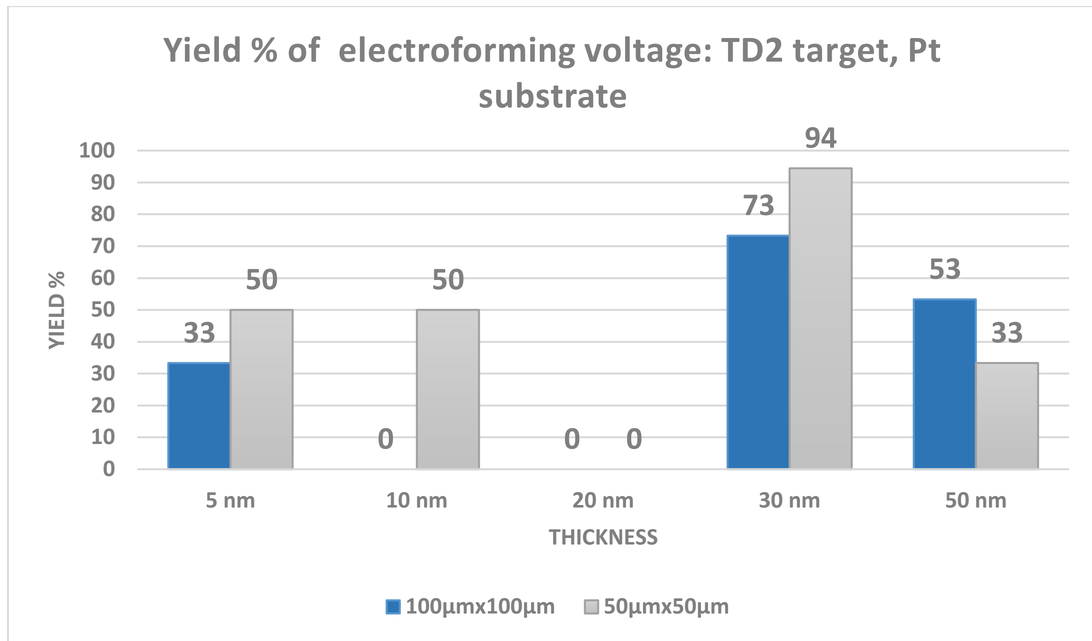

Figure 21. *The yield % of the electroforming data of the samples deposited using the TD2-target on the platinum substrate*

Summary. Again, there was a lot of missing data and the overall yield was low even for the 50nm-thick layer. The size of the standard deviation indicated that it was much lower or higher than 34.1% in comparison to the calculated average which indicated that the obtained data was not normally distributed.

3.2.1.4 *The Interpretation of the experimental results for the electroforming and the effect of the doping*

The aim of the electrical and materials characterization was to make the comparison of the doped and samples without the doping elements. However, as it can be seen from the analysis of the electroforming data, it is extremely difficult to make consistent conclusions.

First, the low yield of the samples deposited using the TD0 target and TD2 target indicated that, unfortunately, the samples deposited by these targets were too conductive immediately after applying the bias. Because these samples were conductive, the samples could not be electroformed due to the absence of the high resistive state at the beginning of the tests.

Second, the obtained data was not normally distributed and much data was missing. Therefore, the comparison of the average values as a result of certain treatment cannot be directly made. However, some pattern can be found provided that the missing data itself can also be interpreted as a trend.

Generally, the expectation is that the electroforming voltage should increase with the thickness. However, the comparison of the average of the non-normally distributed data shows a mixed trend, an opposite trend or lack of any trend based on the thickness of the deposited layer. It is also possible, that if the size of the data increases, the distribution of some parameters can approach normality, but this method was not applicable due to the limitation of the available time and materials for the testing. Additionally, the increase in the number of tested cells for samples deposited on the Pt substrate did not increase the amount of successful data.

Third, the drawing of the above-mentioned data as the box plots in Appendix 6 (Figure1-Figure 12) using the median instead of the mean value also did not help. The data scatters much. The comparison according to the median does not reveal any obvious trends with regards to the thickness or the used targets.

Fourth, the testing or processing parameters, which were used, were not random. Also, the data was distributed non-normally. Therefore, the direct testing of the statistic hypothesis cannot be applied either.

Fifth, the obtained data is rather scattered and has large variability both using the mean or median value.

3.2.2 I-V characteristics

The part of the current-voltage characteristics is shown in chapter 3.2.2 'The I-V characteristics'. However, the additional figures are introduced for all three targets in Appendix 7.

3.2.2.1 The undoped TD0 target

Table 2 shows the overview of the samples deposited using the TD0 target with the corresponding sputtering parameters, which were tested for the switching. Two samples were deposited on the TiN substrate with the rest of the samples sputtered on Pt substrate.

Sample	Substrate	Target	Power	Temperature	Thickness	I-V curves
145-IS	Pt	TD0	150	100	5	38
148-IS	Pt	TD0	150	100	10	96
158-IS	Pt	TD0	150	100	20	165
159-IS	Pt	TD0	150	100	30	91
236-IS	TiN	TD0	150	150	30	278
245-IS	Pt	TD0	150	150	30	103
246-IS	Pt	TD0	150	RT	30	100
249-IS	TiN	TD0	150	RT	30	131

Table 2. *Overview of samples deposited using TDO target at different parameters*

Figure 22 and Figure 23 show two extreme examples of the current-voltage characteristics of the 30-nm-thick sample deposited using the TD0 target on the platinum substrate at 100C. The first memory cell switched with the current compliance of 10^{-5}A and the symmetric voltage bias illustrated the threshold-like behavior. The second memory cell with asymmetric voltage bias and the current compliance of 10^{-4}A showed the metallic type of switching behavior.

The first curve in Figure 22 exhibits the OFF state between -0.2V and +0,2V and was symmetrically biased. This switching behavior can be classified as the unipolar type with a full ON-OFF cycle on the same voltage polarities. Because the horizontal straight line corresponding to current compliance are drawn in the plot, both the positive and negative sides of the curves follow the limitation set by the current compliance.

The second cell in Figure 23 was asymmetrically biased and showed the behavior typically expected in the ECM memories, which corresponds to the bipolar type of switching. The filament created at the positive bias conducts ohmically connecting the opposite electrodes. At the negative bias, the metallic filament is usually assumed to undergo electrochemical dissolution. The cell at the negative bias does not usually follow the level of the negative current compliance because the horizontal line of the current compliance is missing. This type of asymmetric curves can be obtained with the symmetrical voltage bias. In addition, the asymmetric biasing can produce the symmetric curves.

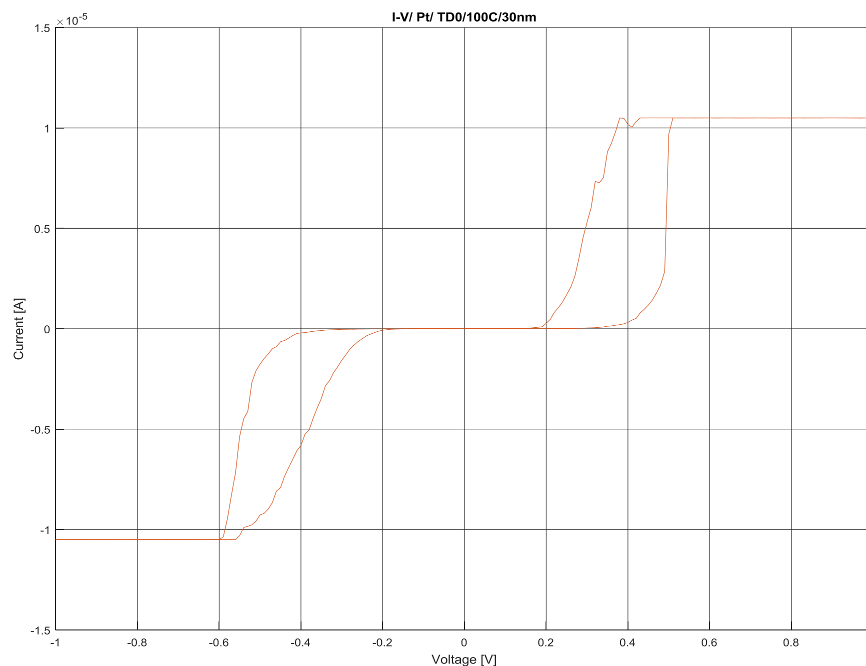

Figure 22. *The current-voltage characteristics of the 30-nm-thick sample deposited using the TD0 target on the platinum substrate at 100C and biased with* 10^{-5}*A and +1V/-1V.*

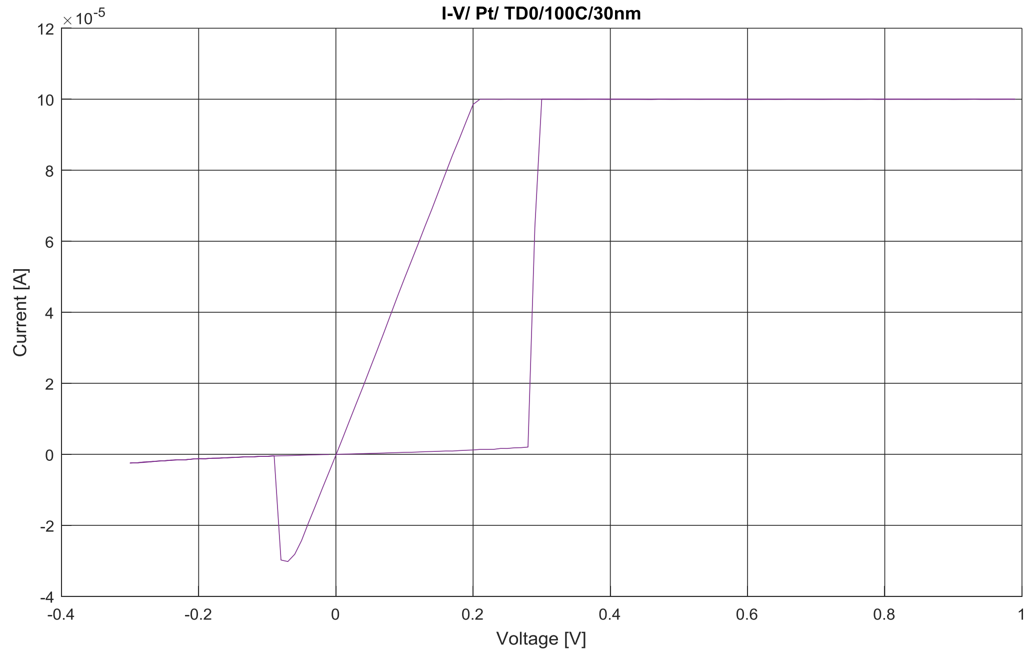

Figure 23. *The current- voltage characteristics of the 30-nm-thick sample deposited using the TD0 target on the platinum substrate at 100C and biased with 10^{-4}A of the current compliance*

Figure 24 displays the I-V and R-V characteristics corresponding to the memory cell deposited on the platinum substrate at 150C with the threshold-like behavior and biased with the current compliance of 0.01A. The same cells are then biased with the current compliance of 0.1A in Figure 25 and 0.001A in Figure 26. The behavior of the memory cell together with the shape of the current-voltage curves is current controlled. The transition from the quadratic to the triangular shape of the curves is induced by the increase in current compliance from 0.01A to 0.1A. On the other hand, the decreasing of the current compliance from 0.01A to 0.001A causes the disappearing of the hysteresis. The corresponding resistance is constant and has the ohmic type of conduction.

In addition, the memory cell in Figure 25 did not follow the limiting current compliance of 0.1A, because the horizontal line of the current compliance was missing. The triangular shape of the current-voltage characteristics was attributed to the fact that the actual current in the cell was much lower than the limit set of 0.1A.

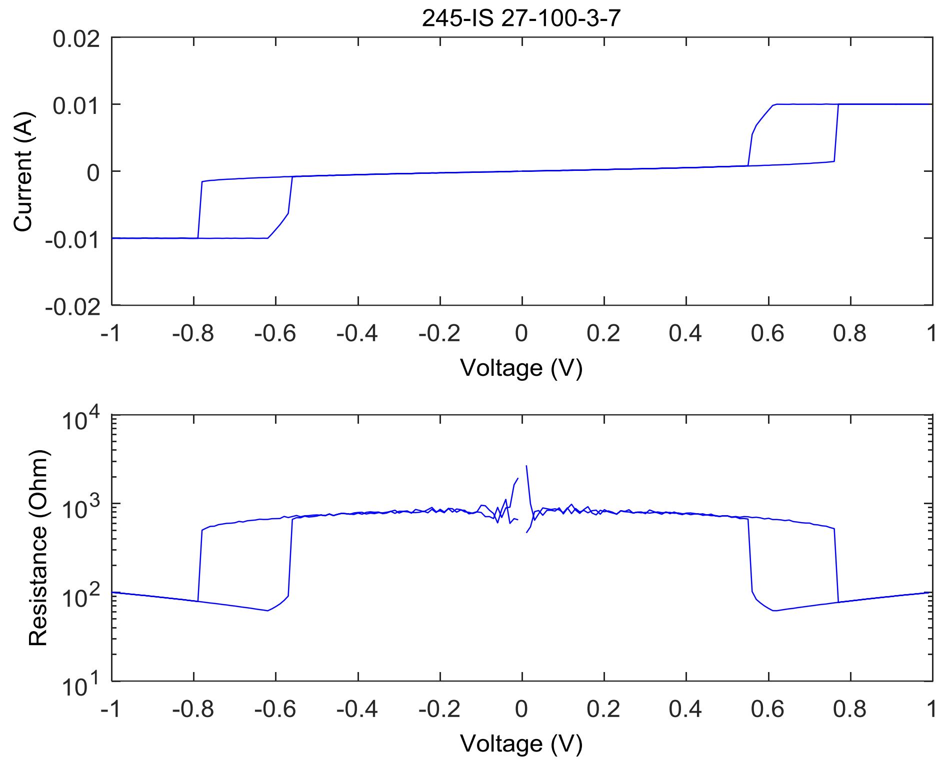

Figure 24.*The I-V and R-V curves related to the memory cell deposited on the platinum substrate at 150C with the threshold-like behavior and biased with the current compliance of 10^{-2}A and symmetric +1V/-1Vvoltage bias*

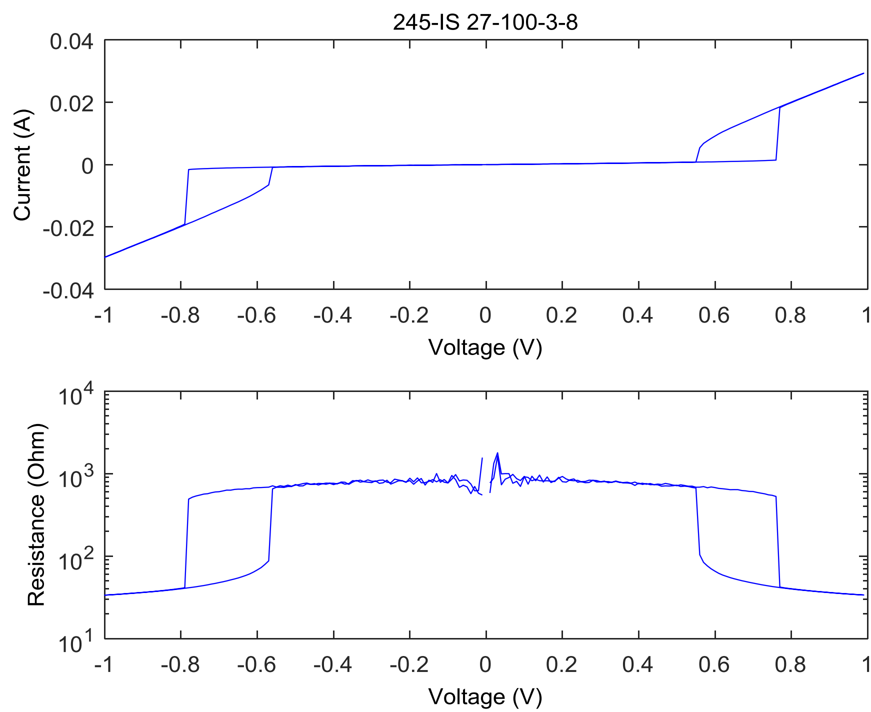

Figure 25. *The I-V and R-V curves of the memory cell deposited on the platinum substrate at 150C with the threshold-like behavior and biased with the current compliance of 0.1A*

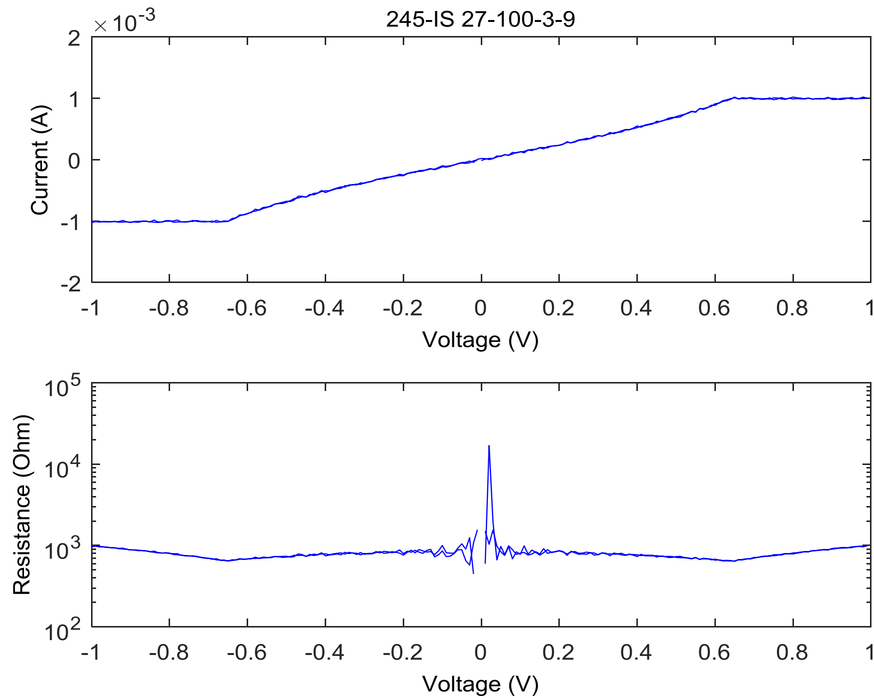

Figure 26. *The I-V and R-V curves of the memory cell deposited on the platinum substrate at 150C with the threshold-like behavior and biased with the current compliance of 1mA*

Figure 27 displays the I-V and R-V curves of the memory cell deposited on the platinum substrate at 150C with the threshold-like behavior and biased with the current compliance of 1mA. This cell from the same 245-IS sample does not show the threshold type of switching. Altogether, there were only a few times with such type of curves. All other curves exhibited the threshold-type of switching behavior.

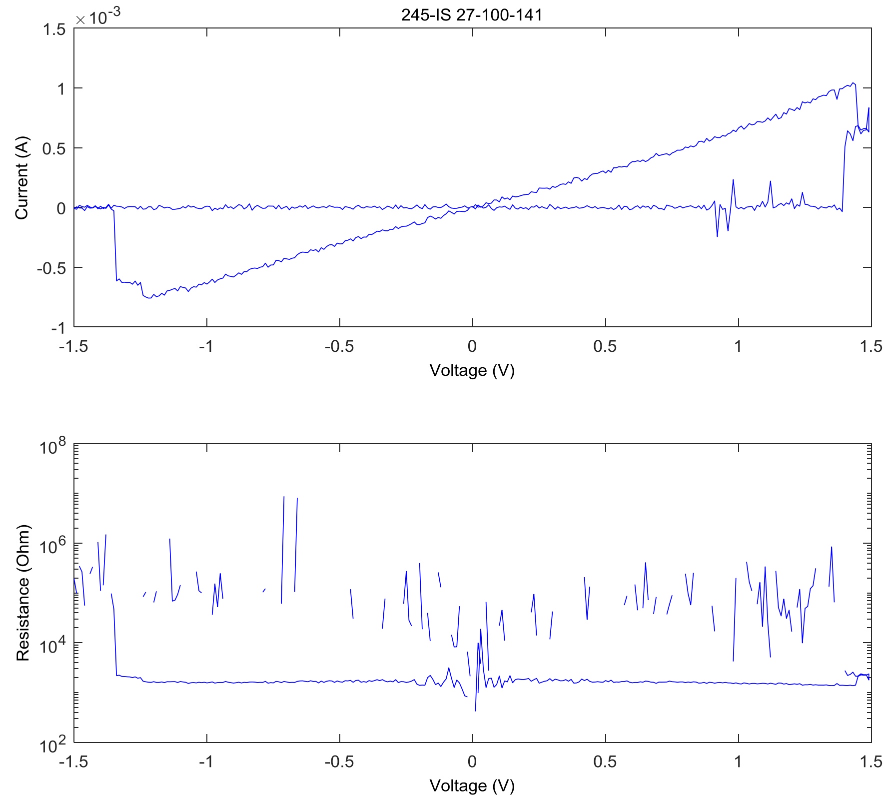

Figure 27. *The I-V and R-V characteristics related to the memory cell deposited on the platinum substrate at 150C biased with the current compliance of 1mA and the voltage of+1.5V/-1.5V.*

Two samples (245-IS and 246-IS) deposited on the platinum substrate showed the threshold-like behavior only. However, in two or three instances they showed the memory type of switching as shown in Figure 27. In addition, the samples N245-IS and 246-IS were tested at the different levels of the current compliance from 10^{-9}A to 0.01A. All the memory cells that were tested were short-circuited in all possible combination of the current except for 0.001A. Both samples showed quite similar behavior and started to switch only at the current compliance between 0.1A and 0.01A. Without any exceptions, the memory cells, which showed the threshold-like switching, made the transition from the triangular shape to the quadratic shape, when current compliance changed from 0.1A to 0.01A. However, the memory switch was closed at 0.001A again. All these changes were reversible and repeatable in any order of the testing for both 245-IS and 246-IS samples. The increasing of the symmetric voltage bias caused the change in the a size of the OFF region in the curve. All tested samples with this type of threshold behavior switched only in the narrow setting window.

3.2.2.2 The TD1 target doped with one doping element

Table 3 shows the overview of the samples deposited using a TD1 target with the corresponding sputtering parameters. Most samples deposited using the TD1 target were sputtered on the TiN substrate.

Sample	Substrate	Target	Power	Temperature	Thickness	I-V curves
192-IS	Pt	TD1	150	100	50	39
204-IS	TiN	TD1	150	100	5	140
205-IS	TiN	TD1	150	100	10	28
206-IS	TiN	TD1	150	100	20	117
207-IS	TiN	TD1	150	100	30	217
208-IS	TiN	TD1	150	100	50	307
215-IS	Pt	TD1	150	RT	30	69
218-IS	Pt	TD1	150	150	30	59
226-IS	TiN	TD1	150	RT	30	23
229-IS	TiN	TD1	150	150	30	57

Table 3. *The overview of the samples deposited using the TD1 target at the different parameters*

Figure 28 shows the I-V curve of the 30-nm-thick sample deposited using the TD1 target on the TiN substrate and biased with the current compliance of 10^{-4}A on the positive side and of $4 \cdot 10^{-5}$A on the negative side with the corresponding voltage +0.6V/-0.6V. This type of curve with the bipolar switching behavior is usually expected in the ECM memory cells. However, the cell again does not follow the current compliance limitation on the negative side because of the missing horizontal line. In addition, the voltage bias was symmetric.

Figure 29 shows the same sample as in Figure 28 biased with the positive current compliance of $2 \cdot 10^{-4}A$ and the negative current compliance of $0.5 \cdot 10^{-4}A$ with the voltage +0.8V/-0.6V. The negative side of the curve does not follow the limitation of the current compliance again. In practice, the cell switches OFF immediately after the transition from the positive to the negative side at 0.05V with the approximate current of $0.1 \cdot 10^{-4}A$. Such behavior can indicate the degradation of the bipolarity and transition to the unipolar type of switching without applying large current or voltage.

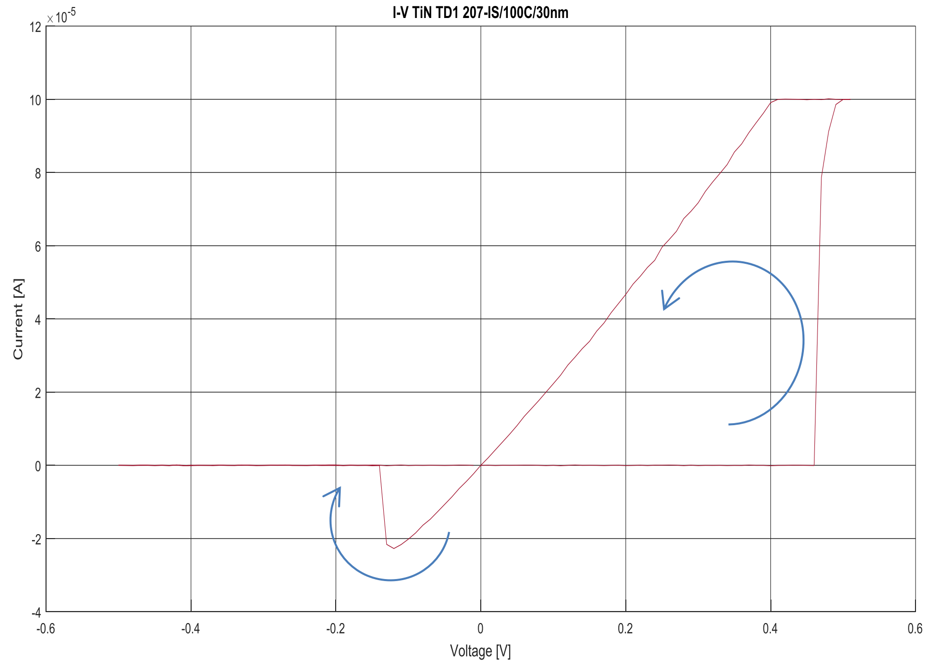

Figure 28. *The current- voltage characteristics of the 30-nm-thick sample deposited using the TD1 target on the TiN substrate at 100C and biased with the positive current compliance of* 10^{-4}*A and the negative compliance of* $4{\cdot}10^{-5}$A *at the voltage +0.6V/-0.6V*

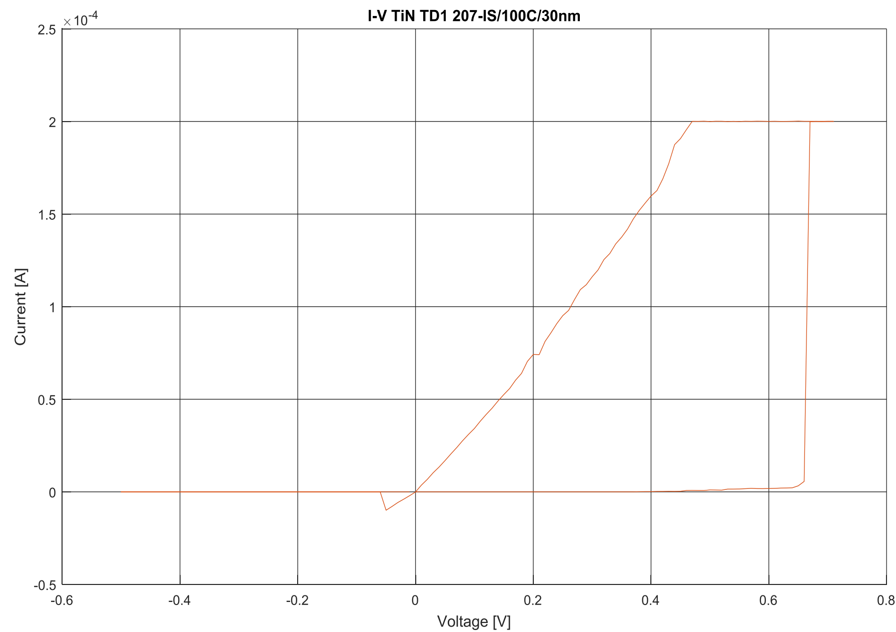

Figure 29. *The current- voltage characteristics of the 30-nm-thick sample deposited using the TD1 target on the TiN substrate at 100C and biased with the positive current compliance of* $2{\cdot}10^{-4}$*A and the negative current compliance of* $0.5{\cdot}10^{-4}$*A with the voltage +0.8V/-0.6V.*

Figure 30 displays the current-voltage curve of the 30-nm-thick sample deposited using the TD1 target on the TiN substrate at 100C and biased with the negative current compliance of $2.5 \cdot 10^{-5}$A at the voltage 0V/-0.8V. Sometimes, the cell was conductive immediately after the application of the positive bias. Therefore, it was suggested that if the conductive path or metallic filament were already created during the fabrication, then testing with the negative bias would help first to dissolve it, for example, before the application of the positive bias.

However, the assumption is usually made that the metallic filament in the ECM cells should dissolve completely under negative bias in order to disconnect the opposite electrodes. This would demonstrate the bipolar type of switching and the corresponding ohmic behavior of the conducting filament. In Figure 30, however, the memory cell stops exhibiting the ohmic behavior after 0.08V. The filament partly dissolved. Therefore, the opposite electrodes remained connected, continued to conduct, however, completely non-ohmically. The conduction mode was probably of the semiconductive type with the exponential dependency of the current and voltage.

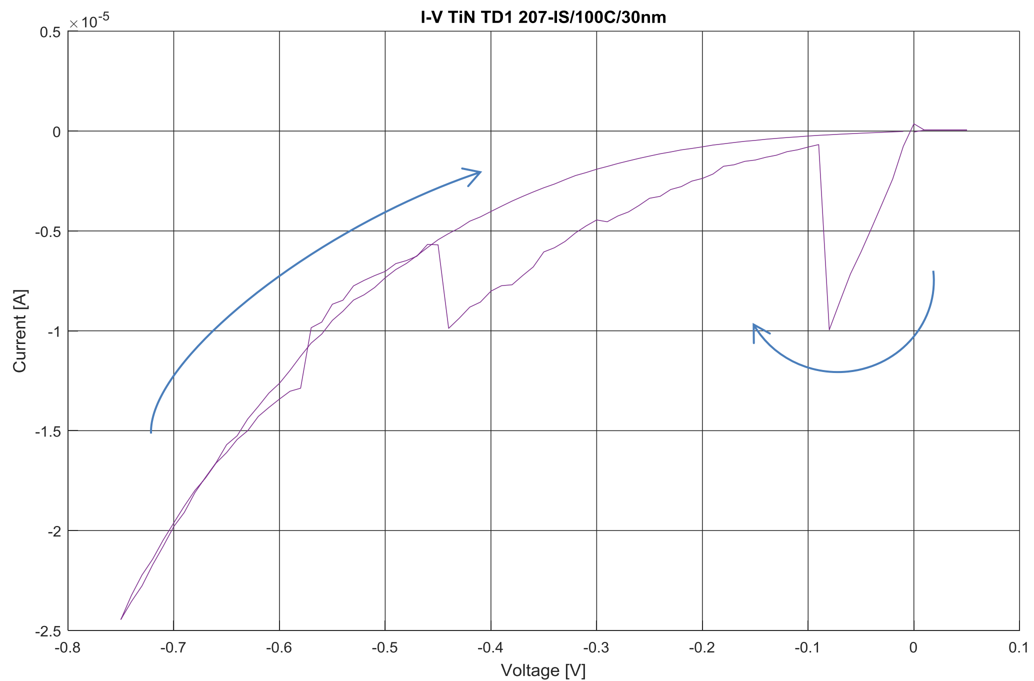

Figure 30. *The current- voltage characteristics of the 30-nm-thick sample deposited using the TD1 target on the TiN substrate at 100C and biased with the negative current compliance of 2.5·10*$^{-5}$*A at the voltage 0V/-0.8V.*

3.2.2.3 The TD2 target doped with two doping elements

Table 4 shows the overview of the samples deposited using a TD2 target at the different sputtering parameters. Almost all samples were deposited on the platinum substrates. Only two samples sputtered on the TiN substrate were fabricated for the comparison with the samples deposited on the platinum substrate at RT and 150C. The reason was that the samples with TiN were much more expensive than the samples on the platinum substrates. Moreover, all free samples with the TiN substrate were already consumed during the tests with the TD1 target. Furthermore, before the testing, the assumption was that the bottom electrode was inert and did not participate in the switching. Therefore it was not expected for there to be any differences in results due to usage of different substrates. In IWE2, the samples with TiN were used only for the ferroelectric memory applications. The samples with platinum substrates were frequently used for the fabrication of VCM memory cells based on the transition metal oxides, however, with considerably lower sputtering power.

Sample	Substrate	Target	Power	Temperature	Thickness	I-V curves
118-IS	Pt	TD2	150	100	20	435
146-IS	Pt	TD2	150	100	5	308
147-IS	Pt	TD2	150	100	10	32
150-IS	Pt	TD2	150	100	20	43
152-IS	Pt	TD2	150	100	30	13
164-IS	Pt	TD2	150	100	50	137
216-IS	Pt	TD2	150	RT	30	53
217-IS	Pt	TD2	150	150	30	50
227-IS	TiN	TD2	150	RT	30	72
230-IS	TiN	TD2	150	150	30	48

Table 4. *The overview of the samples deposited using the TD2 target at different sputtering parameters*

However, it was previously already noted that the samples deposited on the platinum substrate in comparison to those on the TiN substrate were very conductive during the electroforming tests. Additionally, there was a lot of missing data due to zero electroforming yield. The situation was quite the same with all samples deposited using the TD2 target, which had quite a few cells switched with hysteresis.

Figure 31 shows the current-voltage characteristics of the 50-nm-thick sample deposited using the TD2 target on the Pt substrate at 100C and biased with the positive and negative current compliance of $\mathbf{10^{-6}A}$ at voltage +3/-5V. The cell shows the bipolar type of switching with the filament (can be metallic or not). The curve had almost a symmetric shape, which was achieved by the increasing of the overvoltage on the negative side.

Figure 32 displays the current-voltage characteristics of the same sample as in Figure 31 with nearly the same bias, however with a completely different switching behavior. The cell is electroformed on both sides. The cell is OFF near zero and it electroforms again on the negative side.

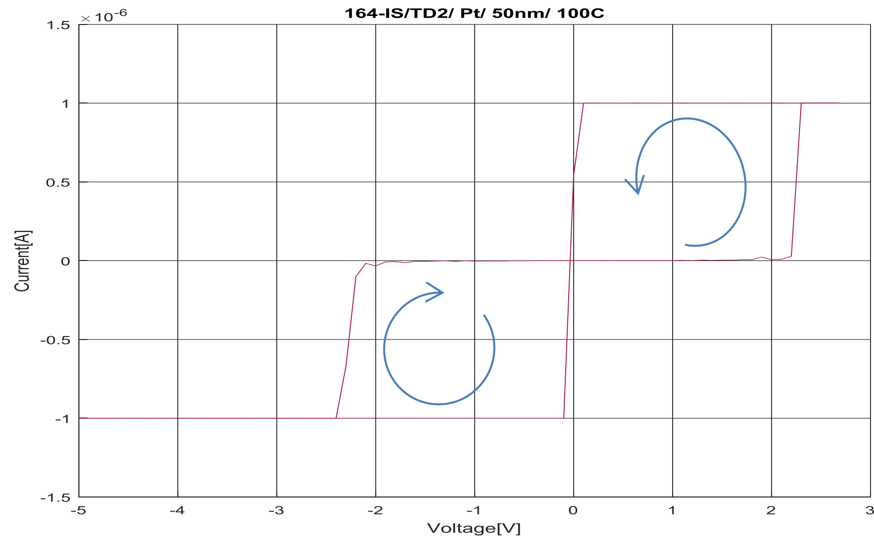

Figure 31. *The current-voltage characteristics of the 50-nm-thick sample deposited using the TD2 target on the Pt substrate at 100C and biased with the positive and negative current compliance of* 10^{-6}*A at the voltage +3/-5V.*

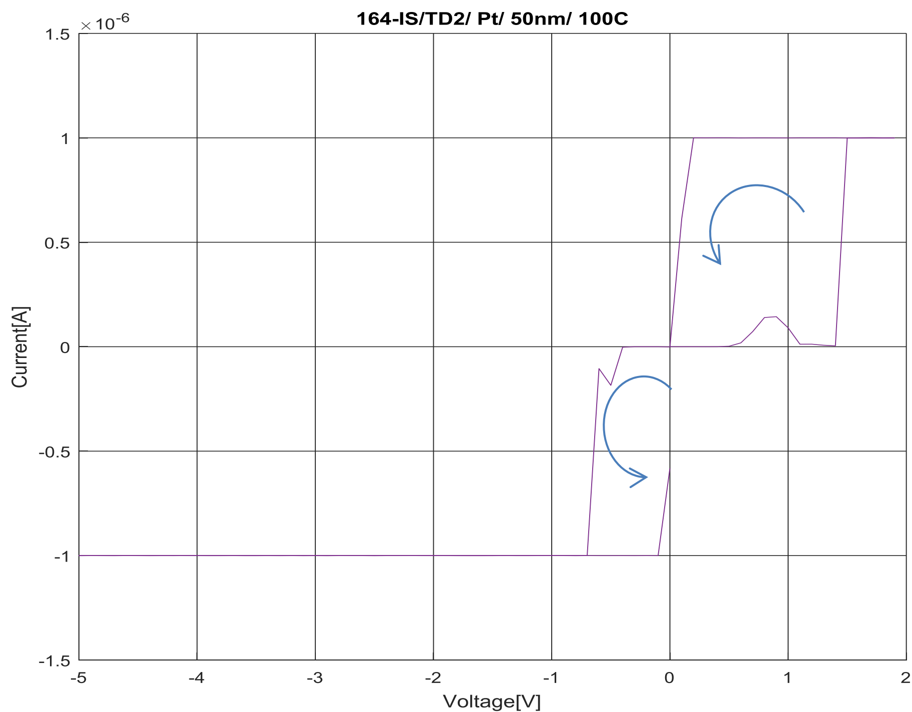

Figure 32. *The current- voltage characteristics of the 50-nm-thick sample deposited using the TD2 target on the platinum substrate at 100C and biased with the positive and negative current compliance of* 10^{-6}*A at the voltage +2/-5V.*

3.2.3 The R-V characteristics

The resistance-voltage characteristics of the samples deposited using the TD0, TD1, and TD2 targets are represented in Appendix 8.

3.2.4 The threshold switching

The additional figures relating to the threshold switching behavior is shown in Appendix 9.

3.2.4.1 *The room temperature*

3.2.4.1.1 The I-V curves

Figure 33, Figure 34 and Figure 35 show the I-V curves having the threshold-like switching behavior for the samples deposited using the TD0 target. The shape of the curves varies from the triangle-like to the more quadratic shape. The memory cell does not follow the limitation of the current compliance because the corresponding horizontal line is missing. However, the quadratic shaped current-voltages characteristics of the samples deposited using the TD0 target on the platinum substrate at RT displays the horizontal line of the current compliance.

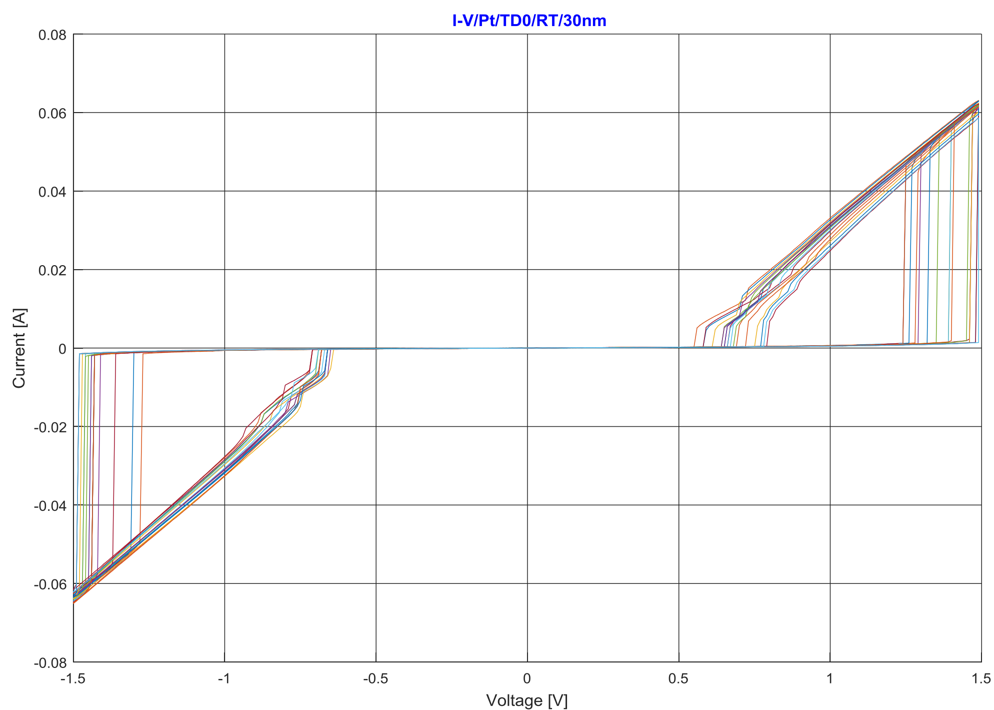

Figure 33. *The ZY view of I-V curves of the samples deposited using the TD0 target on the platinum substrate at RT showing the threshold-like switching behavior*

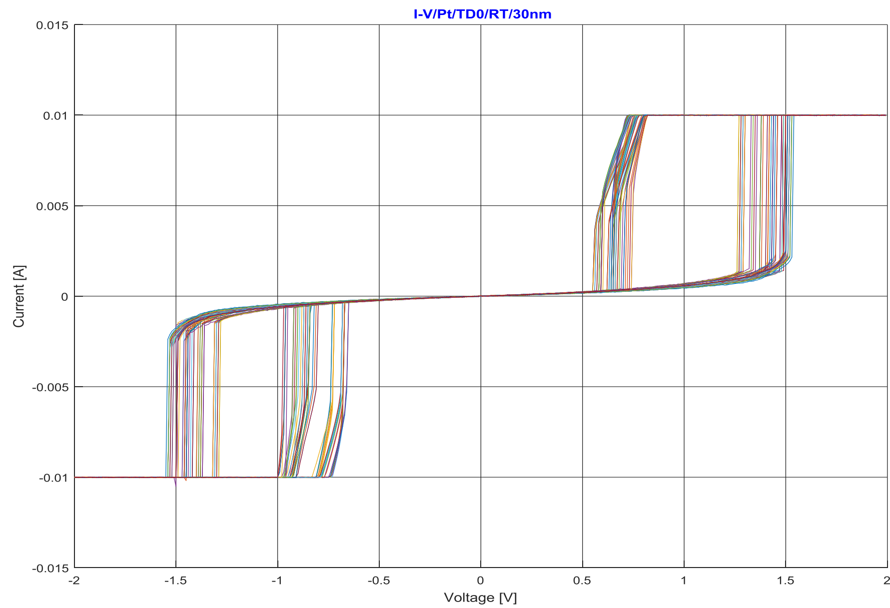

Figure 34. *The ZY view of the I-V curves of the samples deposited using the TD0 target on the platinum substrate at RT showing the threshold-like switching behavior*

Figure 35 shows the last part of the current-voltage characteristics of the samples deposited using the TD0 target on the platinum substrate at RT showing the threshold-like switching behavior. The memory cells do not follow the limitation of the current compliance on both the negative and positive sides. In addition, there is instability of the filament on the positive side due to the observed distortion in I-V curves.

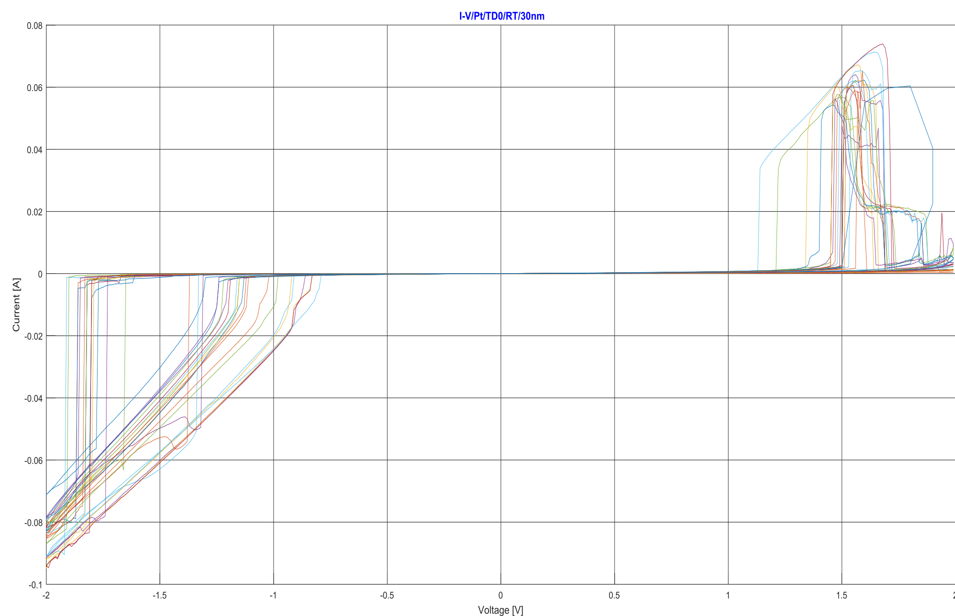

Figure 35. *The ZY view of the I-V curves of the samples deposited using the TD0 target on the platinum substrate at RT showing the threshold-like switching behavior*

3.2.4.1.2 The Schottky emission

Figure 36 shows the ZY view for the fitting of the 100 curves for the identification of the Schottky emission as a conduction mechanism.

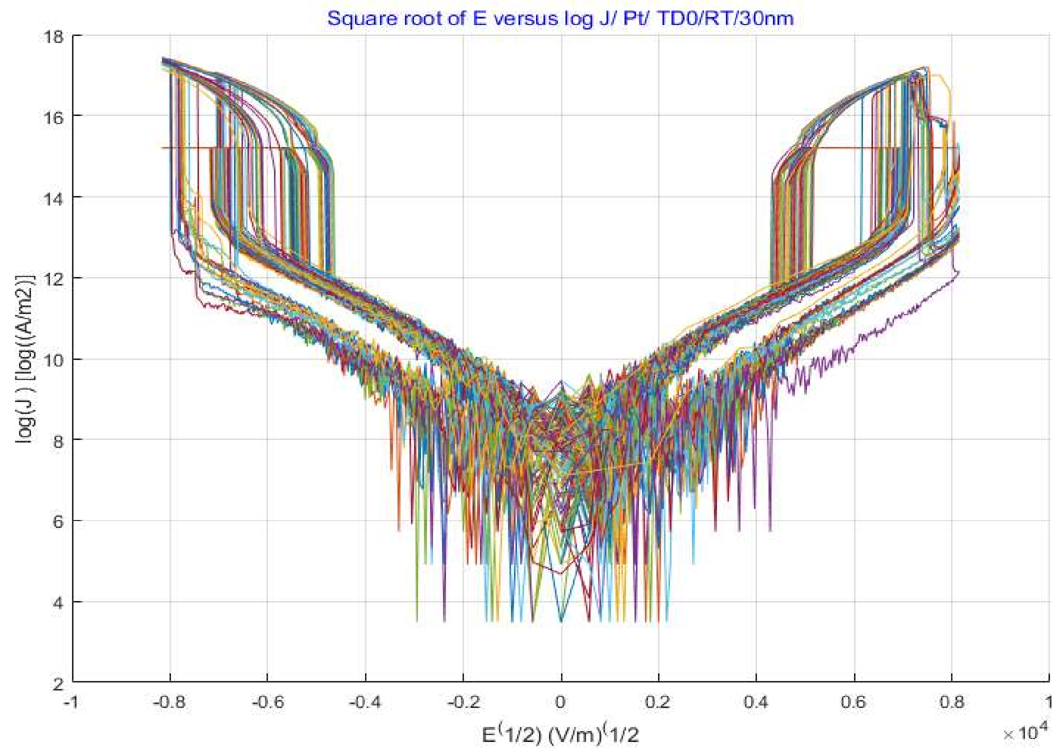

Figure 36. *The test for the Schottky emission: the ZY view of log(J)-sqrt(E) of the sample deposited on the platinum substrate at RT*

3.2.4.1.3 The Frenkel-Poole emission

Figure 37 shows the ZY view of the data fitting of 100 curves for the identification of the Frenkel-Poole emission as the conduction mechanism.

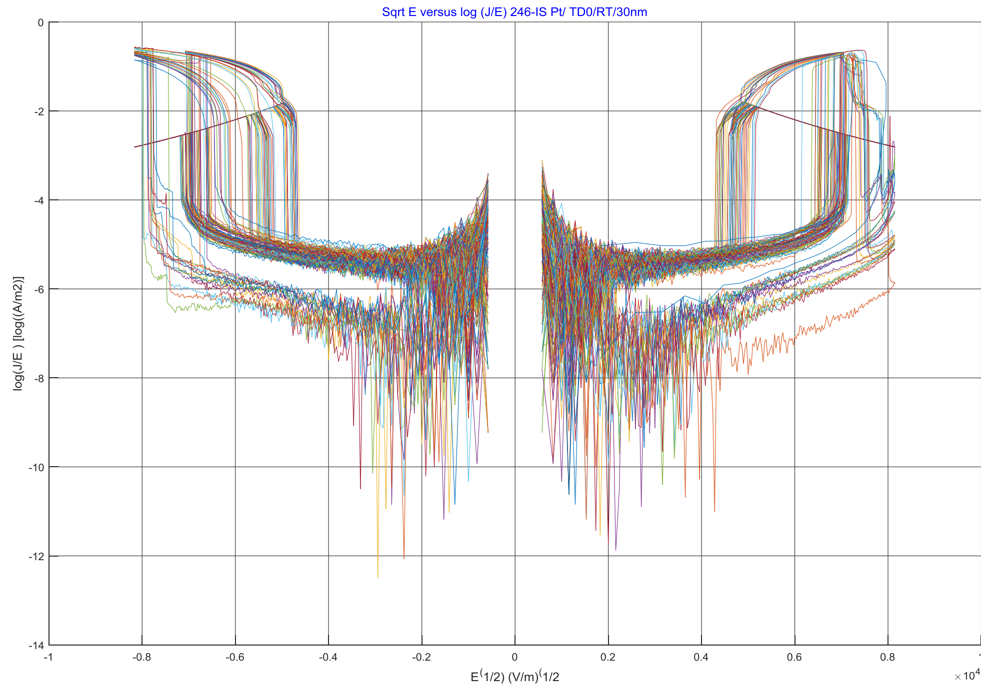

Figure 37. *The test for the Frenkel-Poole emission: the ZY view of log(J)-sqrt(E) of the sample deposited on the platinum substrate at RT*

3.2.4.2 *150C*

3.2.4.2.1 The I-V curves

Figure 38 and Figure 39 show a ZY view of the 103 current-voltage curves of the samples deposited using the TD0 target on the platinum substrate at 150C with a threshold-like switching behavior. In addition, the 3D view of the data and example of the single curve can be seen separately in Appendix 9.

Figure 38 shows the part of the curves with the triangular shape and the overshooting peaks. Despite the overshooting, the memory cells do not follow the limiting current compliance, because the corresponding horizontal line is missing.

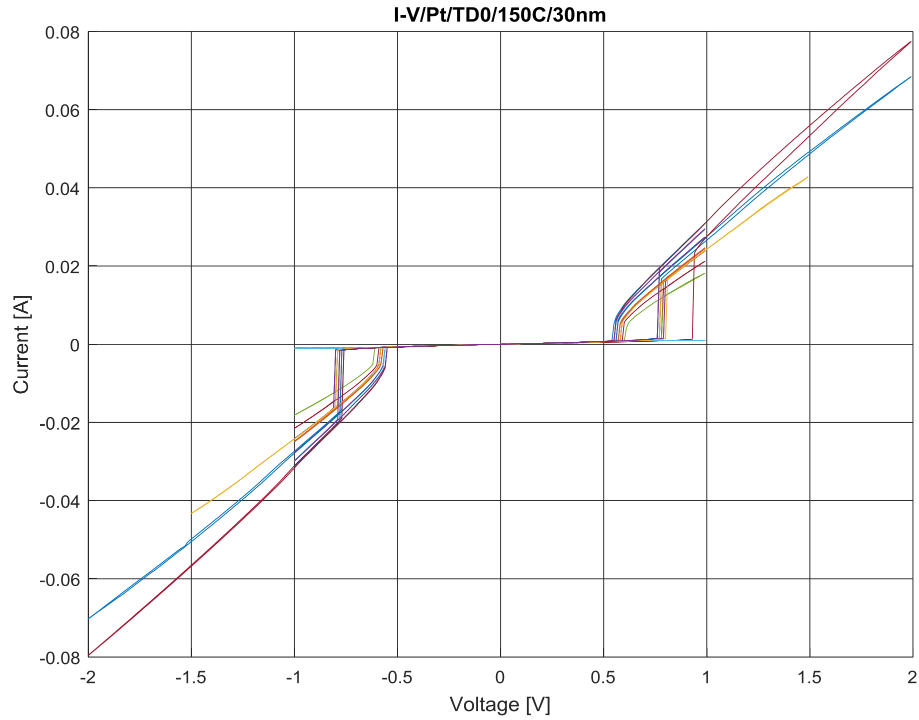

Figure 38. *The part of the current-voltage characteristics of the samples deposited using the TD0 target on the platinum substrate at 150C showing the threshold-like switching behavior*

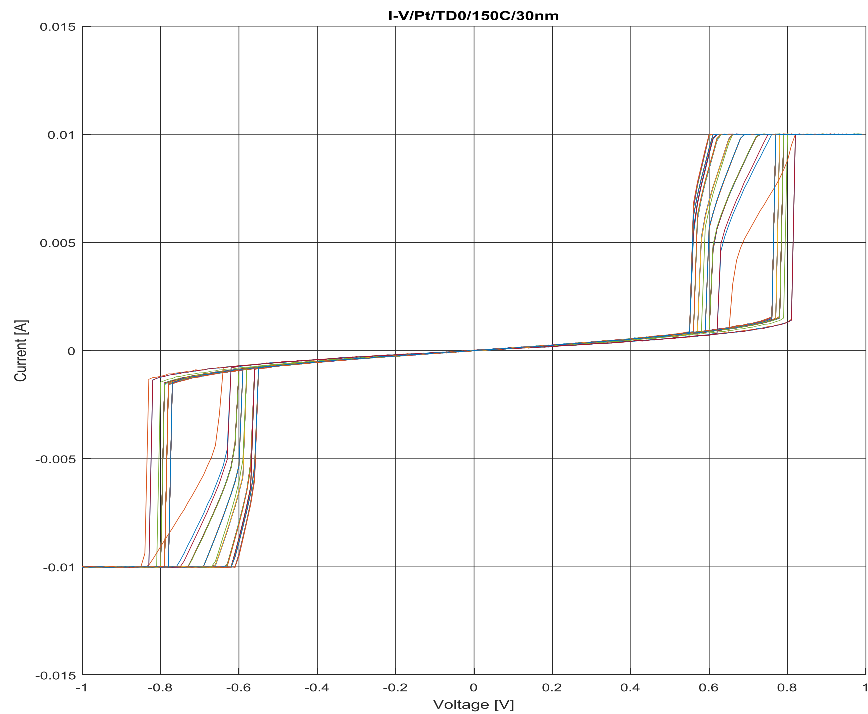

Figure 39. *The part of I-V curves of the samples deposited using the TD0 target on the platinum substrate at 150C showing the threshold-like switching behavior*

3.2.4.2.2 The Schottky emission

Figure 40 shows the ZY view of the data fitting of 103 curves for the identification of the Schottky emission as the conduction mechanism. The same data in 3D view and example of the single curve can be seen in Appendix 9.

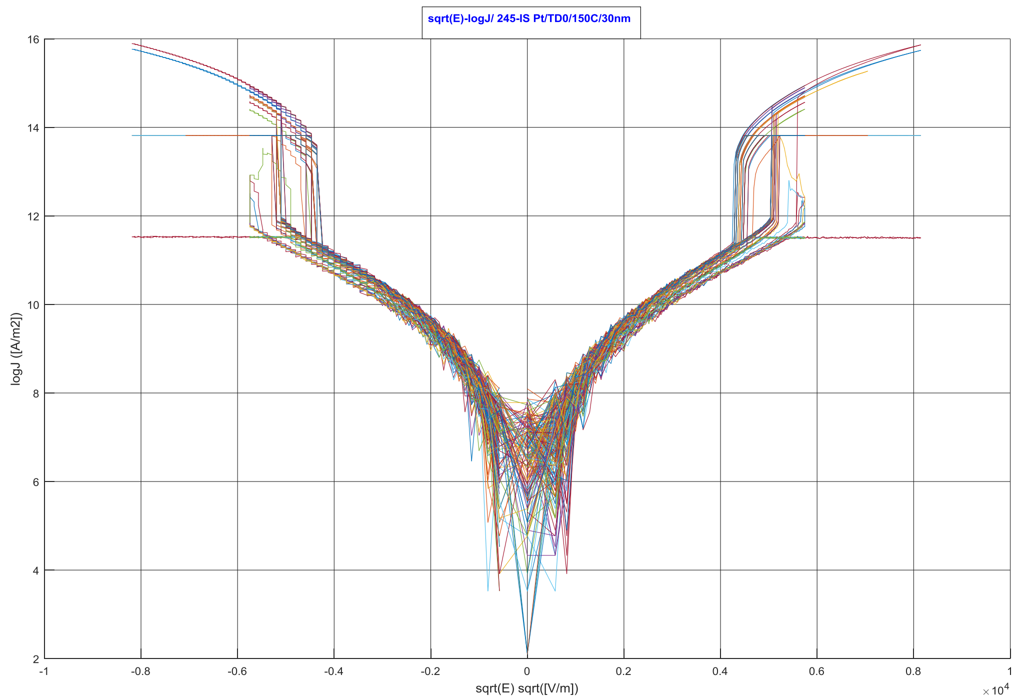

Figure 40. *The test for the Schottky emission: the ln(J) – sqrt(E) of the sample deposited using the TD0 target on the platinum substrate at 150C.*

3.2.4.2.3 Frenkel-Poole emission

Figure 41 shows the ZY view of the data fitting of 103 curves for the identification of the Frenkel-Poole emission as the conduction mechanism. The same data in 3D view and example of the single curve is shown in Appendix 9.

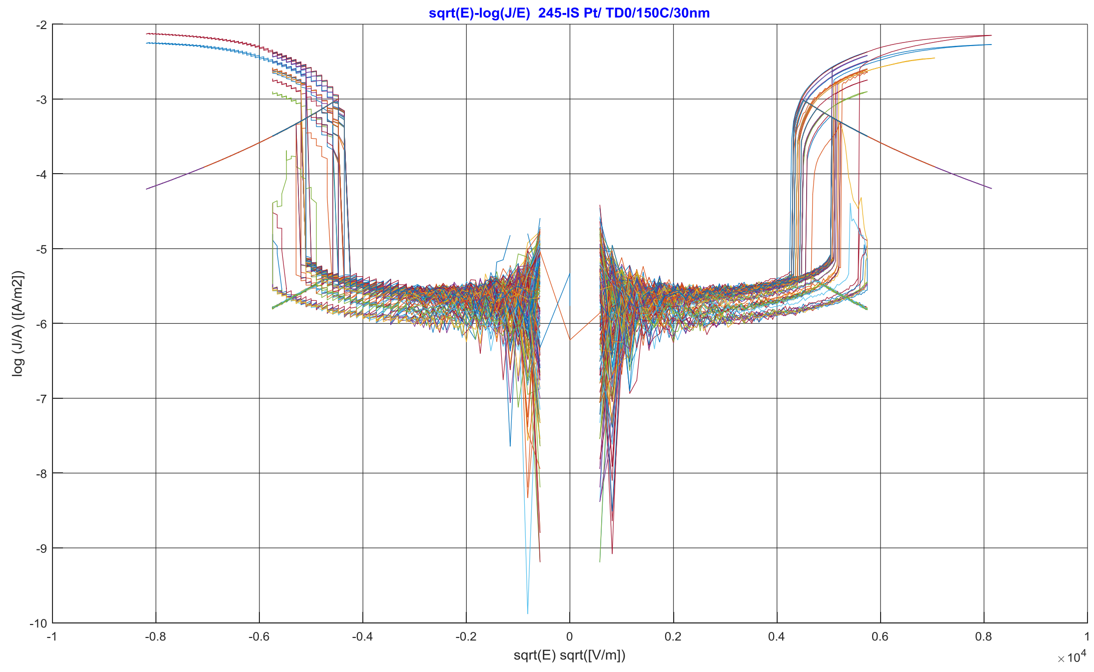

Figure 41. *The test for the Frenkel-Poole emission: the ZY view of the log(J)-sqrt(E) of the sample deposited on the platinum substrate at 150C*

4. CONCLUSIONS

1. The most important *experimental findings* were (1) *the threshold-like switching* in samples deposited using the TD0 target, (2) the existence of *the exponential relationship* between current and voltage, as well as *the stepwise jump of resistance* (3), in samples sputtered using the TD1 target.
2. *The variability* of switching behavior was extremely *high*, except for those with the threshold-like switching. It was impossible to attribute the change in resistivity to the specific target because all the samples were extremely conductive. The threshold-like switching in the samples deposited by the pure SiO2 target was the most pronounced.
3. *The variability* in the switching of samples with the threshold-like behavior was extremely *low*, which was attributed to the existence of the energy barrier, which restricts the ionic transport through the nanopores. The effect was perhaps observed since the relative humidity of the air on the measuring day made was extremely high. Therefore, the switching may be affected by *the moisture uptake*. *The Pourbaix diagram* may be useful for the description of the dynamic switching of ECM cells.
4. The *stepwise change of resistance* is, sometimes, termed as *quantized conductance,e* when the conductance is plotted versus time. The different size of the conductance jump may be related to the *difference in the capacitance of nanopores*, whose geometrical parameters vary. However, in our case, such a behavior was observed in a normal resistance-voltage curve.
5. *The resistance-voltage characteristics* of ReRAM may be useful in determining what types of materials participate in the switching.
6. Investigations of the effects on the *nanoscale* require *the most advanced analytic techniques*, which are able to catch the differences. In addition, the software needs to have support from the manufacturer to get all the advantages.
7. In addition, using the statistical methods requires the careful planning of finance, as well as the design of tests. If the size or quality of the generated data is not enough to perform the traditional statistical analysis, the EDA analysis together with MATLAB software can be useful.
8. In the ECM cell, switching can be controlled by adjusting the current compliance and the voltage bias. Therefore, the ECM cell can be thought of as both *the current- and voltage-controlled nanodevice*.
9. The *emf, threshold-like volatile switching*, as well as the possible *chemical reaction* during switching, indicate that the ECM memory cell *does not* behave as a *passive circuit element*. This deviation from memristive theory requires perhaps the development of a completely new theoretical explanation and classification of ReRAMs. On the other hand, using the memristive theory for the explanation of ReRAM would require redefining the memristors as *active circuit elements*, when memristance may be written as $M < 0$.

REFERENCES

Ahmed, E.M. (2013). Threshold switching in V 2 O 5-ZnO-SrO-FeO glasses, Current Applied Physics, Vol. 13(2), pp. 408-414.

Aratani, K., Ohba, K., Mizuguchi, T., Yasuda, S., Shiimoto, T., Tsushima, T., Sone, T., Endo, K., Kouchiyama, A. & Sasaki, S. (2007). A novel resistance memory with high scalability and nanosecond switching, Electron Devices Meeting, 2007. IEDM 2007. IEEE International, IEEE, pp. 783-786.

Axon Technologies Corp. Axon Technologies Corp. Announces Infineon as New Licensee of Programmable Metallization Cell Nonvolatile Memory Technology https://www.design-reuse.com/news/8739/axon-infineon-licensee-programmable-metallization-cell-nonvolatile-memory-technology.html.

Banerjee, W., Xu, X., Liu, H., Lv, H., Liu, Q., Sun, H., Long, S. & Liu, M. (2015). Occurrence of resistive switching and threshold switching in atomic layer deposited ultrathin (2 nm) aluminium oxide crossbar resistive random access memory, IEEE Electron Device Letters, Vol. 36(4), pp. 333-335.

Bartzsch, H., Glöß, D., Frach, P., Gittner, M., Schultheiß, E., Brode, W. & Hartung, J. (2009). Electrical insulation properties of sputter- deposited SiO2, Si3N4 and Al2O3 films at room temperature and 400 C, physica status solidi (a), Vol. 206(3), pp. 514-519.

Bentarzi, H. (2011). Transport in Metal-Oxide-Semiconductor Structures: Mobile Ions Effects on the Oxide Properties, Springer Science & Business Media, .

Celano, U. (2016). Metrology and physical mechanisms in new generation ionic devices, Springer, .

Chen, J., Su, J., Wang, W. & Reed, M. (2003). Electronic memory effects in self-assembled monolayer systems, Physica E: Low-dimensional Systems and Nanostructures, Vol. 16(1), pp. 17-23.

Chen, W., Tappertzhofen, S., Barnaby, H.J. & Kozicki, M.N. (2017). SiO2 based conductive bridging random access memory, Journal of Electroceramics, pp. 1-23.

Chen, W., Barnaby, H. & Kozicki, M. (2016). Volatile and non-volatile switching in Cu-SiO 2 programmable metallization cells, IEEE Electron Device Letters, Vol. 37(5), pp. 580-583.

Chen, Y., Lee, H., Chen, P., Wu, T., Wang, C., Tzeng, P., Chen, F., Tsai, M. & Lien, C. (2010). An Ultrathin Forming-Free $\ hbox {HfO} _ {x} $ Resistance Memory With Excellent Electrical Performance, IEEE Electron Device Letters, Vol. 31(12), pp. 1473-1475.

Cho, D., Valov, I., van den Hurk, J., Tappertzhofen, S. & Waser, R. (2012). Direct observation of charge transfer in solid electrolyte for electrochemical metallization memory, Advanced Materials, Vol. 24(33), pp. 4552-4556.

Chua, L. (2011). Resistance switching memories are memristors, Applied Physics A, Vol. 102(4), pp. 765-783.

Chua, L. (1971). Memristor- The missing Circuit Element, IEEE Transactions on Circuits and Systems I: Regular Papers, Vol. ct-18.

Chuang, M., Chen, Y., Su, Y., Hsiao, C., Huang, C., Tsai, J. & Yu, H. (2014). Negative differential resistance behavior and memory effect in laterally bridged ZnO nanorods grown by hydrothermal method, ACS applied materials & interfaces, Vol. 6(8), pp. 5432-5438.

Dearnaley, G., Stoneham, A. & Morgan, D. (1970). Electrical phenomena in amorphous oxide films, Reports on Progress in Physics, Vol. 33(3), pp. 1129.

Du, G., Wang, C., Li, H., Mao, Q. & Ji, Z. (2016). Bidirectional threshold switching characteristics in Ag/ZrO2/Pt electrochemical metallization cells, AIP Advances, Vol. 6(8), pp. 085316.

Du, Y., Pan, H., Wang, S., Wu, T., Feng, Y.P., Pan, J. & Wee, A.T.S. (2012). Symmetrical negative differential resistance behavior of a resistive switching device, ACS nano, Vol. 6(3), pp. 2517-2523.

El-Sayed, A., Watkins, M.B., Grasser, T., Afanas'ev, V.V. & Shluger, A.L. (2015). Hydrogen-induced rupture of strained Si─ O bonds in amorphous silicon dioxide, Physical Review Letters, Vol. 114(11), pp. 115503.

Fripp, A. (1975). Dependence of resistivity on the doping level of polycrystalline silicon, Journal of Applied Physics, Vol. 46(3), pp. 1240-1244.

Funabiki, F., Kamiya, T. & Hosono, H. (2012). Doping effects in amorphous oxides, Journal of the Ceramic Society of Japan, Vol. 120(1407), pp. 447-457.

Funck, C., Menzel, S., Aslam, N., Zhang, H., Hardtdegen, A., Waser, R. & Hoffmann-Eifert, S. (2016). Multidimensional Simulation of Threshold Switching in NbO2 Based on an Electric Field Triggered Thermal Runaway Model, Advanced Electronic Materials, .

Galasso, F.S. (2016). Structure and Properties of Inorganic Solids: International Series of Monographs in Solid State Physics, Elsevier, .

Han, D., West, D., Li, X., Xie, S., Sun, H. & Zhang, S. (2010). Impurity doping in SiO 2: Formation energies and defect levels from first-principles calculations, Physical Review B, Vol. 82(15), pp. 155132.

He, M. & Lu, T. (2012). Metal–Dielectric Diffusion Processes: Fundamentals, in: Metal-Dielectric Interfaces in Gigascale Electronics, Springer, pp. 11-22.

Ho, P.S., Leu, J. & Lee, W.W. (2003). Low dielectric constant materials for IC applications, Springer Science & Business Media, .

Hsieh, W., Lam, K. & Chang, S. (2014). Asymmetric resistive switching characteristics of In2O3: SiO2 cosputtered thin film memories, Journal of Vacuum Science & Technology B, Vol. 32(2), pp. 020603.

Huang, X., Chang, K., Chang, T., Tsai, T., Shih, C., Zhang, R., Huang, S., Chen, K., Chen, J. & Wang, H. (2014). Controllable set voltage in bilayer ZnO: SiO 2/ZnO x resistance random access memory by oxygen concentration gradient manipulation, IEEE Electron Device Letters, Vol. 35(12), pp. 1227-1229.

Hudgens, S. (2012). Progress in understanding the Ovshinsky Effect: Threshold switching in chalcogenide amorphous semiconductors, physica status solidi (b), Vol. 249(10), pp. 1951-1955.

Ielmini, D. (2008). Threshold switching mechanism by high-field energy gain in the hopping transport of chalcogenide glasses, Physical Review B, Vol. 78(3), pp. 035308.

Ielmini, D., Bruchhaus, R. & Waser, R. (2011). Thermochemical resistive switching: materials, mechanisms, and scaling projections, Phase Transitions, Vol. 84(7), pp. 570-602.

Ielmini, D. & Zhang, Y. (2007). Analytical model for subthreshold conduction and threshold switching in chalcogenide-based memory devices, Journal of Applied Physics, Vol. 102(5), pp. 054517.

ITRS (2015). International Technology Roadmap for Semiconductors 2.0: Executive Report, .

Jeong, D.S., Choi, B.J. & Hwang, C.S. (2006). Study of the negative resistance phenomenon in transition metal oxide films from a statistical mechanics point of view, Journal of Applied Physics, Vol. 100(11), pp. 113724.

Jeong, D.S., Schroeder, H. & Waser, R. (2007). Coexistence of bipolar and unipolar resistive switching behaviors in a Pt⁄ TiO2⁄ Pt stack, Electrochemical and solid-state letters, Vol. 10(8), pp. G51-G53.

Kilner, J. (2000). Fast oxygen transport in acceptor doped oxides, Solid State Ionics, Vol. 129(1), pp. 13-23.

Kim, S., Park, J., Woo, J., Cho, C., Lee, W., Shin, J., Choi, G., Park, S., Lee, D. & Lee, B.H. (2013). Threshold-switching characteristics of a nanothin-NbO 2-layer-based Pt/NbO 2/Pt stack for use in cross-point-type resistive memories, Microelectronic Engineering, Vol. 107pp. 33-36.

Kim, S. & Choi, Y. (2009). A Comprehensive Study of the Resistive Switching Mechanism in $\ hbox {Al/TiO} _ {x}/\ hbox {TiO} _ {2}/\ hbox {Al} $-Structured RRAM, IEEE Transactions on Electron Devices, Vol. 56(12), pp. 3049-3054.

Konig, D., Hiller, D., Gutsch, S., Zacharias, M. & Smith, S. (2017). Modulation Doping of Silicon using Aluminium-induced Acceptor States in Silicon Dioxide, Scientific reports, Vol. 7pp. 46703.

Kozicki, M.N., Park, M. & Mitkova, M. (2005). Nanoscale memory elements based on solid-state electrolytes, IEEE Transactions on Nanotechnology, Vol. 4(3), pp. 331-338.

Le Gallo, M., Athmanathan, A., Krebs, D. & Sebastian, A. (2016). Evidence for thermally assisted threshold switching behavior in nanoscale phase-change memory cells, Journal of Applied Physics, Vol. 119(2), pp. 025704.

Lee, J. (2011). Review paper: Nano-floating gate memory devices, Electronic Materials Letters, Vol. 7(3), pp. 175.

Lee, S., Kim, K., Oh, J., Kahng, B. & Lee, J. (2013). Origin of variation in switching voltages in threshold-switching phenomena of VO2 thin films, Applied Physics Letters, Vol. 102(6), pp. 063501.

Li, J., Zhang, H., Shao, G., Wu, B. & Ouyang, S. (2014). Negative differential resistance: Another banana? EPL (Europhysics Letters), Vol. 108(2), pp. 27005.

Li, S., Liao, Z., Li, J., Gang, J. & Zheng, D. (2009). Resistive switching properties and low resistance state relaxation in Al/Pr0. 7Ca0. 3MnO3/Pt junctions, Journal of Physics D: Applied Physics, Vol. 42(4), pp. 045411.

Lian, W., Long, S., Lü, H., Liu, Q., Li, Y., Zhang, S., Wang, Y., Huo, Z., Dai, Y. & Chen, J. (2011). Approaches for improving the performance of filament-type resistive switching memory, Chinese Science Bulletin, Vol. 56(4-5), pp. 461-464.

Lim, E.W. & Ismail, R. (2015). Conduction Mechanism of Valence Change Resistive Switching Memory: A Survey, Electronics, Vol. 4(3), pp. 586-613.

Lim, S.W., Shimogaki, Y., Nakano, Y., Tada, K. & Komiyama, H. (1999). Changes in orientational polarization and structure of silicon dioxide film by fluorine addition, Journal of the Electrochemical Society, Vol. 146(11), pp. 4196-4202.

Lin, Y., Ghosh, R.K., Addou, R., Lu, N., Eichfeld, S.M., Zhu, H., Li, M., Peng, X., Kim, M.J. & Li, L. (2015). Atomically thin resonant tunnel diodes built from synthetic van der Waals heterostructures, Nature communications, Vol. 6.

Liu, Q., Liu, M., Long, S., Wang, W., Zhang, M., Wang, Q. & Chen, J. (2009). Improvement of resistive switching properties in ZrO 2-based ReRAM with implanted metal ions, Solid State Device Research Conference, 2009. ESSDERC'09. Proceedings of the European, IEEE, pp. 221-224.

Liu, X., Li, S., Nandi, S.K., Venkatachalam, D.K. & Elliman, R.G. (2016). Threshold switching and electrical self-oscillation in niobium oxide films, Journal of Applied Physics, Vol. 120(12), pp. 124102.

Lu, W., Jeong, D.S., Kozicki, M. & Waser, R. (2012). Electrochemical metallization cells--blending nanoionics into nanoelectronics? MRS Bulletin, Vol. 37(2), pp. 124.

Maier, J. (2005). Nanoionics: ion transport and electrochemical storage in confined systems, Nature materials, Vol. 4(11), pp. 805-815.

Maier, J. (1995). Ionic conduction in space charge regions, Progress in solid state chemistry, Vol. 23(3), pp. 171-263.

McPherson, J., Kim, J., Shanware, A. & Mogul, H. (2003). Thermochemical description of dielectric breakdown in high dielectric constant materials, Applied Physics Letters, Vol. 82(13), pp. 2121-2123.

Meena, J.S., Sze, S.M., Chand, U. & Tseng, T. (2014). Overview of emerging nonvolatile memory technologies, Nanoscale research letters, Vol. 9(1), pp. 526.

Mills, T. & Kroger, F. (1973a). Electrical conduction at elevated temperatures in thermally grown silicon dioxide films, Journal of the Electrochemical Society, Vol. 120(11), pp. 1582-1586.

Mills, T. & Kroger, F. (1973b). Electrical conduction at elevated temperatures in thermally grown silicon dioxide films, Journal of the Electrochemical Society, Vol. 120(11), pp. 1582-1586.

Muller, C., Deleruyelle, D. & Ginez, O. (2012). Emerging memory concepts, in: Design Technology for Heterogeneous Embedded Systems, Springer, pp. 339-364.

Osburn, C. & Ormond, D. (1972). Dielectric Breakdown in Silicon Dioxide Films on Silicon II. Influence of Processing and Materials, Journal of the Electrochemical Society, Vol. 119(5), pp. 597-603.

Pandey, S.K. & Manivannan, A. (2016). Sub-nanosecond threshold-switching dynamics and set process of In3SbTe2 phase-change memory devices, Applied Physics Letters, Vol. 108(23), pp. 233501.

Preu, H., Feilmeier, J., Lang, M., Soellner, N., Walter, J. & Mack, W. (2014). A study on electrochemical effects in external capacitor packages, Microelectronics Reliability, Vol. 54(9), pp. 2023-2027.

Puthenthermadam, S.C.P. (2011). Characterization of Copper-doped Silicon Dioxide Programmable Metallization Cells, Arizona State University, .

Raghavan, G., Chiang, C., Anders, P.B., Tzeng, S., Villasol, R., Bai, G., Bohr, M. & Fraser, D.B. (1995). Diffusion of copper through dielectric films under bias temperature stress, Thin Solid Films, Vol. 262(1-2), pp. 168-176.

Redaelli, A., Pirovano, A., Benvenuti, A. & Lacaita, A. (2008). Threshold switching and phase transition numerical models for phase change memory simulations, Journal of Applied Physics, Vol. 103(11), pp. 6.

Revesz, A.G. (1965). The defect structure of grown silicon dioxide films, IEEE Transactions on Electron Devices, Vol. 12(3), pp. 97-102.

Rogacheva, E. (2008). The problem of doping of non-stoichiometric phases, Journal of Physics and Chemistry of Solids, Vol. 69(2), pp. 259-268.

Roma, G. & Limoge, Y. (2004). Density functional theory investigation of native defects in SiO 2: Self-doping and contribution to ionic conductivity, Physical Review B, Vol. 70(17), pp. 174101.

Saitoh, A., Matsuishi, S., Se-Weon, C., Nishii, J., Oto, M., Hirano, M. & Hosono, H. (2006). Elucidation of codoping effects on the solubility enhancement of Er3 in SiO2 glass: Striking difference between Al and P codoping, The Journal of Physical Chemistry B, Vol. 110(15), pp. 7617-7620.

Schindler, C. (2009). Resistive switching in electrochemical metallization memory cells

, .

Skuja, L., Hirano, M., Hosono, H. & Kajihara, K. (2005). Defects in oxide glasses, physica status solidi (c), Vol. 2(1), pp. 15-24.

Slesazeck, S., Mähne, H., Wylezich, H., Wachowiak, A., Radhakrishnan, J., Ascoli, A., Tetzlaff, R. & Mikolajick, T. (2015a). Physical model of threshold switching in NbO 2 based memristors, RSC Advances, Vol. 5(124), pp. 102318-102322.

Slesazeck, S., Mähne, H., Wylezich, H., Wachowiak, A., Radhakrishnan, J., Ascoli, A., Tetzlaff, R. & Mikolajick, T. (2015b). Physical model of threshold switching in NbO 2 based memristors, RSC Advances, Vol. 5(124), pp. 102318-102322.

Song, J., Prakash, A., Lee, D., Woo, J., Cha, E., Lee, S. & Hwang, H. (2015). Bidirectional threshold switching in engineered multilayer (Cu2O/Ag: Cu2O/Cu2O) stack for cross-point selector application, Applied Physics Letters, Vol. 107(11), pp. 113504.

Srivastava, J., Prasad, M. & Wagner, J. (1985). Electrical conductivity of silicon dioxide thermally grown on silicon, Journal of the Electrochemical Society, Vol. 132(4), pp. 955-963.

Stallings, W. (2000). Computer organization and architecture: designing for performance, Pearson Education India, .

Strukov, D.B., Snider, G.S., Stewart, D.R. & Williams, R.S. (2008). The missing memristor found. Nature, Vol. 453(7191), pp. 80-83.

Sun, H., Liu, Q., Li, C., Long, S., Lv, H., Bi, C., Huo, Z., Li, L. & Liu, M. (2014a). Direct observation of conversion between threshold switching and memory switching induced by conductive filament morphology, Advanced Functional Materials, Vol. 24(36), pp. 5679-5686.

Sun, H., Liu, Q., Long, S., Lv, H., Banerjee, W. & Liu, M. (2014b). Multilevel unipolar resistive switching with negative differential resistance effect in Ag/SiO2/Pt device, Journal of Applied Physics, Vol. 116(15), pp. 154509.

Sunandana, C. (2015). Introduction to solid state ionics: phenomenology and applications, CRC Press, .

Tappertzhofen, S. (2014). Redox and mass transport phenomena in resistively switching thin films, Universitätsbibliothek, .

Tappertzhofen, S., Valov, I., Tsuruoka, T., Hasegawa, T., Waser, R. & Aono, M. (2013). Generic relevance of counter charges for cation-based nanoscale resistive switching memories, ACS nano, Vol. 7(7), pp. 6396-6402.

To, J., Sokol, A.A., French, S.A., Kaltsoyannis, N. & Catlow, C.R.A. (2005). Hole localization in [AlO 4] 0 defects in silica materials, The Journal of chemical physics, Vol. 122(14), pp. 144704.

Toyoda, S., Okabayashi, J., Kumigashira, H., Oshima, M., Ono, K., Niwa, M., Usuda, K. & Hirashita, N. (2003). Effect of nitrogen doping into SiO2 studied by photoemission spectroscopy, Applied Physics Letters, Vol. 83(26), pp. 5449-5451.

Tsai, T., Chang, K., Chang, T., Chang, G., Syu, Y., Su, Y., Liu, G., Liao, K., Chen, M. & Huang, H. (2012a). Origin of Hopping Conduction in Sn-Doped Silicon Oxide RRAM With Supercritical CO2 Fluid Treatment, IEEE Electron Device Letters, Vol. 33(12), pp. 1693-1695.

Tsai, T., Chang, K., Chang, T., Syu, Y., Chuang, S., Chang, G., Liu, G., Chen, M., Huang, H. & Liu, S. (2012b). Bipolar resistive RAM characteristics induced by nickel incorporated into silicon oxide dielectrics for IC applications, IEEE Electron Device Letters, Vol. 33(12), pp. 1696-1698.

Tsuruoka, T., Terabe, K., Hasegawa, T. & Aono, M. (2010). Forming and switching mechanisms of a cation-migration-based oxide resistive memory, Nanotechnology, Vol. 21(42), pp. 425205.

Tsuruoka, T., Terabe, K., Hasegawa, T., Valov, I., Waser, R. & Aono, M. (2012). Effects of Moisture on the Switching Characteristics of Oxide-Based, Gapless-Type Atomic Switches, Advanced Functional Materials, Vol. 22(1), pp. 70-77.

Tsuruoka, T., Valov, I., Tappertzhofen, S., van den Hurk, J., Hasegawa, T., Waser, R. & Aono, M. (2015). Redox reactions at Cu, Ag/Ta2O5 interfaces and the effects of Ta2O5 film density on the forming process in atomic switch structures, Advanced functional materials, Vol. 25(40), pp. 6374-6381.

Tuller, H.L. & Bishop, S.R. (2011). Point defects in oxides: tailoring materials through defect engineering, Annual Review of Materials Research, Vol. 41pp. 369-398.

Valov, I. Redox-based resistive memory cells, web page. Available (accessed 5/26): http://www.laboratory-journal.com/science/material-science/redox-based-resistive-memory-cells.

Valov, I., Linn, E., Tappertzhofen, S., Schmelzer, S., Van den Hurk, J., Lentz, F. & Waser, R. (2013). Nanobatteries in redox-based resistive switches require extension of memristor theory, Nature communications, Vol. 4pp. 1771.

Valov, I. & Lu, W.D. (2016). Nanoscale electrochemistry using dielectric thin films as solid electrolytes, Nanoscale, Vol. 8(29), pp. 13828-13837.

Valov, I. & Waser, R. (2013). Comment on Real-Time Observation on Dynamic Growth/Dissolution of Conductive Filaments in Oxide-Electrolyte-Based ReRAM, Advanced Materials, Vol. 25(2), pp. 162-164.

van den Hurk, J. (2016). Germanium Sulphide Based Resistive Switching Devices, .

Wager, J.F. (2017). Low-field transport in SiO2, Journal of Non-Crystalline Solids, Vol. 459pp. 111-115.

Wang, S., Liu, W., Gao, J., Qiu, X., Feng, Y., Hou, X., Yu, D. & Li, D. (2012). Resistive switching and threshold switching behaviors in La0. 1Bi0. 9Fe1− xCoxO3 ceramics, Journal of Applied Physics, Vol. 112(3), pp. 034110.

Wang, Y., Sohn, Y., An, L., Fan, Y. & Zhang, L. (2006). Oxygen diffusion through Al-doped amorphous SiO2, Journal of phase equilibria and diffusion, Vol. 27(6), pp. 671-675.

Wang, Y., Comes, R.B., Wolf, S.A. & Lu, J. (2016). Threshold Switching Characteristics of Nb/NbO 2/TiN Vertical Devices, IEEE Journal of the Electron Devices Society, Vol. 4(1), pp. 11-14.

Waser, R. & Aono, M. (2007a). Nanoionics-based resistive switching memories, Nature materials, Vol. 6(11), pp. 833-840.

Waser, R., Dittmann, R., Staikov, G. & Szot, K. (2009). Redox-based resistive switching memories–nanoionic mechanisms, prospects, and challenges, Advanced Materials, Vol. 21(25-26), pp. 2632-2663.

Waser, R. & Aono, M. (2007b). Nanoionics-based resistive switching memories. Nature materials, Vol. 6(11), pp. 833-840.

Wedig, A., Luebben, M., Cho, D., Moors, M., Skaja, K., Rana, V., Hasegawa, T., Adepalli, K.K., Yildiz, B. & Waser, R. (2016a). Nanoscale cation motion in TaOx, HfOx and TiOx memristive systems, Nature nanotechnology, Vol. 11(1), pp. 67-74.

Wedig, A., Luebben, M., Cho, D., Moors, M., Skaja, K., Rana, V., Hasegawa, T., Adepalli, K.K., Yildiz, B. & Waser, R. (2016b). Nanoscale cation motion in TaOx, HfOx and TiOx memristive systems, Nature nanotechnology, Vol. 11(1), pp. 67-74.

Williams, J.S. & Poate, J.M. (2014). Ion implantation and beam processing, Academic Press, .

Willis, B.G. & Lang, D.V. (2004). Oxidation mechanism of ionic transport of copper in SiO 2 dielectrics, Thin Solid Films, Vol. 467(1), pp. 284-293.

Yamin, M. (1965). Charge storage effects in silicon dioxide films, IEEE Transactions on Electron Devices, Vol. 12(3), pp. 88-96.

Yang, J.J., Zhang, M., Pickett, M.D., Miao, F., Strachan, J.P., Li, W., Yi, W., Ohlberg, D.A., Choi, B.J. & Wu, W. (2012). Engineering nonlinearity into memristors for passive crossbar applications, Appl.Phys.Lett, Vol. 100(11), pp. 113501.

Yang, Y., Takahashi, M., Abe, H. & Kawazoe, Y. (2008). Structural, Electronic and Optical Properties of the Al2O3 Doped SiO2: First Principles Calculations, Materials transactions, Vol. 49(11), pp. 2474-2479.

Yang, Y., Gao, P., Li, L., Pan, X., Tappertzhofen, S., Choi, S., Waser, R., Valov, I. & Lu, W.D. (2014). Electrochemical dynamics of nanoscale metallic inclusions in dielectrics, Nature communications, Vol. 5.

Yao, J., Sun, Z., Zhong, L., Natelson, D. & Tour, J.M. (2010). Resistive switches and memories from silicon oxide, Nano letters, Vol. 10(10), pp. 4105-4110.

Yoo, J., Woo, J., Song, J. & Hwang, H. (2015). Threshold switching behavior of Ag-Si based selector device and hydrogen doping effect on its characteristics, AIP Advances, Vol. 5(12), pp. 127221.

Zachariasen, W.H. (1932). The atomic arrangement in glass, Journal of the American Chemical Society, Vol. 54(10), pp. 3841-3851.

Zalden, P., Shu, M.J., Chen, F., Wu, X., Zhu, Y., Wen, H., Johnston, S., Shen, Z., Landreman, P. & Brongersma, M. (2016). Picosecond electric-field-induced threshold switching in phase-change materials, Physical Review Letters, Vol. 117(6), pp. 067601.

Zervos, M., Vasile, E., Vasile, E., Karageorgou, E. & Othonos, A. (2015). Current transport properties of CuS/Sn: In2O3 versus CuS/SnO2 nanowires and negative differential resistance in quantum dot sensitized solar cells, The Journal of Physical Chemistry C, Vol. 120(1), pp. 11-20.

Zhang, L., Cosemans, S., Wouters, D.J., Groeseneken, G., Jurczak, M. & Govoreanu, B. (2015). One-selector one-resistor cross-point array with threshold switching selector, IEEE Transactions on Electron Devices, Vol. 62(10), pp. 3250-3257.

Zhang, R., Chang, K., Chang, T., Tsai, T., Chen, K., Lou, J., Chen, J., Young, T., Shih, C. & Yang, Y. (2013). High performance of graphene oxide-doped silicon oxide-based resistance random access memory, Nanoscale research letters, Vol. 8(1), pp. 497.

Zhong, K., Cheng, G., Cheng, X., Zheng, R. & Xiao, Z. (2011). Photoluminescence from SiGe NPs: SiO2 Thin Films Co-doped with Al, Journal of the Korean Physical Society, Vol. 58(4), pp. 934-937.

Zhou, H., Zhu, Y., Wang, H. & Fang, G. (2014). Investigation of threshold switching mechanism based on Mn-doped ZnO/GaN heterojunction by photogenerated carrier injection, Applied Physics A, Vol. 116(3), pp. 1415-1420.

Zhou, Y., Yang, P., Yuan, C. & Huo, Y. (2013). Electrochemical migration failure of the copper trace on printed circuit board driven by immersion silver finish, CHEMICAL ENGINEERING, Vol. 33.

LIST OF APPENDIXES

Appendix 1 Memristor

Appendix 2 Pourbaix Diagram

Appendix 3 Doping of Other Oxides

Appendix 4 The Research Methodology, Material Characterization and Fabrication

Appendix 5 Statistics

Appendix 6 Electroforming

Appendix 7 Current-Voltage Characteristics

Appendix 8 Resistance

Appendix 9 Threshold Switching

Appendix 10 Quantum Size Effects and ionic Coulomb Blockade

APPENDIX 1

" Memristor"

TO THE MASTER THESIS "CHARACTERIZATION OF THE DOPED SILICON DIOXIDE AND ITS IMPLICATION FOR THE RESISTIVE SWITCHING PHENOMENA IN THE ELECTROCHEMICAL METALLIZATION CELLS"

1.1 Memristor

Introduction. In 1971, Leon Chua had suggested that in addition to a capacitor, inductor, and resistor, the fourth fundamental circuit element can exist. He had named it memristor, which is the short form for the memory resistor (Chua 1971). This new circuit element should behave as a non-linear resistor with memory (Chua 1971). After turning the voltage off, the memristor stays at current resistance until it is turned on again, thus it has memory. The resistance of memristors is dependent on the polarity of the voltage and its magnitude (Williams 2008).

In a memristor, which is controlled by charge, the equation $M(q) \equiv d\varphi(q)/dq$ expresses a memristance and $v(t) = M\big(q(t)\big)i(t)$ defines the voltage. At the arbitrary time, the integral of the memristive voltage or current defines the memristance of memristor (Chua 1971).The state vector $q(t) = \int_0^t i\,dt$ refers to the total charge going through the memristor and it is not the stored charge of a capacitor (Oster 1974). The memristor with memristance M establishes a connection between q (charge) and φ (magnetic flux) according to the equation $d\varphi = Mdq$ (Strukov et al. 2008).

Passivity. $\varphi - q$ characteristics of memristor can have a derivative. The behavior of memristor as a circuit element is controlled by charge q flowing through it. If the incremental memristance of the memristor is positive ($i.e., M(q) \geq 0$), then the memristor is passive. (Chua 1971). As a passive circuit element, the memristor always has a positive resistance ($R(x, i) \geq 0$). Therefore, it cannot discharge energy. If the memristor is passive, then the instantaneous power entering the one-port is always non-negative and the discharge of energy is not possible (Chua & Kang 1976). The passive memristor exhibits *non-volatile memory* (Chua 2011). Therefore, if ReRAM exhibits the *volatile* threshold switching, the cell could not be defined as a passive memristor.

Zero cross-point property and the Lissajous figures. The Lissajous figures, which is the hysteretic current-voltage characteristics of memristors, always go through the origin. After the infinite

increase of the frequency, the Lissajous figure degenerates to a straight line without the hysteresis. Due to hysteresis, the system possesses certain inertia, hence it is not able to react quickly. Depending on the biasing point, the memristive one-port may be capacitive or inductive under small-signal conditions. The Lissajous figures always go through the origin. Thus, the memristor's hysteresis decreases as frequency increases, degenerating into a resistive system (Chua & Kang 1976).

The non-linear circuit element. The non-linear dynamic systems called the memristive systems, which behave like resistors. Having a memory with the small- signal capacitive or inductive effects, they cannot discharge energy. In the waveforms, there is no shift in phases of the input and output. As a result, Lissajous figures always pass through the zero origins. The memristive systems behave like non-linear resistors at a very low frequency. However, at extremely high frequencies, memristors reduce to linear resistors (Chua & Kang 1976). In the linear elements, M is constant and the memristance is identical to the resistance. The non-linear $i - v$ characteristics are due to the non-linearity of the relationship between q and φ (Strukov et al. 2008).

The appearance of memristance. Many memristive devices have been wrongly identified as the non-linear resistors. Thermistors, neon bulbs, fluorescent lamps (Chua & Kang 1976) as well as ionic systems and amorphous solid state ovonic devices (Chua 1971) are devices which should be recognized as having memristive properties (Chua & Kang 1976). The memristance has also been found in the human blood and in the biological ion channel. In nanoscale, the metal-oxide-based memristor may exhibit a *negative differential resistance* (Prodromakis et al. 2012). The memristance appears in nanoscales in the titanium-dioxide-based memory cells (Strukov et al. 2008).

TiO2-memristor. In 2008, R.S. Williams from Hewlett- Packard‘s Quantum Science Research Laboratory recognized that the current-voltage characteristics of TiO2 and Chua's memristor resemble each other. Both curves had a ‘pinched –hysteresis loops’ (R. 2008). Under the applied electric field, the resistance of a thin film of TiO2 modulates with a concentration of oxygen vacancies. The slight non-stoichiometry in TiO2 turns it into a conductor where oxygen vacancies act as a shallow donor (Strukov et al. 2010). Applying the positive voltage would repel the positively charged vacancies of oxygen in the TiO_{2-x} layer toward the TiO_2 layer. Under the negative bias, the oxygen vacancies are pushed back and forth out of the TiO_2 and the device turns off (R. 2008).

In the thin films, the hysteretic resistance switching necessitates the rearrangement of atoms modulating the current. Thus, the semiconductive film has a section with a low and high concentration of the doping elements. Under an external bias $v(t)$, two boundary regions move initiating the doping elements to drift with memristance $M(q) = R_{OFF}\left(1 - \frac{\mu_v \cdot R_{ON}}{D^2} \cdot q(t)\right)$. In the

equation, μ_v is the mobility of dopants and D is the film thickness. Thus, the memristance becomes large when the dopant mobility is high and thickness is of nanosize (Strukov et al. 2008). In nanoscales, the memristance can explain the current-voltage switching anomalies, conductance with hysteresis, multiple conductance states, and the negative differential resistance (Tour & He 2008).

Rejection of negative resistance for an ideal memristor. According to Leon Chua, an ideal memristor may exclusively possess one operating point, which is at zero current and voltage. Also, a small-signal negative resistance does exist in memristor if memristor is not active at the origin. This can be the case when an internal power supply such as nuclear or chemical reactions, batteries or light exist in the memristor. Therefore, if such a device without internal power supply shows the small-signal negative resistance, such a device is not an ideal memristor (Chua 2011).

The real memristor and emf. In the nanoionic devices, the chemical gradients potential generates an electromotive force (emf). In all tested ReRAMs, measured potential indicates the presence of an emf and nanosize –battery effect, which violates the zero –crossing properties of the memristor. Due to the inherent activity of the electrochemical systems, the nanoionic- resistive switches as the non-zero-crossing devices cannot be the passive circuit elements. The emf voltage might affect both the operation of the device and the retention (Valov et al. 2013).

Therefore, without the requirement of zero-crossing property, the theory can be significantly extended and include many memristive, memcapacitive and meminductive devices. The memristive theory should take the emf and nanobattery effect into account and consider ReRAM as a real memristor (Valov et al. 2013).

Cons of memristive theory. The claim of finding the physical implementation of missing memristors announced by Strukov et.al in 2008 (Strukov et al. 2008) created a harsh criticism of the memristive theory (Vongehr & Meng 2015). Strukov et.al pointed out that the memristive systems were hidden for so long because the magnetic field, in fact, does not affect the memristance (Strukov et al. 2008). Moreover, in 2011 Leon Chua confirmed the ReRAM nanodevices are memristors (Chua 2011).

The critics of the memristive theory were related to the fact that ReRAM devices were not new and it is known that the nanodevice can work without magnetism which is necessary for the ideal memristor. Furthermore, the memristor, as well as the inductor, are impossible without magnetic flux. The mechanical memristor, if it exists, would need mass as inertia just like magnetism needs electromagnetic inductance. No one could find hypothesized real memristor for so long because it did not exist. It is, therefore, more probable that memristor might be found in electro-optics, rather than in nanotechnology (Vongehr & Meng 2015).

The memristor's advantages. Memristors in the integrated circuits can create the ultra-dense memory, working as the learning networks, having the function of the brain synapse (Strukov et al. 2008). Using memristors, the electronic circuits with the functions of a brain can be possible. The crossbar architecture of the nanoscale circuits has a much higher density of switching elements than ICs (integrated circuits) with transistors (R. 2008). Modeling the new memristive circuit elements and the building blocks would require the implementation of new mathematical methods. The behavior of these novel nanodevices is frequency dependent and are non-linear. These devices display a Coulomb blockade, which is a quantum mechanical effect (Chua 2003).

Redefinition of the memristor concept. So far, the memristor is defined only as the passive circuit elements with $M(q) \equiv (d\varphi(q)/dq) \geq 0$ (Chua 1971; Chua et al. 1976; Chua 2003; Chua 2011). However, if we define negative memristance as $M(q) = \left(\frac{d\varphi(q)}{dq}\right) < 0$.
Then, $\left(\frac{d\varphi(q)}{dq}\right) < 0$, if $d\varphi(q) < 0$ or $dq < 0$, where both the negative conditions are possible and where $d\varphi(q)$ is magnetic flux. Moreover, the electromotive force is defined as $\varepsilon = -\frac{d\varphi(q)}{dt}$. Therefore, if $d\varphi(q) = -\varepsilon\, dt<0$, then the electromotive force should be $\varepsilon > 0$. The electromotive force can have the magnetic or chemical origin. Therefore, theoretically, the memristance can be defined for $M < 0$ if it is necessary.

Based on the above-mentioned, there is no direct contradiction between the memristor theory and emf, except that the condition for $M<0$ has not been defined before. The argument of the necessity of the magnetism (Vongehr & Meng 2015) for the real memristors, as well as the neglecting of the magnetism (Strukov et al. 2008) for the nanoscale, ReRAMs cannot per se be the argument for the proving or abandoning the memristor's concept for ReRAMs. If materials do not exhibit strong bulk magnetism, they are, anyway, diamagnetic. Therefore, the very weak magnetism and magnetic induction would be present in any case. $M>0$ defines memristors as passive electronic circuit elements, but circuit elements with $M<0$ or $R<0$ would be active.

ReRAM as an active circuit element. According to prof. Chua (Chua 2011), *the activity of the memristor* could be also due to the chemical reaction. However, such a possibility for a passive memristor was completely excluded by definition. In addition, the two-terminal memory devices were defined as passive circuit elements, because they exhibit the non-volatile type of memory switching. At that moment, the volatile threshold-type switching in ReRAMs was less known.

The emf and nanobattery effect in ReRAMs (Valov et al. 2013) was used to justify the extension of the memristive theory to other types of capacitive and inductive devices. The existence of emf may also imply that ReRAMs are intrinsically not passive elements.

Possibility of the chemical reaction during switching. At the moment, the explanation of the switching behavior of ECM cells is based on the assumption that Cu ions do not interact with the

oxide matrix and the created conductive filament is entirely metallic. According to the classical explanation of ECM cell (Valov et al. 2013), the creation of the metallic filament means the direct connecting of the opposite electrodes after applying the positive bias. This explanation implies that the connection of the opposite electrodes with the consequent transition from the OFF to the ON state can be actually seen in the resistance-voltage characteristics as an abrupt vertical line. After, this abrupt transition, the conduction type is usually ohmic, which can be seen as the curving line in R-V characteristics on a semilogarithmic scale. This type of behavior was defined as metallic, which implies that conductive path is literally of metallic Cu. The disconnection of the opposite electrodes is usually explained as an electrochemical dissolution of the metallic filament after applying the negative bias. This disconnecting of electrodes can be also seen as the abrupt vertical line in R-V curve.

Unfortunately, the above-mentioned metallic type of switching was sometimes very difficult to obtain. In these cases, the shape of the R-V curves together with the transition zone between the OFF and ON states indicated that conductive path is not of metallic type. The stepwise change of resistance, the inclining line in semilogarithmic R-V curves, as well as a different threshold-like type of curves, indicate that the switching behavior in ECM cell is more complex than just of the metallic type.

The deviation of the simple metallic type of switching behavior could indicate that during the switching the conductive filament undergoes the series of changes which can be seen in the R-V curves. This may indicate that ECM cell undergoes the chemical reaction during switching. In addition, according to Phourbaix diagram explained in Appendix 2, the cations in order to be mobile need to be oxidized as well as the pH value of electrolyte needs to be adjusted. Moreover, the nanoionics assumes that when charged species propagate through the neutral matrix, they polarize the nearby environment. Due to such a polarization, some chemical bonds may be broken. Also, the shape of switching curves may indicate that the filament is oxidized.

Furthermore, the out-diffusion of oxygen from the formed TiN/SiOx/TiN device during switching was also reported (Mehonic et al. 2013; Mehonic et al. 2015; Mehonic et al. 2016). This implies that SiOx also can participate in the resistive switching. Based on above-mentioned, the solid-state chemical reaction during the resistive switching cannot be completely excluded. This is, especially, a case when the shape of switching curves is obviously non-ohmic. The possible chemical reactions are, for example, the creation of oxidized metallic filament and out-diffusion of oxygen from oxide.

The future development of the theoretical explanation of ReRAMs. Despite the controversy, the memristive theory has an influence on the theoretical explanation, modeling and even development of the emerging two- terminal devices based on all types of oxides and chalcogenides. ReRAMs resemble the memristors but deviate from them. ReRAM behaves as a non-linear circuit element,

which can be passive or active. The volatile threshold switching, emf as well as possible chemical reaction, may indicate that, in these particular cases, the ECM cell does not behave as a passive circuit element.

Obviously, the memristive theory needs the modifications when it is in use for the description of the active memory cells. On the other hand, rejecting the concept of memristors for ReRAMs means that a new theoretical explanation of ReRAMs, as the non-linear circuit elements, needs to be proposed.

REFERENCES

Chua, L. (2011a). Resistance switching memories are memristors, Applied Physics A, Vol. 102(4), pp. 765-783.

Chua, L.O. (2003). Nonlinear Circuit Foundations for Nanodevices, Part I: The Four-Element Torus, .

Chua, L.O. & Kang, S.M. (1976). Memristive Devices and Systems, Proceedings of the IEEE, Vol. 64(2), pp. 209-223.

Chua, L. (1971). Memristor- The missing Circuit Element, IEEE Transactions on Circuits and Systems I: Regular Papers, Vol. ct-18.

Chua, L. (2011b). Resistance switching memories are memristors, Applied Physics A: Materials Science and Processing, Vol. 102(4), pp. 765-783.

Chua, L., Mo, K.S. & Leon O.Chua Sung Mo Kang (1976). Memristive devices and systems, Vol. 64(2), .

Mehonic, A., Buckwell, M., Montesi, L., Garnett, L., Hudziak, S., Fearn, S., Chater, R., McPhail, D. & Kenyon, A.J. (2015). Structural changes and conductance thresholds in metal-free intrinsic SiOx resistive random access memory, Journal of Applied Physics, Vol. 117(12), pp. 124505.

Mehonic, A., Buckwell, M., Montesi, L., Munde, M.S., Gao, D., Hudziak, S., Chater, R.J., Fearn, S., McPhail, D. & Bosman, M. (2016). Nanoscale Transformations in Metastable, Amorphous, Silicon-Rich Silica, Advanced Materials, Vol. 28(34), pp. 7486-7493.

Mehonic, A., Vrajitoarea, A., Cueff, S., Hudziak, S., Howe, H., Labbe, C., Rizk, R., Pepper, M. & Kenyon, A.J. (2013). Quantum conductance in silicon oxide resistive memory devices, Scientific reports, Vol. 3pp. 2708.

Oster, G.F. (1974). A Note on Memristors, IEEE Transactions on Circuits and Systems, .

Prodromakis, T., Toumazou, C. & Chua, L. (2012). Two centuries of memristors, Nature Materials, Vol. 11(6), pp. 478-481.

Strukov, D.B., Stewart, D.R., Borghetti, J., Li, X., Pickett, M., Medeiros Ribeiro G., Robinett, W., Snider, G., Strachan, J.P., Wu, W., Xia, Q., Yang, J.J. & Williams, R.S. (2010). Hybrid CMOS/memristor circuits, ISCAS 2010 - 2010 IEEE International Symposium on Circuits and Systems: Nano-Bio Circuit Fabrics and Systems, .

Strukov, D.B., Snider, G.S., Stewart, D.R. & Williams, R.S. (2008). The missing memristor found. Nature, Vol. 453(7191), pp. 80-83.

Tour, J.M. & He, T. (2008). Electronics: The fourth element, Nature, Vol. 453(7191), pp. 42-43.

Valov, I., Linn, E., Tappertzhofen, S., Schmelzer, S., Van den Hurk, J., Lentz, F. & Waser, R. (2013). Nanobatteries in redox-based resistive switches require extension of memristor theory, Nature communications, Vol. 4pp. 1771.

Vongehr, S. & Meng, X. (2015). The missing memristor has not been found, Scientific reports, Vol. 5.

Williams, S. (2008). How We Found the Missing Memristor, IEEE Spectrum, (december), .

APPENDIX 2

” *The Pourbaix diagram*”

TO THE MASTER THESIS “CHARACTERIZATION OF THE DOPED SILICON DIOXIDE AND ITS IMPLICATION FOR THE RESISTIVE SWITCHING PHENOMENA IN THE ELECTROCHEMICAL METALLIZATION CELLS”

LIST OF FIGURES

Figure 1. The Pourbaix equilibrium diagram of the Cu-H2O system (Suh et al. 2016). 4
Figure 2. The combined Pourbaix diagram for Al and Si (Milenkovic et al. 2009)....................... 5

The Pourbaix diagram of Cu. The Pourbaix diagram shows the dependence of the redox behavior on the pH value in the compound (Pourbaix diagram 2008). In practice, the diagram indicates the equilibrium states in the aqueous electrochemical system for the protection against corrosion, for example. The diagram is usually drawn as the plot of the pH value versus the electric potential. The inclining dashed lines in the diagram show the region of stability for the water molecule. Therefore, it is worth to see how the SiO2/H2O and Cu/H2O system would behave in the Pourbaix diagram to find the possible explanation for the observed behavior of the SiO2-based ECM cell. Of course, the Pourbaix diagram can be drawn for a specific electrochemical system. However, a generic diagram may be useful as it can be seen in Figure 1and Figure 2.

Figure 1 displays the Pourbaix diagram for the electrochemical system consisting of Cu and water. Generally, the conductive filament in the ECM cell should be created completely at the positive bias $V > 0$ and dissolved at negative bias $V < O$.

Therefore, when the ECM memory cell is positively biased, the positive Cu electrode (V>0) corresponds to the positive region of the Pourbaix diagram and the negative Pt electrode corresponds to the negative side of the Pourbaix diagram.

Secondly, when ECM memory cell is negatively biased, the negative Cu electrode corresponds to the negative side of the Pourbaix diagram and the positive Pt electrode relates to the positive side of the Pourbaix diagram.

Finally, it can be said that the positive and negative side of ECM changes but the positive side of the Pourbaix diagram would always correspond to the positively charged electrode and the negative side of the diagram to the negatively biased electrode in ECM.

Case 1: Cu electrode is positively biased V>0. As it was pointed out previously (Willis & Lang 2004; He & Lu 2012; Tsuruoka et al. 2012), for the generation of the mobile Cu ions in SiO2, Cu needs to undergo the chemical oxidation in the presence of moisture. After that, the free Cu ions would be created (1). Additionally, the generated Cu ions need to become mobile (2).

The chemical reactions of the Cu oxidation can be depicted as $2Cu + O_2 \rightarrow 2CuO$ or $4Cu + O_2 \rightarrow 2Cu_2O$, for example. The oxidized copper can originate from the fabrication step or due to the oxidation under the influence of an ambient environment. At higher pH >12,3, Cu2O is more stable than CuO and at lower pH CuO would be more stable. Also, at low voltage (0<V<0.3) and pH>2.5, Cu2O can be preferentially generated. However, the Cu2+ can be stable and mobile at pH< 3.5 and V>0.3. It implies that the concentration of hydroxide ions $[OH^-]$ near the positively charged Cu electrode needs to be much higher than the concentration of the hydronium ions [H3O$^+$] in order for Cu ions to be mobile.

The decreasing of the concentration of [H3O$^+$] near the positively charged electrode can occur if these ions travel away from it or H+ proton hops to another water molecule. The H+ proton is very mobile; therefore, it can drift (or hop) toward the negative electrode. In addition, the proton can also attach itself to the dangling bonds of Si or oxygen in SiO2 oxide neutralizing the charged defect and at the same time creating new defects in the matrix due to the requirement of the electroneutrality. Also, attaching to the oxygen dangling bonds can create the silanol bonds.

The hydronium and hydroxide ions in SiO2 would originate from the moisture uptake from the ambient environment. The dashed inclining lines in the Pourbaix diagram indicate the region of the water molecules' stability. At the voltage bias higher than 1.3V, the water would react with the oxygen to produce the hydroxyl ions according to the equation $O_2 + 2H_2O + 4e \rightarrow 4OH^-$. Therefore, the reaction requires the presence of both water and oxygen in addition to electrons for the generation of hydroxide ions. Moreover, the water molecules can dissociate into ions $H_2O + H_2O \rightarrow H_3O^+ + OH^-$at an increased rate with an increase in voltage bias.

Therefore, only the hydroxide ions OH^- should stay near the positive Cu electrode. Moreover, they would discharge on the positive Cu electrode according to the equation $2OH^- \rightarrow O_2 + 2H^+ + 4e^-$. The newly created positive protons H^+ together with previously created ones and Cu ions would migrate away from the positive electrode during the positive bias of the ECM memory cell. The positively charged ions would travel through porous SiO2 in the same way as ions travel through the porous membrane in the traditional electrochemical cell or the electrolytic batteries.

The $H^+$and Cu^{z+}would migrate under applied positive bias toward the negative Pt electrode, where they would discharge themselves according to the equations: $2H^+ + 2e \rightarrow H_2$ and $Cu^{z+} + ze^- \rightarrow Cu$. The reduced Cu electrodeposits on the Pt electrode, and forms the metallic filament growing toward the positive Cu electrode and finally short-circuits the opposite electrodes. The hydrogen molecule can break the Si-O bonds, attaching itself to oxygen and Si dangling bonds.

When the bias is reversed, the Cu electrode would be negative and Pt positive. This situation would be slightly different because the metallic filament (Cu) as an extension of the positive Pt would play the same role as the Cu electrode at the positive bias. Therefore, the Cu filament needs to be oxidized in the same way as the positive Cu electrode is oxidized at the positive bias. Then, generated mobile Cu ions diffuses into the SiO2 matrix and finally disconnects the opposite electrodes. The disconnection probably occurs near the Pt electrode. The behavior and function of the hydrogen and hydroxyl ions would be the same as at the positive bias of Cu electrode.

V(Pt)>0 and V (Cu)<0. At the negative bias, decreasing the pH value with a consequent increase in hydroxide ion concentration would imply the discharging of hydroxide ions onto the positive Pt electrode according to the equation $2OH^- \rightarrow O_2 + 2H^+ + 4e^-$. The H^+-ions would travel toward the negative Cu electrode. Oxygen would be consumed at the reverse bias in order to produce the hydroxide ions again.

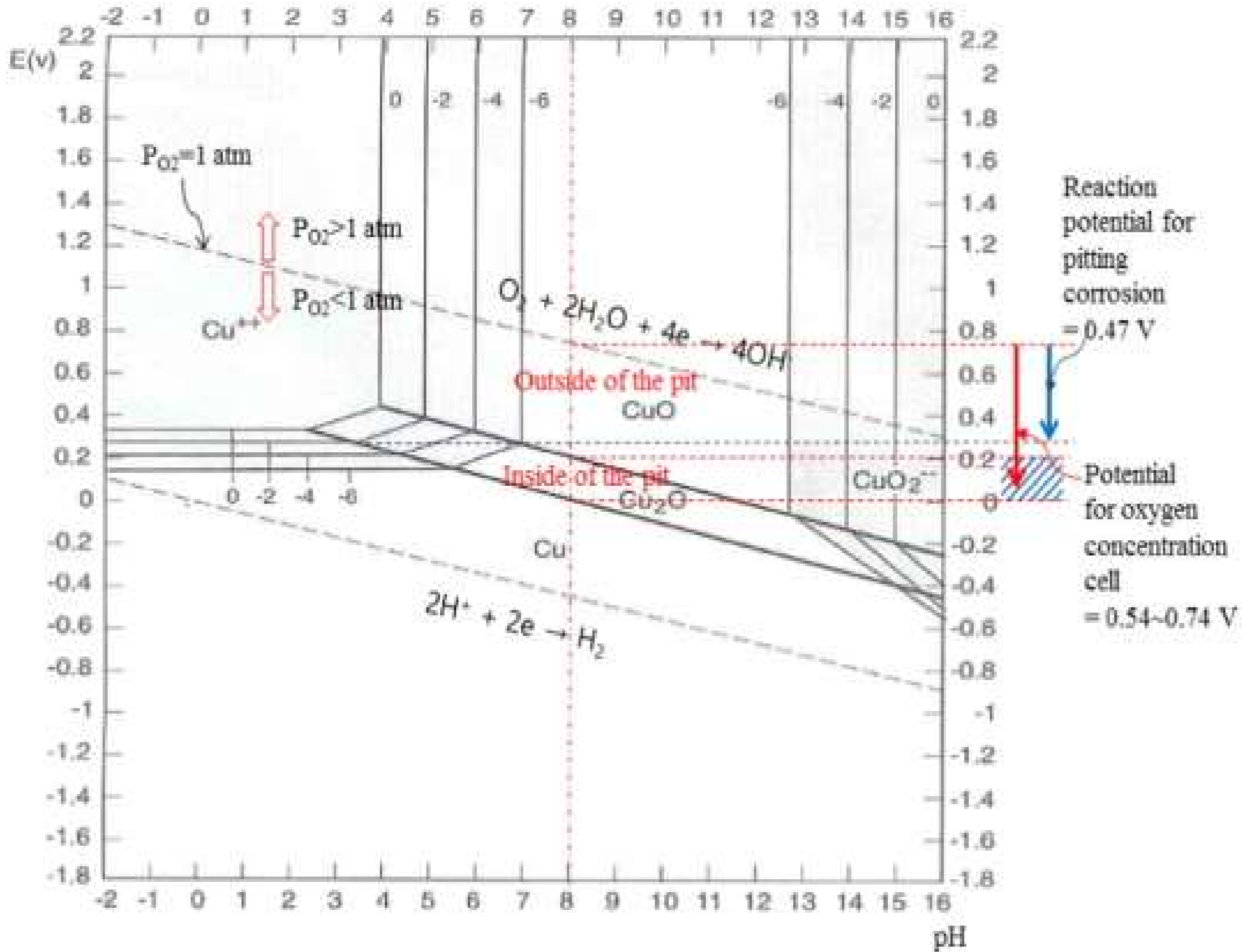

***Figure 1**. The Pourbaix equilibrium diagram of the Cu-H2O system (Suh et al. 2016).*

Figure 2 shows the combined Pourbaix diagram for Al and Si, however, the aim is to investigate the behavior of SiO2 and H2O system only. It can be seen that SiO2 is stable within a wide variety of voltage and pH values. However, Si is more stable at negative bias and therefore near the electrode, which is negatively biased. Si is stable at lower voltage with pH<7 compared to pH>7.

This can have an implication, that Si rather than SiO2 would be stable near the negative electrode, where the environment would be crowded with H^+-ions (or H3O+). The presence of Si in SiO2 near the negative electrode can be interpreted as oxygen vacancy.

Thus, the dissolution of the metallic filament in ECM memory cells occurs in the same way as dissolving the top Cu electrode. It means that the metallic filament needs to be oxidized via formation of copper oxide, then the concentration of hydroxide ions needs to increase in order for Cu ions to be mobile again. Only then, the opposite electrodes can be disconnected.

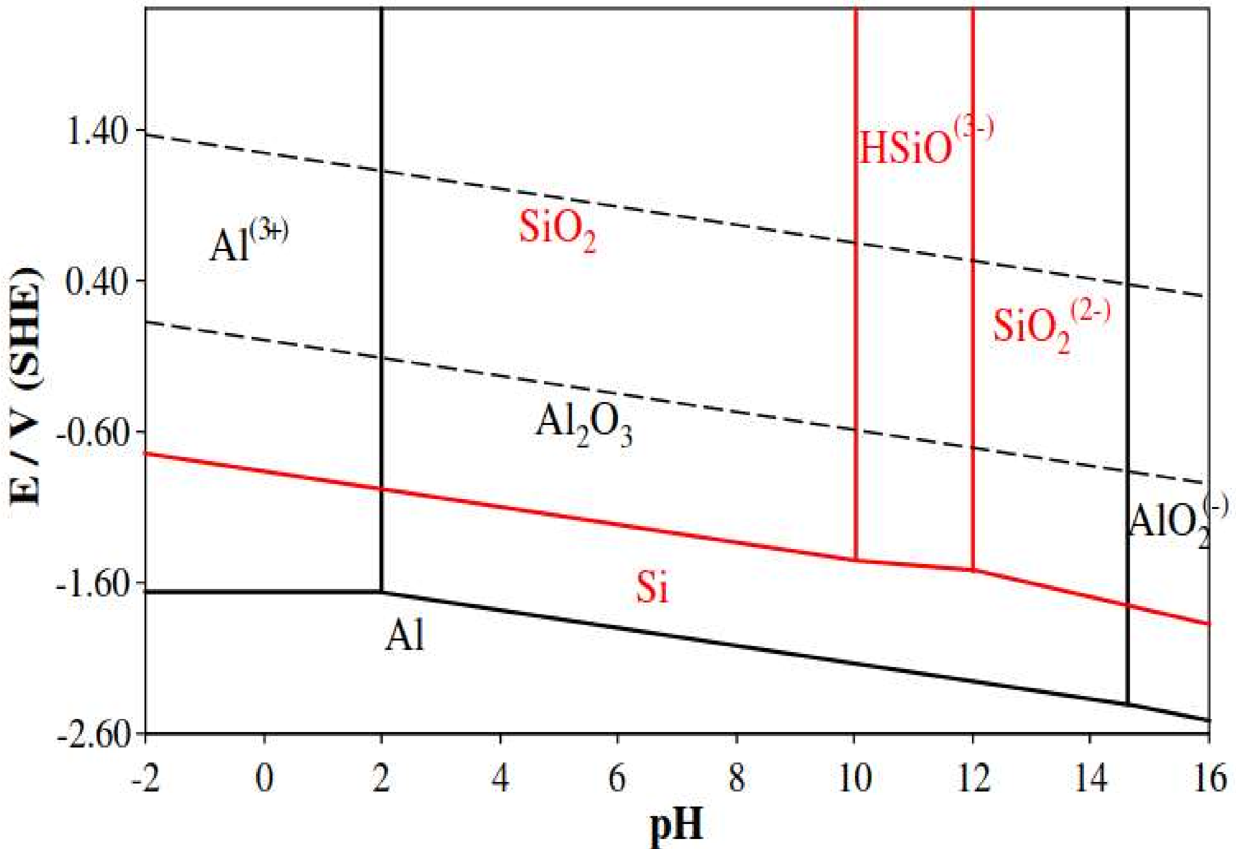

Figure 2. *The combined Pourbaix diagram for Al and Si (Milenkovic et al. 2009).*

Implications on interpretation of switching behavior of ECM memory cells. The effect of moisture on switching behavior of ECM memory cells can be made not only by taking into account of partial chemical reaction on counter electrode as it was proposed by Tsuruoka et.al and Tappertzhofen et.al , but also by taking into account the Pourbaix diagram. This type of diagram usually used for explanation of bulk properties. However, it can give more exact, full and reasonable explanation of possible chemical reactions during switching and also for effect of threshold switching in ECM cells.

REFERENCES

He, M. & Lu, T. (2012). Metal–Dielectric Diffusion Processes: Fundamentals, in: Metal-Dielectric Interfaces in Gigascale Electronics, Springer, pp. 11-22.

Milenkovic, S., Dalbert, V., Marinkovic, R. & Hassel, A.W. (2009). Selective matrix dissolution in an Al–Si eutectic, Corrosion Science, Vol. 51(7), pp. 1490-1495.

Pourbaix diagram (2008). 6th ed., Oxford University Press, .

Suh, S.H., Suh, Y., Yoon, H.G., Oh, J.H., Kim, Y., Jung, K. & Kwon, H. (2016). Analysis of pitting corrosion failure of copper tubes in an apartment fire sprinkler system, Engineering Failure Analysis, Vol. 64pp. 111-125.

Tsuruoka, T., Terabe, K., Hasegawa, T., Valov, I., Waser, R. & Aono, M. (2012). Effects of Moisture on the Switching Characteristics of Oxide-Based, Gapless-Type Atomic Switches, Advanced Functional Materials, Vol. 22(1), pp. 70-77.

Willis, B.G. & Lang, D.V. (2004). Oxidation mechanism of ionic transport of copper in SiO 2 dielectrics, Thin Solid Films, Vol. 467(1), pp. 284-293.

APPENDIX 3

”*THE DOPING OF OTHER OXIDES*”

TO THE MASTER THESIS “CHARACTERIZATION OF THE DOPED SILICON DIOXIDE AND ITS IMPLICATION FOR THE RESISTIVE SWITCHING PHENOMENA IN THE ELECTROCHEMICAL METALLIZATION CELLS”

1.1.1 Doping of the related oxides

Doping of zirconium dioxide. The doping of ZrO2 affects the oxygen vacancy formation. The mean radii of oxygen vacancies are different for different dopants (Yeh & Chou 2008). The nonpolar resistance switching observed in Cu/ZrO2: Cu/Pt devices suggest a filamentary mechanism. Also, the temperature-dependence implies that a metallic filament may be responsible for the conductive ON state (Guan et al. 2008). The Ti-doping of ZrO2 can eliminate the electroforming stage and decrease the variability during resistive switching (Liu et al. 2009).

Doping with Cu and the Cu nanocrystals, or Ti ions improve the switching behavior of Cu/ZrO2/Pt device by the eliminating of the electroforming stage, enhancing the switching uniformity as well as reducing the operation voltage. Also, the better retention and thermal stability in the resistive OFF state are attained (Wang et al. 2012). The Pt/ZrO2/Ti/Pt cells show the unipolar switching, and Pt/ZrO2/TiN shows the bipolar switching. The temperature measurements of the ON-state demonstrate the semiconductive and the metallic types of switching in memory cells (Kärkkänen et al. 2015).

Doping of cerium and gadolinium oxide. Doping by aliovalent cations can create extrinsic point defects as in CeO2 doped by 10-15 mol% of Gd2O3. In doped ceria, the Gd^{3+} ions in Ce^{+4} sites create oxygen vacancies for charge balancing (Kilner 2000). The electrical conductivity of doped CeO2 is dependent on concentration and the dopant types (Inaba & Tagawa 1996).

Fluorite- type oxides, which are doped by aliovalent cations, are known as fast oxygen ion conductors. In the hosting lattice, aliovalent cations create oxygen vacancies. The gadolinia addition to ceria can be illustrated using Kröger-Vink notation, $Gd_2O_3 \Rightarrow 2Gd'_{Ce} + 3O_O^{\mathrm{x}} + V_O^{\bullet\bullet}$, therefore the concentration of vacancies depends on the dopant level (Kilner 2000).

1.1.2 Doping of other oxides

Doping of zinc oxide. 2 at. % Al-doped ZnO films exhibit the band-gap widening owing to the Burstein-Moss effect with the occupied and blocked lowest state of the conduction band (Sernelius et al. 1988). The Burstein-Moss effect indicates that doping with 2% Al makes the semiconductor be degenerated.

The growth rate of the Al-doped ZnO films sputtered by the RF magnetron increases with increasing RF power, but decreases with rising of temperature or pressure. The electrical conductivity of the pure ZnO is less than that of a doped film. Increase in the conductivity is attributed to the Al^{3+} ions substituting the Zn^{2+} ions, interstitials of Al atoms, and oxygen vacancies as well the Zn interstitials (Park et al. 1997).

Cu-doped ZnO films show unipolar switching after the electroforming. Moreover, the conduction mechanism depends on voltage and Cu concentration (Min et al. 2011). Also, switching stability of the magnetron sputtered ZnO was improved by doping with Ti. The formation energy of oxygen vacancies near Ti atoms was low (Li et al. 2013).

Doping of hafnium oxide. The Cd- doping of HfOx makes the distribution of the oxygen vacancies more homogeneous (Gao et al. 2013). The enhanced ON/OFF ratio was found in the Cu-doped HfO2 film. The current, limited by the space charge (SCLC), was supposed to be responsible for the bipolar switching and the migration of the Cu ions for the unipolar switching (Guo et al. 2015). Moreover, Au doping of HfO2 reduces the formation energy of the oxygen vacancies due to the reduced randomness of the filaments (Tan et al. 2014).

Doping of Perovskite. This switching of perovskites originates from the oxygen content modulations, it is attributed to the self-doping effect. The dislocations, which are extended defects, may work as bistable nanowires (Szot et al. 2006). The resistance change in SrTiO3 is due to oxygen migration with subsequent valence changes in the Ti (4+) and the Ti (3+) ions (Baeumer et al. 2015). The formation energy of the oxygen vacancies in SrTiO3 would be less at sites close to the dislocation core (Marrocchelli et al. 2015).

The implication for interpretation on the effect of doping in ECM cells. Both homogeneous and heterogeneous doping is used for improving the electrical and optical properties of oxides. However, it would be extremely difficult to attribute the influence of the specific doping element to the obtained effect without identifying the concentration, valence, ion radii, the position of doping element in host materials as well as the influence of other parameters. Change in resistive switching properties, for example, may be also attributed to other fabrication or testing parameters or their combination. Therefore, not only doping, especially at very low concentration level, but

also other influencing parameters as well conduction mechanisms need to be considered in the interpretation of observed effects.

Doping the silica with aliovalent cations, which may replace Si in the lattice, would increase the concentration of oxygen vacancies. However, the aliovalent cations may take also other positions in host matrix or even create a secondary phase. Doping of silica with Me+ and/or Me++ as well as the interstitials of Me+++ may increase the concentration of non-bridging oxygen (dangling bonds), which increases the diffusion of oxygen. Also, the replacing the Si in SiO2 would require specific fabrication condition. In addition, the location and position of cation in the host material may vary a lot. As a result, the influence of specific cation on resistive switching would vary also depending on the exact position and, of course, on the concentration of dopant. Therefore, based only on electrical characterization, it would be difficult to separate the effect of doping from the influence of other possible parameters.

REFERENCES

Baeumer, C., Schmitz, C., Ramadan, A.H., Du, H., Skaja, K., Feyer, V., Müller, P., Arndt, B., Jia, C. & Mayer, J. (2015). Spectromicroscopic insights for rational design of redox-based memristive devices, Nature communications, Vol. 6.

Gao, B., Chen, B., Zhang, F., Liu, L., Liu, X., Kang, J., Yu, H. & Yu, B. (2013). A novel defect-engineering-based implementation for high-performance multilevel data storage in resistive switching memory, IEEE Transactions on Electron Devices, Vol. 60(4), pp. 1379-1383.

Guan, W., Liu, M., Long, S., Liu, Q. & Wang, W. (2008). On the resistive switching mechanisms of Cu/ZrO2: Cu/Pt, Applied Physics Letters, Vol. 93(22), pp. 223506.

Guo, T., Tan, T. & Liu, Z. (2015). The effect of Cu doping concentration on resistive switching of HfO 2 film, Applied Surface Science, Vol. 351pp. 704-708.

Inaba, H. & Tagawa, H. (1996). Ceria-based solid electrolytes, Solid State Ionics, Vol. 83(1), pp. 1-16.

Kilner, J. (2000). Fast oxygen transport in acceptor doped oxides, Solid State Ionics, Vol. 129(1), pp. 13-23.

Kärkkänen, I., Shkabko, A., Heikkilä, M., Vehkamäki, M., Niinistö, J., Aslam, N., Meuffels, P., Ritala, M., Leskelä, M. & Waser, R. (2015). Impedance spectroscopy study of the unipolar and

bipolar resistive switching states of atomic layer deposited polycrystalline ZrO2 thin films, physica status solidi (a), Vol. 212(4), pp. 751-766.

Li, H., Chen, Q., Chen, X., Mao, Q., Xi, J. & Ji, Z. (2013). Improvement of resistive switching in ZnO film by Ti doping, Thin Solid Films, Vol. 537pp. 279-284.

Liu, Q., Long, S., Wang, W., Zuo, Q., Zhang, S., Chen, J. & Liu, M. (2009). Improvement of Resistive Switching Properties in-Based ReRAM With Implanted Ti Ions, IEEE Electron Device Letters, Vol. 30(12), pp. 1335-1337.

Marrocchelli, D., Sun, L. & Yildiz, B. (2015). Dislocations in SrTiO3: easy to reduce but not so fast for oxygen transport, Journal of the American Chemical Society, Vol. 137(14), pp. 4735-4748.

Min, C.K., Keun, Y.L., Chang, O.K. & Suk-Ho, C. (2011). Effect of doping concentration on resistive switching behaviors of Cu-doped ZnO films, Journal of Korean Physical Society, Vol. 59pp. 304.

Park, K.C., Ma, D.Y. & Kim, K.H. (1997). The physical properties of Al-doped zinc oxide films prepared by RF magnetron sputtering, Thin Solid Films, Vol. 305(1), pp. 201-209.

Sernelius, B.E., Berggren, K., Jin, Z., Hamberg, I. & Granqvist, C. (1988). Band-gap tailoring of ZnO by means of heavy Al doping, Physical Review B, Vol. 37(17), pp. 10244.

Szot, K., Speier, W., Bihlmayer, G. & Waser, R. (2006). Switching the electrical resistance of individual dislocations in single-crystalline SrTiO3, Nature materials, Vol. 5(4), pp. 312-320.

Tan, T., Guo, T. & Liu, Z. (2014). Au doping effects in HfO 2-based resistive switching memory, Journal of Alloys and Compounds, Vol. 610pp. 388-391.

Wang, Y., Liu, Q., Lü, H., Long, S., Wang, W., Li, Y., Zhang, S., Lian, W., Yang, J. & Liu, M. (2012). Improving the electrical performance of resistive switching memory using doping technology, Chinese Science Bulletin, Vol. 57(11), pp. 1235-1240.

Yeh, T. & Chou, C. (2008). Doping effect and vacancy formation on ionic conductivity of zirconia ceramics, Journal of Physics and Chemistry of Solids, Vol. 69(2), pp. 386-392.

APPENDIX 4

" *The RESEARCH METHODOLOGY, MATERIALS CHARACTERIZATION AND FABRICATION***"**

TO THE MASTER THESIS "CHARACTERIZATION OF THE DOPED SILICON DIOXIDE AND ITS IMPLICATION FOR THE RESISTIVE SWITCHING PHENOMENA IN THE ELECTROCHEMICAL METALLIZATION CELLS"

LIST OF FIGURES

Figure 1. The overview of the CT1000 cluster deposition tools (van den Hurk 2016)................. 12
Figure 2. The SEM images of the specimens sputtered using the TD0 target on a platinum substrate at RT at the different RF power setting (a-h)... 15
Figure 3. The SEM images of the samples deposited using the TD0 target on the Al2O3 substrate at RT, 100C, 200C, and 300C (a-d)... 16
Figure 4. The SEM images of the specimens sputtered using the doped TD2 target on an Al2O3 substrate at RT, 100C, 200C, and 300C 17
Figure 5. The SEM images of the specimens fabricated by sputtering the TD1 target on a platinum substrate with and without oxygen.. 19
Figure 6. The SEM images of the specimens fabricated by sputtering the TD1 target on a titanium nitride substrate with and without oxygen 20
Figure 7. The SEM images of the specimens fabricated by sputtering the TD1 target on the platinum substrate with and without oxygen 22
Figure 8. The SEM images of the specimens fabricated by sputtering the Al2O3 substrates coated with carbon (a-b) and aluminum (c-d).. 23
Figure 9. The comparing the grain sizes of the specimens deposited using the TD0 and TD1 targets 24
Figure 10. The comparing the grain sizes of the specimens deposited using the TD0 and TD2 targets 24
Figure 11. The EDX analysis of control specimens with different substrates (platinum, Al2O3, and titanium nitride) i.e. without sputtered SiO2 thin film (in at%)..................................... 26
Figure 12. The EDX analysis of the specimens sputtered using the TD0 target on the platinum substrate (in at%)... 27
Figure 13. The EDX analysis of the specimens sputtered using the TD0 target on the Al2O3 substrate (in at%)... 28

Figure 14. The EDX analysis of the specimens sputtered using the TD1 target on the platinum and TiN substrates (in at%) *29*
Figure 15. The EDX analysis of the specimens sputtered using the TD2 target on the platinum substrate (in at%) *30*
Figure 16. The EDX analysis of the specimens sputtered using the TD2 target on the Al2O3 substrate (in at%) *31*
Figure 17. The XRR analysis of SiO2 deposited on an Al2O3 substrate using the TD0 and the TD1 targets at the different temperatures and the RF power settings *33*
Figure 18. XRR analysis of SiO2 deposited on an Al2O3 substrate using the TD0 and the TD1 targets at the different temperatures and the RF power settings. *34*
Figure 19. The XRR analysis of the samples deposited using the TD0 target on the platinum and the TiN substrates at the different temperature and the RF power settings *35*
Figure 20. The XRR analysis of the specimens sputtered using the TD1 and the TD2 targets on the platinum and the TiN substrates at the different temperature and the RF power settings *36*
Figure 21. The XRR analysis of the samples deposited using the TD0 target on the platinum and the TiN substrates at the 150C and 150W: the variability of the results at the same setting *38*
Figure 22. The XRR analysis of the samples deposited using the TD1 and the TD2 targets on the platinum and the TiN at the different temperature and the RF power settings: 150W versus 100W *39*
Figure 23. The XRR analysis of the samples deposited using the TD0, the TD1 and TD2 targets on the Pt substrate at the same settings (150W, 150C and 50nm-thick layer) *40*
Figure 24. The XRR analysis of the specimens sputtered using the TD0, the TD1 and TD2 targets on the TiN substrate at the same settings (150W, 150C and 50nm-thick layer) *41*
Figure 25. The XRR analysis of all specimens sputtered on the Pt and the TiN substrates *41*
Figure 27. The XRD analysis of the different specimens sputtered using the TD0 target on the platinum, the Al2O3 and the TiN substrates *43*
Figure 28. The XRD analysis of the different specimens sputtered using the TD1 target on the platinum, the Al2O3 and the TiN substrates *44*
Figure 29. The XRD analysis of the different specimens sputtered using the TD2 target on the platinum, the Al2O3 and the TiN substrates *45*

1. RESEARCH METHODOLOGY AND MATERIALS

1.1 SEM

Scanning Electron Microscope or SEM is a useful tool for obtaining a topographical image of a sample. In SEM, the surface image is created by scanning the surface in a raster pattern by a focused electron beam, which is deflected by a magnetic field (Goldstein et al. 2012; CIRP Encyclopedia of Production Engineering 2014).

The resolution of the fine details is often inferior to the specific resolution performance of the SEM. When the object dimensions are comparable to the interaction volume of X-rays, fewer electrons scatter from the sample and more from the substrate. Additionally, artifacts can occur at each measurement stage (Goldstein et al. 2012; CIRP Encyclopedia of Production Engineering 2014).

Identifying the chemical elements as well as the qualitative and quantitative analysis of materials can be done using the emission of characteristic X-rays. A quantitative analysis is possible when a standard reference is used. The intensity of emitted X-rays and a concentration of the chemical elements in the specimen are correlated to each other. The distribution of emitted X-rays is directly affected by an atomic number of chemical elements in the specimens (Goldstein et al. 2012; CIRP Encyclopedia of Production Engineering 2014).

The quantitative chemical analysis of the sample of 1 μm in diameter and 1 μm in depth, and the qualitative identification of the trace elements < 1 wt%, minor 1–10 wt%, and major > 10 wt% elements are possible. However, only the identification of the major elements can be performed with a high degree of confidence (Goldstein et al. 2012).

The sample used in SEM needs to be conductive, whereas nonconductive samples for imaging need to be covered with a conductive layer. In addition, in some cases, a layer of the metal particles of 3-5nm or a continuous metal coating of 1nm may improve the signal-to-noise ratio. For such purposes, for example, Au–Pd, Pt, W, Ti, V, Cr can be used.

1.2 EDX

Definition of EDX. The chemical characterization of samples can be made using the energy dispersive X-ray spectroscopy or EDX, which exploits the inelastic scattering of electrons. The inelastic scattering involves the electron-electron interactions, and it means that the energy lost by the electrons is large enough to be detected in the microscope (Brydson & Hondow 2011).

In the inelastic transition, the fast electrons lose their energy and create an electronic hole. After that, an outer electron moves down into a place of the hole, and consequent X-rays and the Auger electrons will be created. The emitted characteristic X-rays expose the atoms' chemical structure (Brydson & Hondow 2011).

The intensity and energy of the characteristic X-rays correlate to the areal density of the layer and the atomic number. The applied voltage controls the penetrating depth of electrons. This depth is usually between 0.1 μm and several μm (Prencipe et al. 2015).

The identification of the elements in the resulting EDX spectrum is made routinely. The relative heights and the positions of the X-ray peaks related to a certain element can be obtained from the database of the EDX software package (Brydson & Hondow 2011).

With careful analysis and measurement, EDX can identify elements with a concentration of 0.1 atom%, however with $\pm 5\%$ by accuracy. Also, the low energy absorption of X-rays causes serious difficulties for elements with the number< 11. Therefore, the light element quantification can be unreliable without the information about sample thickness, the geometry of the detector and the specimen, and other parameters (Brydson & Hondow 2011).

However, due to the inherent nature of this technique, the distorting and other 'spectral artifacts' are present in the X-ray spectra during the measurements (Goldstein et al. 2012).

Limitations of EDX. First, the emission of X-rays due to the relaxation of excited atoms is more efficient for atoms with atomic numbers Z>30. Also, the detector efficiency for the collection of emitted X-rays is usually less than 1%. Moreover, the signal strength will always be problematic from a thin specimen (Brydson & Hondow 2011).

Having a simple design, the EDX detectors have certain disadvantages. The count rate of the detectors is slow. Only a fraction of electrons produces the characteristic X-rays. Also, the detectors have a poor efficiency of signal collection. Moreover, the comprehensive information related to the densities of the electronic states is missing in the spectra. Also, the X-rays may be radiated from any area, which is illuminated by electrons. Furthermore, it is intrinsically unsuitable for analyzing at atomic scales. By using very thin specimens without the artifacts, the greatest spatial resolution can be achieved with a significant effort, however (Brydson & Hondow 2011).

EDX can be used for qualitative microanalysis. For EDX, the chemical constituents can be defined as the major (>10wt%), the minor (1-10%) or the trace (<1wt%) elements. However, EDX has a detection limit of about 0.1 wt% in bulk materials. EDX can perform a quantitative analysis with the accuracy and precision approaching 1% (Goldstein et al. 2012).

The identification of the major chemical elements can typically be made reliably. However, in the identification of the trace-level elements or the minor elements, error in the peak assignment may occur due to the artifacts, spectral interferences, or the multiplicity of spectral peaks of the high and the intermediate atomic number of the (Goldstein et al. 2012)chemical elements (Goldstein et al. 2012). The sum of all identified chemical elements should be equal to 1.0 or 100%. The deviation from unity is a direct consequence of the measurement's statistical and the systematic errors. Deviation from 100% can indicate the presence of oxide inclusion, for example. With the proper control of all the included elements, the analytical total should be from $98\% \ to\ 102\%$ (Goldstein et al. 2012).

1.3 XRR

Definition of XRR. At a small angle, X-rays can be totally reflected from the surface of the solid. This effect is exploited by XRR or X-rays reflectivity techniques (Compton 1923). Due to the negligible penetrating of the X-rays into the surface in a case of total reflection, the reflected intensity reveals the surface structure. The analysis of the reflected intensity reveals the information about electron density variation with depth as well as information about the state and treatment of the surface. The electron density of a material determines the critical angle and the shape of the XRR curve (Parratt 1954).

If a thin layer is present, the interference or Kiessig fringes (Kiessig 1931) may be seen. These oscillations are dependent on the thickness of the thin film: the thicker the film is, the shorter the oscillation period is (Yasaka 2010). The incident angle is sometimes named as the glancing angle (Parratt 1954) or the grazing incident angle (Bowen & Tanner 1993). The method applies to films from 1 nm to about 1μm in thickness (Bowen & Tanner 1993).

The intensity of the totally reflected X-ray falls rapidly above some critical angle. The reflectivity of the rough surface falls off even more rapidly (Bowen & Tanner 1993). The larger the amplitude of the oscillating Kiessig fringes, the larger the difference in the atomic number between the layer and substrate is. The period of Kiessig fringes has inverse proportionality to the layer thickness. Multilayers give multiplied fringes. The roughening of the interface decreases the fringe amplitude (Bowen & Tanner 1993).

Application of XRR. The XRR method may be implemented for studying single-crystalline, polycrystalline and amorphous (Yasaka 2010) materials as well as liquids (Bowen & Tanner 1993) and liquid-gas interfaces (Lehmkühler et al. 2008). XRR can be used for the determination of interface width and layer structure (Yasaka 2010), the thickness and the roughness of the surface (Bowen & Tanner 1993) and the interface (Bowen & Tanner 1993) as well as the density (Filies et al. 1999) and the composition of a thin layer (Bowen & Tanner 1993). Moreover, the average densities of a porous material, which were obtained using XRR, have been used for evaluating the porosity and layer structure (Suzuki et al. 2006; Yasaka 2010). Additionally, the XRR method can reveal information about the surface treatment or the material state as a result of corrosion, porosity, aging, and annealing (Parratt 1954).

Electron density and mass density. The most common data collection technique is the specimen $\theta - 2\theta$ -scan. The determination of the fringe spacing $\delta\theta$ suffices to estimate the film thickness t if the single periodicity is extracted from the relationship $\delta\theta = \frac{\lambda}{2t}$. In the equation, the wavelength is denoted as λ. Using the critical angle, the refractive index may be calculated (Bowen & Tanner 1993) or from the expression $\cos\theta_i = n_1 \cdot \cos\theta_t$, where θ_i is the incident angle, θ_t totally reflected angle and n_1 the refractive index of the media. The diffraction is not necessary for the implementation of this method, which allows studying amorphous films (Veldhuis et al. 2014).

In addition, the angle of total reflection can be expressed as $\theta_t = \sqrt{\theta_i^2 - 2\delta = 0}$, where dispersive part of the refractive index is defined as δ and the refractive index as $n = 1 - \delta - i\underbrace{\beta}_{0} = 1 - \delta$. Therefore, only at very small angles, the total external reflection may occur. At the total external reflection, the critical angle is therefore defined by $\theta_c \approx \sqrt{2\delta}$, which is between $0.1° \, and \, 0.4°$ for $Cu\ K\alpha$ irradiation. If the stoichiometry is known in mono-atomic material, the mass density ρ_m is directly calculated from ρ_e: $\rho_m = \frac{\rho_e \cdot A}{N_A \cdot Z}$, where ρ_e and ρ_m are the electron and the mass density. Also, the atomic weight is denoted as A, the atomic number as Z, and the Avogadro's number as N_A. For materials with more complex structures, the mass density of the unit cell can be calculated by the summation of all atoms (Veldhuis et al. 2014).

Fitting procedure. The most commonly used formalisms in XRR simulation are the Fresnel formulae and the Parrat's recursive algorithm (Bowen & Tanner 1993; Filies et al. 1999) and its modifications based on the theory of Nevot-Croce for roughness (Fujii 2013), for example. The XRR fitting method assumes the deposited layer is isotropic. In thin films, the thickness and interface roughness can be estimated by fitting of the XRR curve only in part at angle$> \theta_C$.

Consequently, the parameters calculated in such a way are rather imprecise. In the proposed method, the fitting of a complete curve is not necessary (Veldhuis et al. 2014).

However, the fitting using standard software is very labor-intensive and time-consuming. Also, the extraction of the numerical data related to thickness, roughness, and density in the nanoscale from the measured XRR curves using the standard fitting tool software includes difficulties due to the used standard algorithms which do not take into account a large variety of non-ideal surfaces.

Curve fitting can be difficult especially for the non-standard layers and the multilayers. Therefore, some additional shortcuts, approximations, or some other parameters such as the diffuse scattering and the effective roughness (Fujii 2013) are usually applied. For the sol-gel films, for example, also the first Born approximation theory is implemented (Yang et al. 2009). AFM (Atomic Force Microscope) calculation before the fitting procedure of X-ray reflectivity was performed together with the evolutionary computation and coupling with a local optimization technique (Solookinejad et al. 2014). Additionally, a pseudo-critical angle, using the 3rd derivative approach, was calculated to obtain the calibration curves. Within the error margin, the densities of the sample obtained in combined SEM and RBS analysis and using the XRR method were consistent (Veldhuis et al. 2014).

Conclusion. XRR technique is beneficial, when the surface and interfaces of differently fabricated thin films are investigated, such as multilayered thin films (Fujii 2013), sol-gel prepared thin films, physical vapor deposited thin films (Veldhuis et al. 2014) and slightly bent mica nanofilms (Briscoe et al. 2007). The XRR method is non-destructive and compatible with the clean-room technology (Bowen & Tanner 1993) which can be used for a wide variety of purposes.

1.4 XRD

Definition of XRD. The elastic scattering of X-ray photons from a periodic lattice of atoms is called X-ray diffraction (XRD). Following Bragg's law $n\lambda = 2d\ sin\theta$, the constructive interference occurs when the monochromatic X-rays scatter from the atomic planes. In Bragg's law, n means an integer, as well as the wavelength, is denoted as λ. The incident angle of the electron beam is θ and distance between the crystal planes is d. By measuring the angle θ, d can be determined for each single crystalline phase. The position of the peak and the intensities in the X-ray pattern are usually used for qualitative analysis. Moreover, the X-ray diffraction pattern is useful for the determination of the lattice constant and the internal (residual) stress in the sample. Furthermore, peak angles together with peak width can be useful for the determination of particle size, crystallization degree, and the structure of the sample (Ramachandran & Beaudoin 2000).

The absorption of X-rays. Intensity (I) of X-rays decreases when the beam propagates through the matter. Change in intensity is proportional to the distance traveled by the X-rays through a thickness x according to equation $I_x = I_0 e^{-\mu x}$, where I_x denotes the intensity at the thickness x,

I_0 is the incident beam's intensity, and μ is the linear absorption coefficient (Röntgen 1898; Cullity & Stock 2001). μ/ρ is the mass absorption coefficient, which is a constant tabulated for various wavelengths. In materials, the mass absorption coefficient does not depend on the physical state. If the material is a solution, a mechanical mixture, or chemical compound, the coefficient for the compound is calculated by the weighted average of its constituents (Cullity & Stock 2001).

Applications. The XRD technique is usually used together with other analytic techniques. XRD can be employed for the mapping of local strain changes in the individual grains, for example. Also, the impact on the strain due to the replacing of a compound with another (Schäfer et al. 2016), the influence on the resistivity due to Al and Ti doping of ZnO (Davoodi et al. 2016) can be studied. XRD can be used for ensuring that the thin film is amorphous (Sankar et al. 2016). Moreover, the phase transformation of Y_2O_3 due to annealing as a function of the residual stress (Gaboriaud et al. 2016) have been investigated. Furthermore, the impact of Al-doping on the resistance of ZnO (Islam et al. 1996), as well as the effect of the porosity in Si (Bellet & Dolino 1996) have been studied by XRD.

It is especially interesting that, in thin films, the XRD can be used for studying the *microstrain* as a result of the doping and the porosity. In individual grains, the planar and linear defects influence the overall microstrain distribution in the $Cu(In,Ga)Se2$ solar cell. The replacing of 80% of the atoms of In by Ga in $Cu(In,Ga)Se2$ induces microstrain, which affects the electrical and the optoelectronic properties of the solar cell (Schäfer et al. 2016).

The doping of ZnO with Ti and Al causes a stress due to the difference in the radii between the doping elements and the zinc ions, decreasing the roughness because of a grain size reduction and a decrease in resistivity. The minimum resistivity has been measured in ZnO doped with both dopants simultaneously (Davoodi et al. 2016).

In the ferroelectric perovskite films (PbTiO3), the doped elements, such as Ni and Pd, were added. The incorporation of the substituting ions into the lattice causes the variation of the XRD diffraction peaks. The addition of the substitutes reduces the grain size of the perovskite films (Zhou et al. 2016).

According to XRD*, the doping of ZnO* with isovalent Al (<2 at. %) causes an increase in the *lattice parameters* but with the same c/a ratio. It has been impossible to detect aluminum in the Al-doped ZnO film due to the low concentration of Al and the low ionization level of the cross-sections. The stoichiometry and the lattice spacing of doped and pure ZnO appear to be similar. However, the conductivity of the doped sample has been ten times higher than that of the pure ZnO (Islam et al. 1996).

The effect of oxidation on the strain in porous Si has studied. The lattice parameter in the ambient atmosphere, as well as due to aging, is increased linearly with the quantity of fabricated SiO_2. The oxidation of bulk silicon causes a volume increase by 2.3 times, therefore producing the stress in the material (Bellet & Dolino 1996).

All in all, the above-mentioned XRD techniques can be used for obtaining useful information about the sample structure after some specific treatment.

2. FABRICATION OF ECM

2.1 Sputtering by CT1000

Definition. Thin film deposition is usually made under a glow discharge by the application of either direct current (DC) or RF power. The systematic variations of the deposition parameters help to find the optimal conditions (Westwood 1976). Sputtering is useful for the fabrication of nanomaterials, which can be classified being zero-, one-, two-dimensional. Quantum dots, for example, are nanomaterials of zero dimensions, having all three dimensions in the nanosize. Quantum wires as one-dimensional nanomaterials have two dimensions of the nanoscale. Instead, the thin films and the superlattices are two-dimensional nanomaterials with just one dimension of the nanosize (Wasa et al. 2004).

During sputtering, the incident ions interact with the atoms on the surface of the target. The energy, the target materials, the incident angles, and the crystalline structure of the target affect the sputter yield. The decrease in the target thickness and the loss of the target weight define the sputter yield. The quality of the target surface, as well as its crystallinity, affect the angular distribution of particles and the sputtering yield. If the target consists of the polycrystalline materials, then the angular distribution can be over or under the cosine law. Often, a single crystal target produces a non-uniform angular distribution (Wasa et al. 2004).

During sputtering, the mean energy of the neutral atoms is less than the energy of ions. The initiation of the sputtering event occurs by the colliding of atoms with the incident ions on the target surface (Wasa et al. 2004).

Controlling the properties of the deposited layer, it is necessary to investigate the impacts of the sputtering settings on the layer structure. Most important sputtering parameters include the target composition, the deposition rate or the sputtering power, the temperature, and the substrate material. In thin film, these parameters have an impact on the chemical composition, crystallinity, as well as microstructure and stresses (Wasa et al. 2004).

The quenching of the melt and the vapor creates the amorphous substance. The quenching of the vapor is employed by the various thin film deposition techniques, including sputtering. The amorphous thin films need to be sputtered at substrate temperatures below the crystallization temperature (Wasa et al. 2004).

Stress. In sputtered films, stress, which is intrinsic, may be either tensile or compressive, which depends on how energetic the deposition was. The deposition technique influences the thin film microstructure, which consequently defines the magnitude and nature of the stress. The particle flux and the energy are dependent on the discharge voltage, pressure, gas- mass ratio, the shape

of the cathode, the orientation of the substrate, and biasing voltage. Tensile stress in the porous films is explained to be due to the relaxation of the grain boundaries, whereas in the dense films compressive stress is related to the peening mechanism of the atoms. The temperature of deposition and the intrinsic stress are inversely correlated (Windischmann 1992).

Sputtered thin film has a two-dimensional structure, which changes the physical properties of the layer. This occurs because the layer is fixed on the substrate. Thin films may have physical properties, which are different from bulk materials. The thin films may have a strong internal stress or a high density of lattice defects, which increases the elastic strength. In thin films, the strengths can be much larger than those in bulk material. The mismatch of the thermal expansion between the substrate and thin film as well as differences in the lattice parameters cause internal stress. In thin films, the tensile and compressive stresses affect their electrical properties such Curie temperature, the giant permittivity, pyroelectricity, and superconducting critical temperature (Wasa et al. 2004).

Applications. Sputtering is broadly exploited for various purposes, such as thin film deposition and surface etching and cleaning. The high-energy particles can be ions, neutral atoms, neutrons, electrons, and photons (Wasa et al. 2004). Thin film is a material with low dimensions (less than 3 D) created by the condensing of the matter. Thickness can be less than several microns. The technology is used for the fabrication of nanomaterials and superlattices. The deposition method affects the properties of thin films. Sputtering is widely used in the semiconductor industry (Wasa et al. 2004).

In thin film materials, the decreased mobility μ in the metals and semiconductors, the space – charge limited current through the insulators, the voltage-controlled negative resistance, the tunnel current, the thickness dependence on the dielectric constant as well as the tensile and the compressive stress effects are usually expected (Wasa et al. 2004).

Doping. Sputtering allows the doping of the impurity atoms into the semiconductor at a low temperature. In the semiconductive films, the co-sputtering of the dopants is beneficial for adjusting their conductivity. However, in the traditional sputtering equipment, Cu- and Al-co-sputtering during the deposition of ZnO has no impact on the conductivity of the deposited films, whereas sputtering with the use of a magnetron affects the resulting conductivity largely. Cu as the dopant in ZnO decreases the conductivity by approximately three times while Al improves the conductivity to the same amount. Also, in dc magnetron sputtering, copper is perhaps incorporated as an acceptor and Al as a donor. In the traditional technique, the dopant atoms are located at the crystal boundaries without incorporating in the crystal lattice (Wasa et al. 2004).

The CT1000 cluster deposition tools. The CT1000 cluster deposition tools were designed for the deposition of high-quality GeSx thin films. New equipment were intalled because thin films

deposited by the equipment available before were suffered from contamination and unwanted interface modification in the ambient atmosphere. The first Ar-plasma ignition was made on 20st May 2010 (van den Hurk 2016).

Figure 1. *The overview of the CT1000 cluster deposition tools (van den Hurk 2016)*

Figure 1 shows the CT100 cluster deposition tool, which has two independently usable sides with a shared vacuum load lock, different process chambers with a sputter deposition system, and a vacuum pump system. Maximum RF plasma excitation is possible with the maximum power of 300W. The CT1000 cluster tool uses a computer-based control system, which allows controlling the gas flow, pressure, and power of the RF generator (van den Hurk 2016).

One of the used process chambers was equipped with a stationary and one with a rotating sample holder. Both chambers for the purposes of this project were equipped with heaters at the later stage of the project.

3. RESULTS AND ANALYSIS

The part of obtained results related to a physical characterization of deposited layers is introduced in the Master Thesis and another part in this Appendix 4.

3.1 Structural and morphological characterization

In the following sections, both the theoretical description of used analytic techniques related to the structural and morphological characterization of sputtered SiO2 as well as results obtained using SEM, EDX, XRR and XRD techniques are introduced.

3.1.1 SEM

Preface. At the beginning of our project, it was necessary to find the optimal condition for the sputtering of a thin film by CT1000. In the previous experimental work, SiO2 was deposited either using other techniques or more powerful sputtering equipment. From the previous sputtering experiments by Schindler (Schindler 2009), it was known that the deposition of SiO2 needs at least the power of 300W from the RF power generator. According to the technical documentation of the CT1000 cluster deposition tools, the maximum available RF power was 300W. However, in practice, the equipment cannot withstand such loading more than 3 minutes because originally CT1000 was designed for the deposition of gallium sulfides (van den Hurk 2016) and other transition metal oxides, which usually require much less RF power for the deposition.

First deposition trials were made before starting this thesis work. Unfortunately, the quality of the deposited SiO2 thin film was low, because the thin films had a visible columnar structure, which would have affected the electrical performance of ReRAM. Therefore, at the beginning of this thesis, it was decided to continue the trials with higher achievable RF power and by varying the pressure and the oxygen content during the sputtering. The evaluation of the deposited thin films was made using SEM.

Figure 2 shows the samples that were deposited by the TD0 target at room temperature (RT) using the different power of the RF generator. After many trials, it was decided that all the samples deposited with RF power less than 100W did not have sufficient quality (Figure 2: a-d) because the layers were rough and not dense enough. Furthermore, it was found that the RF generator cannot work sufficiently more than 30 minutes without the overheating at a power higher than 150W. Therefore this value was used later as the starting point for the sputtering of the SiO2 using CT1000 cluster deposition tools.

a)TD0 target /Pt substrate/RT/50W

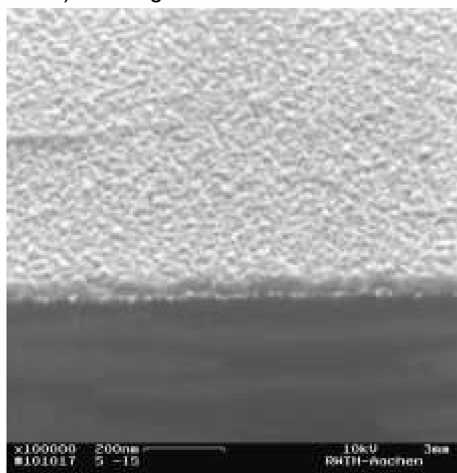

b)TD0 target /Pt substrate/RT/50W

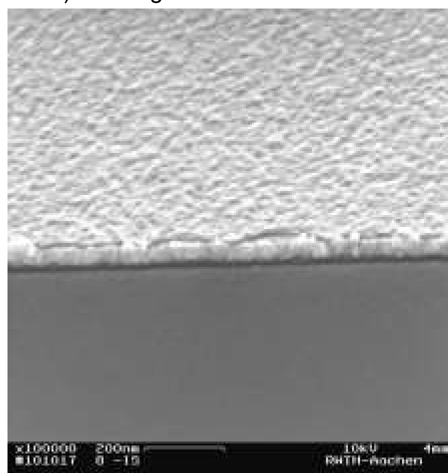

c)TD0 target/Pt substrate/RT/70W

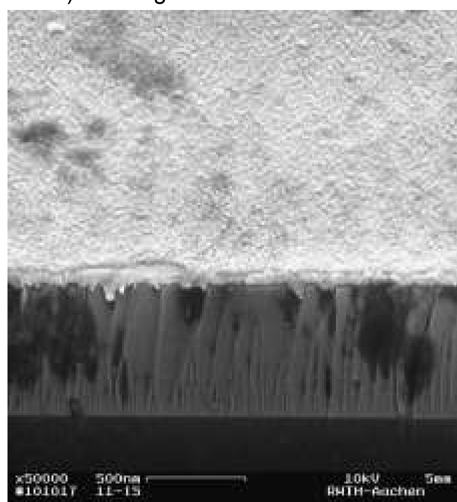

d) TD0 target/Pt substrate/RT/90W

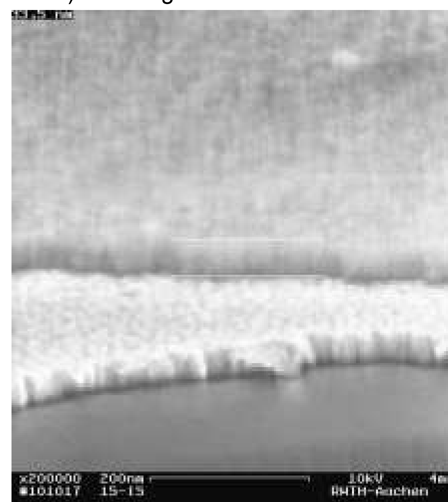

e)TD0 target/Pt substrate/RT/150W

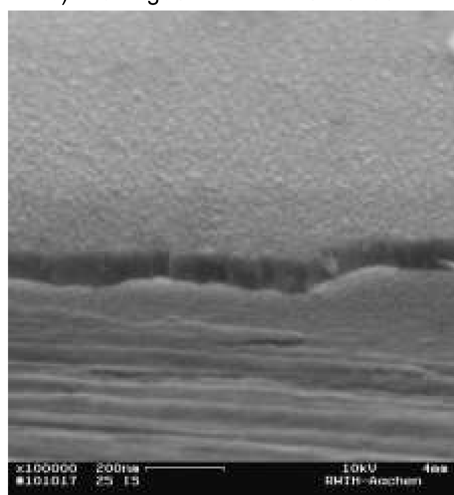

f)TD0 target/Pt subsrate/RT/200W

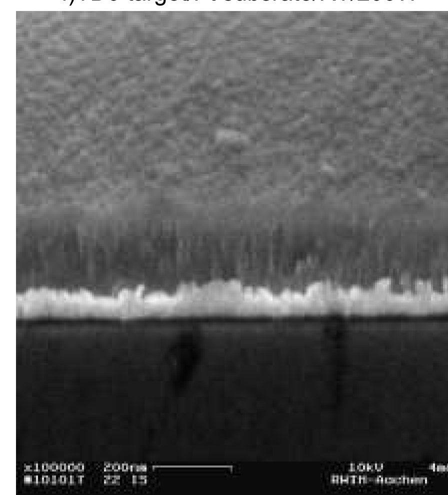

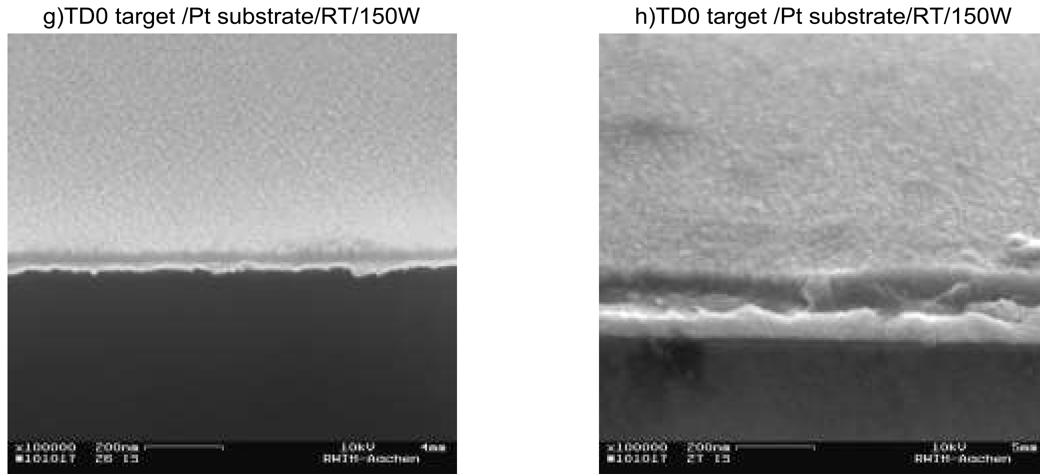

Figure 2. *The SEM images of the specimens sputtered using the TD0 target on a platinum substrate at RT at the different RF power setting (a-h).*

Figure 3 displays the SEM images of the specimens deposited at a constant power on an Al2O3 substrate using the TD0 target at different temperatures. Higher temperature promotes slightly larger grain size.

a)TD0 target /Al2O3 substrate/RT/150W

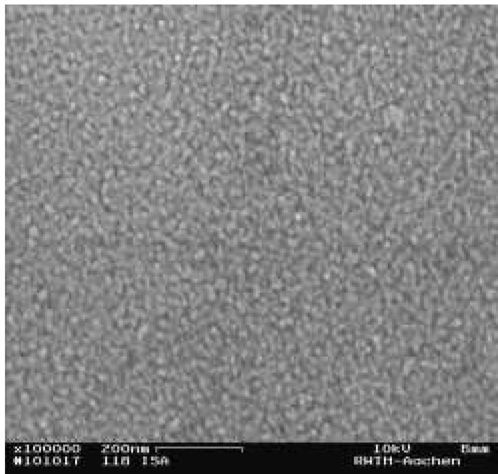

b)TD0 target/ Al2O3 substrate/100C/150W

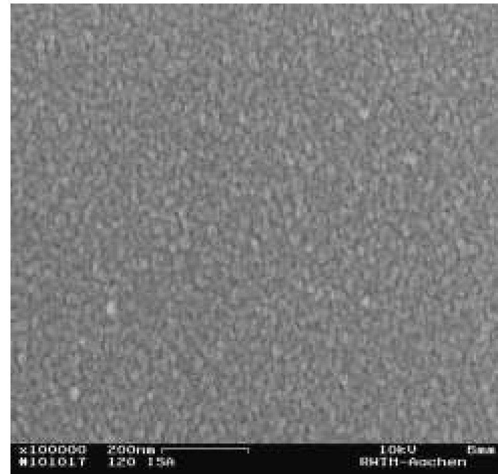

c)TD0 target/Al2O3 substrate/200C/150W

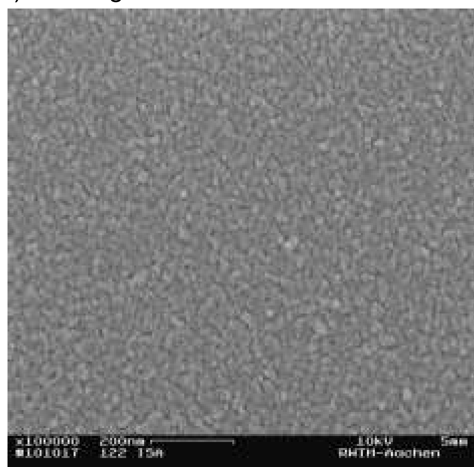

d) TD0 target/Al2O3 substrate/300C/150W

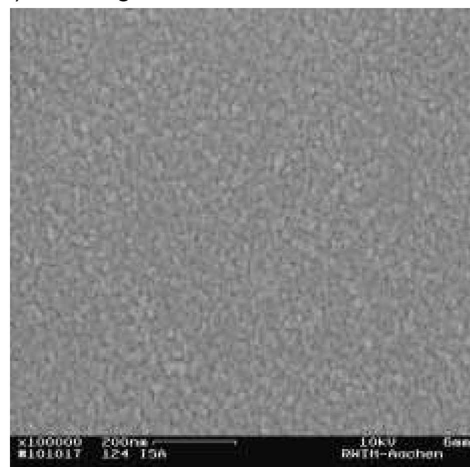

Figure 3. *The SEM images of the samples deposited using the TD0 target on the Al2O3 substrate at RT, 100C, 200C, and 300C (a-d)*

Figure 4 shows similar images as Figure 3 for the TD2 target doped with the dopants 1 and 2. The effect of increasing the grain sizes with the temperature can be clearly observed up to 200C. However, at 300C, the grain size slightly decreases.

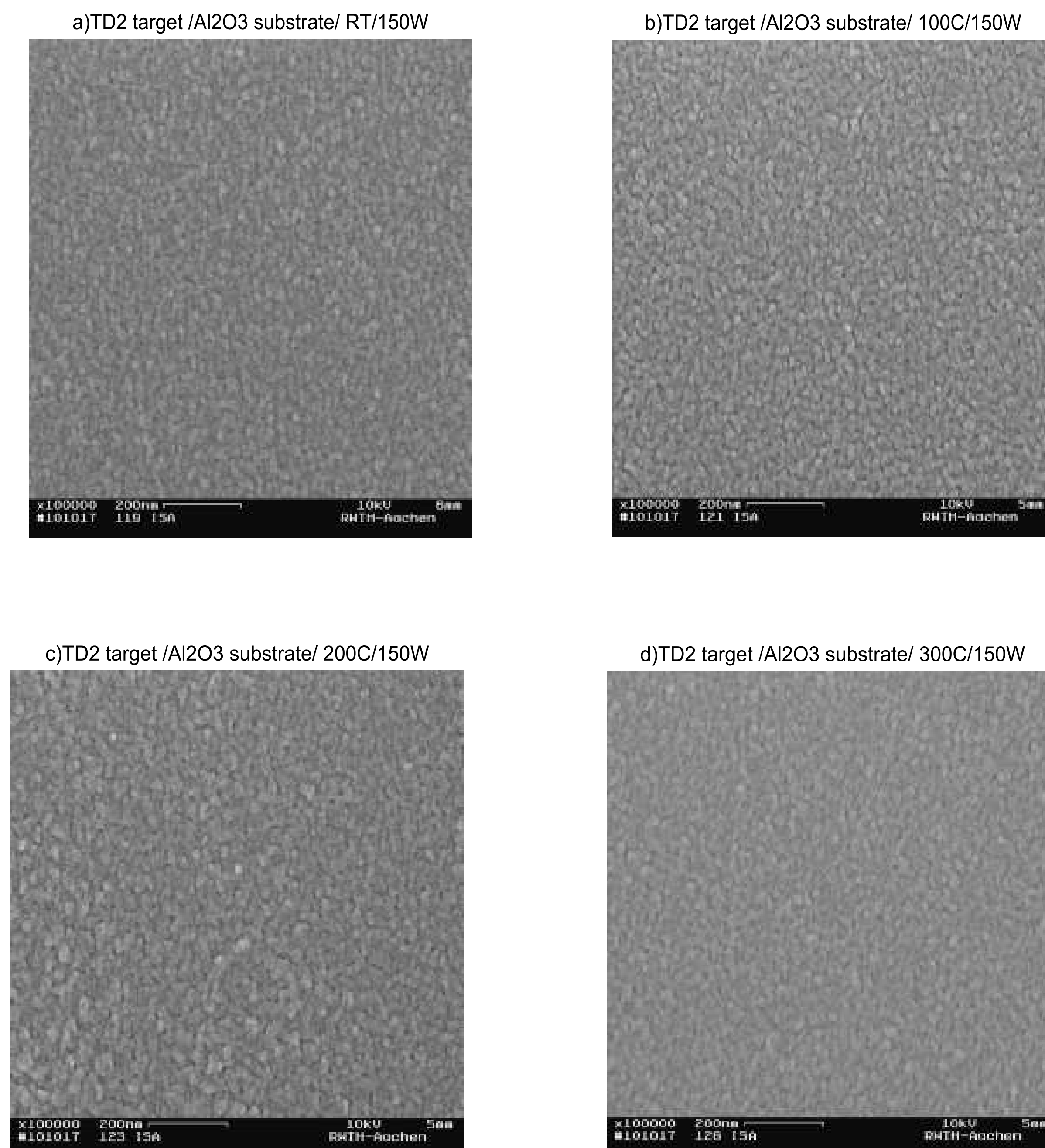

Figure 4. *The SEM images of the specimens sputtered using the doped TD2 target on an Al2O3 substrate at RT, 100C, 200C, and 300C*

The SEM images of the specimens sputtered using the TD1 target at a constant 150W power with oxygen and without oxygen added during the sputtering are shown in Figure 5. The samples deposited without oxygen have a visible columnar structure, but the samples with an addition of oxygen are dense and homogeneous without a visible structure. The sputtering parameters of the sample deposited on the platinum substrate at 100C with the addition of oxygen at 150W were used as the best reference for further experiments.

a) TD1 target/Pt substrate/RT/150W/Without O2

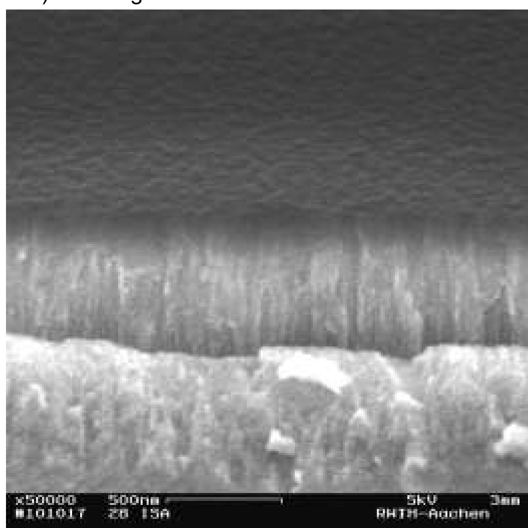

d)TD1 target/Pt substrate/RT/150W/WithO2

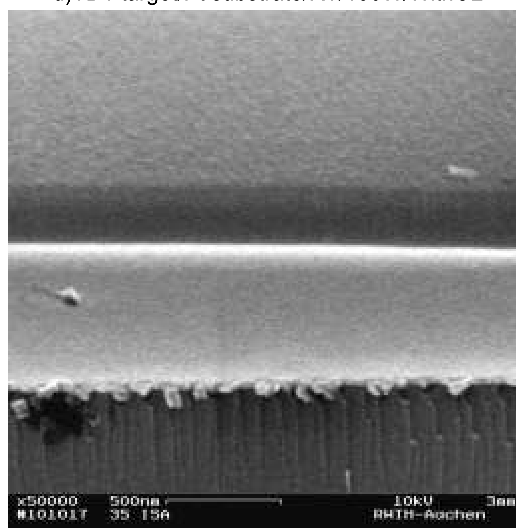

b) TD1 target/Pt substrate/100C/150W/Without O2

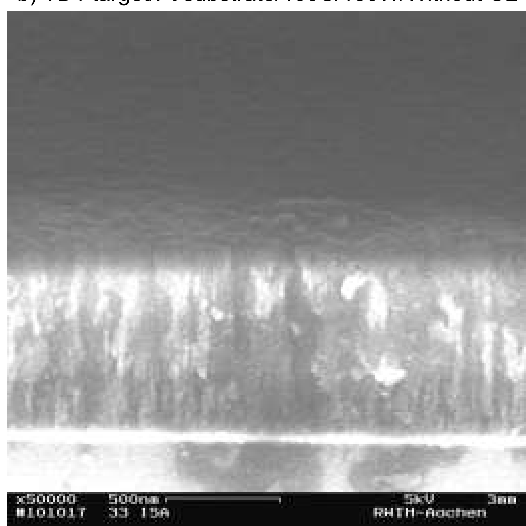

e) TD1 target/Pt substrate/100C/150W/With O2

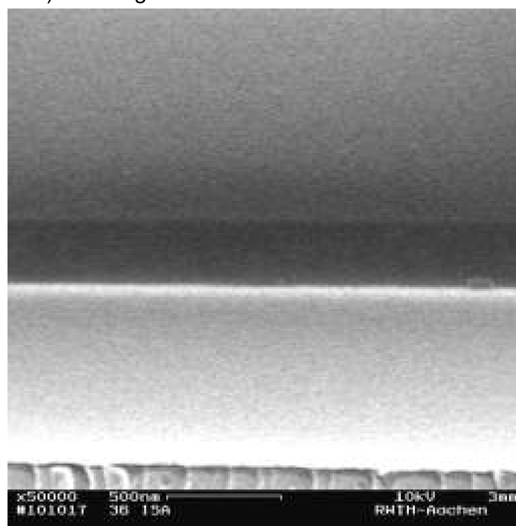

c) TD1 target/Pt substrate/200C/150W/Without O2

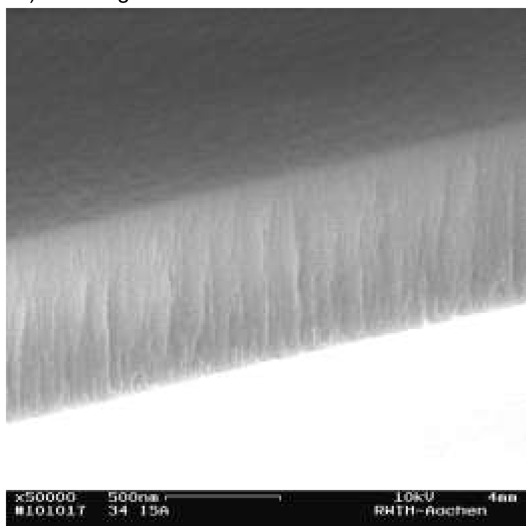

f) TD1 target/Pt substrate/200C/150W/With O2

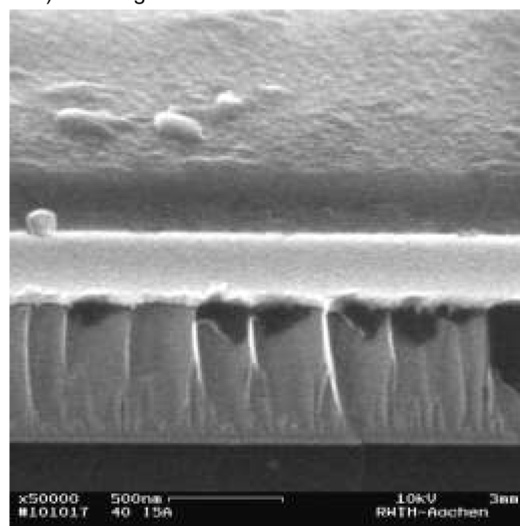

Figure 5. *The SEM images of the specimens fabricated by sputtering the TD1 target on a platinum substrate with and without oxygen*

Like Figure 5, Figure 6 displays the SEM images of the specimens sputtered on a titanium nitride substrate. As for samples deposited on the platinum substrate, the sputtered layer without oxygen on the titanium nitride substrate has a visible columnar structure. On the other hand, the layer sputtered with oxygen has a relatively dense and homogenous structure.

a)TD1 target /TiN substrate/RT/150W/Without O2

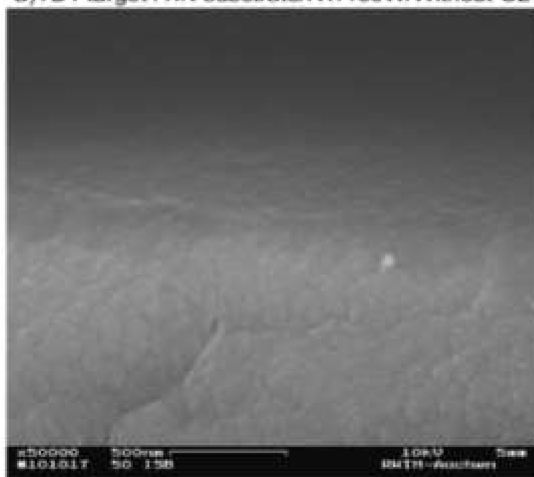

d)TD1 target /TiN substrate/RT/150W/With O2

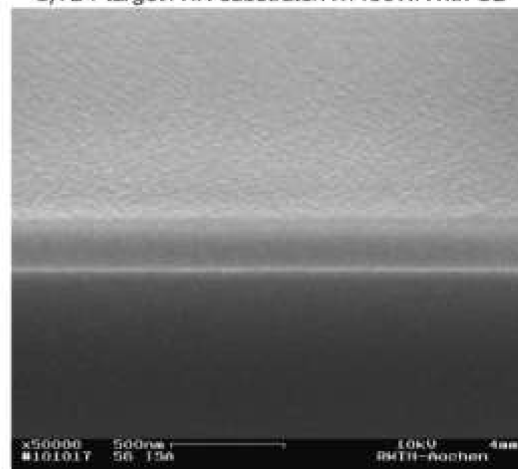

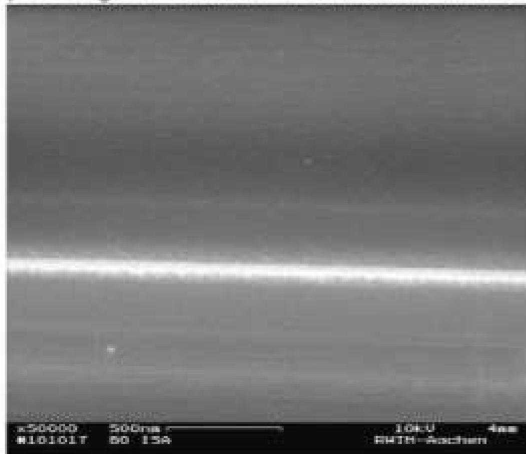

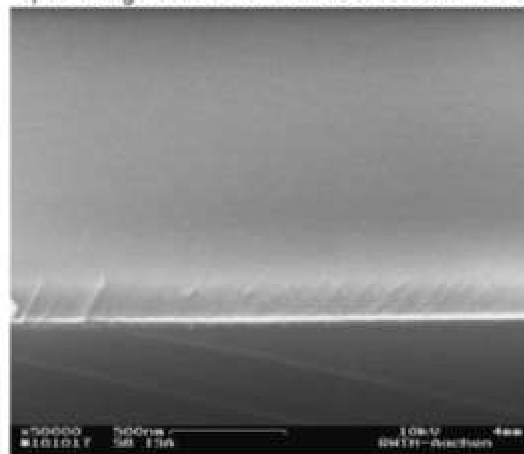

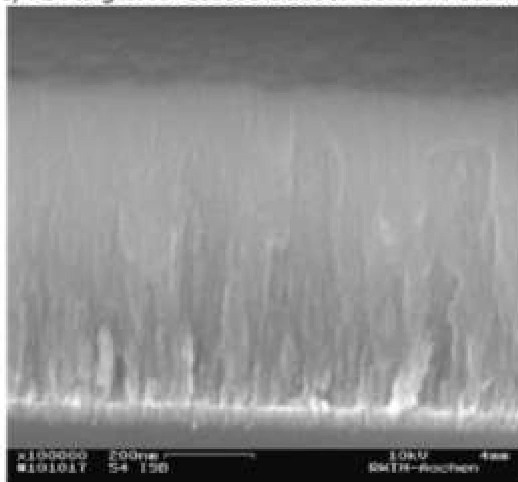

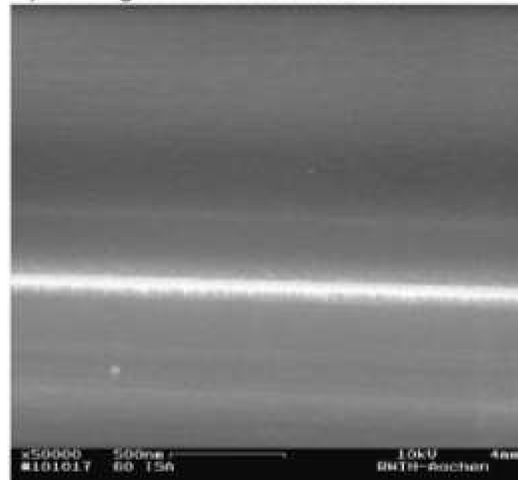

Figure 6. *The SEM images of the specimens fabricated by sputtering the TD1 target on a titanium nitride substrate with and without oxygen*

Figure 7 displays the same phenomenon of the deposition with and without oxygen observed in the SEM images of the samples with a view from above. Both the temperature and varying the oxygen content have an impact on the grain size. The oxygen addition in (d-f) causes the reduction in the grain size.

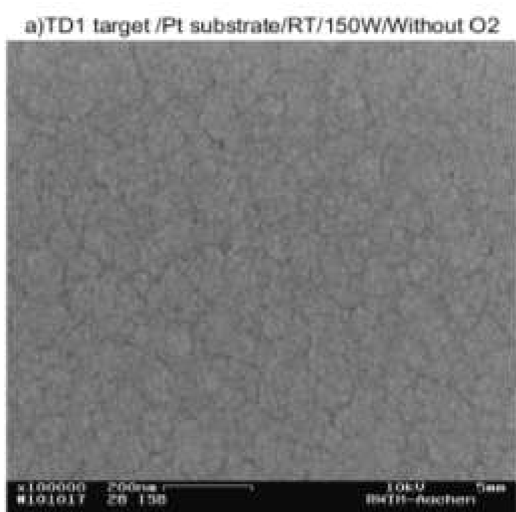

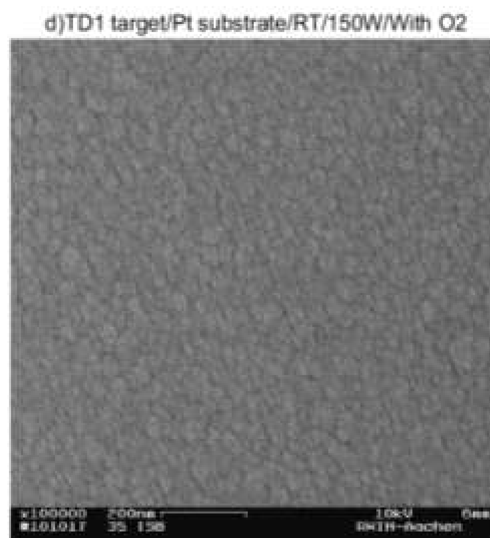

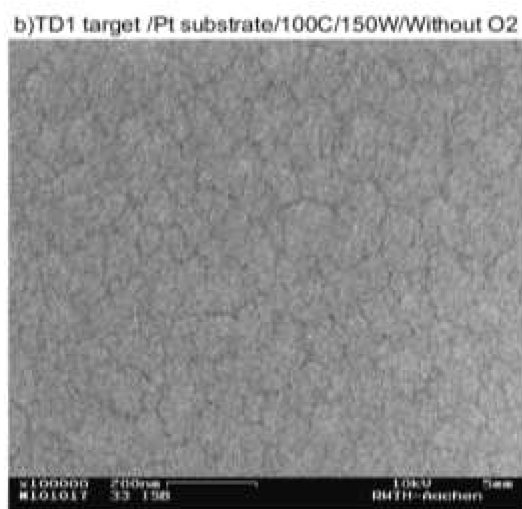

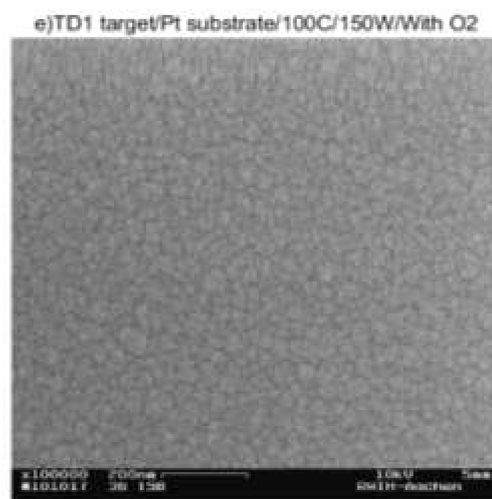

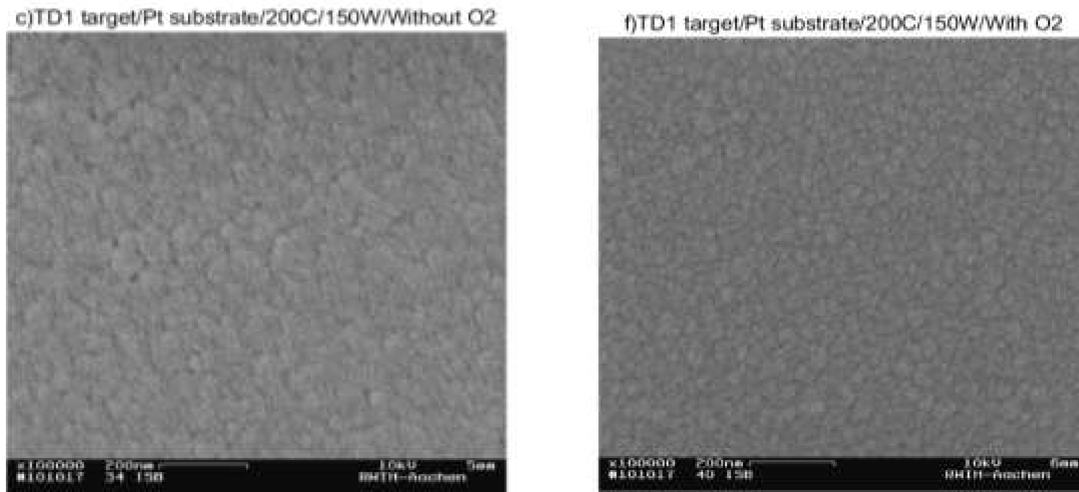

Figure 7. *The SEM images of the specimens fabricated by sputtering the TD1 target on the platinum substrate with and without oxygen*

The requirement for the SEM imaging is that the sample is conductive. However, the Al2O3 substrate is an insulating material. All samples with the usual silver paste coating created only a very bright image without any fine details due to the charging of the substrate. To obtain a view from the side and in order to avoid charging up, two different coatings (see Figure 8) were tested. First, the samples were coated with aluminum. Unfortunately, the actual thickness of the Al coating of the sample was much thicker than expected, and, in addition, the Al film completely masked all the fine details. The carbon coating did not help either because it was not conductive enough, and the sample was charged too. Also, the C-coating appeared to be approximately twice too thick in comparison with the expected deposited rate of carbon. Therefore, due to the limitations of the available techniques, it was impossible to obtain the SEM images of good quality using the specimens sputtered on the Al2O3 substrate.

a)TD0 target /Al2O3 substrate/200C/150W/C- coating

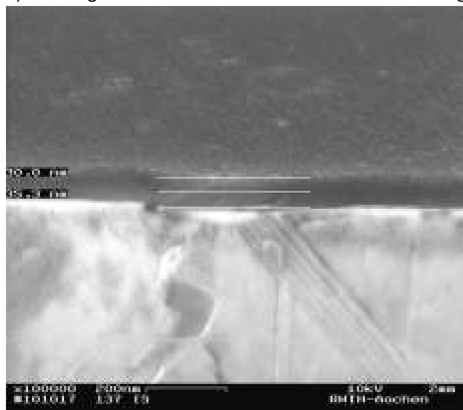

b)TD2 target /Al2O3 substrate/200C/150W/C- coating

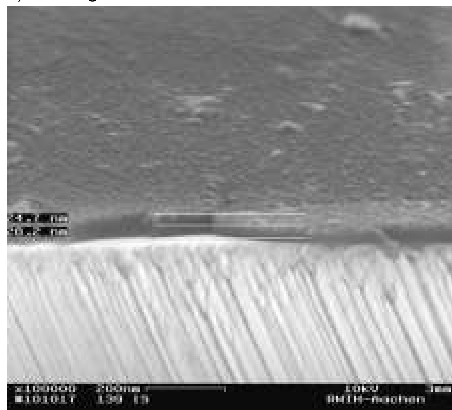

c)TD0 target /Al2O3 substrate/200C/150W/Al- coating

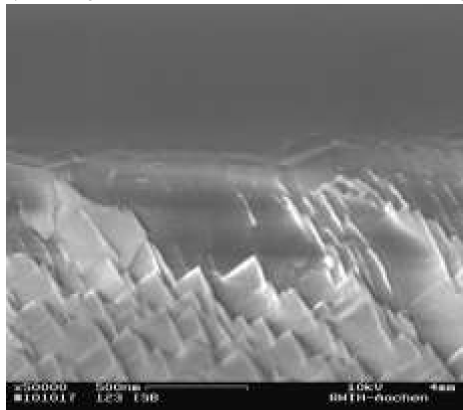

d)TD2 target /Al2O3 substrate/200C/150W/ Al coating

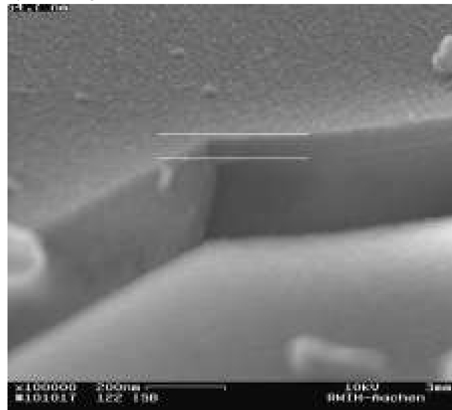

Figure 8. *The SEM images of the specimens fabricated by sputtering the Al2O3 substrates coated with carbon (a-b) and aluminum (c-d)*

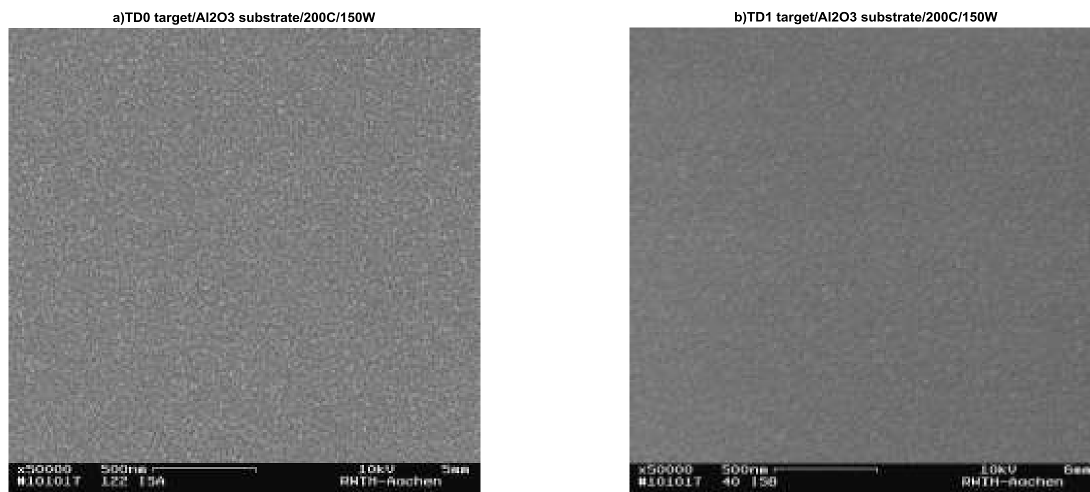

Figure 9. *The comparing the grain sizes of the specimens deposited using the TD0 and TD1 targets*

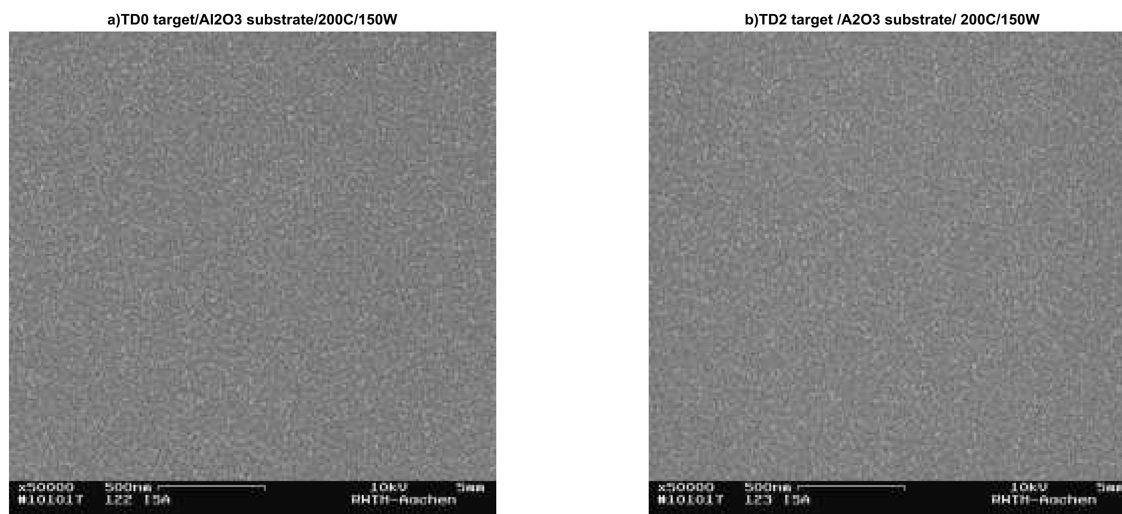

Figure 10. *The comparing the grain sizes of the specimens deposited using the TD0 and TD2 targets*

3.1.2 EDX

Preface. Even though EDX has certain obstacles and limitations, with some cautions the technique can be used for obtaining useful information about the samples. Due to the large penetrating depth of X-rays and the small thickness of the layers, a large portion of the information comes from the substrates and possibly even from the sample holder in a vacuum chamber of SEM/EDX. Due to the fact that only 1-2% of the detected signal in EDX spectra comes from the deposited SiO2, the detection of very small concentration of the doped elements would be highly improbable. However, because the objective was to compare the switching behavior of samples deposited using the different targets, substrates, as well as other parameters, the EDX characterization was performed for excluding the possibility of unexpected contamination of samples.

Interpretation of the results. The overall EDX results were according to expectations. For example, it was known that samples on platinum substrate contain Ti and are fabricated on SiO2-wafer. Also, the titanium nitride substrate is on top of the Si- wafer respectively. In addition, the Al2O3 substrate should be pure Al2O3. As a result, the EDX confirms the presence of all these elements and even their relative concentrations. In addition, the identification of a small amount of Al in the spectra can relate to the sample holder made of aluminum. However, a trace amount of Cu, mostly below the normal detection limit of EDX, can be related to measurement artifacts, especially in the control samples and the samples deposited by the TD0 target. On the other hand, the contamination or impurities incorporated during the fabrication cannot be completely excluded.

Figure 11 (a-c) shows the chemical compositions of the control samples without a deposited SiO2 layer. In addition to this, Figure 11 (a) shows that platinum is deposited on a Si- rich SiO2 wafer because of the atomic ratio of Si:O is not 1:2. This can refer to the fact that there are such localized Si –regions in the wafer, or more probably that the original Si- wafer is only partly oxidized below the surface. Moreover, the N and O are not detected in samples deposited on the TiN substrate. Of course, the EDX technique has difficulties in the detection of light and minor elements. However, this result can indicate the presence of metallic Ti or Ti- rich regions in TiN in the location where this signal originated.

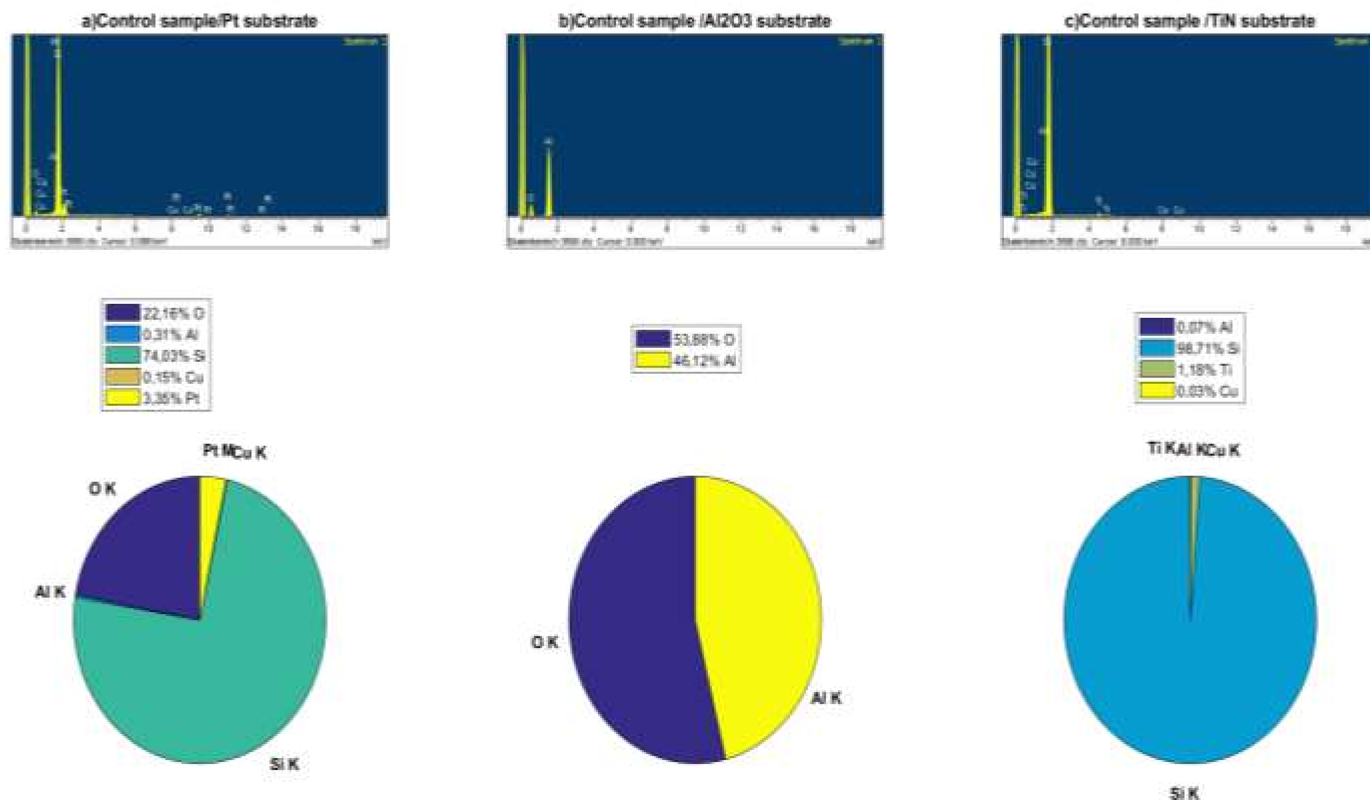

Figure 11. *The EDX analysis of control specimens with different substrates (platinum, Al2O3, and titanium nitride) i.e. without sputtered SiO2 thin film (in at%)*

Figure 12 and Figure 13 show the EDX result for samples deposited using the TD0 target on the platinum and Al2O3 substrates. According to the EDX results from the samples deposited on the Al2O3 substrate, the amount of the deposited SiO2 in the signal can be from 0.77 at% to 1.31 at% (see Figure 13(a-d). Therefore, these values can be used in the evaluation of the SiO2 amount in the samples with the platinum substrate on a SiO2 wafer.

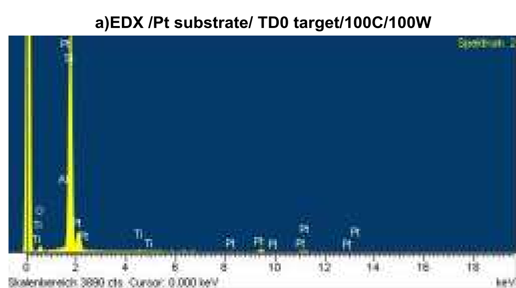

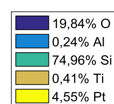

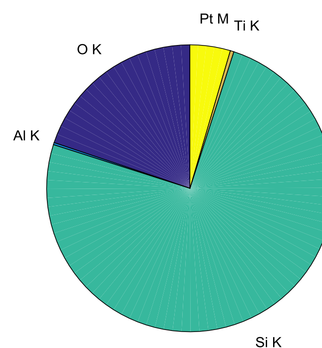

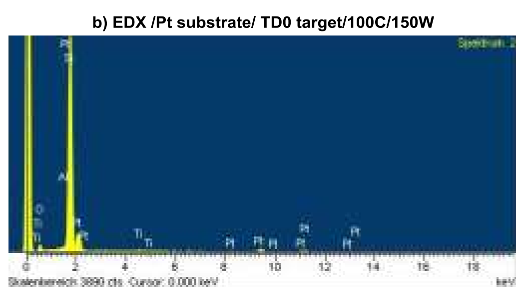

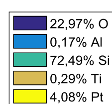

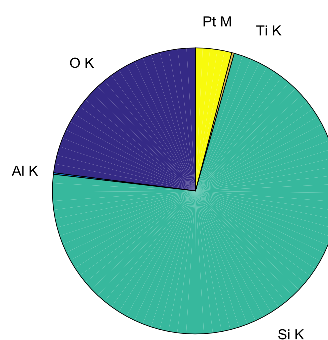

Figure 12. *The EDX analysis of the specimens sputtered using the TD0 target on the platinum substrate (in at%)*

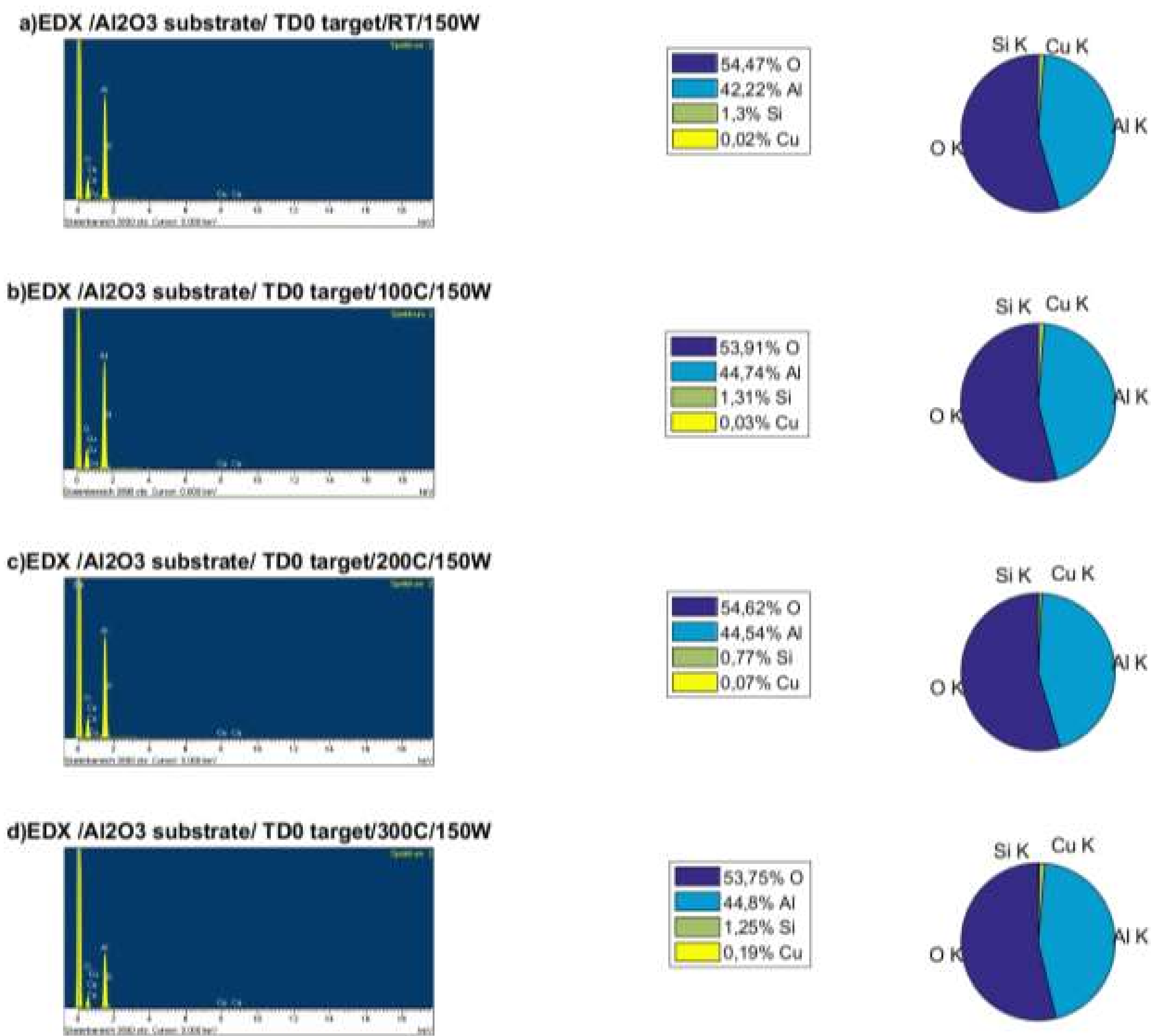

Figure 13. *The EDX analysis of the specimens sputtered using the TD0 target on the Al2O3 substrate (in at%)*

Figure 14 shows the samples deposited on the platinum and the TiN substrates using the doped TD1 target. Due to the complex composition of the samples deposited on the platinum substrate, it is difficult to make decisive conclusions based on the results, except for the slight modulation of oxygen and Si content under the different conditions. However, the EDX results for the samples on the TiN substrate are quite interesting, because referring to Figure 11(c), the samples do not contain O or N. In Figure 14 (c-d), the 6.87-7% at% of oxygen is detected in the samples on the TiN substrates. These amounts exceed the atomic ratio (1:2) needed to obtain a layer of SiO2 and

the oxidation of the titanium in TiN to TiO2. Also, there are concerns about the decreased amount of the detected Si ($\approx 92\ at\%$) in comparison to the control sample (98,71 at%). These results can partly explain the unexpected results of the electrical characterization of the samples deposited on TiN.

a) TD1 target/Pt substrate/100C/100W

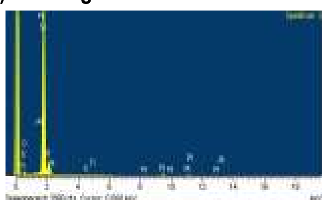

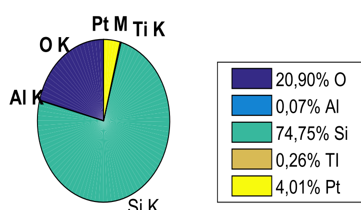

b) TD1 target/Pt substrate/100C/150W

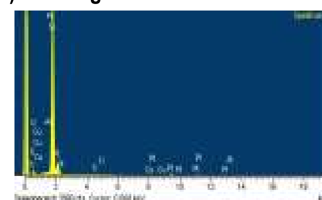

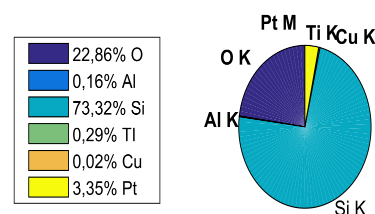

c) TD1 target/TiN substrate/100C/150W

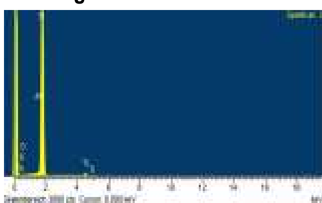

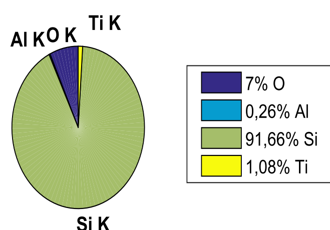

d) TD1/TiN substrate/100C/150W

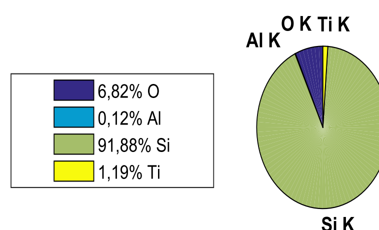

Figure 14. *The EDX analysis of the specimens sputtered using the TD1 target on the platinum and TiN substrates (in at%)*

Figure 15 and Figure 16 show the samples deposited using doped TD2 targets on the platinum and the Al2O3 substrates. As with all samples deposited on the platinum substrates, the content of

oxygen and silicon modulates slightly in comparison with the controls sample shown in Figure 11 (a). In addition, the Si content in the sputtered thin film is between 0.7 at% and 1.24% at%, but the oxygen content does not modulate in the same proportion. Therefore, it can be suggested that the deposited samples on the platinum substrate can have lower oxygen concentration implying Si-rich SiO2. On the other hand, in a sample deposited on a TiN substrate, a high oxygen content is detected. Indeed, the found differences can relate to the limitation of the EDX technique and even to the measurement artifacts. However, these results should be kept in mind when evaluating the results of the electrical characterization of the related samples.

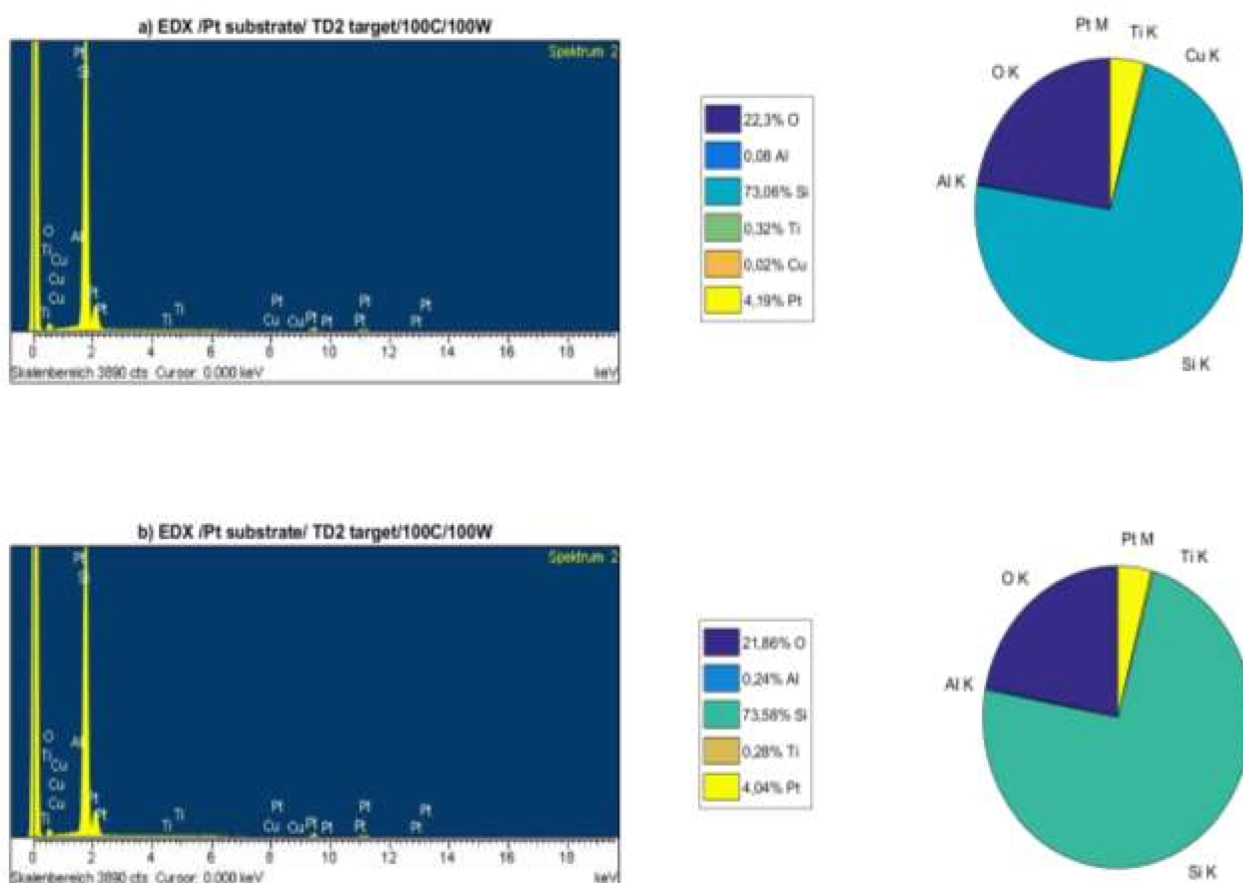

Figure 15. *The EDX analysis of the specimens sputtered using the TD2 target on the platinum substrate (in at%)*

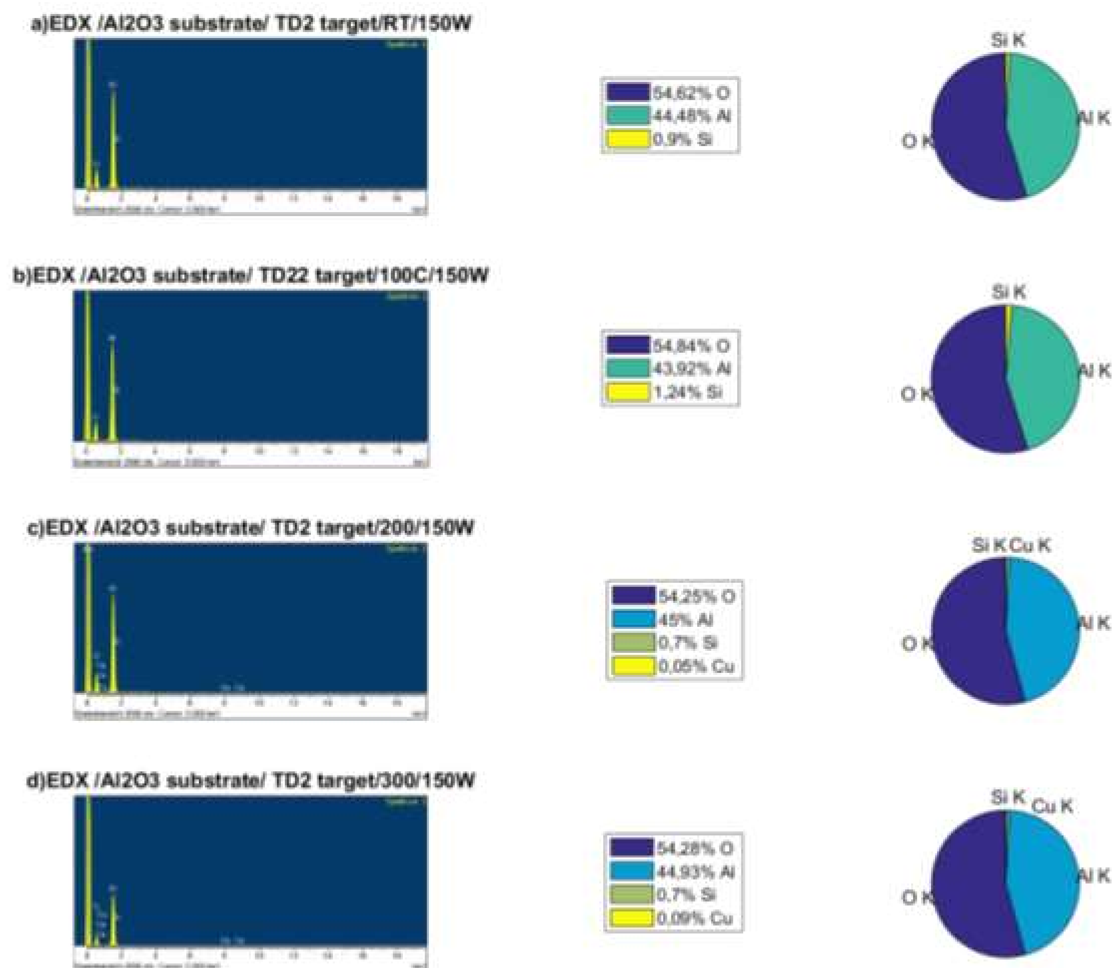

Figure 16. *The EDX analysis of the specimens sputtered using the TD2 target on the Al2O3 substrate (in at%)*

3.1.3 XRR

Preface. The influence of the RF power and the temperature of the deposition on the thickness, density, and roughness of SiO2 layers deposited on the platinum, Al2O3 and TiN substrates, was studied using the XRR techniques. The available power of the RF generator is an important sputtering parameter influencing the physical properties of the fabricated thin films as well as the deposition rate of the sputtering. Knowledge of the actual deposition rate allows controlling the thickness of the deposited layer since many features of thin films are dependent on thickness. Also, the temperature during the sputtering has a direct influence on the density, roughness, and thickness of the deposited layer. Additionally, the morphological structure of substrate should be

considered. The more ordered the structure of the deposition substrate has, the more regular the created layer will be. The last can be seen from how regular the oscillating period in XRR curve is. A change in a period of oscillating and the amplitude indicates that the density and the roughness are not constant through the layer. The reflectivity of a rough surface falls off even more rapidly and therefore the different slopes of XRR curves for the same deposition condition indicate a difference in the roughness.

Interpretation of the results. Figure 17 shows the XRR analysis of the samples deposited using TD0 and TD1 targets on an Al2O3 substrate. The larger the period of Kiessig fringes is, the thinner is the layer. Increasing the RF power from 50W to 150W at the constant temperature of 150C in Figure 17 decreases the oscillation period of the Kiessig fringes, indicating that the layer becomes thicker with increasing RF power. In addition, it also corresponds to the increasing deposition rate. Changing the amplitude means a change in the density, whereas the change of period corresponds to the change in thickness. A decrease in the amplitude means increasing the density of the layer.

Figure 18 shows the XRR analysis of SiO2 deposited on an Al2O3 substrate using the TD0 and the TD1 targets at RT and 100C at 150W. The change in the temperature at the constant power causes the change in the period and amplitude of oscillation. However, the variability of oscillations is high even for exactly the same deposition parameters shown in the insert in Figure 18 separately. Indeed, the insert in Figure 18 indicates that the variability in the amplitude and the period of oscillation for exactly the same parameters can be higher than for the supposed treatment effect like the temperature.

Figure 19 shows samples deposited using the TD0 target on the platinum and the TiN substrates, whereas Figure 20 displays the samples deposited using the TD1 and the TD2 targets. Opposite to the samples deposited on the Al2O3 substrate, the layers on the platinum and the TN substrates are more irregular because the slope, period and amplitude of the oscillation are changing in the same layer. For obtaining the numerical values, thickness, the roughness, and density of measured and simulated curves need to match each other using the fitting software. However, the curves with such an irregular shape are extremely difficult to fit using only the standard software. Therefore, one can usually see the difference in the measured curves, but at the same time, a reliable numerical value for the comparison between different treatments will be difficult to obtain.

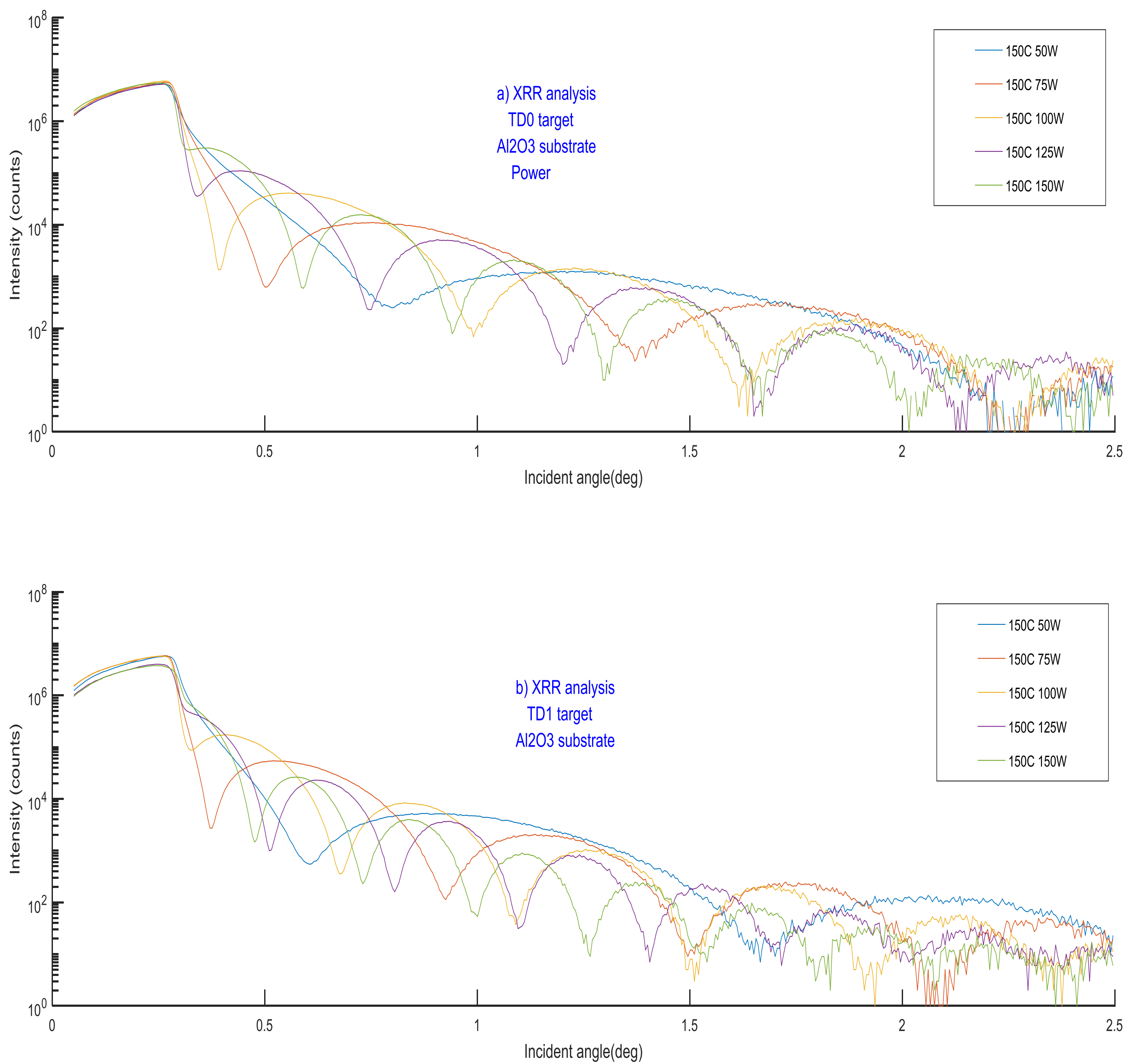

Figure 17. *The XRR analysis of SiO2 deposited on an Al2O3 substrate using the TD0 and the TD1 targets at the different temperatures and the RF power settings*

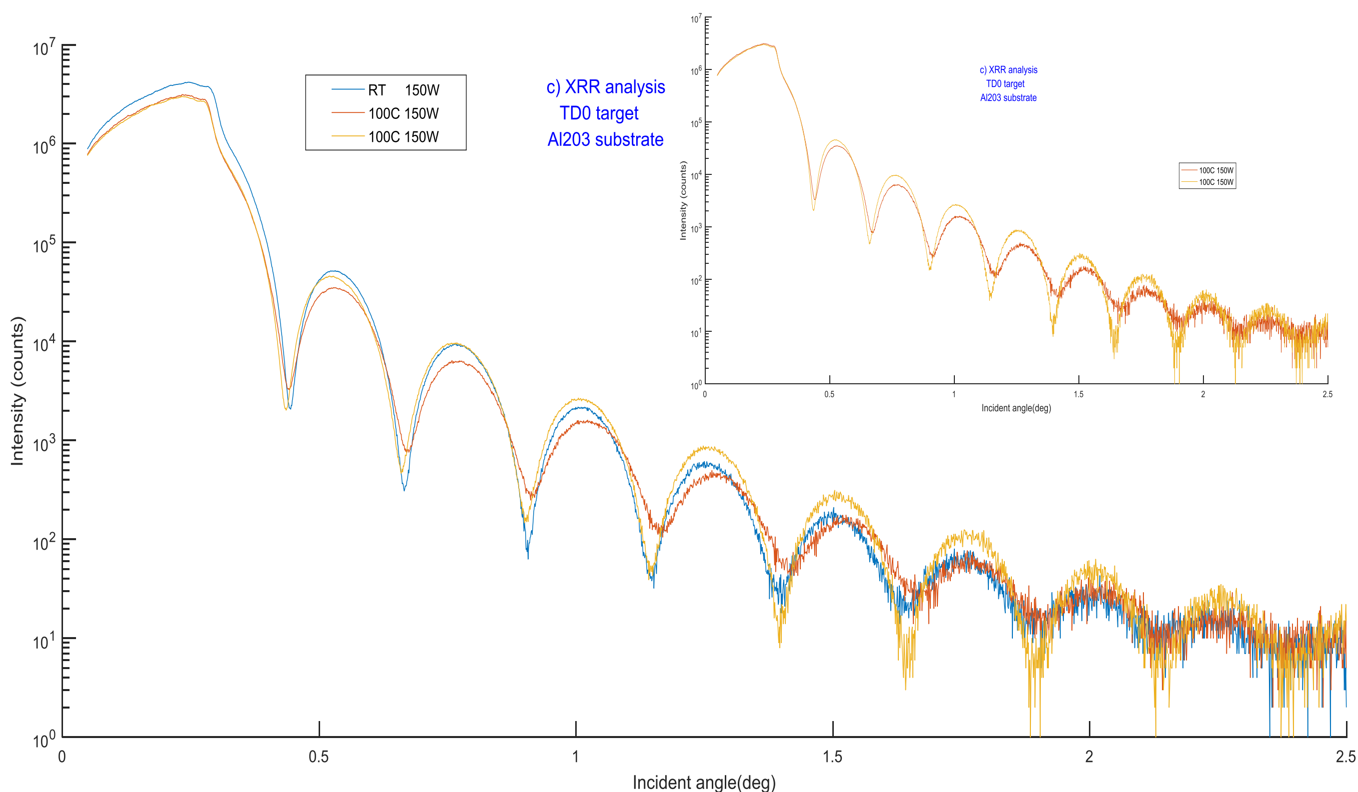

Figure 18. *XRR analysis of SiO2 deposited on an Al2O3 substrate using the TD0 and the TD1 targets at the different temperatures and the RF power settings.*

Increasing the temperature at the constant power (see Figure 19 a, c) changes the slope of the curves. The reflectivity of a rough surface falls off even more rapidly. Therefore, the sample treated at a higher temperature has more rough structure and therefore the slope of the curve is larger. In Figure 20(a), increasing RF power at a constant temperature creates a less dense structure while an increased deposition rate causes a less dense structure of the layer. Instead, in Figure 20 (c), increasing power at constant temperature causes increases in the slope, indicating increased roughness.

In Figure 19 (b, c) and Figure 20 (b, d), the samples deposited on the TiN substrate show less sensitivity to the roughness than the samples deposited on the platinum substrate, since the slope of the curve changes to a much less extent. However, the amplitude and therefore the density in the same samples vary a lot, showing a denser structure near the substrate and a less dense structure near the surface.

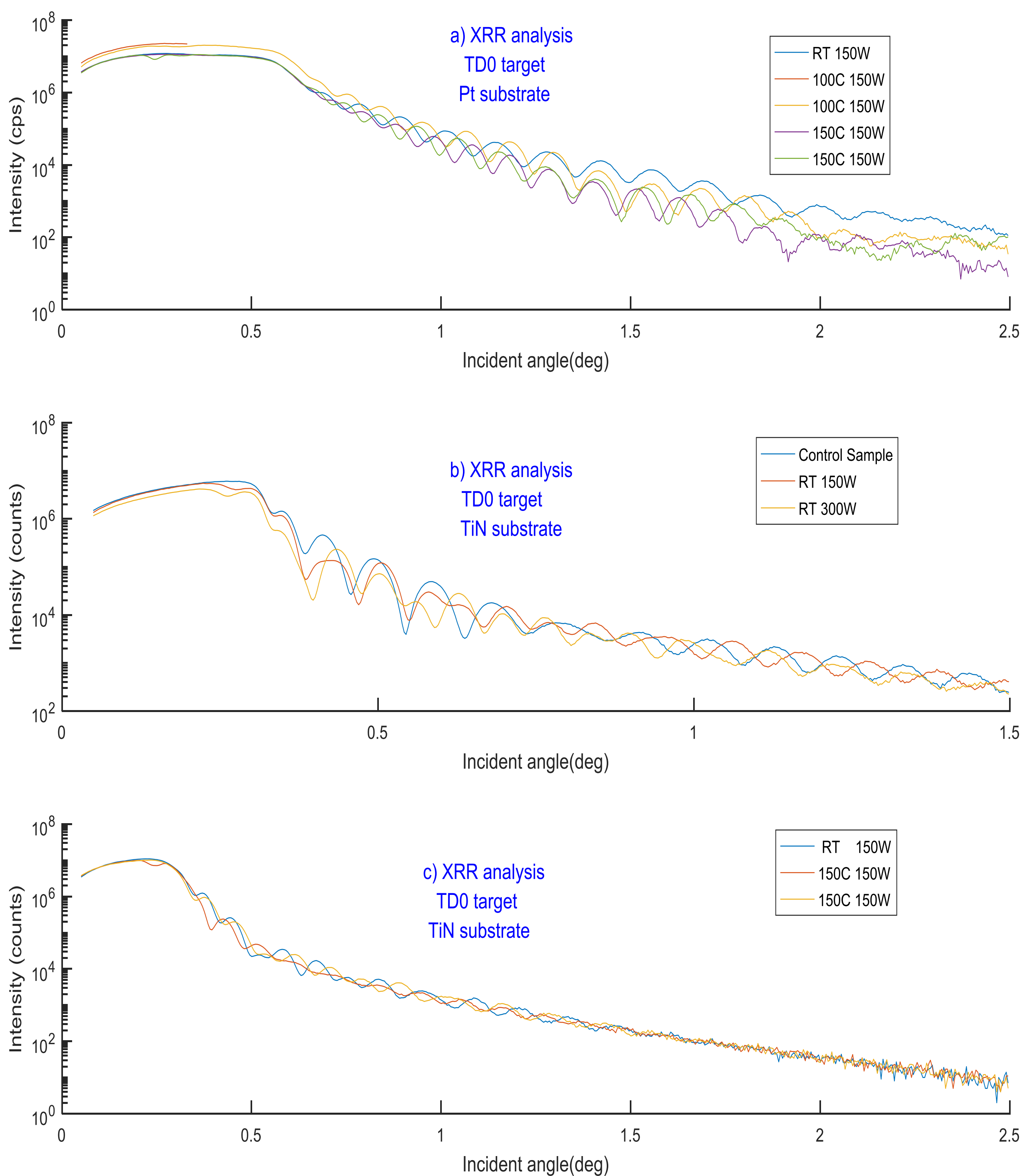

Figure 19. *The XRR analysis of the samples deposited using the TD0 target on the platinum and the TiN substrates at the different temperature and the RF power settings*

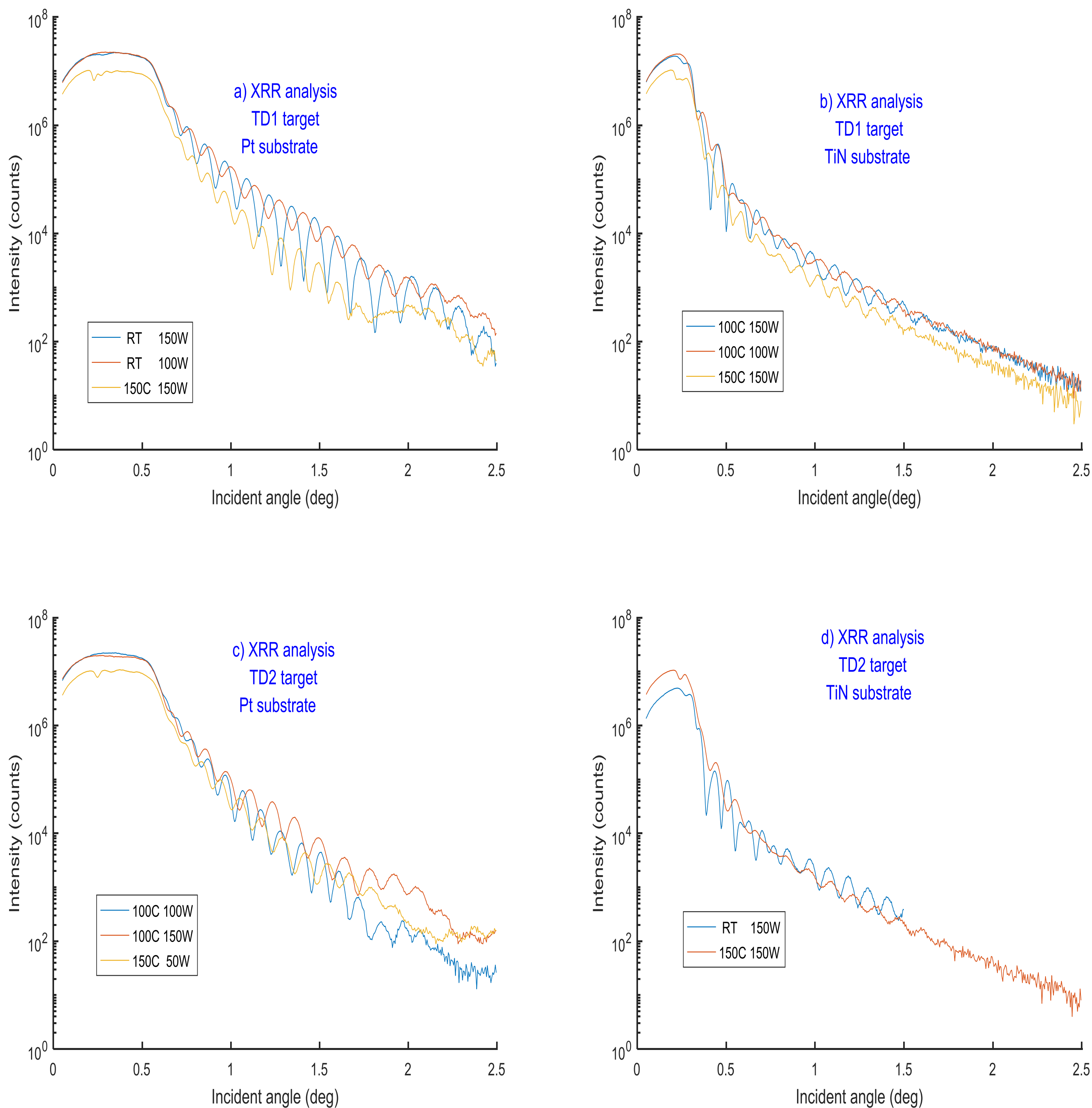

Figure 20. *The XRR analysis of the specimens sputtered using the TD1 and the TD2 targets on the platinum and the TiN substrates at the different temperature and the RF power settings*

Figure 21 shows the XRR analysis two samples deposited using the same setting: 150C and 150W. The samples were deposited using the TD0 target on the platinum and the TiN substrates. The purpose of this research was not to investigate the variability in fabrication at the same setting. Therefore the only limited amount of samples may be compared. Some of the testing procedures are destructive, therefore double samples were fabricated for electric and others characterizations at different stages of this project. By accident, these samples were fabricated by exact the same setting.   It can be seen in Figure 21 that samples deposited on platinum substrates have the larger variability than those deposited on the TiN substrates. The most important issue is the variability related to the first layers deposited on the substrate.

Figure 22 shows the XRR analysis of the samples deposited using the TD1 and the TD2 targets on the platinum and the TiN at the different temperature and the RF power settings: 150W versus 100W. The samples deposited on the platinum substrate at RT at 100W and 150W have the different amplitude, slopes and period of oscillating fringes. The samples deposited on platinum substrates show the higher sensitivity to RF change than that on TiN substrate.

Figure 23 shows the XRR analysis of the samples deposited using the TD0, the TD1, and TD2 targets on the Pt substrate at the same settings (150W, 150C, and 50nm-thick layer). It can be seen that variability is quite high. The samples deposited on the same substrate at the same parameters but deposited using different targets possess different morphological properties. The quality of the deposited layer, therefore, depends on the used target.

Figure 24 shows the XRR analysis of the specimens sputtered using the TD0, the TD1, and TD2 targets on the TiN substrate at the same settings (150W, 150C, and 50nm-thick layer). It can be seen that these samples show less variability than those deposited on the platinum substrate shown in Figure 23. Therefore, not only the target but also the substrate, on which thin film is deposited, are important.

Figure 25 shows the XRR analysis of all the specimens sputtered on the Pt and the TiN substrates. The overview of all samples deposited on two different substrates confirm the general observation during the electrical testing of samples. The samples deposited on platinum and TiN behave electrically differently. The XRR curves highlight that intensity is different due to differences in electron density. The variability of all the samples deposited on TiN is less than on the platinum substrate. The morphology and structure of the layer look very different.

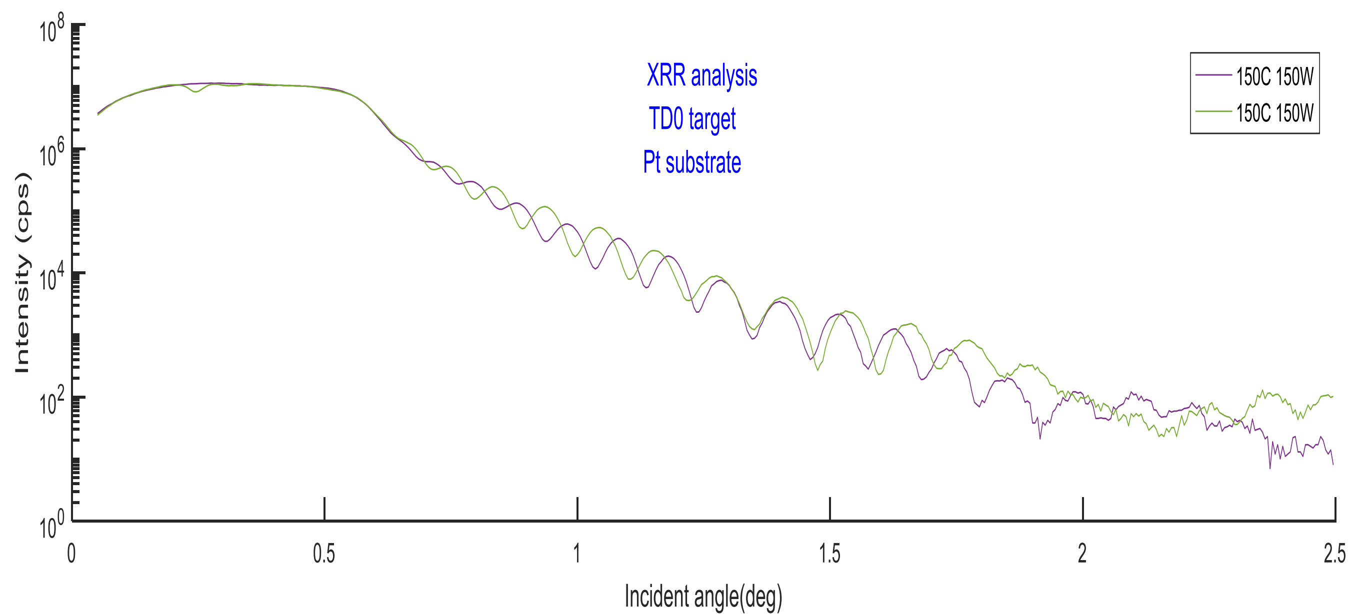

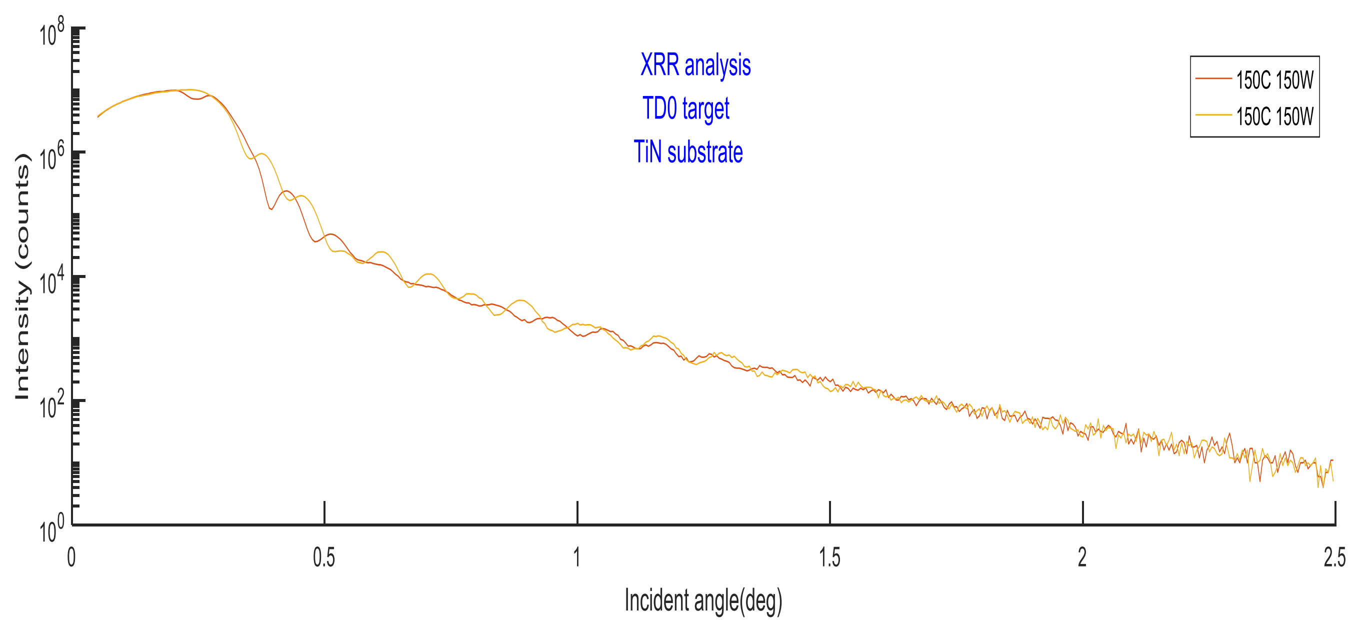

Figure 21. *The XRR analysis of the samples deposited using the TD0 target on the platinum and the TiN substrates at the 150C and 150W: the variability of the results at the same setting*

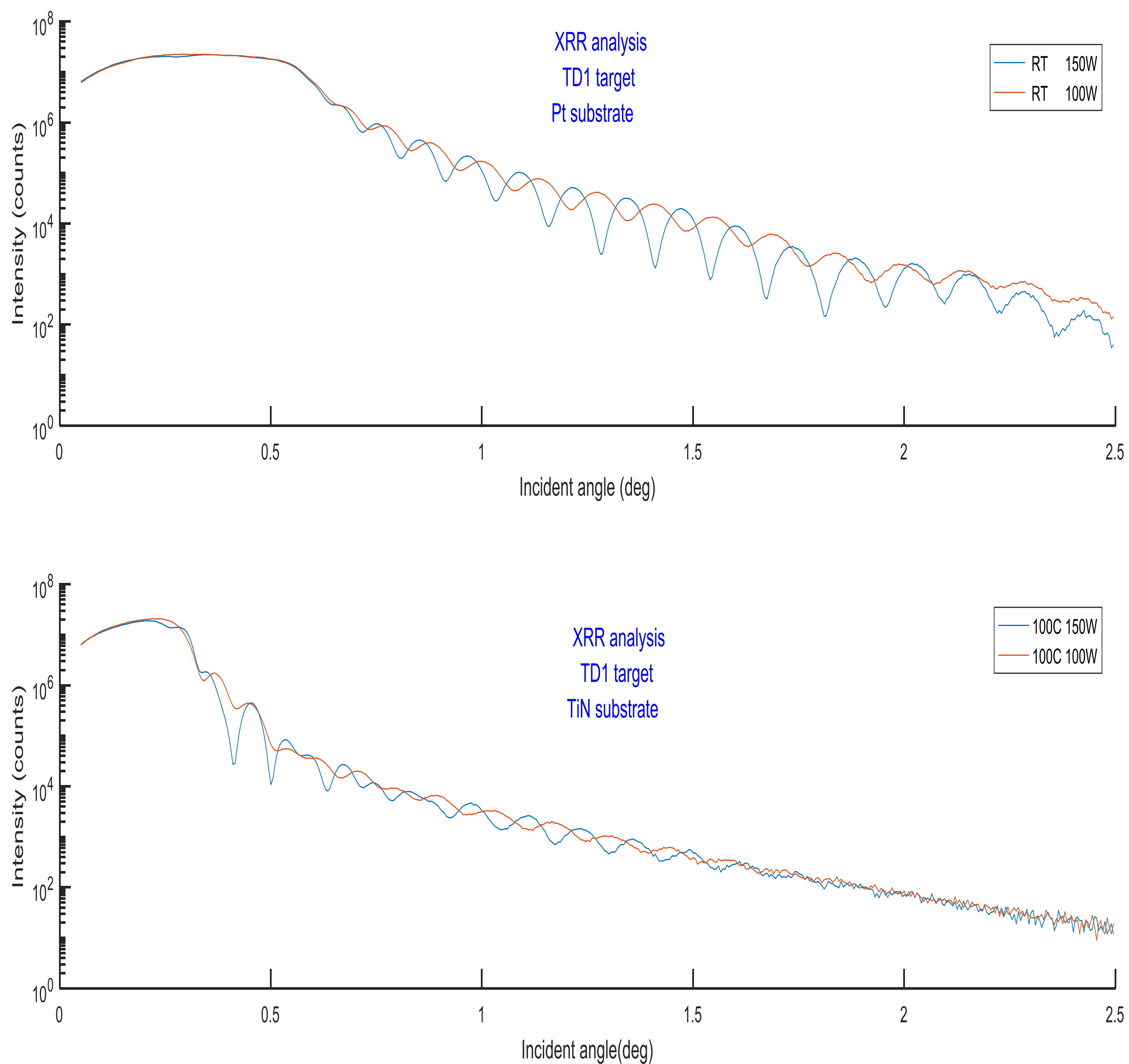

Figure 22. *The XRR analysis of the samples deposited using the TD1 and the TD2 targets on the platinum and the TiN at the different temperature and the RF power settings: 150W versus 100W*

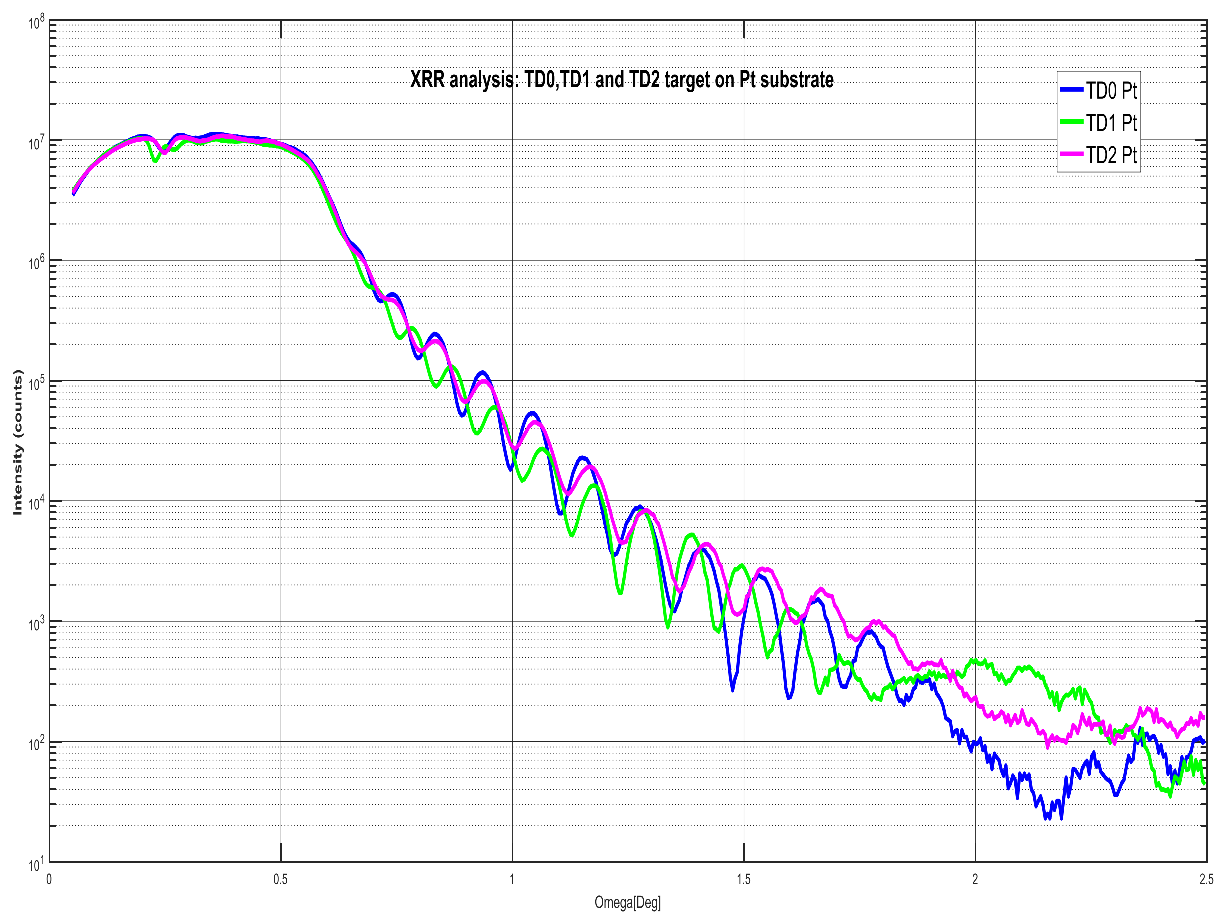

Figure 23. *The XRR analysis of the samples deposited using the TD0, the TD1 and TD2 targets on the Pt substrate at the same settings (150W, 150C and 50nm-thick layer)*

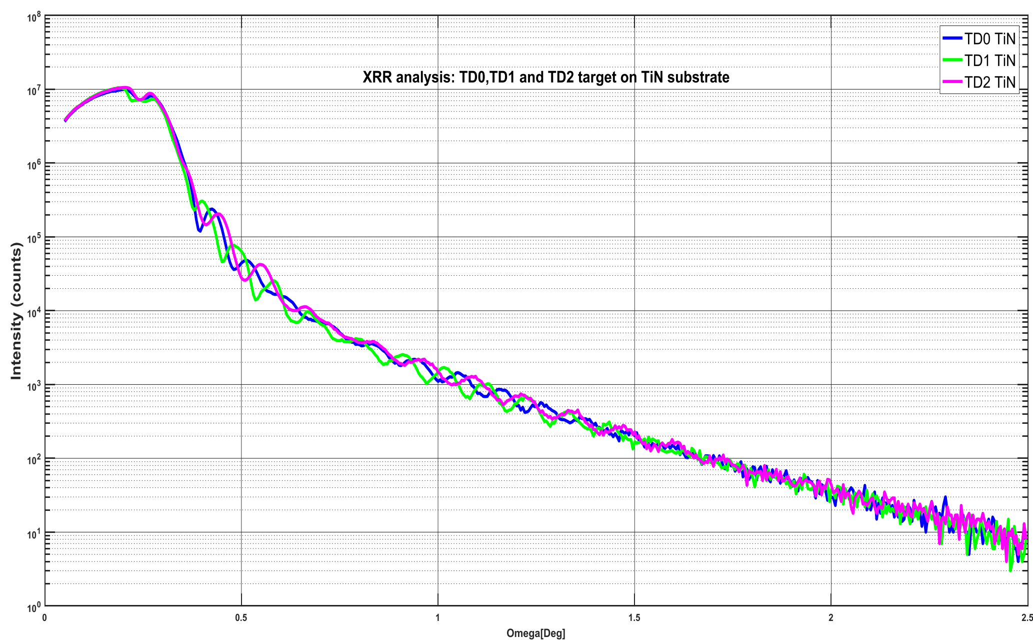

Figure 24. *The XRR analysis of the specimens sputtered using the TD0, the TD1 and TD2 targets on the TiN substrate at the same settings (150W, 150C and 50nm-thick layer)*

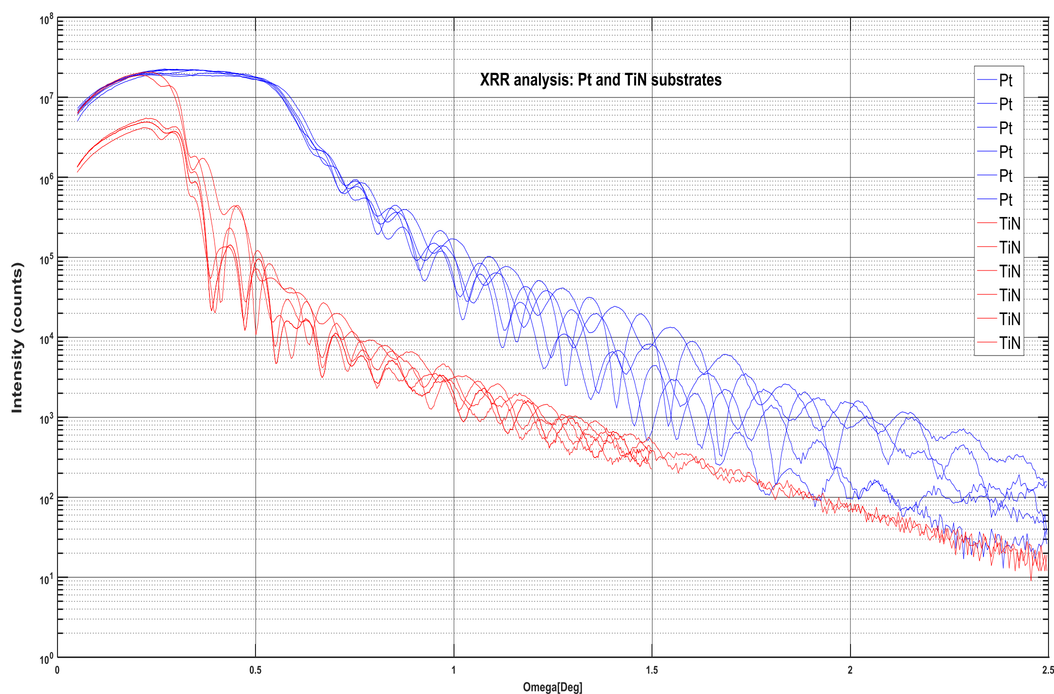

Figure 25. *The XRR analysis of all specimens sputtered on the Pt and the TiN substrates*

3.1.4 XRD

Figure 26 displays the XRD analysis of the different specimens deposited using TD0 target on the platinum, the Al2O3, and the TiN substrates.

The XRD curves are arranged according to the used RF power and the temperature. First of all, the penetration depth of X-rays is usually much higher than the thickness of the layers under study. As in the case of EDX, most of the signal comes from the substrate itself. The Al2O3 substrate was used as a reference. The aim of the XRD analysis is usually to ensure that the deposited layer is amorphous, which means that it should not have any peaks in the XRD spectrum. This is exactly the case for all samples deposited on the Al2O3 substrate. Both the substrate and the layer are amorphous because the curves contain no peaks. In contrast, the other layers deposited on the platinum and the TiN substrates have peaks in their spectra. These peaks, however, relate to the used substrates, and it can be noted that the TiN and the platinum substrates have a different degree of crystallinity. The XRD curves are sensitive to both temperature and the used RF power.

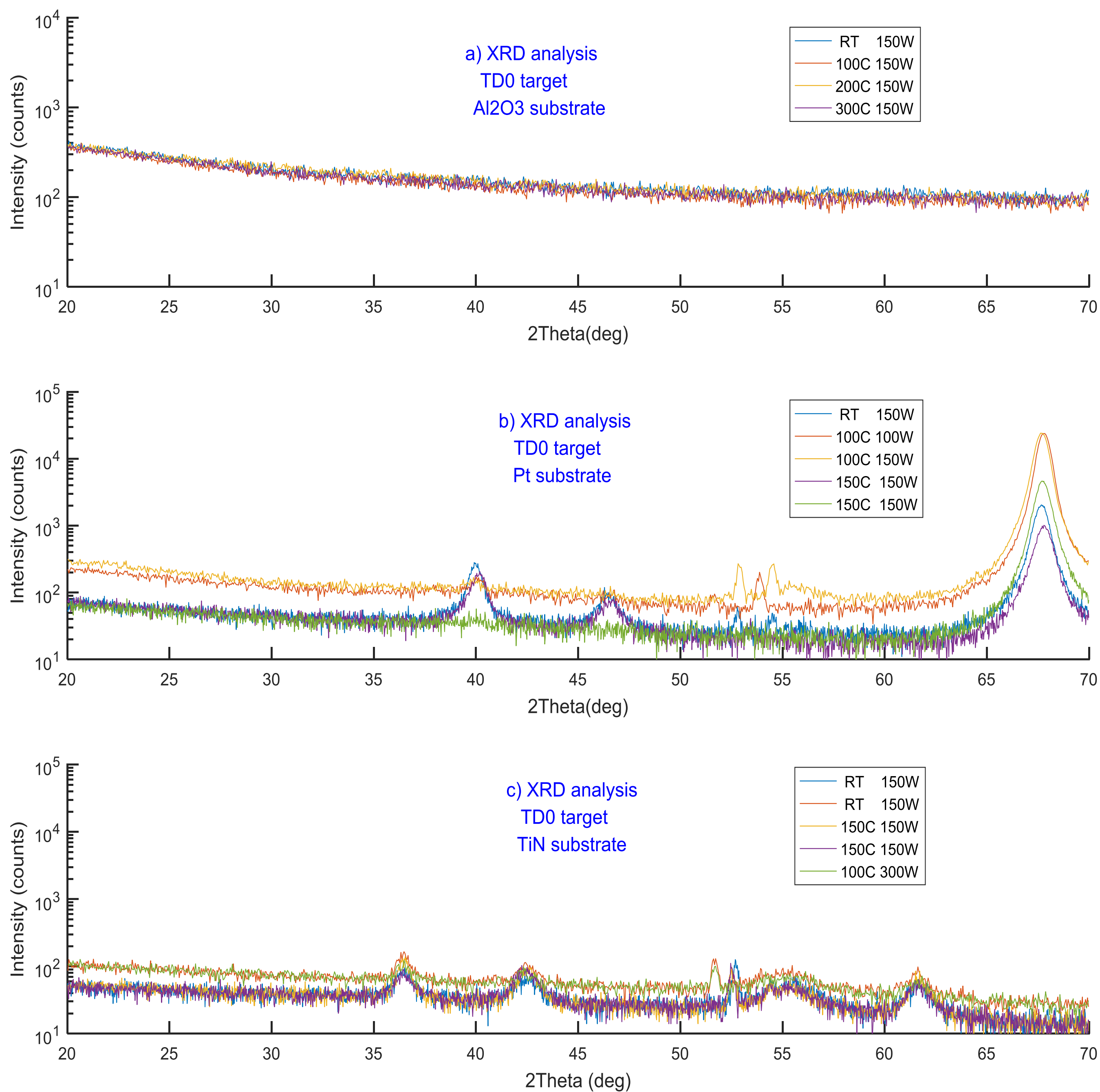

Figure 26. *The XRD analysis of the different specimens sputtered using the TD0 target on the platinum, the Al2O3 and the TiN substrates*

Figure 27 displays the XRD analysis of the different specimens deposited using the TD1 target on the platinum, the Al2O3 and the TiN substrates.

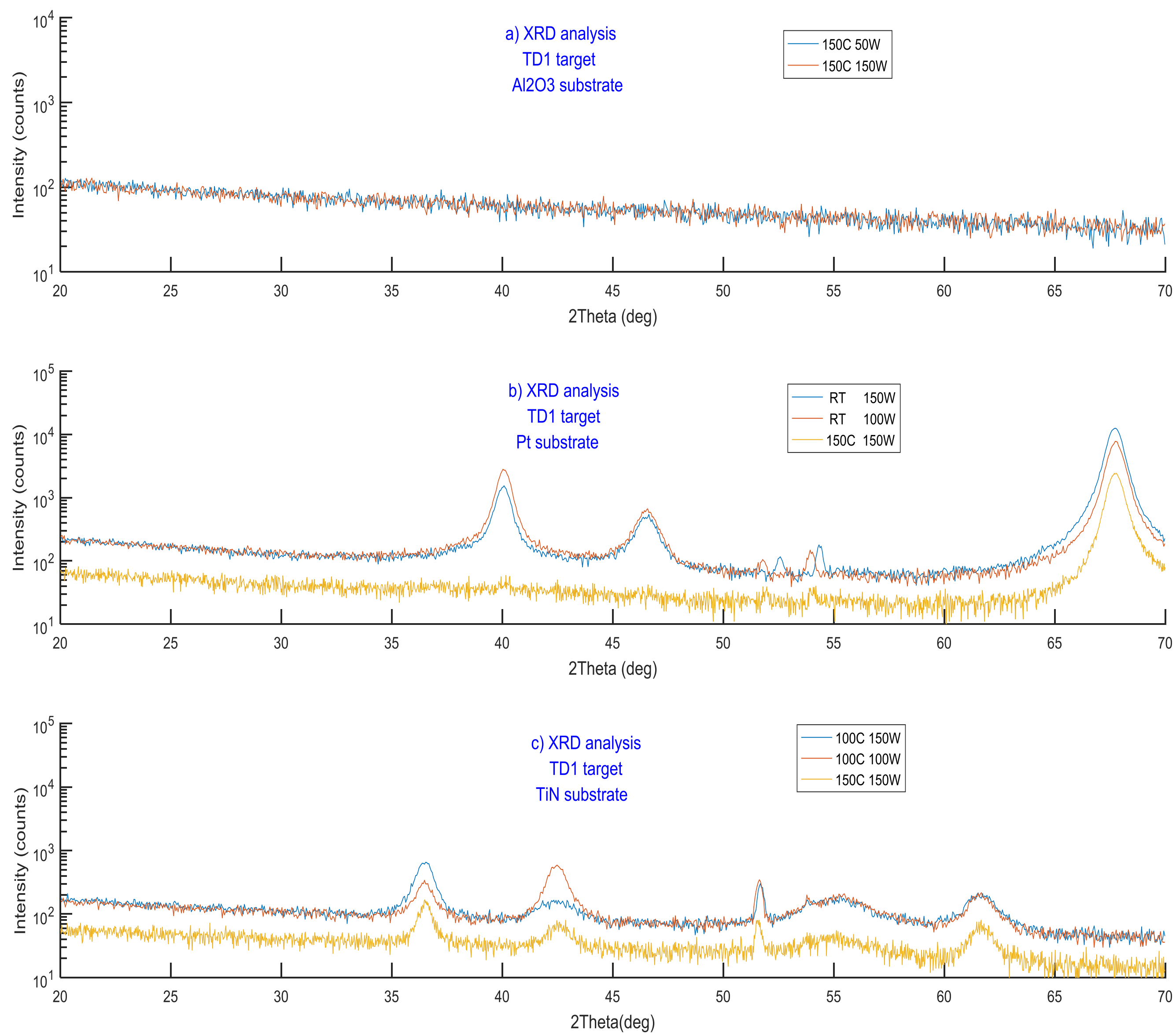

Figure 27. *The XRD analysis of the different specimens sputtered using the TD1 target on the platinum, the Al2O3 and the TiN substrates*

Figure 28 displays the XRD analysis of the different specimens deposited using the TD2 target on the platinum, the Al2O3 and the TiN substrates.

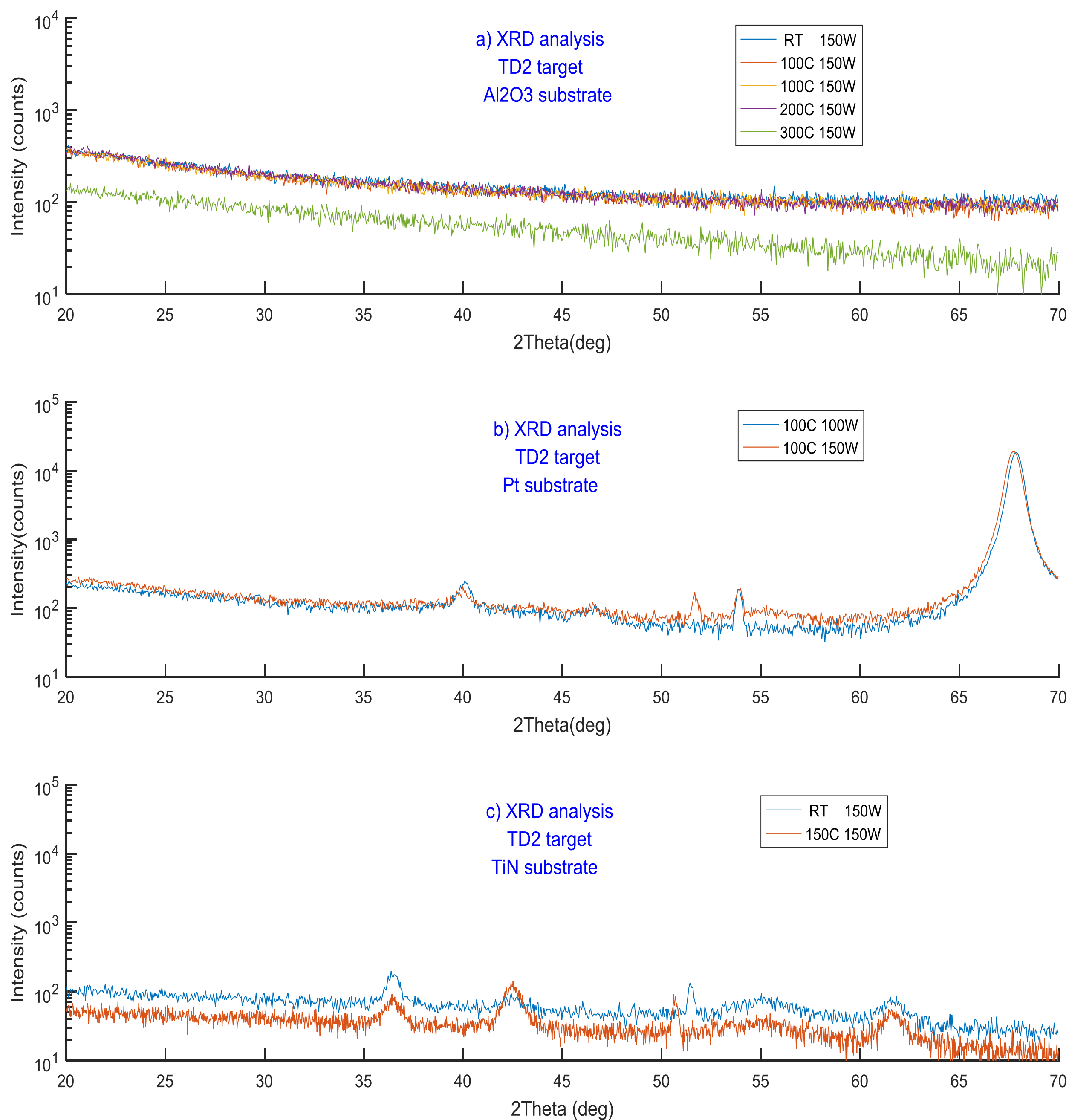

Figure 28. *The XRD analysis of the different specimens sputtered using the TD2 target on the platinum, the Al2O3 and the TiN substrates*

3.1.5 Conclusions

SEM, EDX, XRD, as well as XRR, are analytical tools, which can be useful for material characterization. However, the investigation of effects on nanoscales requires the most advanced and modern tools. These tools need to be are specifically designed for investigating in nanoscales. In addition, the sophisticated devices need to have enough license support from the manufacturer of the software.

In all above-mentioned techniques, only XRR analysis was sensitive enough to catch a change in used parameters or treatment. Nevertheless, using XRR requires careful design and systematic planning of tests and used parameters in order to obtain meaningful information. When many parameters were changed simultaneously, it would be seen also in the XRR response. However, the interpretation would be difficult due to the sensitivity of XRR.

PANalytical provided the used X-rays diffractometer and standard simulation software, which was used for the extraction of parameters for the thickness, roughness, and density of thin films. However, the used algorithm in the standard version of the software is more suitable for the regular layer but not for multilayers and irregular layers. The more advanced software or the diffractometers of other manufacturers with related software are able to extract such kind of information. Also using XRD techniques would usually need additional license support when more advanced information needs to be extracted. Nevertheless, XRR and XRD with enough software support may very useful for engineering the thin film with properties in demand: the nanostructure, morphology, or porosity, for example.

REFERENCES

Bellet, D. & Dolino, G. (1996). X-ray diffraction studies of porous silicon, Thin Solid Films, Vol. 276(1), pp. 1-6.

Bowen, D. & Tanner, B. (1993). Characterization of engineering surfaces by grazing-incidence X-ray reflectivity, Nanotechnology, Vol. 4(4), pp. 175.

Briscoe, W.H., Chen, M., Dunlop, I.E., Klein, J., Penfold, J. & Jacobs, R.M. (2007). Applying grazing incidence X-ray reflectometry (XRR) to characterising nanofilms on mica, Journal of colloid and interface science, Vol. 306(2), pp. 459-463.

Brydson, R. & Hondow, N. (2011). Electron Energy Loss Spectrometry and Energy Dispersive X-ray Analysis, Aberration-Corrected Analytical Transmission Electron Microscopy, pp. 163-210.

CIRP Encyclopedia of Production Engineering (2014).

Compton, A.H. (1923). CXVII. The total reflexion of X-rays, The London, Edinburgh, and Dublin Philosophical Magazine and Journal of Science, Vol. 45(270), pp. 1121-1131.

Cullity, B. & Stock, S. (2001). Elements of X-ray diffraction, .

Davoodi, A., Tajally, M., Mirzaee, O. & Eshaghi, A. (2016). Fabrication and characterization of optical and electrical properties of Al–Ti Co-doped ZnO nano-structured thin film, Journal of Alloys and Compounds, Vol. 657pp. 296-301.

Filies, O., Böling, O., Grewer, K., Lekki, J., Lekka, M., Stachura, Z. & Cleff, B. (1999). Surface roughness of thin layers—a comparison of XRR and SFM measurements, Applied Surface Science, Vol. 141(3), pp. 357-365.

Fujii, Y. (2013). Recent Developments in the X-Ray Reflectivity Analysis for Rough Surfaces and Interfaces of Multilayered Thin Film Materials, Journal of Materials, Vol. 2013.

Gaboriaud, R., Paumier, F. & Lacroix, B. (2016). Disorder–order phase transformation in a fluorite-related oxide thin film: In-situ X-ray diffraction and modelling of the residual stress effects, Thin Solid Films, Vol. 601pp. 84-88.

Goldstein, J., Newbury, D.E., Echlin, P., Joy, D.C., Romig Jr, A.D., Lyman, C.E., Fiori, C. & Lifshin, E. (2012). Scanning electron microscopy and X-ray microanalysis: a text for biologists, materials scientists, and geologists, Springer Science & Business Media, .

Goldstein, J., Newbury, D.E., Echlin, P., Joy, D.C., Romig Jr, A.D., Lyman, C.E., Fiori, C. & Lifshin, E. (2012). Scanning electron microscopy and X-ray microanalysis: a text for biologists, materials scientists, and geologists, Springer Science & Business Media, .

Islam, M.N., Ghosh, T., Chopra, K. & Acharya, H. (1996). XPS and X-ray diffraction studies of aluminum-doped zinc oxide transparent conducting films, Thin Solid Films, Vol. 280(1), pp. 20-25.

Kiessig, H. (1931). Interferenz von Röntgenstrahlen an dünnen Schichten, Annalen der Physik, Vol. 402(7), pp. 769-788.

Lehmkühler, F., Paulus, M., Streit-Nierobisch, S. & Tolan, M. (2008). Determination of microscopic interaction constants by X-ray reflectivity measurements, Fluid Phase Equilibria, Vol. 268(1), pp. 95-99.

Parratt, L.G. (1954). Surface studies of solids by total reflection of X-rays, Physical review, Vol. 95(2), pp. 359.

Prencipe, I., Dellasega, D., Zani, A., Rizzo, D. & Passoni, M. (2015). Energy dispersive x-ray spectroscopy for nanostructured thin film density evaluation, SCIENCE AND TECHNOLOGY OF ADVANCED MATERIALS, Vol. 16(2), pp. 25007-25015.

Ramachandran, V.S. & Beaudoin, J.J. (2000). Handbook of analytical techniques in concrete science and technology: principles, techniques and applications, Elsevier, .

Röntgen, W.S. (1898). Ann Phys (second ser.) 64 (1898) 1, 13, 19. From Proc
Physical Medical Assoc Würzburg 1895 (Situngber der Würzburger
Physik-Medic Gesellsch); translated by A. Stanton in Nature 53 No. 1369
(1896) 274,.

Sankar, S., Sharma, S.K. & Kim, D.Y. (2016). Synthesis and characterization of mesoporous SiO2 nanoparticles synthesized from Biogenic Rice Husk Ash for optoelectronic applications, .

Schindler, C. (2009). Resistive switching in electrochemical metallization memory cells.

Schäfer, N., Wilkinson, A.J., Schmid, T., Winkelmann, A., Chahine, G.A., Schülli, T.U., Rissom, T., Marquardt, J., Schorr, S. & Abou-Ras, D. (2016). Microstrain distribution mapping on CuInSe 2 thin films by means of electron backscatter diffraction, X-ray diffraction, and Raman microspectroscopy, Ultramicroscopy, Vol. 169pp. 89-97.

Solookinejad, G., Rozatian, A. & Habibi, M. (2014). Characterization of Zinc Oxide Thin Film Using Atomic Force Microscopy and Optimized X-Ray Reflectivity by Genetic Algorithm, Experimental Techniques, Vol. 38(1), pp. 21-27.

Suzuki, T., Omote, K., Ito, Y., Hirosawa, I., Nakata, Y., Sugiura, I., Shimizu, N. & Nakamura, T. (2006). Small angle X-ray scattering measurements of porous low-k films using synchrotron radiation, Thin Solid Films, Vol. 515(4), pp. 2410-2414.

van den Hurk, J. (2016). Germanium Sulphide Based Resistive Switching devices, .

Veldhuis, S.A., Brinks, P., Stawski, T.M., Göbel, O.F. & Johan, E. (2014). A facile method for the density determination of ceramic thin films using X-ray reflectivity, Journal of Sol-Gel Science and Technology, Vol. 71(1), pp. 118-128.

Wasa, K., Kitabatake, M. & Adachi, H. (2004). Thin film materials technology: sputtering of control compound materials, Springer Science & Business Media, .

Westwood, W. (1976). Glow discharge sputtering, Progress in Surface Science, Vol. 7(2), pp. 71-111.

Windischmann, H. (1992). Intrinsic stress in sputter-deposited thin films, Critical Reviews in Solid State and Material Sciences, Vol. 17(6), pp. 547-596.

Yang, L., Ge, D., Wei, H., Zhao, H., He, F. & He, X. (2009). Description of surface roughness of sol–gel films/coatings by X-ray reflectivity technique, Applied Surface Science, Vol. 255(19), pp. 8226-8229.

Yasaka, M. (2010). X-ray thin-film measurement techniques, The Rigaku Journal, Vol. 26(2), .

Zhou, W., Deng, H., Yang, P. & Chu, J. (2016). Designing tunable band-gap and magnetization at room-temperature in Pb (Ti 1-x M x) O 3-δ (M= Ni and Pd) thin films, Materials Letters, Vol. 185pp. 323-326.

APPENDIX 5

” STATISTICS”

TO THE MASTER THESIS “CHARACTERIZATION OF THE DOPED SILICON DIOXIDE AND ITS IMPLICATION FOR THE RESISTIVE SWITCHING PHENOMENA IN THE ELECTROCHEMICAL METALLIZATION CELLS”

1.1 The Exploratory Data Analysis (EDA)

The EDA is short for the exploratory data analysis, which is a way of doing the data analysis and the state of mind. The EDA highlights the importance of the visualization of data, includes the randomness, and is open to the alternative explanations of data (Hartwig & Dearing 1979).

The EDA bases on the principles of the openness and the skepticism. The openness means the freedom to make the data reexpression in order to find the unanticipated patterns. Moreover, the skepticism in the EDA means the skepticism toward the statistical summaries, which often rely on an assumption about the data, such as normality in the distributions or linearity of the relationships, for example. The openness and the skepticism principle in the EDA means the possibility of the alternative modeling, emphasizing the data visualization on the basis of the resistant statistics, which does not change when outliers are added (Hartwig & Dearing 1979).

Exploring the data helps to discover the unexpected patterns. The specific nonlinear relationship, for example, can only be found by looking at the data and discovering what type of relationship is there and then comparing it with the theoretical expectation. The alternative models and the explanations of the relationship between the variables should every time be considered (Hartwig & Dearing 1979).

The EDA has no restrictions on the procedures to be used. EDA’s objective is to find interesting indications in the data. Opposite to the EDA, the conventional methods of the mathematical statistics emphasize the sampling distributions, the models, and the hypothesis testing, which are rarely applicable to the real data. The EDA means learning from the data. However, there is no clear border between the statistics and EDA (Morgenthaler 2009).

In the EDA, the most fundamental concepts are $data = smooth + rough$. The data smooth is a simplified structure, the pattern or regularity in the data. The data smooth should be extracted from the data while the data would almost never match the smooth. The rough is the difference

between the measured data points and the smooth. First, the data is studied to discover the smooth, then from the data, models are generated, which then are compared to the theoretical model (Hartwig & Dearing 1979).

There are no differences in the EDA for the multivariate, the univariate, and the bivariate analysis. The underlying point in all three is to get to know your data. Data analysis should be a confrontation between theory and data (Hartwig & Dearing 1979). In the exploratory multivariate analysis, each variable should be linearized and implicitly understood, as well as the relationships between all pairs of the variables. In addition, the multivariate relationships should be based on the bivariate relations by the additional explanatory variables with the smooth and the successive rough. The causal implications should be drawn from the relationships between the parts of the roughs (Hartwig & Dearing 1979).

The re-expression is simply the use of a numeric scale of the measurement other than the one on which a variable was originally recorded, and this is accomplished by the transforming of the observed data points using some arithmetic function (Hartwig & Dearing 1979). First, the re-expression is an efficient way to handle the non-normal distributions. Also, the re-expression can linearize the scatter plots. However, the non-normality and the non-linearity often go hand in hand and, because of this, the re-expression is a useful response to both problems (Hartwig & Dearing 1979).

There are linear and nonlinear transformations of the data during the re-expression. After the linear transformation, a plot of the new values against the original ones will be a straight line. In contrast to a linear transformation, transforming a variable by logs, roots, power, and exponentials will change relative distances between data points, modifying the shape of the distributions. However, simple transformations are preferable to more complex ones (Hartwig & Dearing 1979).

If the data is positive, then re-expressing in the logarithmic scale can be useful. Other functions can be implemented for the re-expression such as the square, the square root, and the inverse values (Morgenthaler 2009).

During the transformation of the data, the numerical values, the relative distance between them, and the rank order of the value can change. The linear functions for the transformation are the simplest because they only affect the numerical values. In contrast, squaring a set of positive number will not only assign the different numerical values, but it will also change the relative distance between them (Hartwig & Dearing 1979).

The box plots are one of the most implemented methods of EDA. The data is defined by two extremes (E), the median (M), and two hinges (H). H-spread shows the batch variation. The whiskers start from the box and continue to the extremes (E). Whenever several batches of the

number are available, the box plots in parallel is very useful for the visualization of the information (Morgenthaler 2009).

1.2 Traditional statistics

General notes. The goal of scientific research is creating a new as well as reproducible knowledge through independent experiments (Vaux et al. 2012), which does not occur by chance or coincidence (Chow 2010). However, there is an important difference between the replicate and the independent repeat of the experiments. While the replicates are important for the quality controls, the testing of the statistic hypothesis should be done through the independent experiments (Vaux et al. 2012). If the results from one representative experiment are made, then n = 1 and statistics does not apply despite the large amount of replicates (Vaux 2013). Moreover, the difference between the treatments can be attributed to the specific parameter if and only if there is only one factor of the difference in the treatment. In addition, the alternative interpretations of a result should always be made (Vaux et al. 2012). Finally, the generalizations of the results can be made only about the population from which the samples were taken (Persaud 2010; Vaux et al. 2012).

ANOVA. The repeated measurements under the different treatment conditions can be, inter alia, plotted or analyzed using the univariate ANOVA (the analysis of the variance) designs, for example (Gurevitch & Chester 1986; Keselman et al. 2001; Oberfeld & Franke 2013; Westgate & Burchett 2017). Nevertheless, the violation of the assumptions on which ANOVA is based can mistakenly claim the positive treatment effect when it in fact does not exist (Type I error)(Keselman et al. 2001; Pole & Bondy 2010; Oberfeld & Franke 2013; Westgate & Burchett 2017). The ANOVA is sensitive to the violation of the equality of the group size (Keselman et al. 2001) , the normality assumption (Oberfeld & Franke 2013), the small size of data (Westgate & Burchett 2017) and the independency of the repeats (Pole & Bondy 2010; Ranstam 2012).

The conventional ANOVA statistics assume the equal group size. However, the real measured data not always complete and can be missing. Thus, the groups can be unequal for the different reasons. The dropout of the data can be random, unpredictable and independent of the individual characteristics or the treatments or predictable in some way and dependent from the parameters or the treatment (Keselman et al. 2001). Moreover, increasing the sample size does not guarantee the robustness and the low level of Type I error, when the data is non-normal and correlated (Oberfeld & Franke 2013). The requirement of the data independence is difficult to achieve in practice. Moreover, when the independent repeats and replicates are confused in analysis, the incorrect variability and the degree of freedom or required number of observations can be chosen (Ranstam 2012), with a consequence of a false positive result (Pole & Bondy 2010; Ranstam 2012).

Therefore, the specific type of data usually needs most appropriate and suitable statistic techniques for the analysis (Looney & Stanley 1989). Some others ANOVA-type statistics is more robust to

the violations of the assumptions (Keselman et al. 2001). The univariate ANOVA analysis assumes that the variables are independent whereas the multiple measurements are often correlated (Gurevitch & Chester 1986).

The testing of the statistical hypothesis usually requires the normal (or Gaussian) distribution (Miller & Miller 1988; Pole & Bondy 2010), the independence, and the common variance (Pole & Bondy 2010). The common variance implies that the samples have similar variability (Pole & Bondy 2010). However, the real data can be distributed non-normally and be skewed (or asymmetric), which would mean that the observed values do not have random variability, and it might be a result of the unidentified systematic influence (Pole & Bondy 2010). According to the Central Limit Theorem, sampling distribution for the mean values of the data, which is non-normally distributed, tends to normalize as n increases (Miller & Miller 1988). However, the increase in the size of the data increases the variability (Bland & Altman 1996).

The variability in the repeated experiments can be partly controlled by the randomization, the blocking, the replication, and the design of the experiments. The reproducibility of the average should not be confused with the response of the sample, which can be quite variable (Altman & Krzywinski 2015).

The careful design of the experiments can minimize both the systematic and the random errors during the experiments. The random error affects the repeatability or precision while the systematic error has a direct impact on the accuracy. The random error causes the random fluctuation in the measurement value around the mean value whereas the systematic error causes the fluctuation of the result around a central value in a particular pattern (Miller & Miller 1988).

The box plot. A box-and-whisker plot or simply the box plot can display the parallel groups of the data through their medians, means, quartiles, minimum and maximum, as well as the distribution and the symmetry of data. In the normally distributed data, the box is symmetric with the mean line located close to the median. For a non-normal distribution, the skewness can be detected from a box plot (Liu 2008). A distribution is skewed if one of its two tails is longer than the other. The median is more robust than the mean value in the presence of the outliers and if the distribution is skewed (Salkind 2010b). However, the length of the box plots, sometimes, can be interpreted erroneously due to the different length of the whiskers (Salkind 2010a). Also, the area of the box is frequently misinterpreted as the frequency or proportion of the observations. However, it is the density or the relative spread of the data within each interval (Lem et al. 2014). The variability can be easily identified by looking at the length of the box in the box plot. The longer boxes illustrate the greater variability around the median (Salkind 2010a).

Choice of suitable statistic methods for data analysis. The choice of suitable statistic method depends on quality and type of available data and also on purposes of research. Moreover, when

the statistical analysis needs to be performed, it should be taken into account at very early stage of research planning. The limitations can be financial or related to the availability and cost of used devices and materials. The statistical analysis needs to have enough amount of replications and repeats appropriate to the specific type of statistical analysis.

In our cases, not all materials were available for testing and the non-equivalent amount and asymmetric data was created. Also, the first analysis reveals, that obtained data was asymmetric, skewed and non-normally distributed. In addition, the variability and scattering of data was extremely high numerically and physically, if one has a look at different curves. Also, despite the significant efforts (time and experimental trials), a lot of data was simply missing, because the sputtering device continuously stops to work due to overheating. The request to decrease the number of repeats (related to different parameters) and increase the number of replications was declined. Moreover, generated data was large, however, not enough to perform the classical type of statistical analysis.

Therefore, another statistical and graphical method such as EDA was chosen in order to perform the statistical analysis. EDA method as exploratory data analysis is more convenient to the first analysis of unstable, distorted and non-normally distributed data. If the data is normally distributed at least in some part, then classical methods can be used. Anyways, EDA together with suitable graphical software like MATLAB is a very powerful tool to reveal the unexpected pattern. It can be used alone or even together with classical methods.

REFERENCES

Altman, N. & Krzywinski, M. (2015). Points of significance: Sources of variation, Nature methods, Vol. 12(1), pp. 5-6.

Bland, J.M. & Altman, D.G. (1996). Measurement error, BMJ (Clinical research ed.), Vol. 313(7059), pp. 744.

Chow, S.L. (2010). Replication.

Gurevitch, J. & Chester, S. (1986). Analysis of repeated measures experiments, Ecology, Vol. 67(1), pp. 251-255.

Hartwig, F. & Dearing, B.E. (1979). Exploratory data analysis, Sage.

Keselman, H., Algina, J. & Kowalchuk, R.K. (2001). The analysis of repeated measures designs: a review, British Journal of Mathematical and Statistical Psychology, Vol. 54(1), pp. 1-20.

Lem, S., Onghena, P., Verschaffel, L. & Van Dooren, W. (2014). Experts' misinterpretation of box plots–A dual processing approach, Psychologica Belgica, Vol. 54(4).

Liu, Y. (2008). Box plots: use and interpretation, Transfusion, Vol. 48(11), pp. 2279-2280.

Looney, S.W. & Stanley, W.B. (1989). Exploratory repeated measures analysis for two or more groups: review and update, The American Statistician, Vol. 43(4), pp. 220-225.

Miller, J.C. & Miller, J.N. (1988). Basic statistical methods for analytical chemistry. Part I. Statistics of repeated measurements. A review, Analyst, Vol. 113(9), pp. 1351-1356.

Morgenthaler, S. (2009). Exploratory data analysis, Wiley Interdisciplinary Reviews: Computational Statistics, Vol. 1(1), pp. 33-44.

Oberfeld, D. & Franke, T. (2013). Evaluating the robustness of repeated measures analyses: The case of small sample sizes and nonnormal data, Behavior Research Methods, Vol. 45(3), pp. 792-812.

Persaud, N. (2010). Random Selection,.

Pole, J.D. & Bondy, S.J. (2010). Normality Assumption.

Ranstam, J. (2012). Repeated measurements, bilateral observation and pseudoreplicates, why does it matter? Repeated measurements, bilateral observations and pseudoreplicates, why does it matter?

Salkind, N. (2010a). Box-and-Whisker Plot.

Salkind, N. (2010b). Median.

Vaux, D.L. (2013). Know when your numbers are significant, Know when your numbers are significant,.

Vaux, D.L., Fidler, F. & Cumming, G. (2012). Replicates and repeats--what is the difference and is it significant? A brief discussion of statistics and experimental design, EMBO reports, Vol. 13(4), pp. 291-296.

Westgate, P.M. & Burchett, W.W. (2017). On the analysis of very small samples of Gaussian repeated measurements: an alternative approach, Statistics in medicine, Vol. 36(6), pp. 958-970.

APPENDIX 6

” *THE ELECTROFORMING*”

TO THE MASTER THESIS “CHARACTERIZATION OF THE DOPED SILICON DIOXIDE AND ITS IMPLICATION FOR THE RESISTIVE SWITCHING PHENOMENA IN THE ELECTROCHEMICAL METALLIZATION CELLS”

LIST OF FIGURES

Figure 1. The electroforming voltage of the ECM cells deposited using all three targets on the platinum substrate at 100C: 100µmx100µm........ 2
Figure 2. The electroforming voltage of the ECM cells deposited using all three targets on the platinum substrate at 100C: 50µmx50µm........ 2
Figure 3. The electroforming voltage of the sample deposited using the TD1 target on the TiN substrate at 100C at the different thicknesses. 3
Figure 4. The electroforming voltage of the samples deposited using the target TD1 on the platinum substrate at RT and 100C. 3
Figure 5. The electroforming voltage of the samples deposited on the TiN substrate arranged according to the thickness of SiO2......... 4
Figure 6. The distribution of the electroforming data of the 20 nm- and 50nm- thick samples deposited on the TiN substrate........ 4
Figure 7. The distribution of the electroforming voltage for the 100µm x100µm memory cells deposited using the TD2 target on the platinum substrate arranged according to the thickness of the layer........ 5
Figure 8. The distribution of the electroforming voltage for the 50µm x50µm memory cells deposited using the TD2 target on the platinum substrate arranged according to the thickness of the layer........ 5
Figure 9.The electroforming voltage of the samples deposited using the TD0 target on the platinum substrate......... 6
Figure 10. The electroforming voltage of the samples deposited using the TD1 target on the TiN substrate........ 6
Figure 11. The electroforming voltage of the samples deposited using the TD1 target on the platinum substrate........ 7
Figure 12. The electroforming voltage of the samples deposited using the TD2 target on platinum substrate........ 7

Figure 1 displays the box plots comprising the electroforming data of the memory cells with the size of 100µmx100µm deposited using the different targets on the platinum substrate.

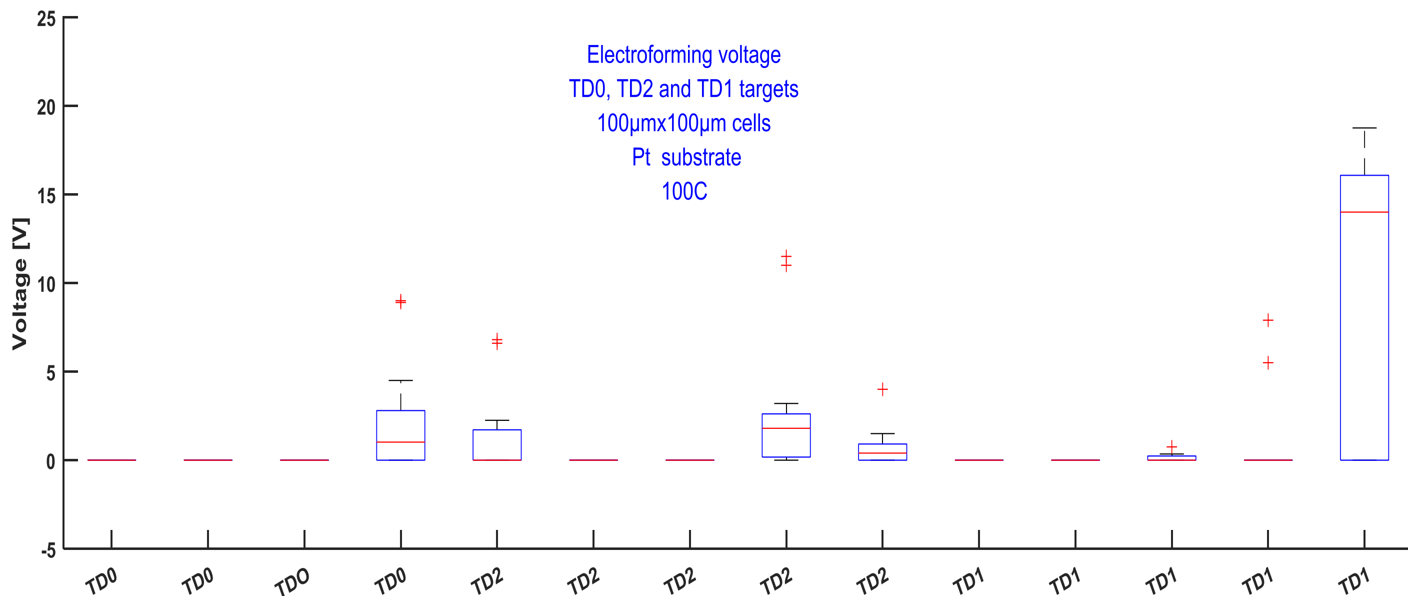

Figure 1. *The electroforming voltage of the ECM cells deposited using all three targets on the platinum substrate at 100C: 100µmx100µm*

Figure 2 shows the electroforming data for the memory cells with the size of 50µmx50µm deposited using the different targets on the platinum substrate.

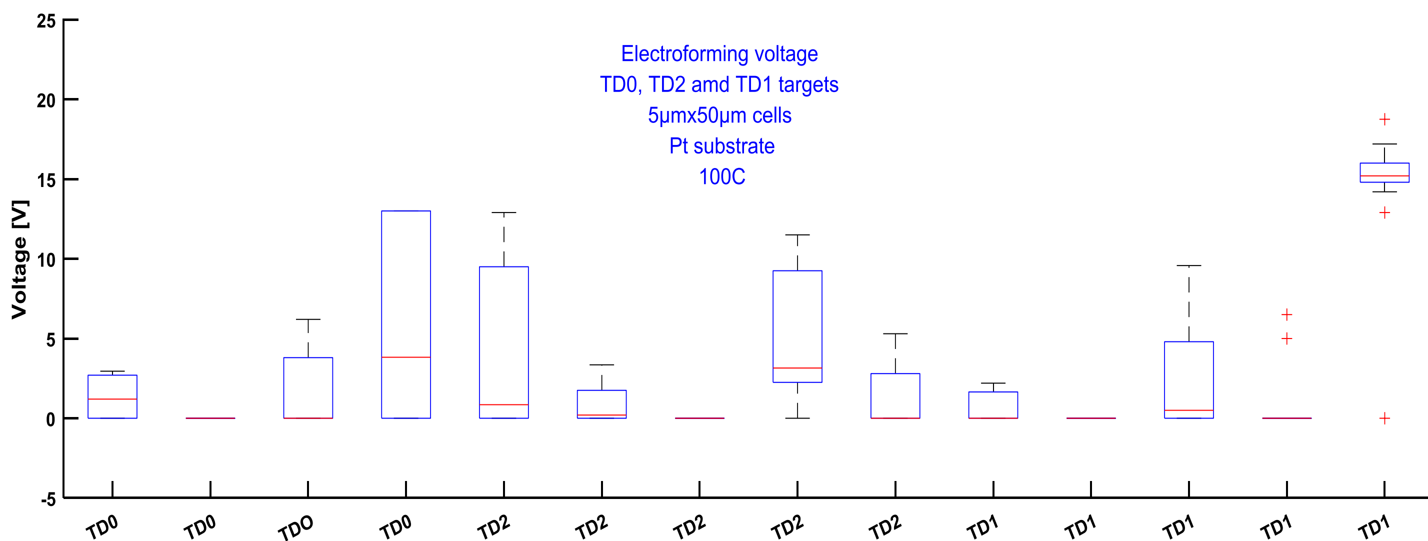

Figure 2. *The electroforming voltage of the ECM cells deposited using all three targets on the platinum substrate at 100C: 50µmx50µm*

Figure 3 and Figure 4 show the electroforming data of the memory cells with 100µmx100µm and 50µmx50µm sizes for the samples deposited on the TiN substrate.

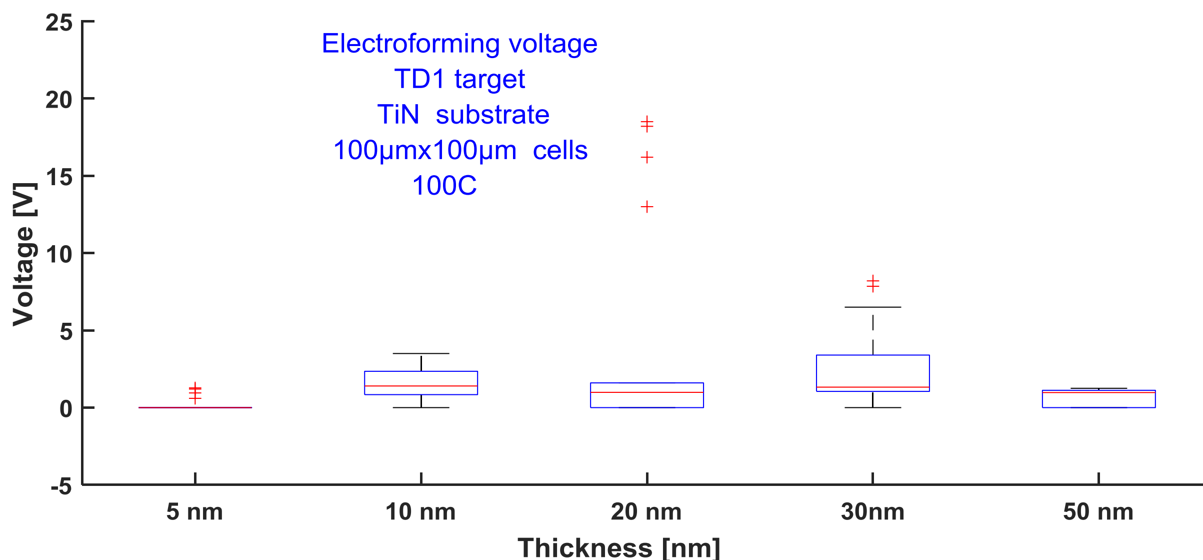

Figure 3. The *electroforming voltage of the sample deposited using the TD1 target on the TiN substrate at 100C at the different thicknesses.*

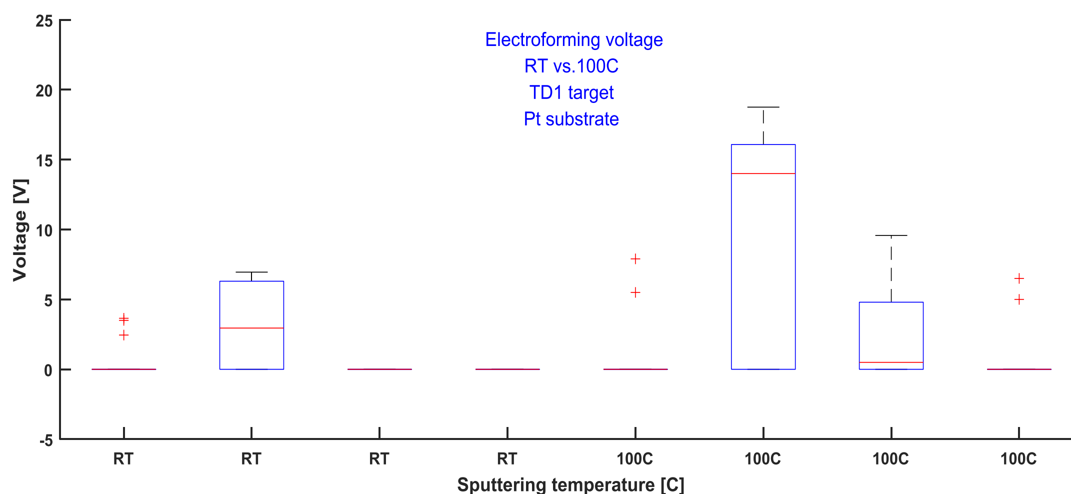

Figure 4. *The electroforming voltage of the samples deposited using the target TD1 on the platinum substrate at RT and 100C.*

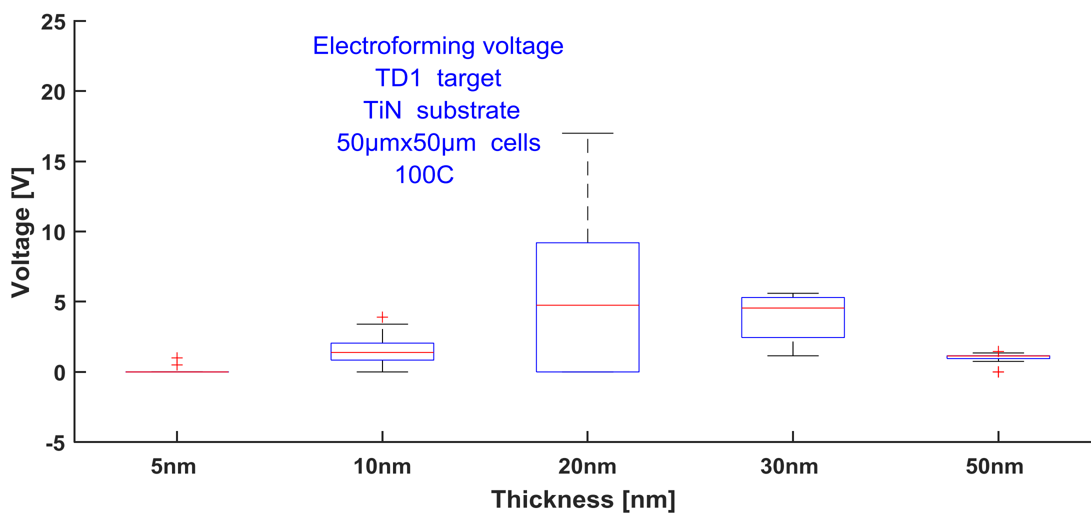

Figure 5. *The electroforming voltage of the samples deposited on the TiN substrate arranged according to the thickness of SiO2.*

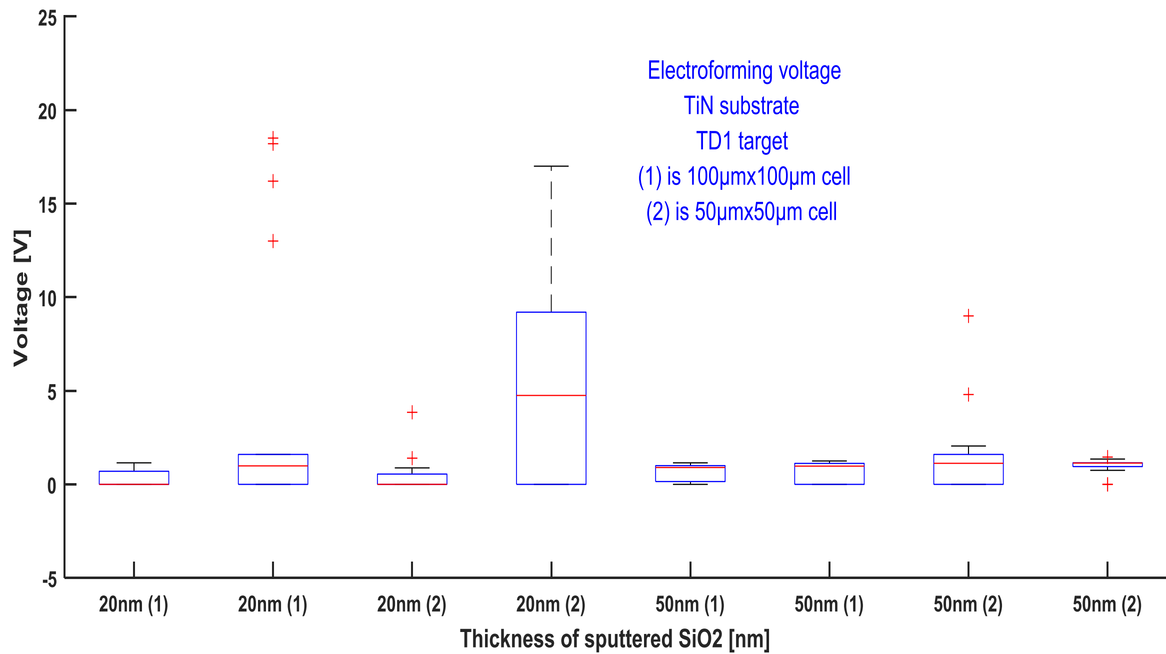

Figure 6. *The distribution of the electroforming data of the 20 nm- and 50nm- thick samples deposited on the TiN substrate*

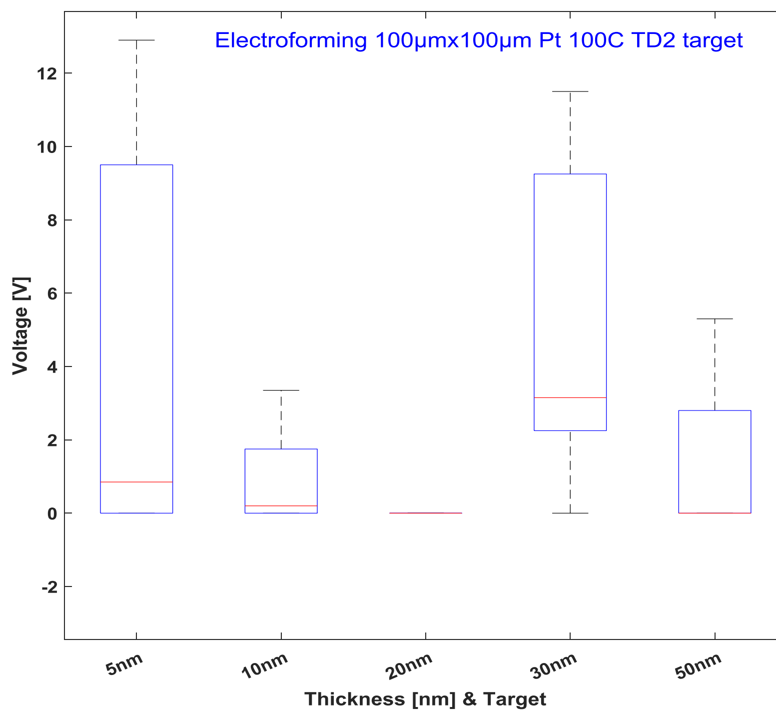

Figure 7. *The distribution of the electroforming voltage for the 100µm x100µm memory cells deposited using the TD2 target on the platinum substrate arranged according to the thickness of the layer*

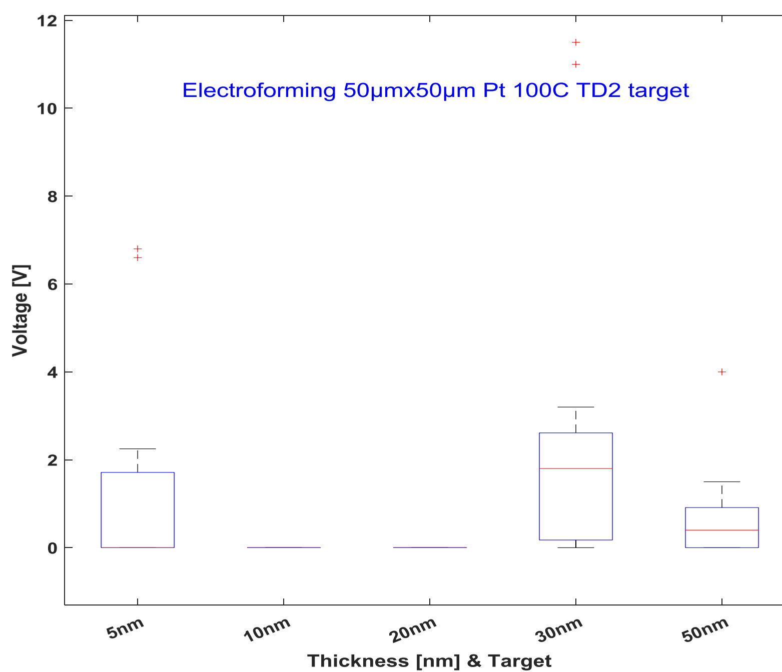

Figure 8. *The distribution of the electroforming voltage for the 50µm x50µm memory cells deposited using the TD2 target on the platinum substrate arranged according to the thickness of the layer*

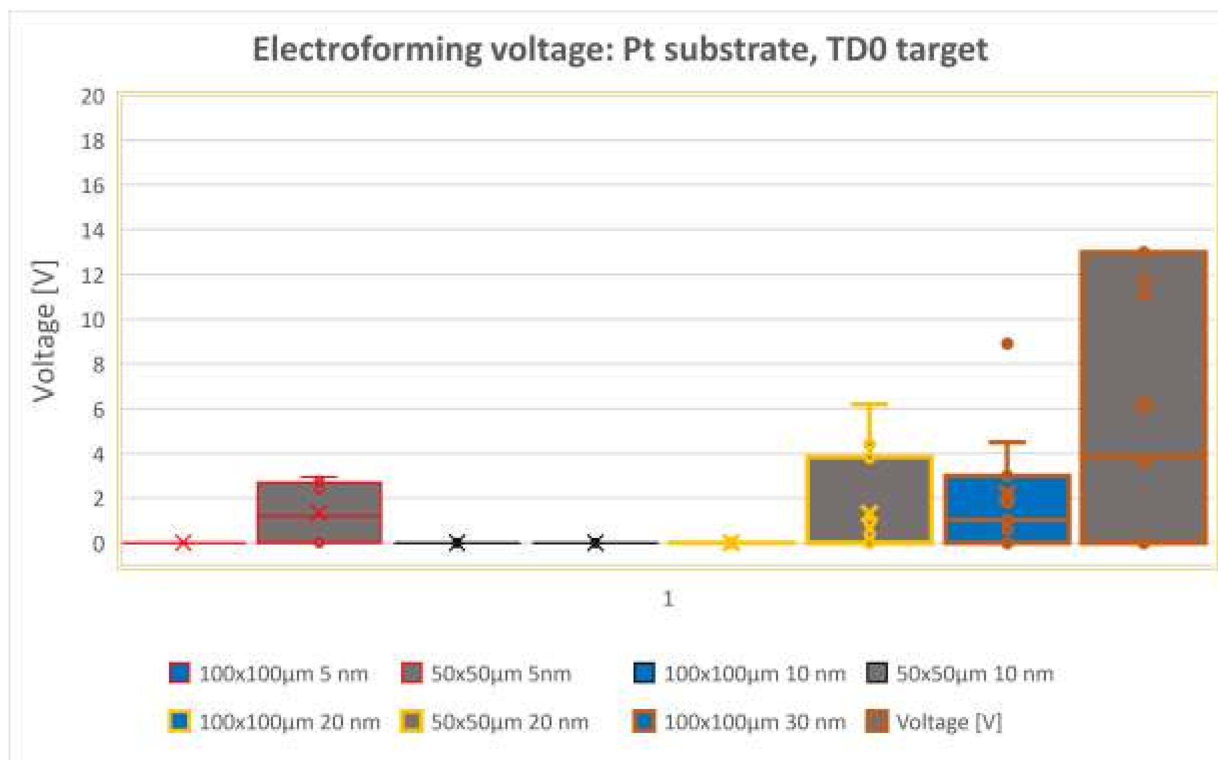

Figure 9*.The electroforming voltage of the samples deposited using the TD0 target on the platinum substrate.*

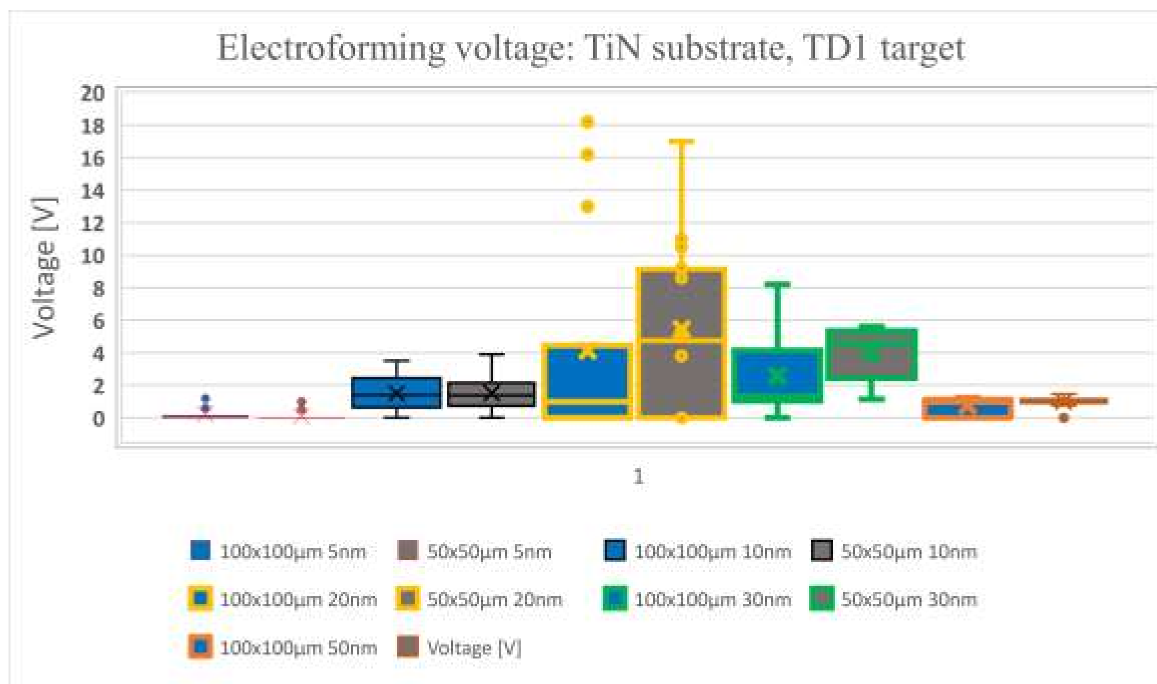

Figure 10. *The electroforming voltage of the samples deposited using the TD1 target on the TiN substrate*

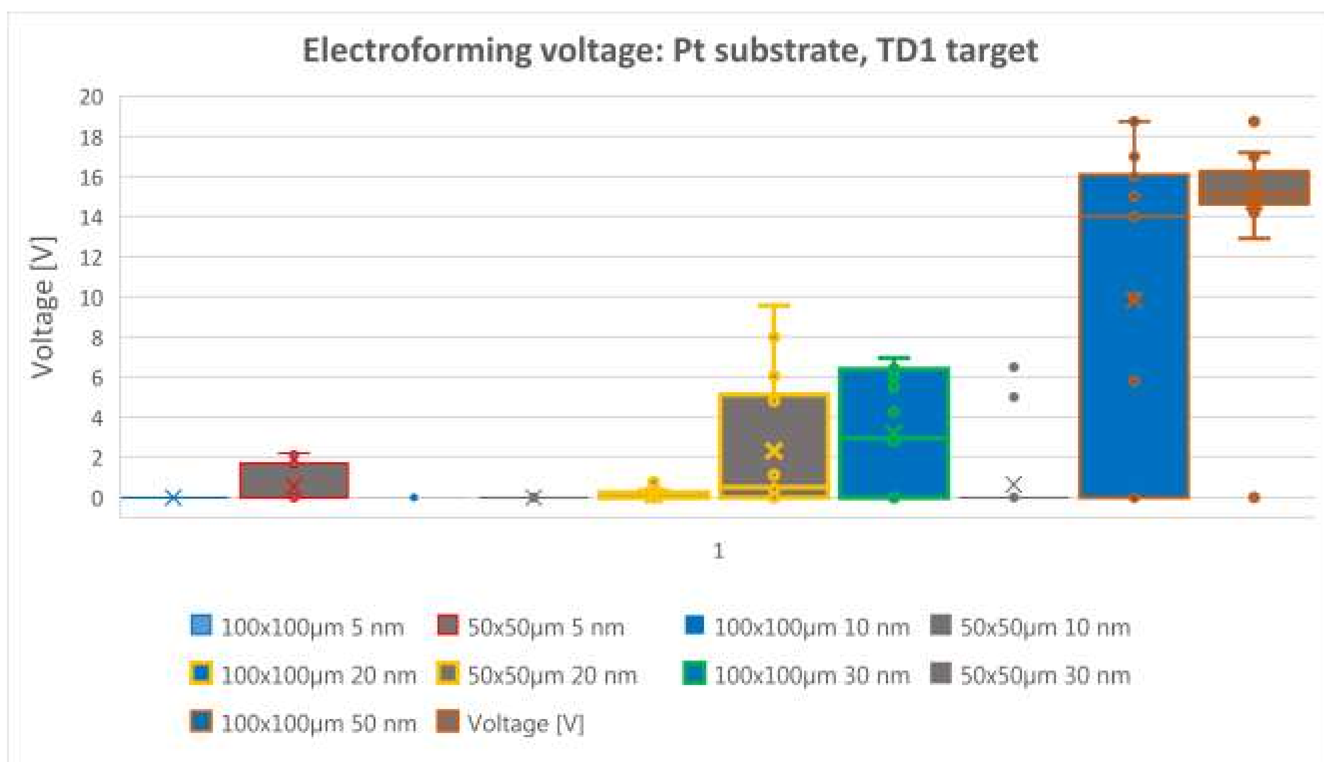

Figure 11. *The electroforming voltage of the samples deposited using the TD1 target on the platinum substrate*

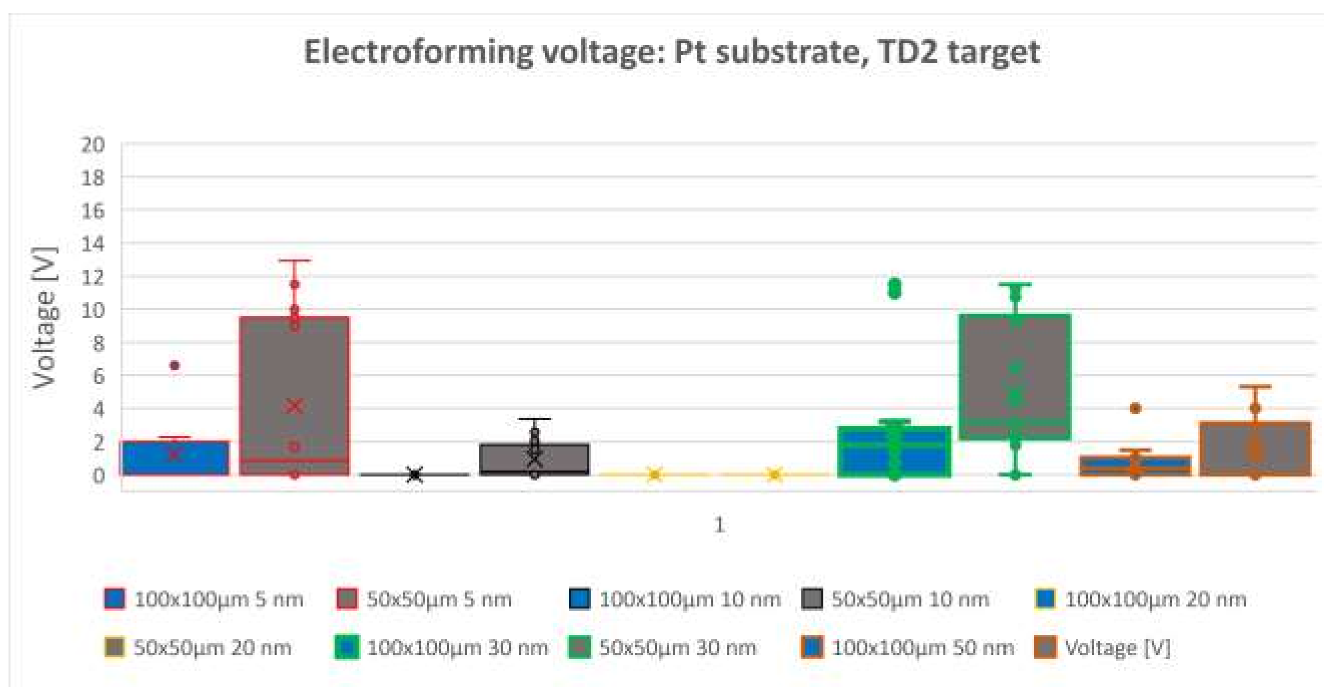

Figure 12. *The electroforming voltage of the samples deposited using the TD2 target on platinum substrate*

Interpretation of results. In Appendix 6, Figures 1-12 represent the obtained data using median with corresponding box plots. In Section 3.2.1 of Master thesis, the same data was represented using mean and standard deviation.

The overall impression is that there is no consistent trend in electroforming data due to different mean or median as a result of certain treatment. However, few indirect trends can be noticed.

First, data is non-normally distributed and skewed with very large statistical variability, which can be seen from different sizes of box plots. Non-normally distributed data with non-equivalent size of standard deviation makes the testing of statistical hypothesis near impossible. Therefore, an alternative approach using the Exploratory Data Analysis instead of classic ANOVA was implemented.

Second, there is a lot of missing electroforming data associated with samples deposited on Pt substrate in comparison to TiN substrate. Also, the electroforming voltage of samples deposited on Pt substrate was higher than for samples deposited on TiN substrate.

Third, of course, the observed trend can be related to the non-equivalent sizes of data for samples deposited on Pt and TiN substrates. However, the different behavior of samples deposited on different substrates can be associated with different nanostructure, roughness, morphology, porosity, and conductivity of deposited layers, as it can be seen from XRR analysis in Appendix 4.

Fourth, the inequality of data size for different substrates as well as a non-random choice of parameters with correspondent missing data makes the statistical comparison difficult due to a large amount of possible parameters which could affect the result.

Fifth, addition of doping element 1 deposited using the TD1 target seems to introduce the instability to the conductive filament, which can be seen from Figure 13 and Figure 14 in Section 3.2.1 of Master thesis. Eliminating of an electroforming stage, as a result of layer doping, could not be tested due to a large amount of missing data. Here, missing data means that the ECM cells were very conductive immediately after application of positive bias. This result suggests that adding of doping element in the used concentration increases the conductivity of a switching layer, however, in a larger extent than it is necessary. As a result, the resistive state or the OFF state degenerates, which causes the increase in amount of missing data.

Sixth, to avoid the instability of conductive filaments shown in Figure 13 and Figure 14 in Section 3.2.1 of Master thesis electroforming and switching voltage was increased. Increasing voltage is supposed to strengthen the conductive filament. However, this causes the corresponding increase in a mean value of electroforming voltage. Also, the severely electroformed ECM cell cannot switch further as a result of a very thick conductive filament. Therefore, useful settings for electroforming and switching of ECM cell are very narrow. Very low voltage creates a weak filament causing instability in current-voltage characteristics. Very high electroforming or switching voltage generates a very strong filament, which can prevent further switching of ECM cell.

APPENDIX 7

” *THE CURRENT-VOLTAGE CHARACTERISTICS FOR THE TD0, TD2 AND TD2 TARGETS***”**

TO THE MASTER THESIS “CHARACTERIZATION OF THE DOPED SILICON DIOXIDE AND ITS IMPLICATION FOR THE RESISTIVE SWITCHING PHENOMENA IN THE ELECTROCHEMICAL METALLIZATION CELLS”

LIST OF FIGURES

Figure 1. The current- voltage curve corresponding to the 10-nm-thick sample deposited using the TD0 target on the platinum substrate at 100C and biased with the current compliance of 1mA and the asymmetric voltage bias +1V/-0.5V. 4
Figure 2. The current- voltage curve corresponding to the 30-nm-thick sample deposited using the TD0 target on the platinum substrate at 100C and biased with the current compliance of $2.5 \cdot 10^{-4}$A. 5
Figure 3. The current- voltage characteristics of the 10-nm-thick sample deposited using the TD0 target on the platinum substrate at 100C and biased with the current compliance 5mA 6
Figure 4. The current- voltage characteristics of the 10-nm-thick sample deposited using the TD0 target on the platinum substrate at 100C and biased with the current compliance 1µA and the voltage of +0.6V/-1V. 7
Figure 5. The I- V curve corresponding to the 30-nm-thick sample deposited using the TD1 target on the TiN substrate at 100C biased with the symmetric current compliance of 10^{-5}A at the voltage 2V/-0.5V. 8
Figure 6. The current- voltage characteristics of the 30-nm-thick sample deposited using the TD1 target on the TiN substrate at 100C and biased with the positive current compliance of 10^{-5}A and the negative compliance of $1.2 \cdot 10^{-4}$A at voltage of +1.4V/-0.6V 9
Figure 7. The current- voltage characteristics of the 30-nm-thick sample deposited using the TD1 target on the TiN substrate at 150C and biased with the current compliance of 10^{-6}A and with the voltage of +4V/-5V. 10
Figure 8. The current- voltage characteristics of the 30-nm-thick sample deposited using the TD1 target on the TiN substrate at 150C and biased with the current compliance of 10^{-6}A and with the voltage of +4V/-5V. 11

Figure 9. The current- voltage characteristics of the 30-nm-thick sample deposited using the TD1 target on the TiN substrate at 150C and biased with the current compliance of 10^{-6}A and with the voltage of +4V/-5V. *12*
Figure 10. The current- voltage characteristics of the 30-nm-thick sample deposited using the TD1 target on the TiN substrate at 100C and biased with the positive current compliance of $1.1\cdot10^{-5}$A and the negative compliance of $1.1\cdot10^{-5}$A at the voltage of +2/-1V. *13*
Figure 11. The current-voltage characteristics of the 30-nm-thick sample deposited using the TD1 target on the TiN substrate at 100C and biased with the positive current compliance of $3\cdot10^{-4}$A and the negative compliance of $2\cdot10^{-4}$A at the voltage of +0.5V/-1V *13*
Figure 12. The current- voltage characteristics of the 50-nm-thick sample deposited using the TD1 target on the TiN substrate at 100C and biased with the positive current compliance of 10^{-4}A and the negative compliance of $1.1\cdot10^{-4}$A at a voltage of +1/-1V. *14*
Figure 13. The current- voltage characteristics of the 30-nm-thick sample deposited using the TD1 target on the TiN substrate at 100C and biased with the positive current compliance of $3\cdot10^{-4}$A and the negative compliance of $1.5\cdot10^{-4}$A at the voltage of +1.4V/-0.4V *15*
Figure 14. The current- voltage characteristics of the 30-nm-thick sample deposited using the TD1 target on the TiN substrate at 100C and biased with the positive current compliance of $3\cdot10^{-4}$A and the negative compliance of $1.5\cdot10^{-4}$A at the voltage of +1V/-0.4V *15*
Figure 15. The current-voltage characteristics of the 50-nm-thick sample deposited using the TD2 target on the Pt substrate at 100C and biased with the positive and the negative current compliance of 10^{-6}A at the voltage of +2/-5V. *16*
Figure 16. The current-voltage characteristics of the 5-nm-thick sample deposited using the TD2 target on the platinum substrate at 100C and biased with the positive current compliance of $3\cdot10^{-6}$A and the negative compliance of $6\cdot10^{-6}$A at the voltage of +0.5/-0.5V. *17*
Figure 17. The current- voltage characteristics of the 50-nm-thick sample deposited using the TD2 target on the Pt substrate at 100C and biased with the positive and the negative current compliance of 10^{-6}A at the voltage of +5V/-5V. *18*
Figure 18. The current- voltage characteristics of the 5-nm-thick sample deposited using the TD2 target on the platinum substrate at 100C and biased with the positive and negative current compliance of 10^{-5}A at the voltage of +0.5/-0.5V. *18*
Figure 19. The current-voltage characteristics of the 30-nm-thick sample deposited using the TD2 target on the TiN substrate at 100C and biased with the positive and the negative current compliance of 10^{-6}A at the voltage of+1V/-5V. *19*
Figure 20. The current -voltage characteristics of the 30-nm-thick sample deposited using the TD2 target on the TiN substrate at 100C and biased with the positive and the negative current compliance of 10^{-6}A at the voltage of +2/-5V. *20*
Figure 21. The current-voltage characteristics of the 30-nm-thick sample deposited using the TD2 target on the TiN substrate at 100C and biased with the positive and the negative current compliance of 10^{-6}A at the voltage of +2/-5V. *20*

1. I-V CHARACTERISTICS

1.1 The undoped TD0 target

Figure 1 shows the I-V curve corresponding to the 10-nm-thick sample deposited using the TD0 target on the platinum substrate at 100C. The sample was biased with the current compliance of 1mA asymmetrically with a voltage of +1V/-0.5V. At the negative bias, the behavior of the memory cell in Figure 1 is different, because the dissolution curve is the straight vertical line with a slight slope not until zero but approximately until 0.3mA and 0.2V. Therefore, the filament dissolves partly after the applying negative bias. After that, the current drops continuously with the increasing voltage until 0.1mA and 0.5V. Even after that then the filament stays ohmically conductive until zero, however with a different slope.

The change of the slope of the straight line can indicate that the resistance is changed due to the change of the filament's geometric parameters. This relates to the first and last stage of the current-voltage curve on the negative side, denoted by blue arrows in Figure 1. These regions exhibit clearly ohmic conductive behavior. The first region denoted by bold blue arrows exhibits positive differential resistance when the current and voltage grow ($\Delta i > 0$ and $\Delta v > 0$). The second region denoted with normal blue arrow exhibits positive differential resistance when both current and voltage drops ($\Delta i < 0\ and\ \Delta v < 0$).

Between these ohmic regions, there is a transition region with two distinct behavior and different slopes. It can be seen that the filament does not dissolve directly but through the different steps as denoted with green and yellow arrows. In addition, the fact that part of the curve (yellow arrow) is not smooth can indicate the surface oxidation of the metallic filament, for example.

In addition, both regions denoted by green and yellow arrows can be also the indication of negative differential resistance, when the current drops ($\Delta i < 0$) while the voltage grows ($\Delta v > 0$) at negative bias between -0,1V and -0.5V.

The presence of regions exhibiting the negative differential resistance, as well as dissolution of the conductive filament through different steps, contradict with a classical explanation of dissolution of the metallic filament directly after applying negative bias. These different steps can also indicate that solid- state device (ECM) undergoes the chemical reaction at negative bias. Such a chemical reaction can be the oxidation of the metallic filament after partial dissolution. This is consistent with the small current at higher voltage bias in the region denoted with a normal blue arrow in Figure 1.

This, in turn, contradicts to a memristic explanation of ECM cells as a passive electronic device. In this case, the memory cell should be defined as an active device if the device undergoes the chemical reaction during switching according to the definition proposed by Prof. Leon Chua.

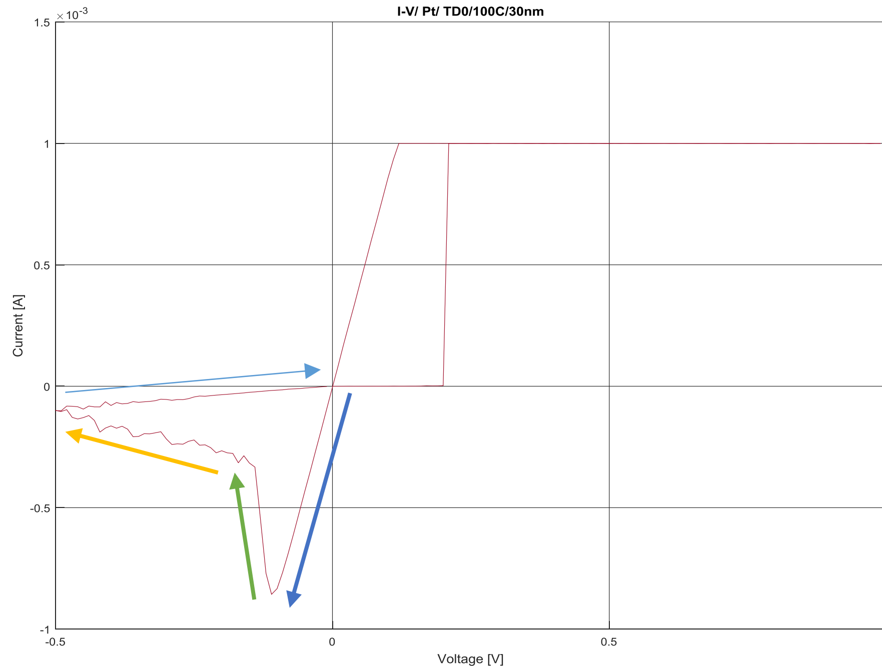

Figure 1. *The current-voltage curve corresponding to the 10-nm-thick sample deposited using the TD0 target on the platinum substrate at 100C and biased with the current compliance of 1mA and the asymmetric voltage bias +1V/-0.5V.*

Figure 2 displays the example of the current- voltage curve corresponding to the 30-nm-thick sample deposited using the TD0 target on the platinum substrate at 100C and biased with the current compliance of $2.5\cdot10^{-4}$A and the asymmetric voltage +1V/-0.5V. However, the curve has vague shape without the horizontal line of the current compliance. At the positive bias, the cell is OFF until 0.2V. Such type of curves can often be observed in the VCM memory cells, where the conduction is usually attributed to the oxygen vacancies.

On a linear scale, this vague curve in Figure 2 is obviously non-ohmic, because it is not a straight line at this scale. In this particular ECM cell and with these biasing parameters, such a behavior may indicate that a conductive path is not metallic. This contradicts with the classical explanation that ECM cell can conduct only due to the creation and dissolution of the metallic filament.

In addition, the curve does not follow the limitation of current compliance. The cell starts to conduct after approximately +0.2V. During the backward sweep between +1V and +0.75V, the

curve has a region with possibly negative differential resistance when the current grows ($\Delta i > 0$) and voltage drops ($\Delta v < 0$).

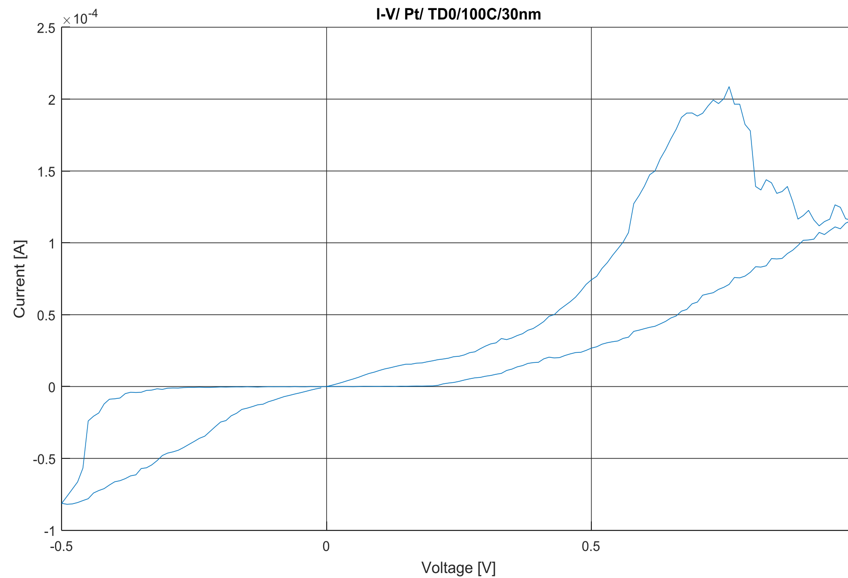

Figure 2. *The current- voltage curve corresponding to the 30-nm-thick sample deposited using the TD0 target on the platinum substrate at 100C and biased with the current compliance of* $2.5{\cdot}10^{-4}$*A.*

Figure 3 displays the current-voltage curve corresponding to the 10-nm-thick sample deposited using the TD0 target on the platinum substrate at 100C and biased with the current compliance of 5mA and the voltage bias of +0.5V/-0.5V. However, the cell does not follow the limitation of the current compliance, because the corresponding horizontal line is missing. The cell is in the ON state immediately after the applying of the positive bias. The curve is mostly ohmic, however with the hysteresis consisting of the straight lines of the different slopes, which indicates the change of the resistance due to the changing of the geometric parameters of the filament.

In Figure 3, there is a non-ohmic conduction region between +0.4V and +0.5V. In addition, there is a region where the current grows at almost constant +0.4V and where the current exhibit saturating non-linear growth between +0.4V and 0.45V. Between +0.45V and +0.48V, the curve can be approximated as a straight line again. At +0.48V, the current start to grow whereas the voltage stays almost constant. Therefore, it can be stated that ECM cell shows a quite complex conductive behavior and undergoes the transition between different resistive states. This may refer to a chemical reaction like the oxidation of the metallic filament, which can explain the existence of negative differential resistance together with regions, where the current is almost independent of the voltage.

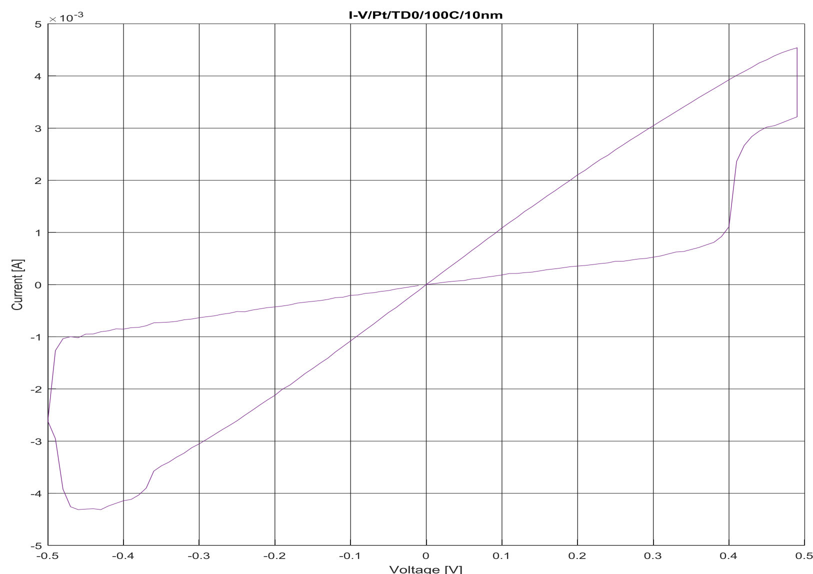

Figure 3. *The current-voltage characteristics of the 10-nm-thick sample deposited using the TD0 target on the platinum substrate at 100C and biased with the current compliance 5mA*

Figure 4 displays the current-voltage curve corresponding to the 10-nm-thick specimen deposited using the TD0 target on the platinum substrate at 100C and biased with the current compliance 1μA and voltage of +0.6V/-1V. The curve is unstable near the zero voltage and the current implying that the electrodes are disconnected near zero. Then, the memory cells are electroformed at the negative bias creating the metallic filament again. Such a switching type may be de defined as unipolar, however without the applying of the large current or voltage.

The instability of the metallic filament shown in Figure 4 can indicate the presence of the mechanical stress alone or together with the electric stress associated with a change of bias polarity. Such a mechanical stress may be tensile in a very fine metallic filament. The presence of mechanical stress is supported by the fact, that the filament is unstable near the zero point at a low electric field. In addition, the tensile strength of thin metallic filament may explain the abrupt transition to OFF state at approximately +0.05V.

Moreover, the fact, that the ECM cell can create the conductive filament again after applying negative bias contradict the classical explanation of ECM, which may undergo only the electrochemical dissolution of the metallic filament after applying the negative voltage. However, it worth noting that the shape of the curve depends on using current and voltage. Here, the metallic filament created using the voltage bias of +0.6V was very weak and unstable, because the cell was OFF at +0.05V without applying the negative bias. Using a negative bias of -1V is explained by the fact that this was only one of continuously random series testing trials devoted to finding the conditions where the conductive filament would be stable at least directly after the applying of

negative bias. An additional requirement was that the created filament should not be, however, very strong, in order to avoid the short-circuiting of ECM cell.

In addition, even applied bias is slightly asymmetric on the negative side +0.6V/-1V, the actual current-voltage curve was near symmetric +0.6V/-0.6V. Therefore, the asymmetry, existing in ECM cell may be overcome by slight over-biasing on the negative side. In this particular case, using a small negative bias causes the ECM cell to stack in the OFF state at a negative bias, because the cell was already OFF on the negative side.

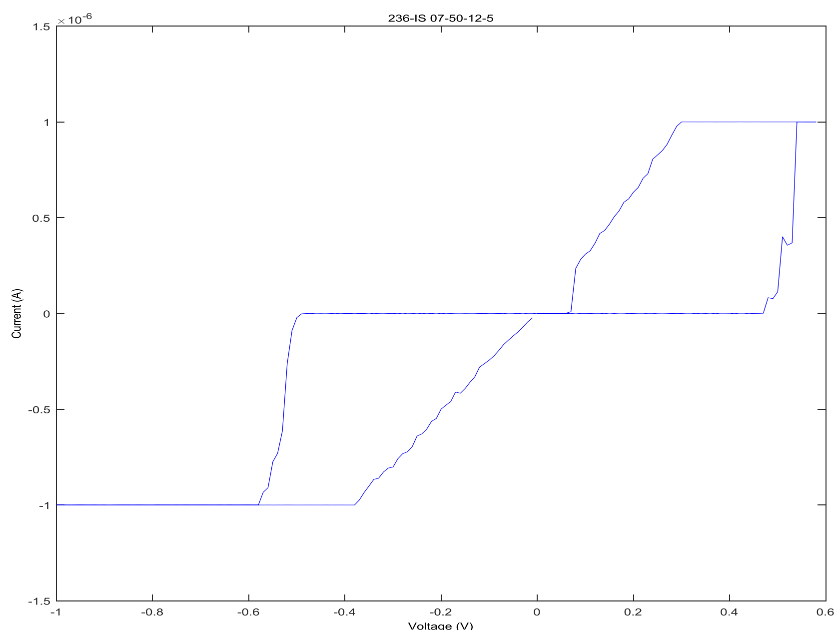

Figure 4. *The current- voltage characteristics of the 10-nm-thick sample deposited using the TD0 target on the platinum substrate at 100C and biased with the current compliance 1µA and the voltage of +0.6V/-1V.*

1.2 The TD1 target doped with one doping element

Figure 5 shows the memory cell from the same sample biased with the symmetric current compliance of $10^{-5}A$ at the asymmetric voltage bias of 2V/-0.5V. The current on the negative side does not follow the limiting current compliance because the horizontal line is missing. Once more, the filament is supposedly dissolved immediately after the changing of the polarity at -0.05V, and then, the cell continues to conduct, however, non-ohmically with negligible hysteresis between -0.05V and -0.5V, because the curve is not a straight line on a linear scale. This non-linear region can be explained by the oxidation of the rest of metallic filament, which was not completely dissolved between -0.05V and -0.5V.

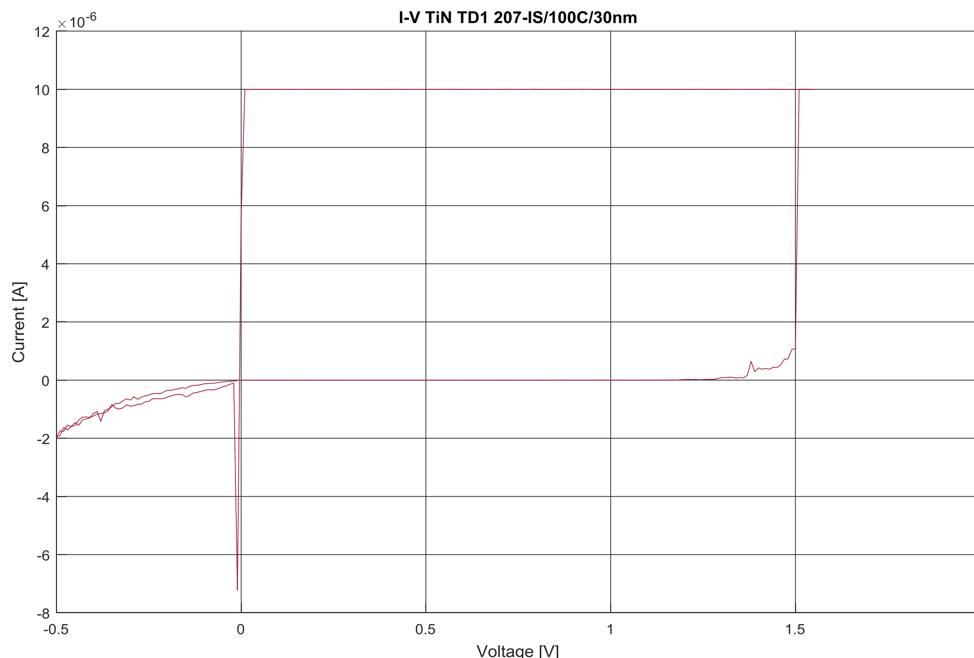

Figure 5. *The I- V curve corresponding to the 30-nm-thick sample deposited using the TD1 target on the TiN substrate at 100C biased with the symmetric current compliance of $10^{-5}A$ at the voltage 2V/-0.5V.*

Figure 6 displays the current-voltage curve corresponding to the 30-nm-thick sample deposited using the TD1 target on the TiN substrate at 100C and biased with the positive current compliance of $10^{-5}A$ and the negative compliance of $10^{-4}A$ at voltage +1.4V/-0.6V. The cell conducts ohmically on the negative side between 0V and -0.005V. Between -0.005V and -0.065V, the cell exhibits the small region of negative differential resistance, where current drops while the voltage growth. Between -0.065V and -0.085V the cell conducts ohmically again because the curve becomes a straight line. At approximately -0.1V, there is a small region, where the current is near independent of voltage. After that, the cell undergoes many gradual sub-steps between -0.1V and -0.39V. This behavior may indicate a changing the ohmic resistance as a result of the change in the geometric parameters such as the area of the filament, for example.

Then, the cell in Figure 6 makes the abrupt transition between -0.39V to -0.5V to the more resistive state and start to conduct completely non-ohmically with the completely curved line until zero. Such a type of the curve at negative bias can be also observed in TiO2-type of the cell, which is, however, the VCM type of cell. Such behavior can correspond to the possible oxidation of the metallic filament. After oxidation, the conductive part starts to conduct in a semiconductive way, implying that the conductivity with the corresponding number of the charge carriers decreases with the decreasing of the voltage. Such a behavior implies that the current and voltage are exponentially dependent on each other.

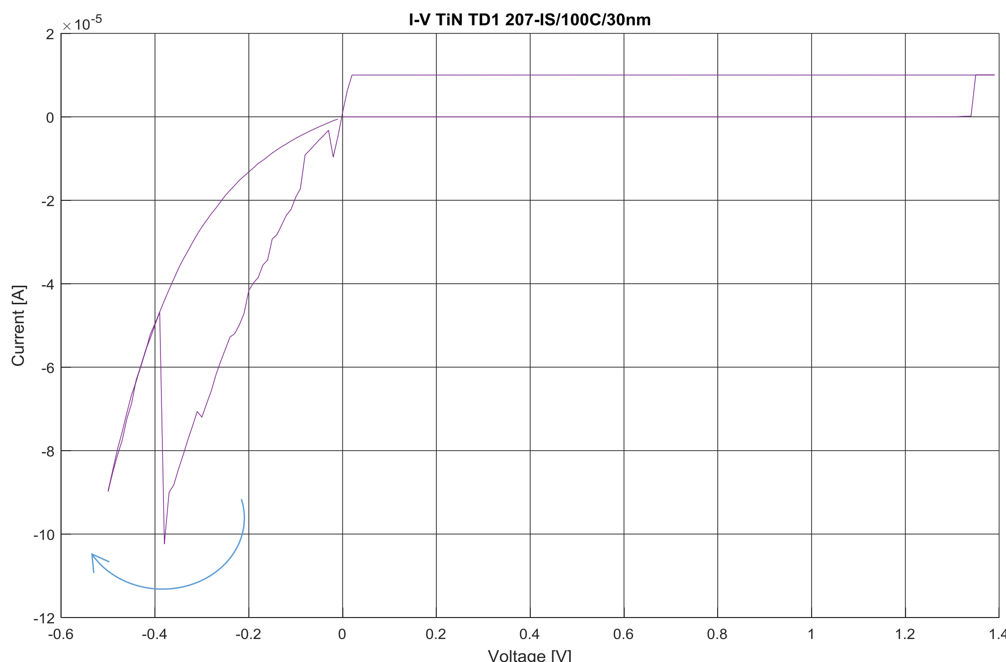

Figure 6. *The current- voltage characteristics of the 30-nm-thick sample deposited using the TD1 target on the TiN substrate at 100C and biased with the positive current compliance of 10^{-5}A and the negative compliance of $1.2 \cdot 10^{-4}$A at voltage of +1.4V/-0.6V*

Figure 7 shows the current-voltage curve corresponding to the 30-nm-thick sample deposited using the TD1 target on the TiN substrate at 150C and biased with the current compliance of 10^{-6}A and with the voltage of +4V/-5V. Both the positive and the negative sides are close to being symmetric. The switching behavior is unipolar. The filament is supposedly metallic due to the abrupt change from the OFF to the ON state at both the positive as well as the negative bias. In fact, the cell electroforms on both sides. Despite the relatively large electroforming voltage, the filament is still unstable and the opposite electrodes are OFF near zero voltage. At the negative bias, the cell is electroformed again.

The reason for the instability of the metallic filament cannot be assumed due to the large electrical stress. The aim of using the large electroforming voltage was to create the metallic filament, which is stable and strong. The additional condition is that the relatively strong filament can be dissolved at the negative bias. The observed instability of the filament near zero point of the current and the voltage can be explained either as being due to the change of the polarity near zero point or with the presence of the mechanical stress inside the layer during the switching. The shape of the curve implies that conduction between +0.5V and 0V is not ohmic. This can be explained as a surface oxidation of the metallic filament, for example. The oxidized surface and metallic core of the filament have different mechanical properties. The hard oxide may exert compressive stress on the ductile core of the metallic filament and cause the instability of it near the zero bias.

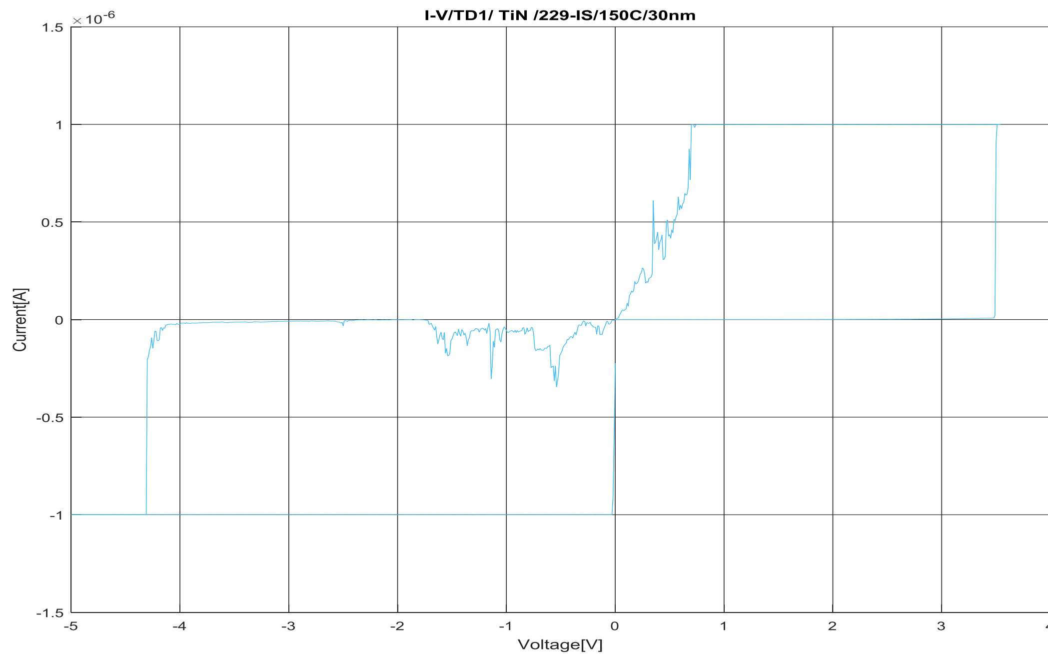

Figure 7. *The current- voltage characteristics of the 30-nm-thick sample deposited using the TD1 target on the TiN substrate at 150C and biased with the current compliance of 10^{-6}A and with the voltage of +4V/-5V.*

Figure 8 shows the behavior similar to that in Figure 9, with more abrupt and sudden transition from the ON to the OFF state with the disconnection of the opposite electrodes. Such behavior, for example, can be explained by the presence of tensile stress inside the metallic filament. It is worth noting that this instability of the supposedly metallic filament is observed despite the quite large positive +4V and negative -5V bias. The cell was electroformed hardly on both sides but the current-voltage curve was still unstable in the middle.

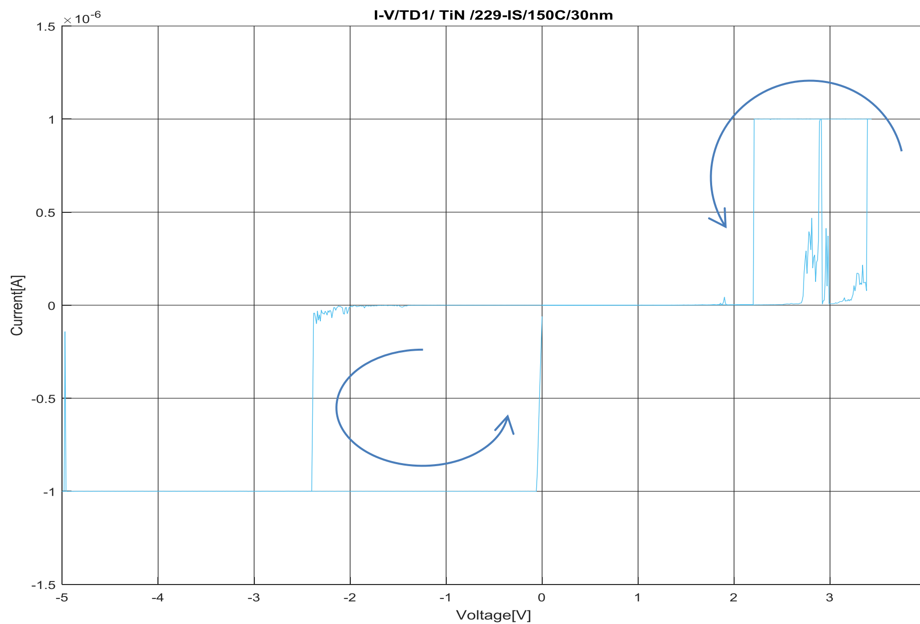

Figure 8. *The current- voltage characteristics of the 30-nm-thick sample deposited using the TD1 target on the TiN substrate at 150C and biased with the current compliance of 10^{-6}A and with the voltage of +4V/-5V*

Figure 9 shows the threshold like switching behavior with a supposedly semiconductive response. The transition from the OFF to the ON state is not abrupt, which implies that the filament is only partly metallic. At the end of the positive cycle, the cell is OFF near zero again. Then, at the negative bias, the cell is electroformed at -3.7V, but at -3V it starts to conduct non-ohmically with a circular-like curve, which implies an exponential correlation between the current and the voltage and refers perhaps to the filament oxidation. After that, the conduction can be explained as occurring through the semiconductive oxide. This contradicts with a classical explanation of ECM cell behavior at negative bias. Here, first, the cell is electroformed from the OFF state. Then, the shape of the curve implies that metallic filament perhaps oxidizes. In this particular case, the conductive filament (either originally metallic or already oxidized one) is unstable.

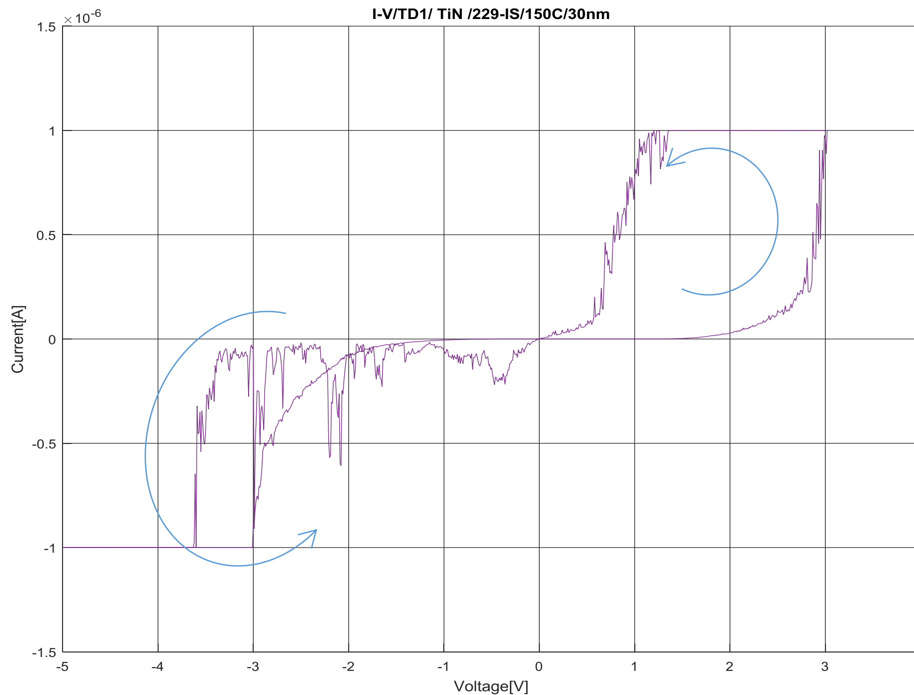

Figure 9. *The current- voltage characteristics of the 30-nm-thick sample deposited using the TD1 target on the TiN substrate at 150C and biased with the current compliance of 10^{-6}A and with the voltage of +4V/-5V.*

Figure 10 shows the threshold-like type of switching behavior with the supposedly metallic filament. The transition from the OFF to the ON state is abrupt. The region in curves with ohmic behavior are the straight lines with slightly different slopes. The current compliance was symmetric with $1.1 \cdot 10^{-5}$A and the asymmetric voltage of +2V/-1V. The cell shows the instability of the metallic filament in the middle. This can be explained by threshold type of switching or even by the presence of mechanic stress.

In Figure 10, the applied bias was not small, which implies that, in fact, the metallic filament should not be very weak. Therefore, the threshold –like switching behavior is more probable for the explanation of such a curve shape. In addition, the blockade of ionic transport in nanoscale until a specific threshold voltage is achieved could be also a reason for such an effect. The existence of the threshold voltage may imply that the energy barrier to the ionic transport needs to be considered.

Figure 11 shows the curve without a well-defined OFF state at the positive bias. The cell is in the conductive mode with a small hysteresis directly after the application of positive bias. Such memory cells, which are immediately conductive after applying a bias, cannot be electroformed. The cell exhibit a small region of negative differential resistance where the current drops while the

voltage grows. These small regions of perhaps differential negative resistance were frequently observed in curves at positive bias.

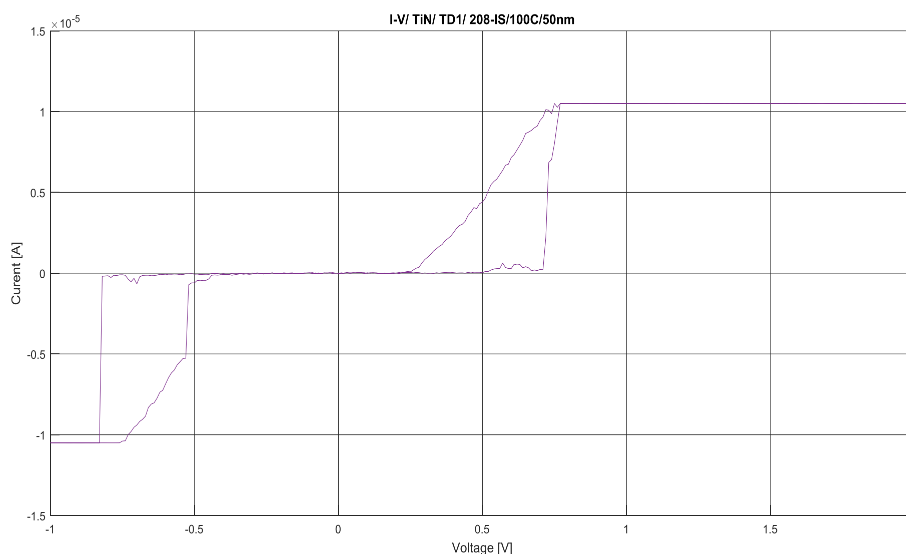

Figure 10. *The current- voltage characteristics of the 30-nm-thick sample deposited using the TD1 target on the TiN substrate at 100C and biased with the positive current compliance of $1.1 \cdot 10^{-5}$A and the negative compliance of $1.1 \cdot 10^{-5}$A at the voltage of +2/-1V.*

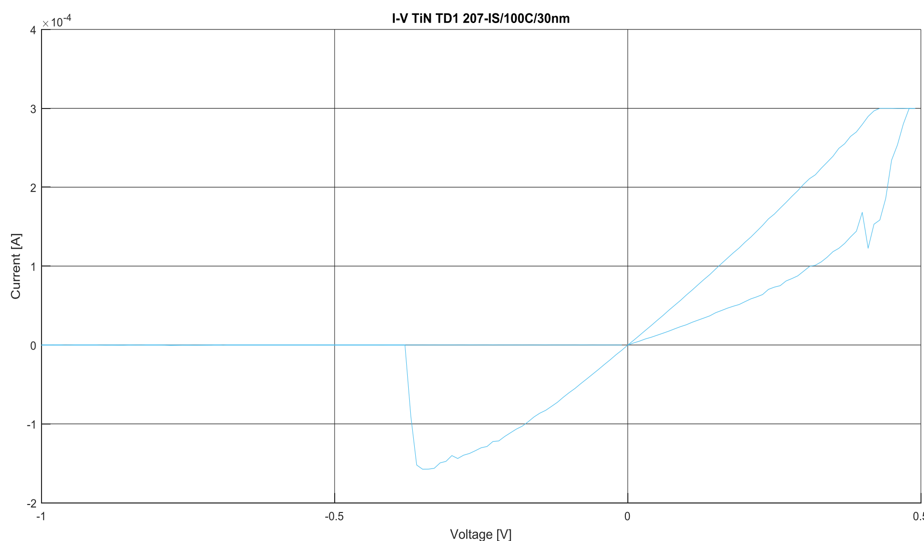

Figure 11. *The current-voltage characteristics of the 30-nm-thick sample deposited using the TD1 target on the TiN substrate at 100C and biased with the positive current compliance of $3 \cdot 10^{-4}$A and the negative compliance of $2 \cdot 10^{-4}$A at the voltage of +0.5V/-1V*

Figure 12 displays the I-V curve corresponding to the 50-nm-thick sample deposited using the TD1 target on the TiN substrate at 100C. The cell is conductive immediately after applying positive bias implying the existence of a metallic path. However, the opposite electrodes are disconnected at +0.18V. The decrease in current with an increase in voltage can indicate the presence of negative differential resistance. Then, after 0.22V, the cell starts to conduct again, however, with a non-metallic fingerprint. At the backward direction, the cell was OFF again and was electroformed on the negative side.

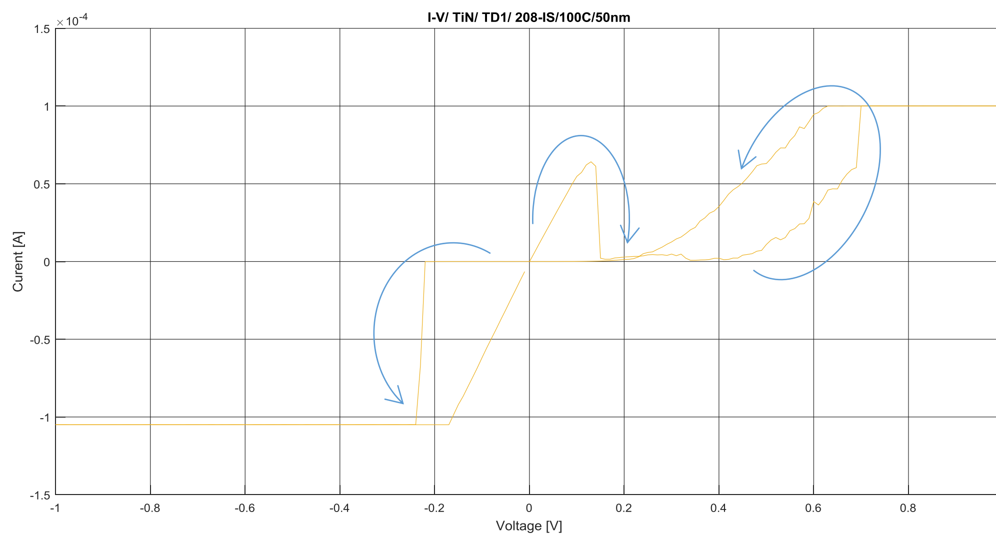

Figure 12. *The current- voltage characteristics of the 50-nm-thick sample deposited using the TD1 target on the TiN substrate at 100C and biased with the positive current compliance of 10^{-4}A and the negative compliance of $1.1 \cdot 10^{-4}$A at a voltage of +1/-1V.*

Figure 13 displays the I-V characteristics corresponding to the 30-nm-thick sample biased with the positive current compliance of $3 \cdot 10^{-4} A$ and the negative compliance of $1.5 \cdot 10^{-4} A$ at the voltage of +1.4V/-0.4V. On the negative side, the straight line corresponding to the metallic filament previously created at the positive bias changes the slope several times. It can indicate the change in the resistance due to the change in the geometric parameters of the metallic filament in a stepwise manner.

Figure 14 shows two successive sweeps of the memory cell with similar behavior as shown in Figure 13. The second sweep in the same memory cell is shown with blue arrows. After the first sweep, the cell is immediately ON with the metallic type of curve. However, the negative part of the curve is completely degraded, because it conducts and the cell is OFF near zero.

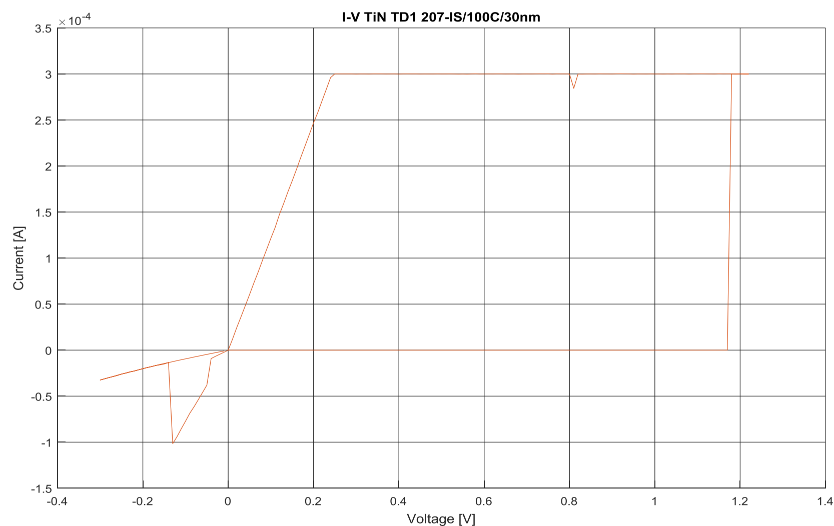

Figure 13. *The current- voltage characteristics of the 30-nm-thick sample deposited using the TD1 target on the TiN substrate at 100C and biased with the positive current compliance of $3\cdot10^{-4}$A and the negative compliance of $1.5\cdot10^{-4}$A at the voltage of +1.4V/-0.4V*

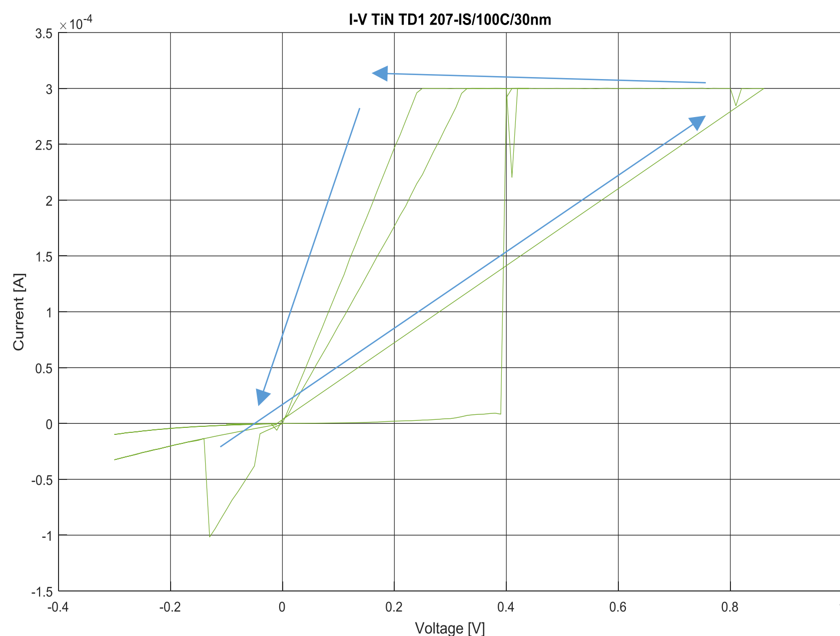

Figure 14. *The current- voltage characteristics of the 30-nm-thick sample deposited using the TD1 target on the TiN substrate at 100C and biased with the positive current compliance of $3\cdot10^{-4}$A and the negative compliance of $1.5\cdot10^{-4}$A at the voltage of +1V/-0.4V*

1.3 The TD2 target doped with two doping elements

Figure 15 displays the current- voltage characteristics of the 50-nm-thick sample deposited using the TD2 target on the Pt substrate at 100C and biased with the positive and the negative current compliance of 10-6A at a voltage of +2/-5V. The memory cell exhibits the degraded bipolar switching near zero on the negative side. Then, the cell electroforms on the negative side again. Here, there is a small region of perhaps negative differential resistance, where the current growth while the voltage drops.

Figure 16 shows the current-voltage characteristics of the 5-nm-thick sample deposited using the TD2 target on the platinum substrate at 100C and biased with the positive current compliance of $3 \cdot 10^{-6}A$ and the negative compliance of $6 \cdot 10^{-6}A$ at the voltage of +0.5/-0.5V. The cell shows the threshold-like behavior. The cell does not follow the limitation of the current compliance on the negative side and only touches the limitation on the positive side.

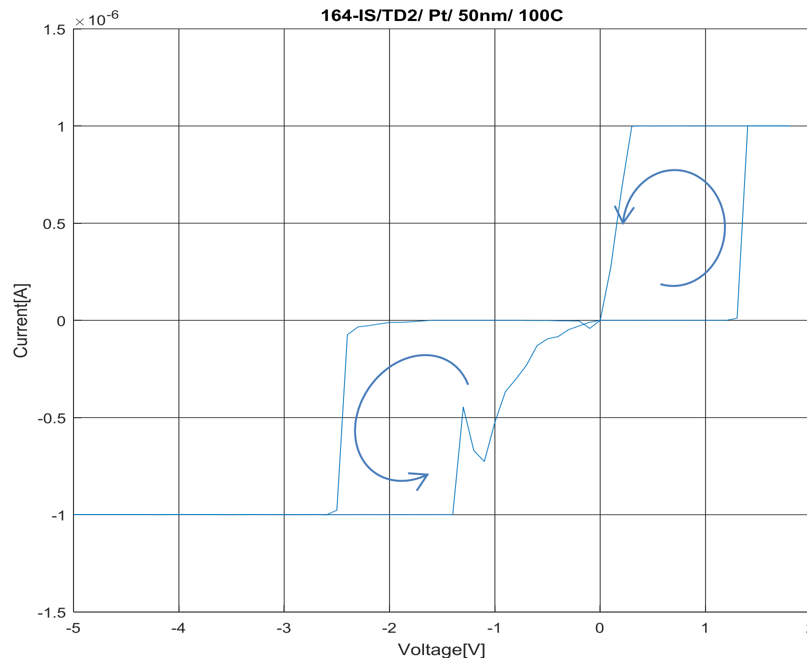

Figure 15. *The current-voltage characteristics of the 50-nm-thick sample deposited using the TD2 target on the Pt substrate at 100C and biased with the positive and the negative current compliance of* $10^{-6}A$ *at the voltage of +2/-5V.*

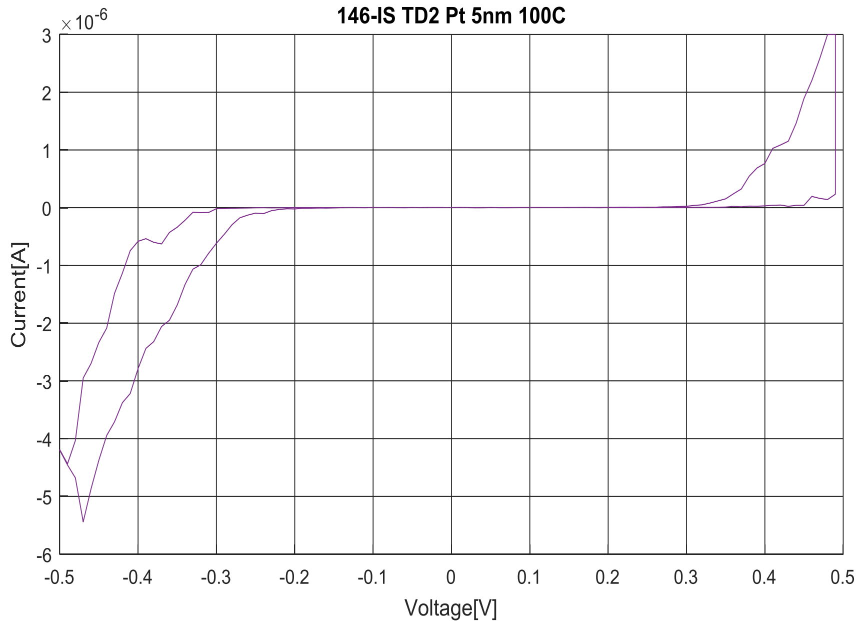

Figure 16. *The current-voltage characteristics of the 5-nm-thick sample deposited using the TD2 target on the platinum substrate at 100C and biased with the positive current compliance of* $3\cdot10^{-6}$*A and the negative compliance of* $6\cdot10^{-6}$*A at the voltage of +0.5/-0.5V.*

Figure 17 shows the I-V curve corresponding to the 50-nm-thick sample deposited using the TD2 target on the platinum substrate at 100C and biased with the positive and the negative current compliance of 10^{-6}A at the voltage of +5V/-5V. The cell stacks on the negative side. The cell conducts but does not switch. The performance degrades due to the formation of a very strong and supposedly metallic filament. Here, the frequently seen problem of instability of the metallic filament in samples was attempted to resolve by the formation of the stronger filament, which, however, caused degrading the switching behavior in ECM cell. The next sweep of such a cell causes the short-circuited type of curves as may be observed in Figure 18, for example.

Figure 18 displays the typical short-circuiting curves, which can be frequently seen in both the electroforming and the switching test. Such cells cannot be electroformed because they do not have a well-defined resistive OFF state. Such a cell does not switch because it conducts ohmically without any type of hysteresis. In such cases, the galvanic contact between the opposite electrode is very strong and the metallic filament short-circuits them. To avoid this frequently seen failure mode, the repetitive cyclic loading intended to provoke the fatigue of the metallic filament was implemented, however, without success. The idea was to test the bipolarity as it was defined in literature for the ECM cell. The metallic filament dissolves and disconnects the opposite electrodes after applying a negative bias.

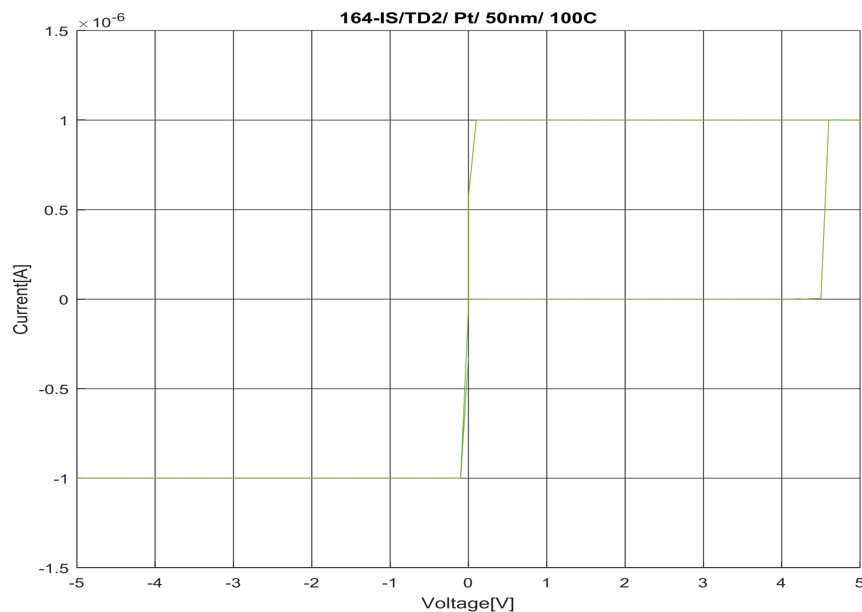

Figure 17. *The current- voltage characteristics of the 50-nm-thick sample deposited using the TD2 target on the Pt substrate at 100C and biased with the positive and the negative current compliance of* 10^{-6}*A at the voltage of +5V/-5V.*

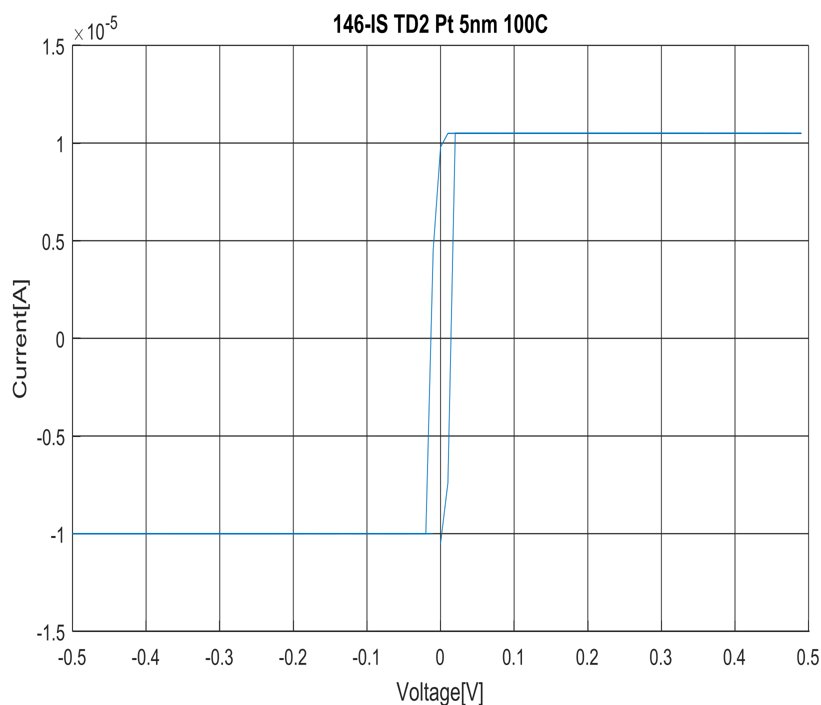

Figure 18. *The current- voltage characteristics of the 5-nm-thick sample deposited using the TD2 target on the platinum substrate at 100C and biased with the positive and negative current compliance of* 10^{-5}*A at the voltage of +0.5/-0.5V.*

Figure 19 shows the I-V curve corresponding to the 30-nm-thick sample deposited using the TD2 target on the TiN substrate at 100C and biased with the positive and the negative current compliance of 10^{-6}A at the voltage of +1V/-5V. Part of the I-V characteristics is a curved line with the non-abrupt shape implying the partly non-ohmic behavior.

Figure 20 displays the I-V curve corresponding to the same sample as in Figure 19 biased with the positive and the negative current compliance of $10^{-6}A$ and the slightly different voltage of +2/-5V. The cell shows the instability, however, on the negative side. It displays the bipolar switching until 0.6V and then it starts to electroform again.

Figure 21 displays the I-V curve corresponding to the same sample as in Figure 20 biased with the same current compliance and the voltage, however, with the threshold-like behavior. The cell shows the non-ohmic type of conducting, with the semiconductive fingerprints despite the same biasing parameters as in Figure 20. The shape of the curve is circular-like on a linear scale. This shape can be explained by the oxidation of the metallic filament or more likely due to the oxidation of both dopant 1 (D1) and metallic filament. However, not only non-metallic type of conduction is observed here but also the threshold-like type of switching, which implies a blocked or restricted ionic transport until a specific threshold voltage is achieved.

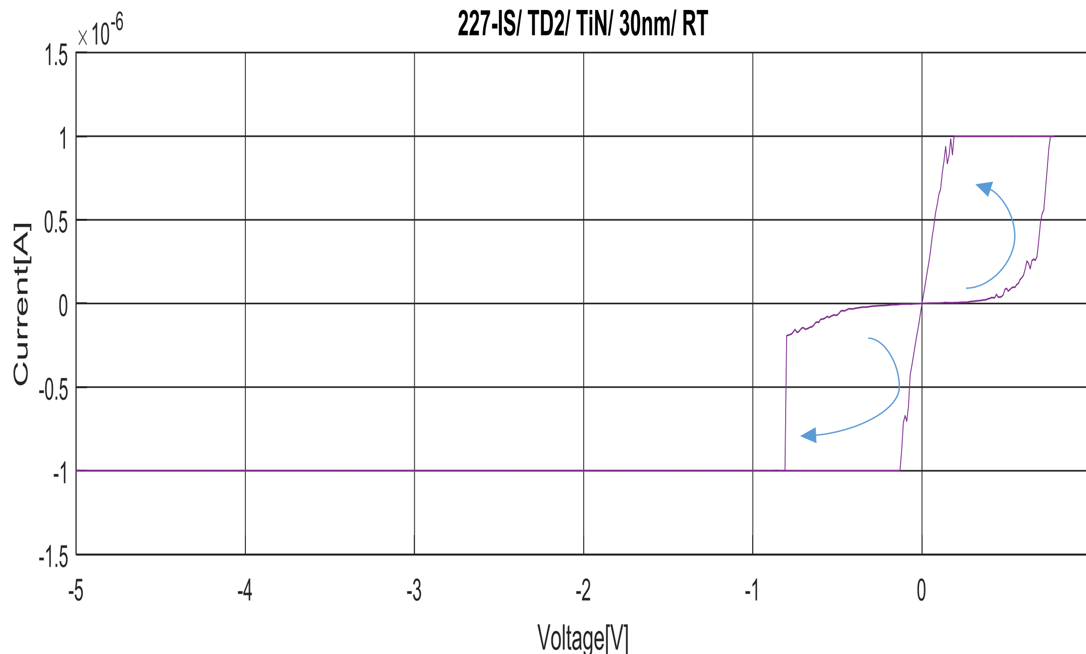

Figure 19*. The current-voltage characteristics of the 30-nm-thick sample deposited using the TD2 target on the TiN substrate at 100C and biased with the positive and the negative current compliance of 10^{-6}A at the voltage of+1V/-5V.*

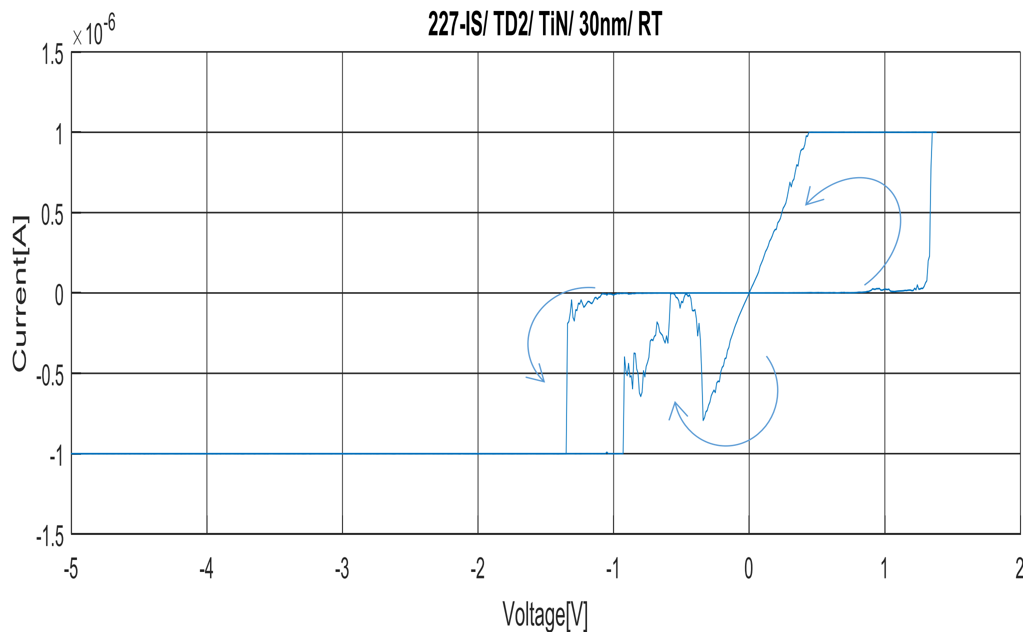

Figure 20. *The current -voltage characteristics of the 30-nm-thick sample deposited using the TD2 target on the TiN substrate at 100C and biased with the positive and the negative current compliance of* $10^{-6}A$ *at the voltage of +2/-5V.*

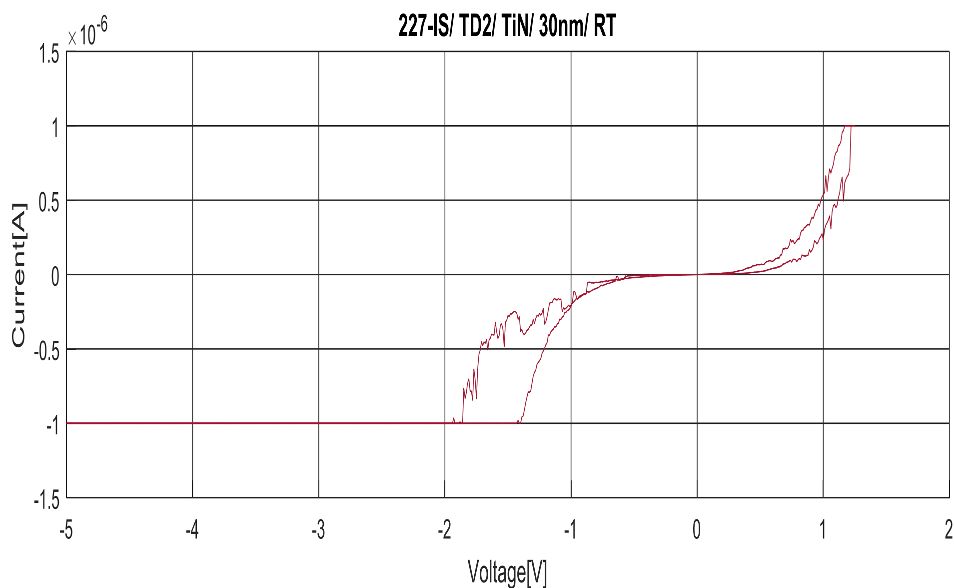

Figure 21. *The current-voltage characteristics of the 30-nm-thick sample deposited using the TD2 target on the TiN substrate at 100C and biased with the positive and the negative current compliance of* $10^{-6}A$ *at the voltage of +2/-5V.*

Interpretation of results. As it can be seen from above-mentioned figures, there is a wide variety of the observed switching behavior of different types. The differences lie not only in used fabrication or testing parameters but also in completely different switching behavior even in the same sample. The variability in switching was so high that it was impossible to attribute only one type of a switching response to the specific target. In this Appendix 7, only a small amount of different types of behavior in ECM cells is presented. The threshold –like switching behavior is separately represented in Appendix 9.

In general, there was a problem with the instability of the conductive filament either due to the presence of mechanical stress, the negative differential resistance or due to threshold-like switching behavior. In addition, the existence of the circular-like shapes of curves can imply the oxidation of the conductive filament. It seems that description of the behavior of ECM cell at negative bias as the only electrochemical dissolution of the metallic filament depicts the behavior of ECM cell badly. The ECM cell undergoes the different type of transition between resistive states indicating that the chemical reaction should occur in ECM cell. Neither the differential negative resistance nor the circular-like shape of the curve cannot be attributed to the conductive filament with pure metallic form.

In addition, the overall impression was that all samples deposited by doped and pure SiO2 target were very conductive. In many cases, adding of dopants (TD1 or TD2) to SiO2 causes the complete degradation of the resistive OFF state in ECM cell. Such a cell can be neither electroformed nor switched repeatedly.

APPENDIX 8

” *Resistance*”

TO THE MASTER THESIS “CHARACTERIZATION OF THE DOPED SILICON DIOXIDE AND ITS IMPLICATION FOR THE RESISTIVE SWITCHING PHENOMENA IN THE ELECTROCHEMICAL METALLIZATION CELLS”

LIST OF FIGURES

Figure 1. The resistance – voltage characteristics of the 30nm-thick sample deposited using the TD0 target on the platinum substrate at 100C *5*
Figure 2. The resistance – voltage characteristics of the 30nm-thick sample deposited using the TD0 target on the platinum substrate at 100C *5*
Figure 3. The overview of the ON and the OFF resistance of the 5nm-30nm-thick samples deposited using the TD0 target on the platinum substrate (ZY view) *7*
Figure 4. The overview of the ON and the OFF resistance of the samples deposited using the TD0 target on the platinum and the TiN substrates at RT and 150C (ZY view) *8*
Figure 5. The resistance – voltage characteristics of the 20nm-thick sample deposited using the TD1 target on the TiN substrate at 100C *10*
Figure 6. The resistance – voltage characteristics of the 10nm-thick sample deposited using the TD1 target on the TiN substrate at 100C *10*
Figure 7. The resistance – voltage characteristics of the 20nm-thick sample deposited using the TD1 target on the TiN substrate at 100C *13*
Figure 8. The resistance – voltage characteristics of the 10nm-thick sample deposited using the TD1 target on the TiN substrate at 100C *14*
Figure 9. The resistance – voltage characteristics of the 10nm-thick sample deposited using the TD1 target on the TiN substrate at 100C *15*
Figure 10. The overview of the ON and the OFF resistance of the 5nm-50nm-thick samples deposited using the TD1 target (ZY view) *17*
Figure 11. The overview of the ON and the OFF resistance of the samples deposited using the TD1 target on the platinum and the TiN substrates at RT and 150C (ZY view) *18*
Figure 12. The resistance – voltage characteristics of the 10nm-thck sample deposited using the TD2 target on the platinum substrate at 100C *20*
Figure 13. The resistance – voltage characteristics of the 30nm-thick sample deposited using the TD2 target on the TiN substrate at 150C *20*

Figure 14. The resistance – voltage curve corresponding to the 30nm-thick sample sputtered using the TD2 target on the TiN substrate at RT... 21
Figure 15. The resistance – voltage characteristics of the 30nm-thick sample deposited using the TD2 target on the TiN substrate at RT... 21
Figure 16. The resistance – voltage characteristics of the 30nm-thick sample deposited using the TD2 target on the TiN substrate at RT... 22
Figure 17. The resistance – voltage characteristics of the 30nm-thick sample deposited using the TD2 target on the TiN substrate at RT... 23
Figure 18. The resistance – voltage characteristics of the 30nm-thick sample deposited using the TD2 target on the TiN substrate at RT... 24
Figure 19. The resistance – voltage characteristics of the 30nm-thick sample deposited using the TD2 target on the TiN substrate at RT... 24
Figure 20. The resistance – voltage characteristics of the 50nm-thick sample deposited using the TD2 target on the platinum substrate at 100C 25
Figure 21. The resistance – voltage characteristics of the 50nm-thick sample deposited using the TD2 target on the platinum substrate at 100C 25
Figure 22. The resistance – voltage characteristics of the 50nm-thick sample deposited using the TD2 target on the platinum substrate at 100C 26
Figure 23. The overview of the ON and the OFF resistance of the samples with the thickness between 5and 50nm deposited using the TD2 target on the platinum substrate at 100C (ZY view) 27
Figure 24. The overview of the ON and the OFF resistance of the samples deposited using the TD2 target on the platinum and TiN substrates at RT and 150C (ZY view)... 28

1. R-V CHARACTERISTICS

The OFF state refers to the resistance of the ECM cell directly after applying the voltage bias, however, before the creation of either the conductive path or metallic filament. Therefore, it refers to the resistance of oxide due to the fabrication and concentration of oxygen in SiOx (Tomozeiu 2011).

However, the observed resistance is in general also the function of the applied current compliance (Balakrishnan et al. 2006). The choice of the limiting current is dependent upon the research purposes, and in many cases, it can be chosen to some extent relatively freely. Nevertheless, the memory cell creates the response on the applied current and voltage. Sometimes, the actual cell current is much less, than the limiting current compliance and it can be seen by the absence of a corresponding horizontal line in I-V curves.

Sometimes, the current can overshoot the current limit and then the current spikes can be observed (Wouters 2012). Sometimes, the current limit needs to be switched completely OFF for the observing of the real behavior of the memory cell (Mehonic et al. 2013), however with a risk of the cell breakdown.

Additional difficulties with a choice of the current compliance are to find the actual level of the current compliance when the cell starts to switch with the hysteresis. The actual switching window for the fabricated sample can be very narrow and different for the memory cell depending on different fabrication condition, substrate, thickness, and area of the memory cell or doping. In addition, if the cell switches in some way, the switching parameters can be adjusted at some extents according to the equation of the power law $P = U \cdot I$.

1.1 The TD0 target

Figure 1 displays the resistance-voltage curve corresponding to the 30nm-thick sample deposited using the TD0 target on the platinum substrate at 100C. The curves show the resistance-voltage curve with the ohmic conduction expected in ECM memory cells. The conductive path is assumed to be the metallic filament. The abrupt change of the resistance from the OFF to ON state with the consequent constant ON resistance indicates that the opposite electrodes are connected via the metallic filament. The ON state resistance is a horizontal straight line, which means that the resistance is constant. Such a conducting behavior is intrinsic to metals. Then, the disconnection of the electrodes via the dissolving the metallic filament takes place after applying the negative bias. Such switching behavior is bipolar. The conductive paths are stochastic because they are not the same. However, the conduction mechanism seems to be the same.

In Figure 1, the OFF resistance is the inclining line at the semilogarithmic scale on both the positive and the negative side. It refers however to the non-ohmic type of conduction, the non-constant amount of charge carriers during the OFF state as well as the conductivity of SiO2 due to the vacancies of oxygen, the Si-rich regions or defects in oxides. Anyway, after the application of the electric field, the OFF state is a dynamic change in resistance of SiO2. The abrupt change to the ohmic conduction precedes by a change in resistance during the transition from the OFF to the ON state. The same is true in the opposite direction since the transition from the ON to OFF state also requires the change in conductivity in SiO2. This may indicate that SiO2 participates also in switching even when the metallic filament is created. The actual voltage window for the metallic type of switching in Figure 1 is between +0.4V and -0.3V. Moreover, the materialized resistance is between $1.1 \cdot 10^3 Ohm$ and $1.8 \cdot 10^5 Ohm$. In this case, both the resistance as well as voltage windows are very narrow.

Figure 2 shows two different curves for the same sample shown in Figure 1. The red curve is the same metallic type with an abrupt transition from two resistive states as in the previous figure. However, the blue line shows the non-ohmic and the threshold-like type of switching behavior. Both curves are located at different levels of resistance with only slightly overlapping regions in resistance. Both types of switching behavior are frequently seen in all samples, however, in many cases with some modifications and distortions.

It can be seen in Figure 2 that the blue and curves locate in different level of resistance and voltage. The switching behavior denoted by red curve can be explained in similar way as in Figure 1. However, the switching behavior in the blue curve is completely different. First, it exhibits threshold-like switching with the OFF state in region, where the cell with metallic type of switching is usually ON as shown in the red curve in Figure 2 and in all the curves in Figure 1.

In a blue curve shown in Figure 2, the transition from ON to OFF and vice versa can be approximated as a straight line, which indicates the exponential dependence on the current and voltage. Unlike the abrupt jump of resistance in red curve metallic type of switching, the transition in the blue curve is rather exponentially accelerated change in resistance at a higher voltage than for metallic type. As soon as the voltage, as well as an electric field, are decreased below a certain value, the cell returns to the OFF state at the same polarity. This implies that this threshold-like type of switching is more like double unipolar than a bipolar type of switching. The metallic type of switching sometimes is named as memory switching, which depends on what issue one would like to highlight. The metallic type of switching implies that the metallic filament is created with typical behavior shown in Figure 1. Both metallic and threshold-like type of switching may exclude each other's as in a case of sample N245-IS and N246-IS explained in Appendix 9.

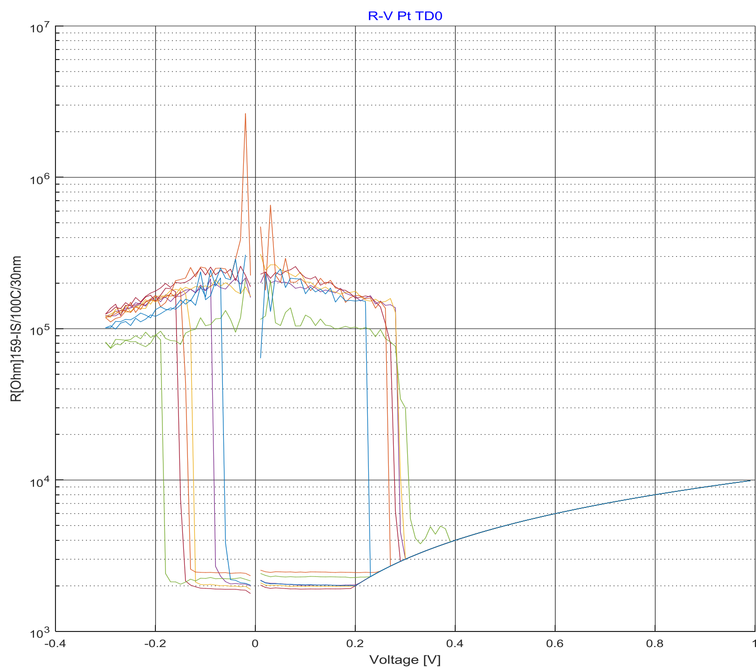

Figure 1. *The resistance – voltage characteristics of the 30nm-thick sample deposited using the TD0 target on the platinum substrate at 100C*

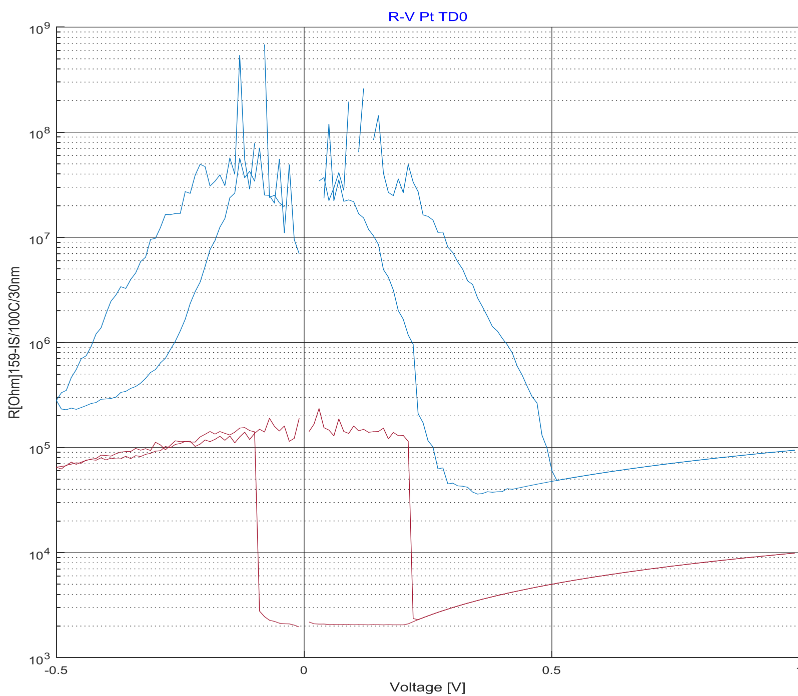

Figure 2. *The resistance – voltage characteristics of the 30nm-thick sample deposited using the TD0 target on the platinum substrate at 100C*

Figure 3 shows the ON and the OFF resistance of the 5-50nm-thick samples deposited using the TD0 target. Very short vertical lines in the plot mean that the conduction is ohmic without the hysteresis. The hysteresis means there are at least two different resistive states during the electroforming or switching.

The absence of the hysteresis together with the galvanic connection of the opposite electrode via the metallic filament implies the short-circuiting of the electrodes immediately after applying the positive voltage bias. Such behavior can be explained by the very high mobility of the metallic cations dissolved from the active electrode in the ECM cell due to the large applied voltage or current. However, some of the memory cells deposited using the target without any dopants were short-circuited with all chosen parameters.

The short-circuiting at the very low level of the current compliance indicates that the deposited SiOx has non-negligible conductivity. This can also be seen from the low level of the OFF resistance state. Half of the samples deposited using the TD0 show the OFF resistance less than 10^8Ohms. The ON resistance or low resistive state varies from 20 Ohms to 10^6Ohms. Based on the calculated density of the sputtered SiO2 together with the observed level of the OFF resistance, it can be suggested that the fabricated SiO2 is probably more likely SiOx with $x<2$.

In addition, the ON resistance of 20nm of pure SiO2 is on the level of 10^6Ohms, which indicates the relatively resistive ON state. Such situation can correspond to the blue curve in Figure 2 with the threshold-like non-ohmic switching behavior.

The 5nm-thick sample has two vertical short-circuited lines in the high resistive region. It can mean that there are also surface charge states, which can be responsible for such unusual behavior. The 10nm- and the 30nm-thick samples exhibit the resistance less than zero ($R<0$).

Figure 4 displays the ON/OFF resistance corresponding to the specimens sputtered on the platinum as well as the TiN substrates at RT and 150C. The specimens sputtered on the platinum substrate exhibit the threshold-like switching behavior. The sample deposited at RT is more conductive in the ON state and more resistive in the OFF state than samples deposited at 150C. Therefore, the ON and OFF ratio of the samples sputtered at RT is larger than that fabricated at 150C. This difference can be explained by the temperature-induced change in the nanostructure, morphology, or even chemical composition.

However, the samples deposited on the TiN substrates do not show such trends. They switch, and even at times short-circuit but without the threshold-like behavior. A higher level of the OFF resistance in the samples deposited on the TiN substrate indicates that the memory cells switch at a lower level of the voltage and the current than those on the platinum substrate.

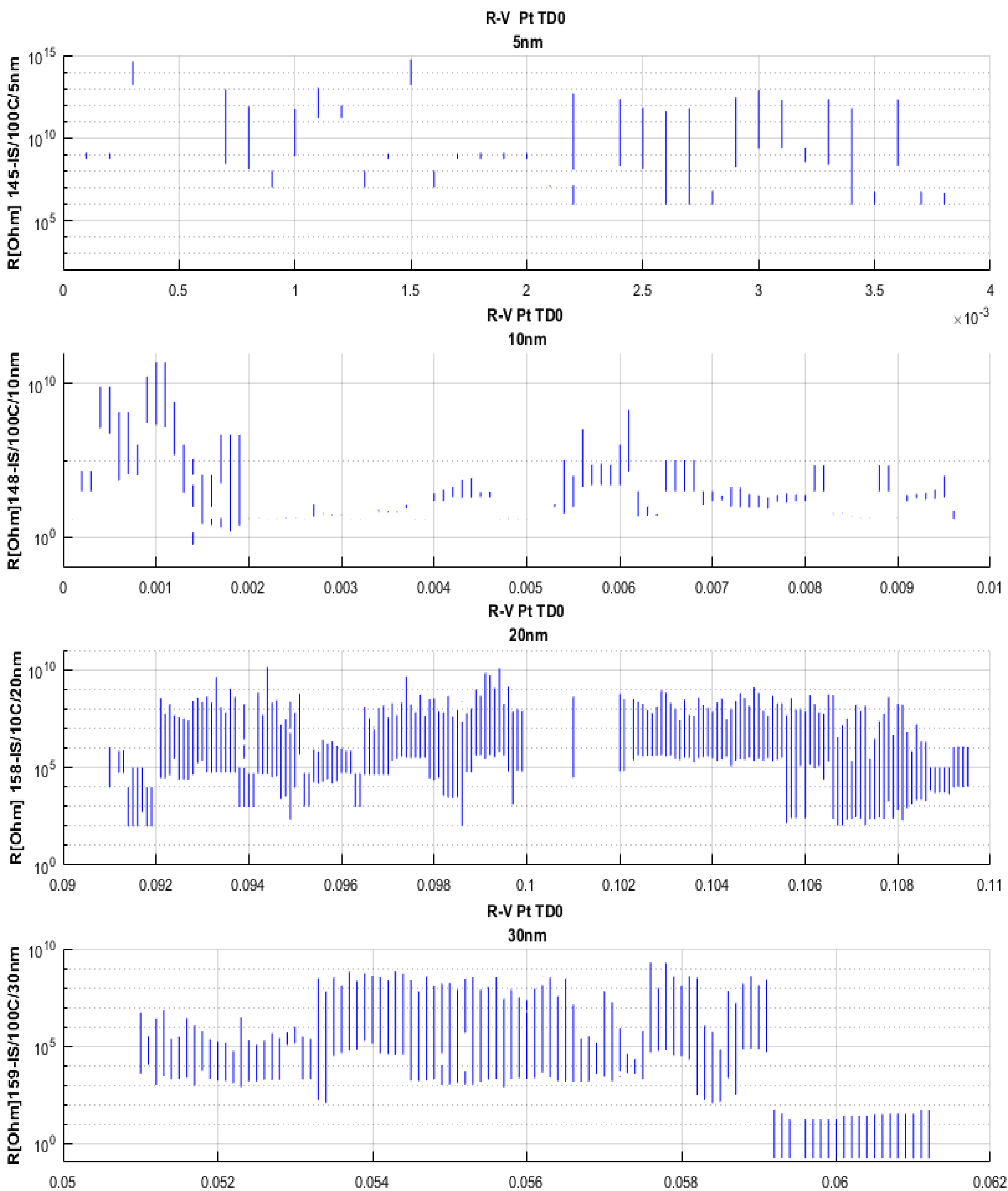

Figure 3. *The overview of the ON and the OFF resistance of the 5nm-30nm-thick samples deposited using the TD0 target on the platinum substrate (ZY view)*

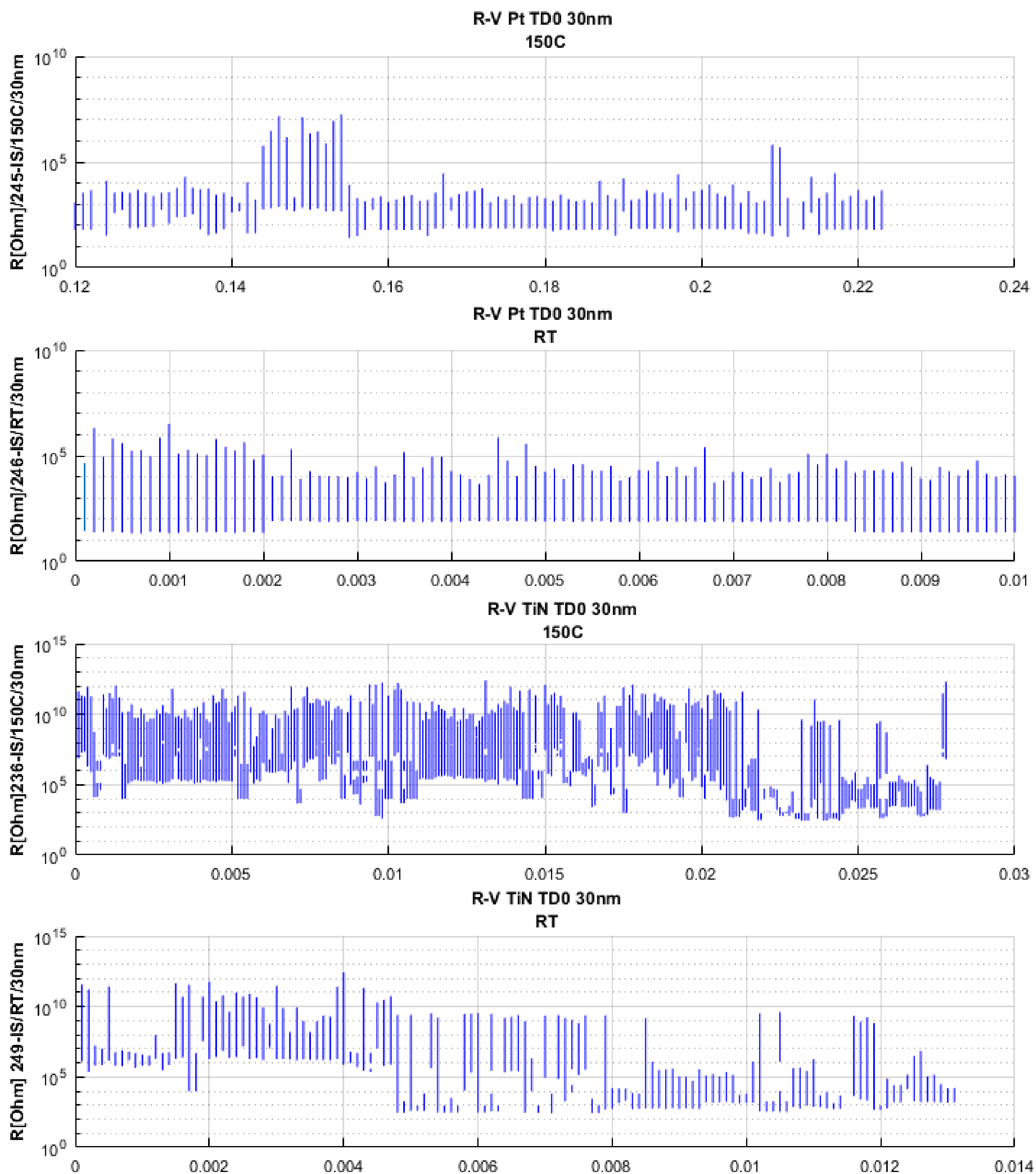

Figure 4. *The overview of the ON and the OFF resistance of the samples deposited using the TD0 target on the platinum and the TiN substrates at RT and 150C (ZY view)*

1.2 TheTD1 target doped with one doping element

Figure 5 shows the resistance – voltage characteristics of the 20nm sample deposited using the TD1 target on the TiN substrate at 100C. The memory cell shows the metallic type of electroforming behavior with an abrupt transition from the OFF to the ohmic ON state. However, this type of curve is very non-typical for the specimens sputtered on the TiN substrates. First, the electroforming voltage is exceptionally high even if the samples would be deposited on the platinum substrate. Second, the samples sputtered on the TiN substrates rarely show such metallic type of switching behavior.

Figure 6 shows the resistance – voltage characteristics of the 10nm-thick sample deposited using the TD1 target on the TiN substrate at 100C. This type of the electroforming curves is more typical for the samples sputtered on the TiN substrate. It is worthwhile to mention that there is no such an abrupt transition from the OFF to the ON state like in the metallic type of switching. This change in resistance level from the OFF to the ON state can be stepwise or sometimes gradual. On a semilogarithmic scale, this transition can sometimes be approximated as the inclining straight line. This indicates that the current and the voltage have exponential dependence with each other. However, the last ON stage is the curving line on the same scale implying that such a behavior is ohmic.

In addition, this gradual transition from OFF to ON state in Figure 6 is not abrupt like in metallic type of switching. This indicates that cell undergoes the change of resistance during transition. This can refer to either the SiO2-matrix participates in switching or metallic ions oxidizes immediately without creating of metallic filament before transition to the last conductive stage, which is, however, ohmic. The last ohmic stage is circular-like curve at a semilogarithmic scale, which corresponds to straight line at a linear scale. Such not abrupt transition may refer to chemical reaction in ECM cell during the transition step. The shape of curve at a semilogarithmic scale suggests the exponential dependence of current and voltage and conduction through the semiconductive oxide rather through metallic filament. The abrupt change in resistance, on the other hand, refers to creation of metallic filament, which connects the opposite electrode.

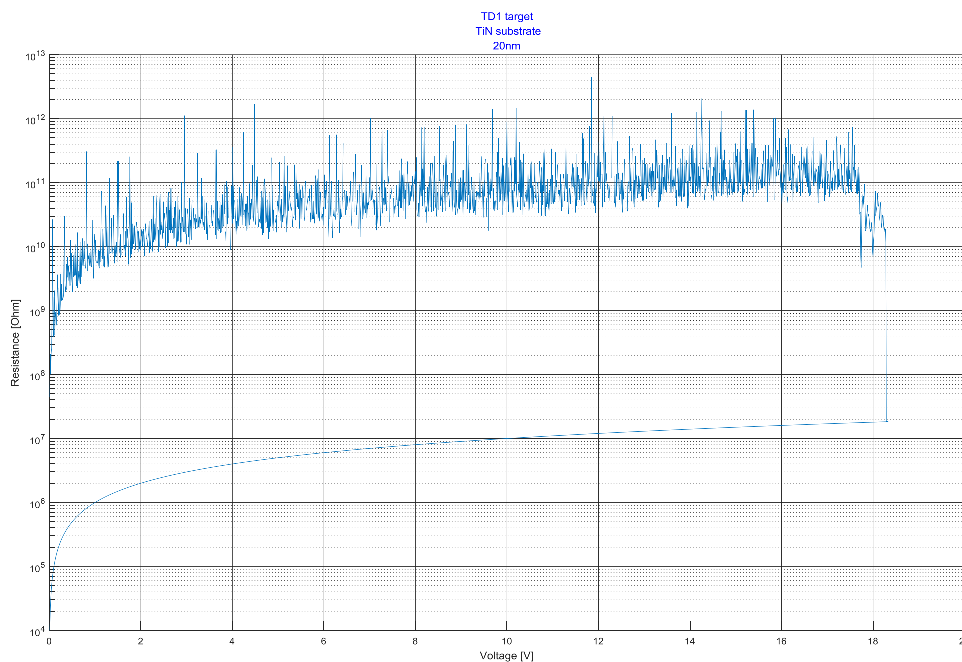

Figure 5. *The resistance – voltage characteristics of the 20nm-thick sample deposited using the TD1 target on the TiN substrate at 100C*

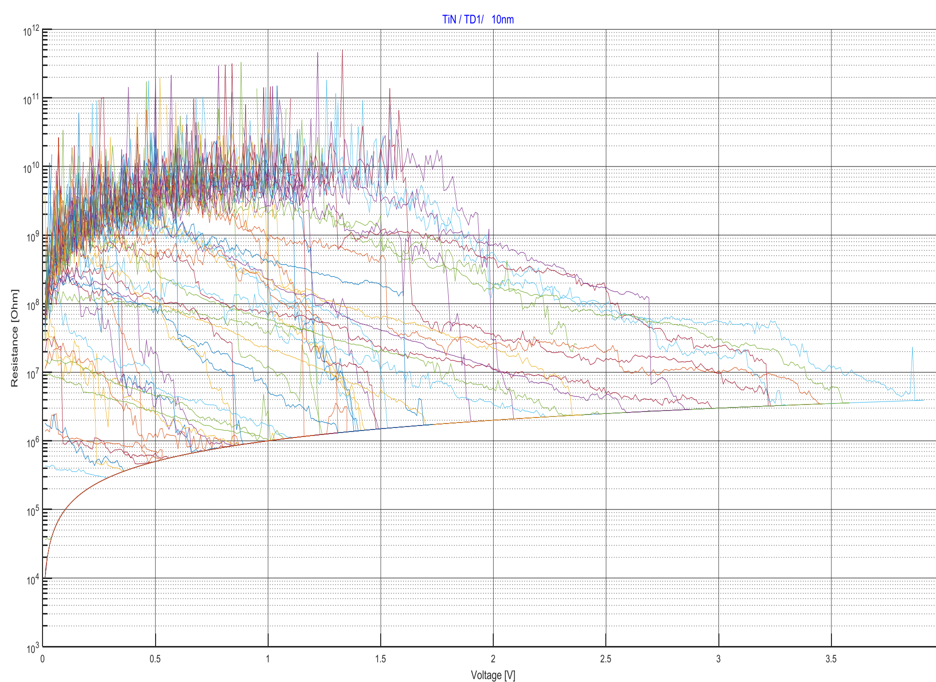

Figure 6. *The resistance – voltage characteristics of the 10nm-thick sample deposited using the TD1 target on the TiN substrate at 100C*

Figure 7 shows the resistance-voltage characteristics of the 20nm-thick sample deposited using the TD1 target on the TiN substrate at 100C. The change in resistance from the OFF state to the ON state is vague. This curve, however, is the straight line on the semilogarithmic scale in the opposite direction from the ON to the OFF state. This implies the exponential dependence between current and voltage. It is worthwhile to note that the memory cell is switched OFF at the same polarity implying that the switching is unipolar, however, without applying the high current.

This kind of plots shown in Figure 7 with straight line in semilogarithmic scale may be used for check if the conduction type may be ionic, for example.

For *ionic type of conduction*, the current density can be approximately written using the equations

$$J_{low} \propto \underbrace{\left(vr^2 \frac{e}{kT}\right)}_{A} \cdot E \cdot \underbrace{\exp\left(\frac{-\Delta G^{\neq}}{kT}\right)}_{B} \qquad \text{for low electric field (1)}$$

$$\text{and } J_{high} \propto \underbrace{vr \cdot \exp\left(\frac{-\Delta G^{\neq}}{kT}\right)}_{C} \cdot \exp\left(\underbrace{\frac{\frac{1}{2}re}{kT}}_{D} \cdot E\right) \text{ for high electric field (2)}$$

In equations, the jumping distance of ions is denoted by r, the Debye frequency is denoted as v, electric field is denoted by E, as well as activation entalpy by $\Delta G^{\neq}$ (Lim & Ismail 2015).

First equation (1) can be simply written in as $J_{low} \propto \underbrace{A \cdot B}_{F} \cdot E = F \cdot E$, which implies that ionic current density and electric field have linear dependence at low electric field. It means that on the linear scale this curve is usually straight line, which intercepts the zero point.

Second equation (2) can be also written in simple form as $J_{high} \propto C \cdot \exp(D \cdot E)$, which implies that, at high electric fields, the current density and electric field have exponential relationship.

In Figure 7, the straight line in a semilogarithmic scale has a general equation (Equations of straight lines on various graph papers) $y = k \cdot 10^{mx} = ke^{mx} = k \cdot \exp mx$, where k is intersept with y axis and m is slope of straight line, which can be positive and negative depending if the straight line is ascending and descending. In more specific form, the equation can be written as $R = k \cdot \exp(-mU)$ (3), where R is resistance, U is voltage, k is intersect with R axis and k is slope

of straight line. If the resistance can be written as $R = \frac{U}{I}$, current density as $J = \frac{I}{A^2}$ and electric field as $E = \frac{U}{d}$, then the equation (3) can be written as

$$\frac{U}{I} = k \cdot \exp(-mU)$$

$$I = \frac{U}{k \cdot \exp(-mU)}$$

$$I = J \cdot A^2 \text{ and } U = E \cdot d$$

$$J \cdot A^2 = \frac{E \cdot d}{k \cdot e^{-m \cdot E \cdot d}}$$

$$J = \underbrace{\frac{d}{k \cdot A^2}}_{F} \cdot E \cdot e^{\overbrace{md}^{G} \cdot E}$$

Therefore, the straight line in Figure 7 can be written using the current density and electric field as

$$J = F \cdot E \cdot \exp(G \cdot E) = F \cdot E \cdot e^{GE} \qquad \text{Equation (4)}$$

If one compares the equation (4) with the equations (1) and (2), one can see that the equations are different. At low electric field (equation (1)), the current density depends linearly on electric field whereas, at high electric fields (equation (2)), they are related exponentially.

The equation (4) suggests more strong dependence of current density from electric field that it would be when the conduction is of ionic type even at high electric field, because it has not only linear but also exponential component in equation.

Moreover, the change in resistance depicted by the straight line shown in Figure 7 suggests that this resistance value is dependent on applied voltage or the electric field. Therefore, when the voltage drops the cell returns back to OFF state. It also worth noting that applied electroforming voltage was extremely high, because the purpose was to create the strong metallic filament. This attempt failed, because the cell did not create the strong and stable metallic filament but started to conduct completely differently. The cell is OFF at the end of the electroforming stage even without applying the negative bias.

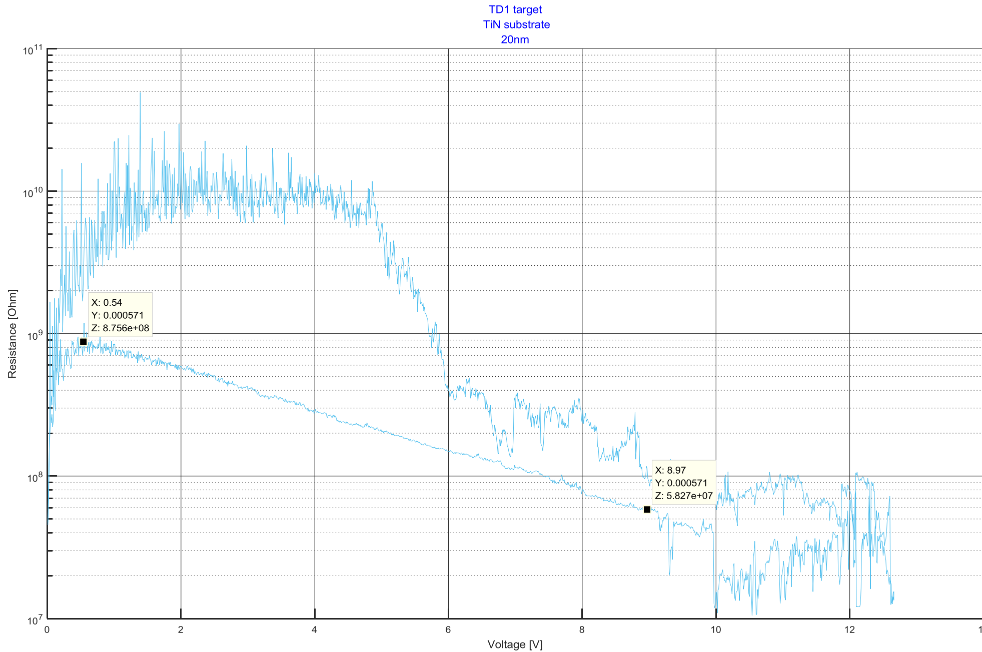

Figure 7. *The resistance – voltage characteristics of the 20nm-thick sample deposited using the TD1 target on the TiN substrate at 100C*

Figure 8 shows the resistance – voltage characteristics of the 10nm-thick sample deposited using the TD1 target on the TiN substrate at 100C. It can be seen that the transition from the OFF to the ON state occurs via many steps. The first region between 0.5V to 1.5V is the inclining line on the semilogarithmic scale implying that mathematical dependence between the voltage and the current is exponential. Then, two abrupt jumps can be observed at 1.6 and 2.6V. Then, again, there is a vague region between 2.6V and 3.4V. At the backward sweep, the cell conducts ohmically and stays ON at point zero.

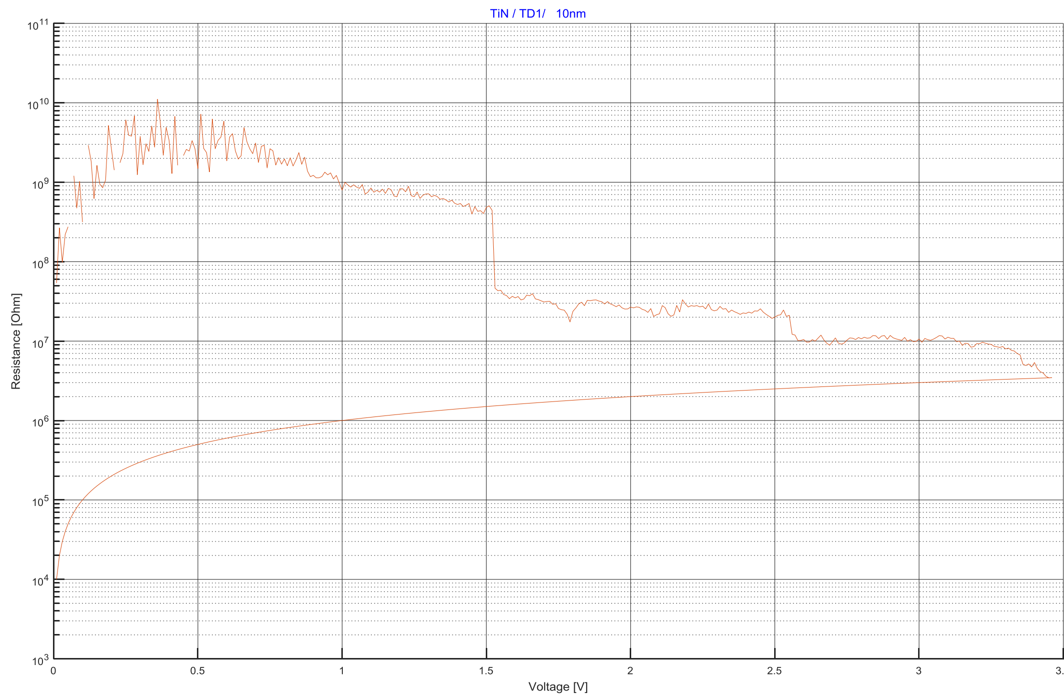

Figure 8. *The resistance – voltage characteristics of the 10nm-thick sample deposited using the TD1 target on the TiN substrate at 100C*

Figure 9 shows the resistance – voltage characteristics of the 10nm-thick sample deposited using the TD1 target on the TiN substrate at 100C. Both the forward and the backward sweeps are the straight lines on the semilogarithmic scale. At the end, the cell is OFF at approximately +0.2V. Again, the straight line on the semilogarithmic scale implies the non-ohmic conduction type and the exponential dependence between the current and the voltage. The behavior of this cell is similar to that shown in Figure 7, however, at much lower level of voltage and electric field. Again, these straight lines at both forward and backward sweeps, can be expressed by the equation

$$J = F \cdot E \cdot e^{GE}.$$

Therefore, the ionic type of conduction may be not completely appropriate for such type of switching behavior. This can also be explained in such way that concentration of charge carriers is increased when electric field increases. The resistivity of Si-doped silicon decreases when the concentration of doping elements increases. The increased electric field accelerated the mobile charge carriers or chemical reaction.

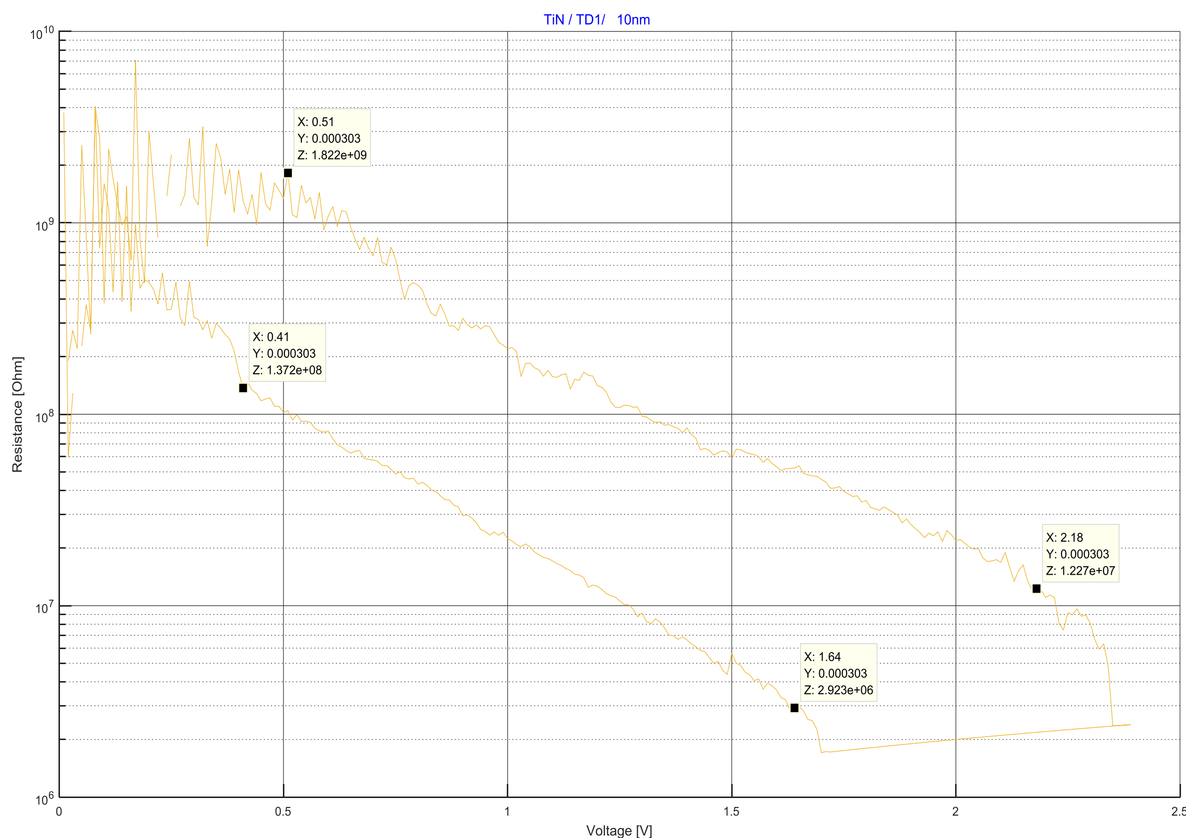

Figure 9. *The resistance – voltage characteristics of the 10nm-thick sample deposited using the TD1 target on the TiN substrate at 100C*

Figure 10 shows the overview of the ON and the OFF resistance of the 5nm-50nm-thick samples deposited using the TD1 target. It can be seen that these samples are more resistive in the OFF state in the comparison with the samples sputtered by the TD0 target shown in Figure 3. For example, if the OFF resistance of 10^{-10} Ohm is taken to the comparison, all samples in Figure 3 with one exception (5nm-thick sample) have resistance under 10^{-10} Ohm, but the samples in Figure 10 have resistance larger than 10^{-10} Ohm for most of the cases.

In addition, comparing the ON resistance with 10^{-5} Ohm, for example, reveals that the ON resistance of the samples deposited using the TD1 target is larger than those deposited using the TD0 target. However, again there are the exceptions in the 5-nm-thick samples for both targets and in the 30nm-thick sample for the TD1 target.

Figure 11 shows the overview of the ON and the OFF resistance of the samples deposited using the TD1 target on the platinum and the TiN substrates at RT and 150C. It can be seen that in the OFF state, the resistance is over 10^{-10} Ohm for both substrates and temperatures. The ON resistance is in all cases is near 10^{-5} Ohm. However, the ON resistance of the samples deposited on the Pt

substrate in many cases is under 10^{-5} Ohm but less than that for the samples deposited on the TiN substrate. It seems that the samples on the TiN substrates are slightly more resistive than on the platinum substrate in the ON state.

The comparison with the similar samples in Figure 4 reveals that there were not significant differences in the OFF resistance in the samples deposited on the TiN substrate because in all cases the resistance was larger than 10^{-10} Ohm. There is larger variability of the ON resistance on both sides of 10^{-5} Ohm in the samples deposited using the TD0 than the TD1 target. However, the OFF and the ON resistance of the samples deposited using the TD0 target on the Pt substrate in Figure 4 is much less. These samples show the threshold-like behavior.

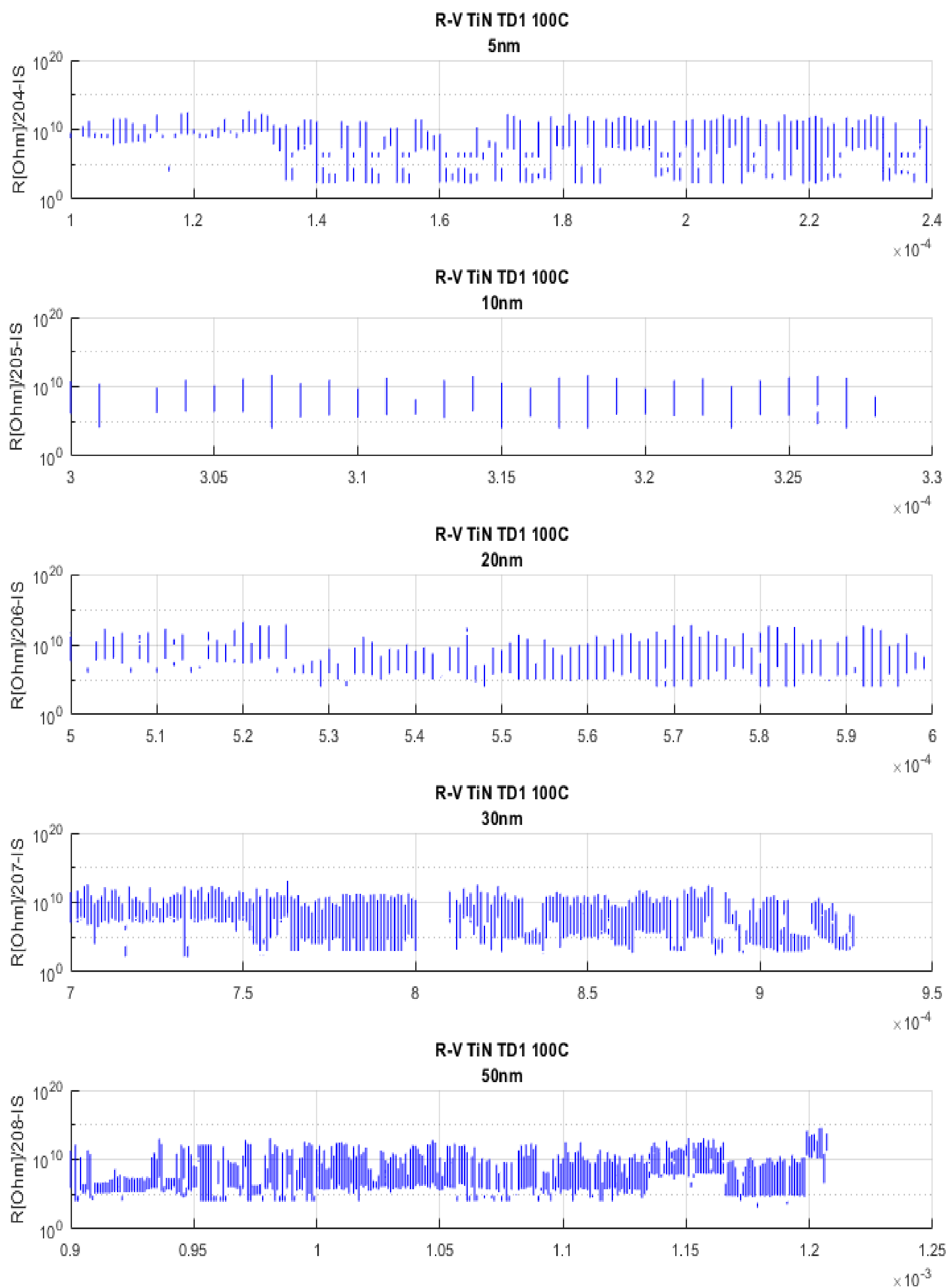

Figure 10. *The overview of the ON and the OFF resistance of the 5nm-50nm-thick samples deposited using the TD1 target (ZY view)*

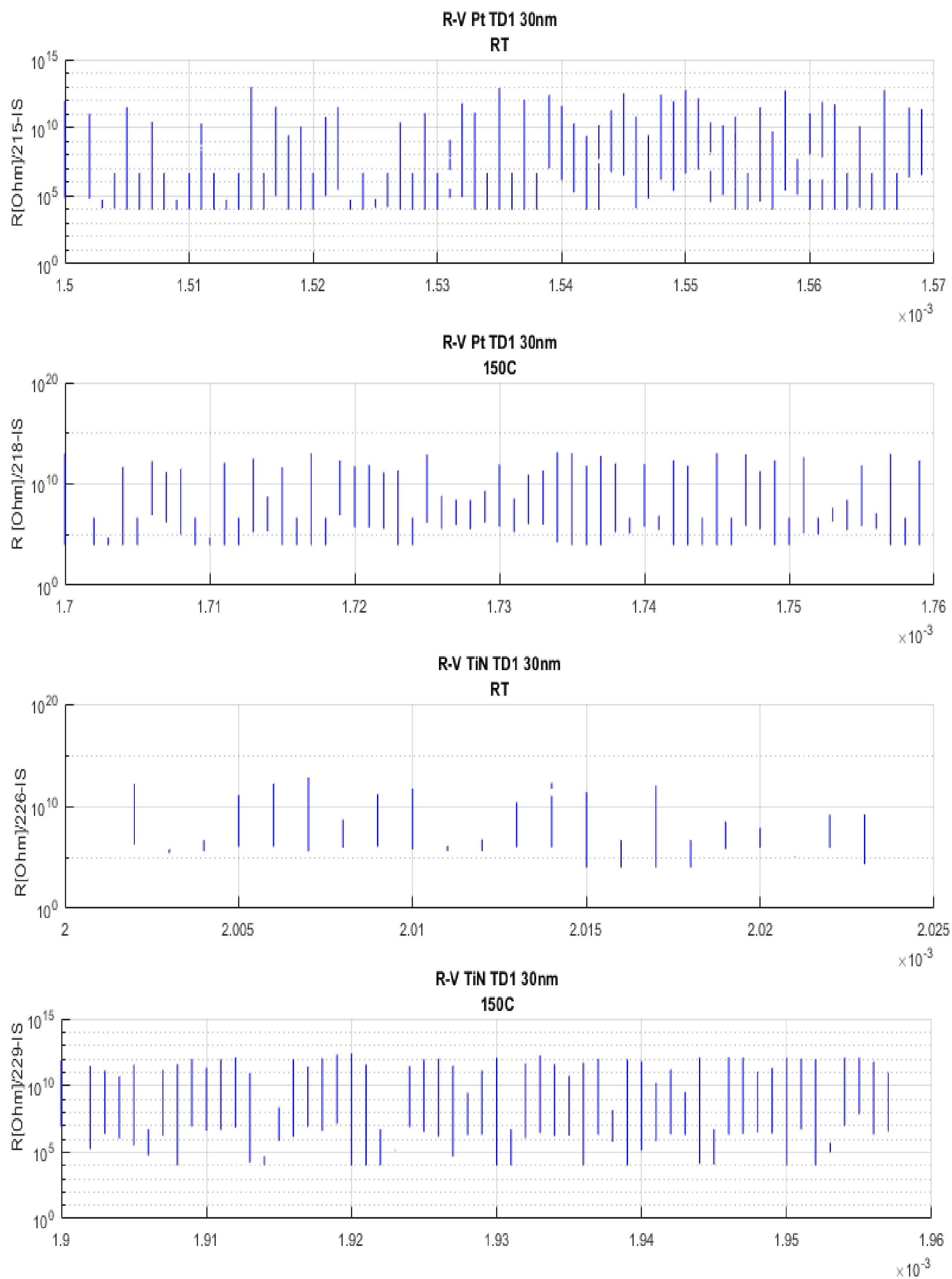

Figure 11. *The overview of the ON and the OFF resistance of the samples deposited using the TD1 target on the platinum and the TiN substrates at RT and 150C (ZY view)*

1.3 The doped TD2 target

Figure 12 shows the resistance – voltage characteristics of the 10nm-thick sample deposited using the TD2 target on the platinum substrate at 100C. The transition from the OFF to the ON state occurs mostly through two steps. The first step is the gradual continuous increase in the conductivity and the second step is an abrupt transition to the ohmic ON state.

Figure 13 shows the R – V characteristics corresponding to the 30nm-thick sample deposited using the TD2 target on the TiN substrate at 150C. The transition between OFF and ON states is mostly not abrupt. In addition, the last conductive stage of the curve is not ohmic as in Figure 12. Instead, on the semilogarithmic scale, it is rather a straight line implying exponential dependence. In addition, at the end of the positive or negative sweep, the cell is OFF near the zero point.

Figure 14 shows the resistance – voltage characteristics of the 30nm-thick sample deposited using the TD2 target on the TiN substrate at RT. The transition from the OFF to the ON state occurs in two steps. First, there is an abrupt transition to a certain level and then a gradual transition to the ON state, however, with the vague curve's shape.

Figure 15 shows the resistance – voltage characteristics of the same sample as in Figure 14. The electroforming curve is mostly of the metallic type, however, at the end, the cell is OFF near the zero point.

Figure 16 shows the resistance – voltage characteristics of the same sample shown in Figure 14 and Figure 15. The transition from the OFF to the ON state is not abrupt but rather gradual on the negative side. The conductive ON state is ohmic. On the negative side, however, the cell first makes the transition to the more resistive state and at the end of the backward sweep, the curve can be approximated as the inclining line on the semilogarithmic scale.

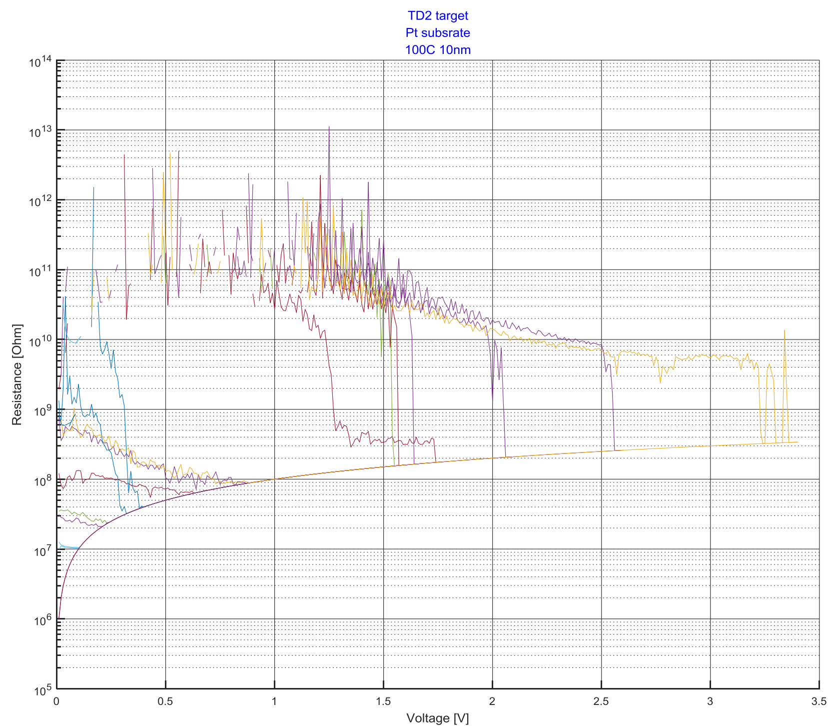

Figure 12. *The resistance – voltage characteristics of the 10nm-thck sample deposited using the TD2 target on the platinum substrate at 100C*

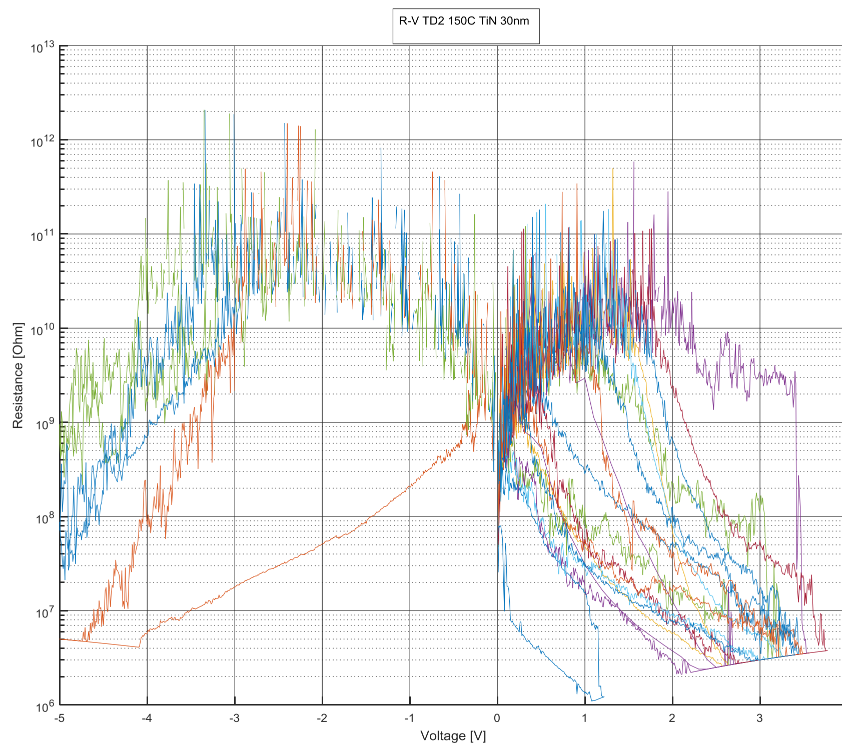

Figure 13. *The resistance – voltage characteristics of the 30nm-thick sample deposited using the TD2 target on the TiN substrate at 150C*

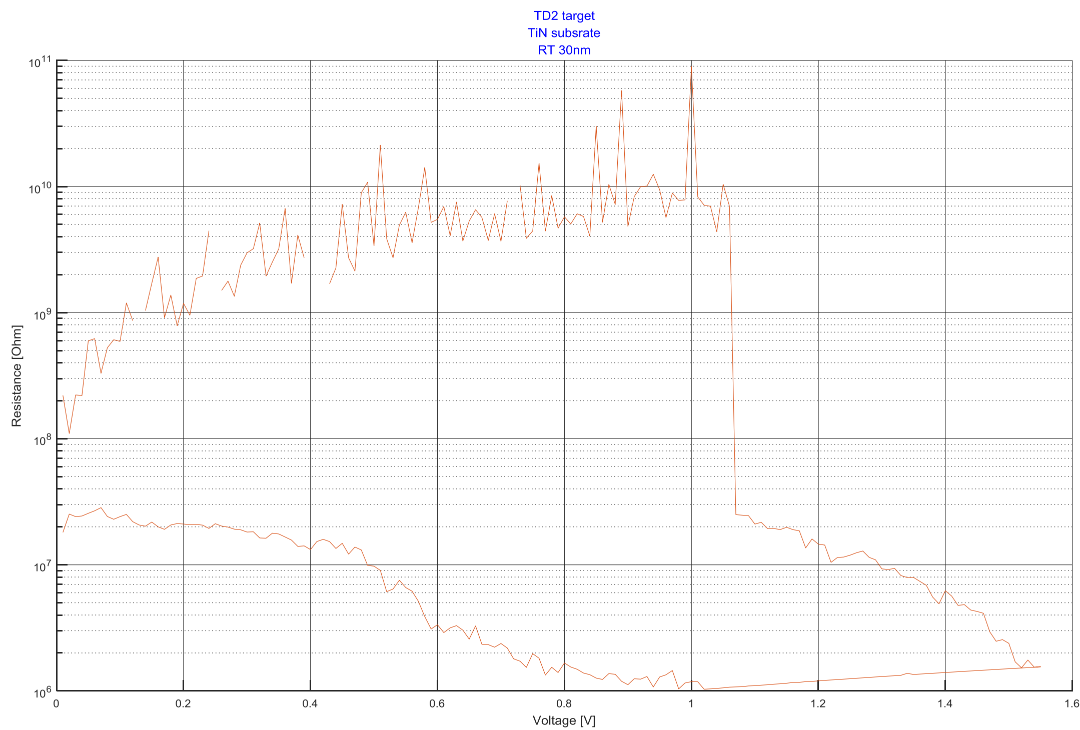

Figure 14. *The resistance – voltage curve corresponding to the 30nm-thick sample sputtered using the TD2 target on the TiN substrate at RT*

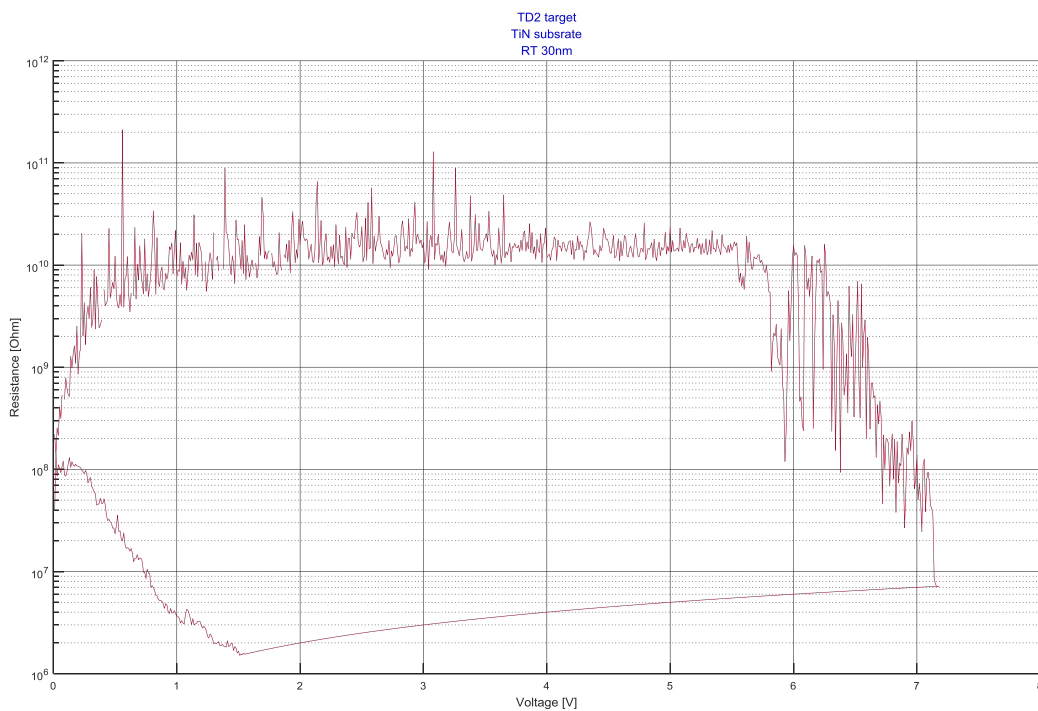

Figure 15. *The resistance – voltage characteristics of the 30nm-thick sample deposited using the TD2 target on the TiN substrate at RT*

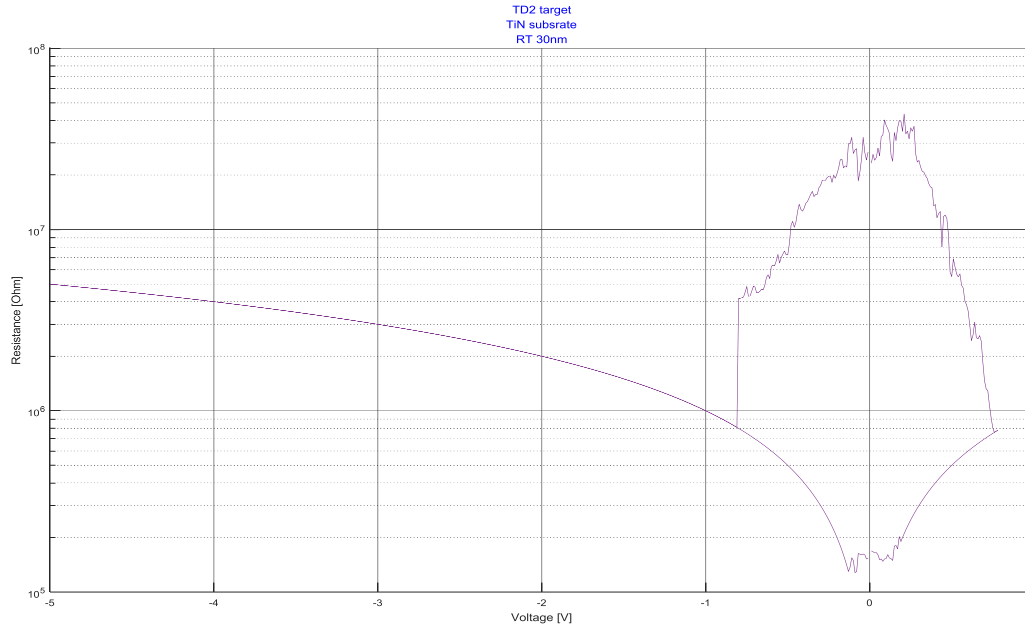

Figure 16. *The resistance – voltage characteristics of the 30nm-thick sample deposited using the TD2 target on the TiN substrate at RT*

Figure 17 shows the resistance – voltage characteristics of the 30nm-thick sample deposited using the TD2 target on the TiN substrate at RT. When the semilogarithmic scale is used, the transition between the OFF and the ON states seems to be a straight line.

Figure 18 shows the resistance – voltage characteristics corresponding to the same sample as in Figure 17. At the end of the backward sweep on the negative side, when the semilogarithmic scale is used, the curve becomes the straight line.

Figure 19 shows the resistance – voltage characteristics corresponding to the same sample shown in Figure 17 and Figure 18. The transition from the OFF to the ON state is abrupt at the positive bias. In addition, the cell is OFF at the end of the positive cycle again. At the negative bias, the cell makes the gradual transition from the OFF to the ON state and in the opposite direction.

Figure 20 shows the resistance – voltage characteristics of the 50nm-thick sample deposited using the TD2 target on the platinum substrate at 100C. The cell shows the typical metallic type of switching with the symmetric transition from the OFF to the ON state on both the positive and the negative sides.

Figure 22 shows the resistance – voltage characteristics of the same sample shown in Figure 20 and Figure 21. There was a very high rising rate of voltage, which was then adjusted for further testing. However, it looks like some sort of threshold-like switching.

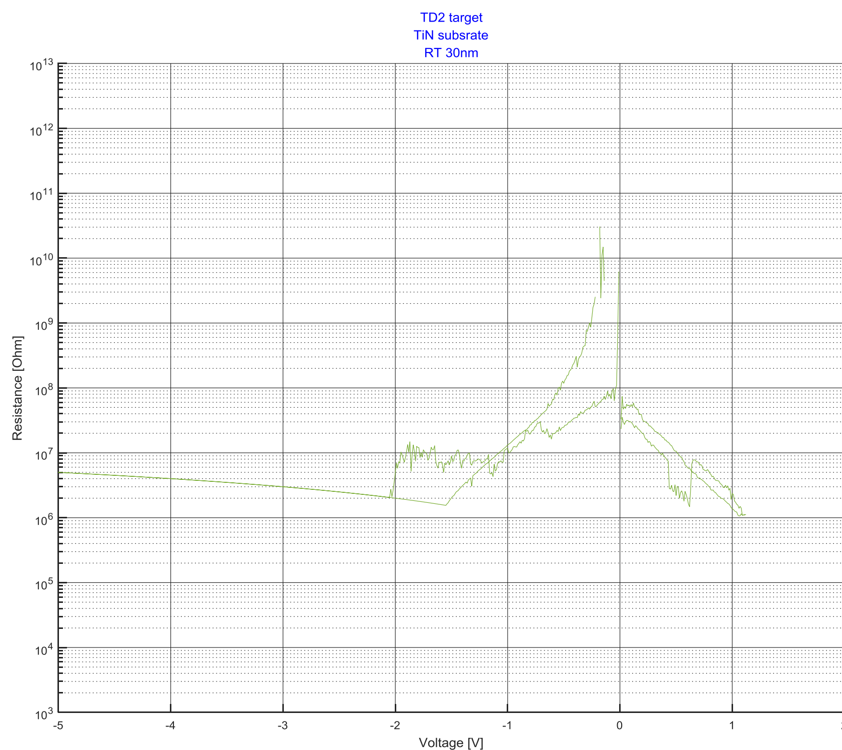

Figure 17. *The resistance – voltage characteristics of the 30nm-thick sample deposited using the TD2 target on the TiN substrate at RT*

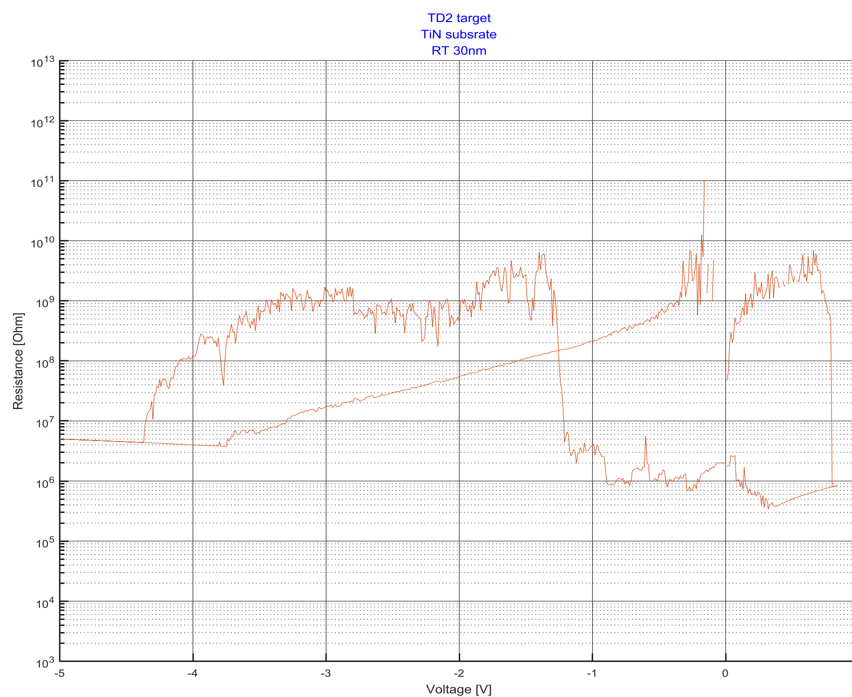

Figure 18. *The resistance – voltage characteristics of the 30nm-thick sample deposited using the TD2 target on the TiN substrate at RT*

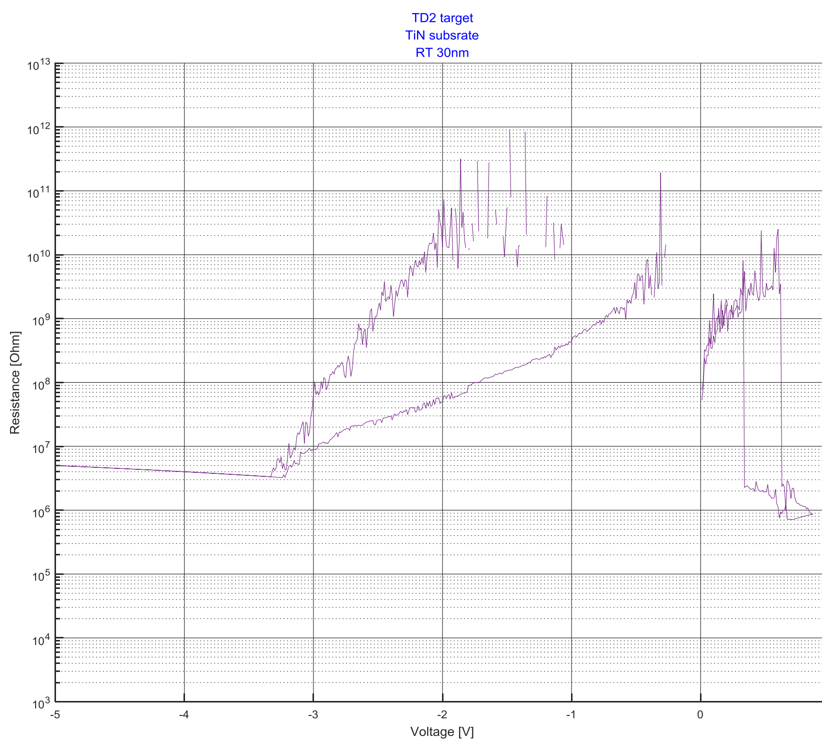

Figure 19. *The resistance – voltage characteristics of the 30nm-thick sample deposited using the TD2 target on the TiN substrate at RT*

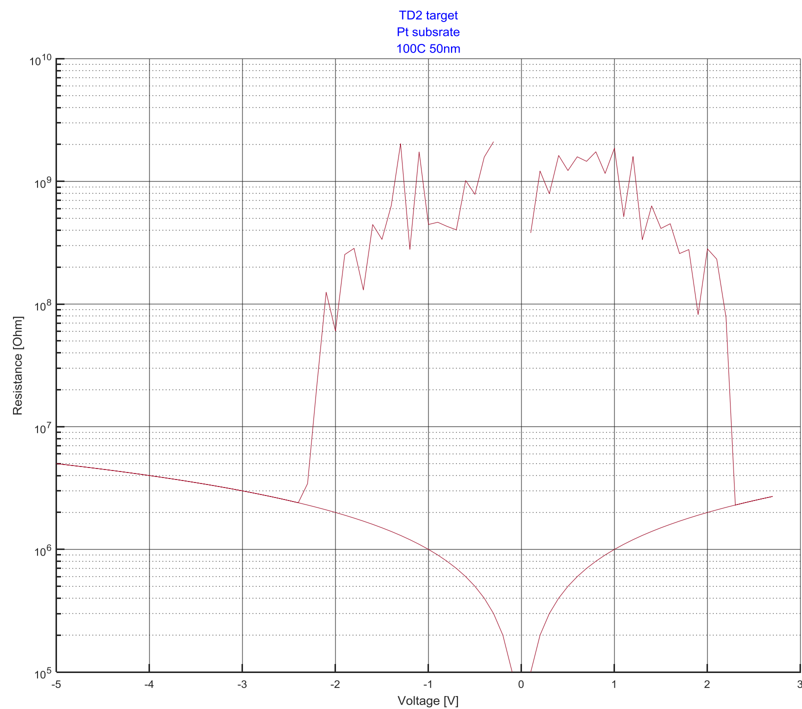

Figure 20. *The resistance – voltage characteristics of the 50nm-thick sample deposited using the TD2 target on the platinum substrate at 100C*

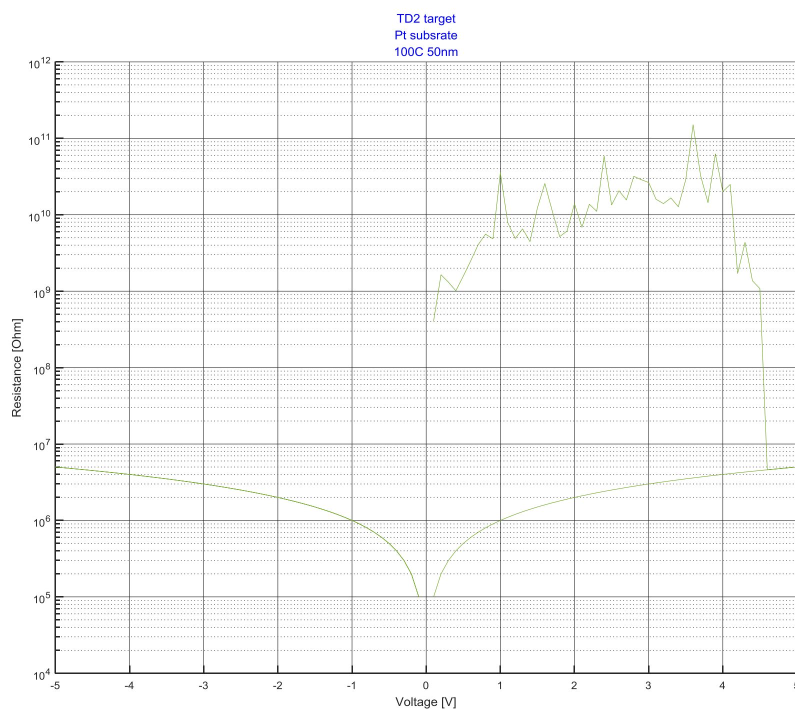

Figure 21. *The resistance – voltage characteristics of the 50nm-thick sample deposited using the TD2 target on the platinum substrate at 100C*

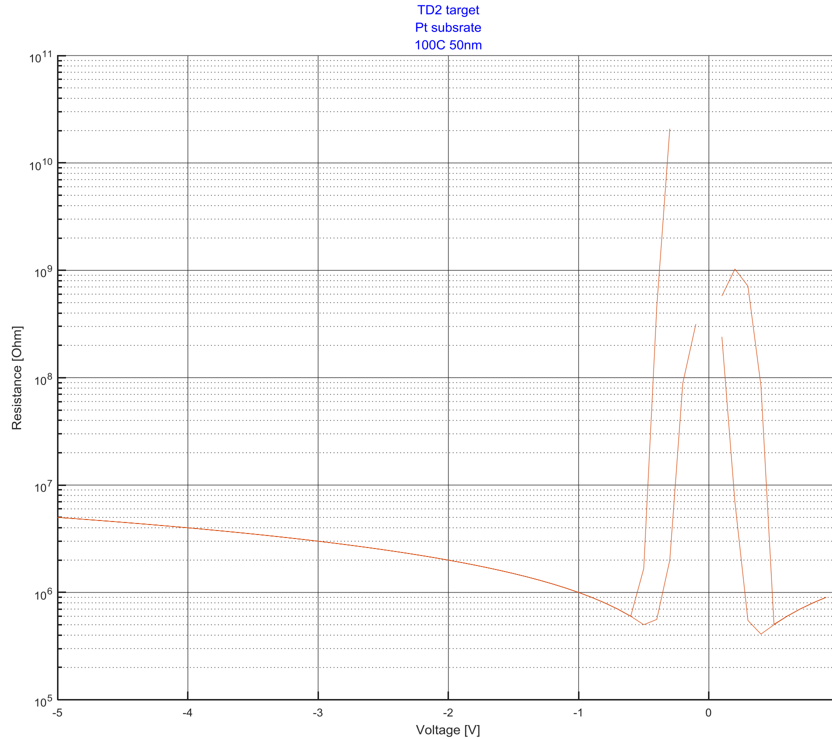

Figure 22. *The resistance – voltage characteristics of the 50nm-thick sample deposited using the TD2 target on the platinum substrate at 100C*

Figure 23 shows the overview of the ON and OFF resistance of the samples with the thickness between 5nm and 50nm deposited using the TD2 target on the platinum substrate at 100C. It can be seen there is a varying trend in the OFF and ON states. Some samples show the OFF resistance more than or less than 10^{-10}Ohms. The same trends are seen in the ON state. However, there are many short-circuited curves.

Figure 24 shows the overview of the ON and OFF resistance of the samples deposited using the TD2 target on the platinum and TiN substrates at RT and 150C. The samples deposited on the platinum substrates have slightly more short-circuited curves. The temperature effect was negligible for the TiN substrate; however, the sample deposited on the platinum substrate at 150C was more conductive than that deposited at RT due to a larger number of the short-circuited curves.

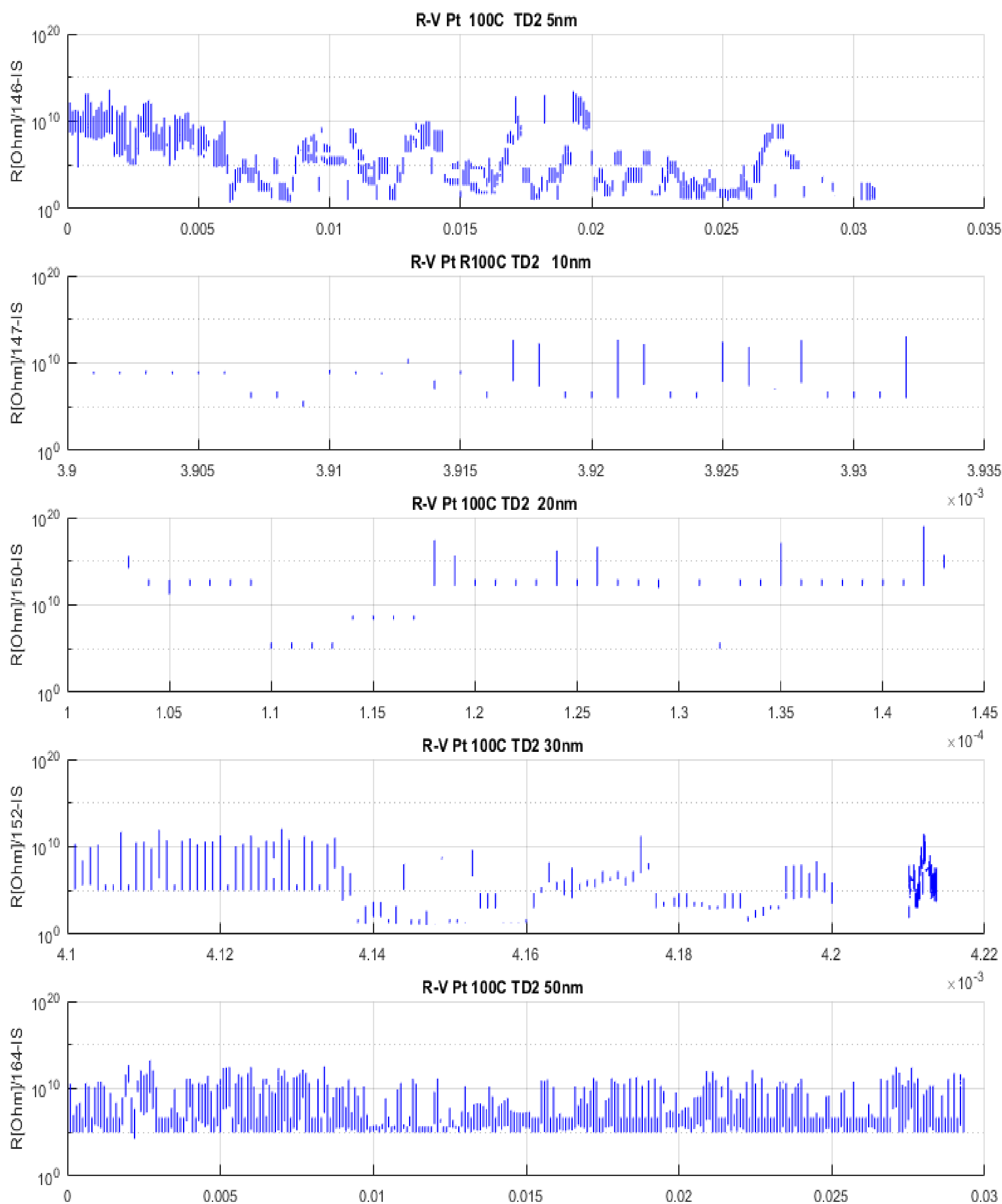

Figure 23. *The overview of the ON and the OFF resistance of the samples with the thickness between 5and 50nm deposited using the TD2 target on the platinum substrate at 100C (ZY view)*

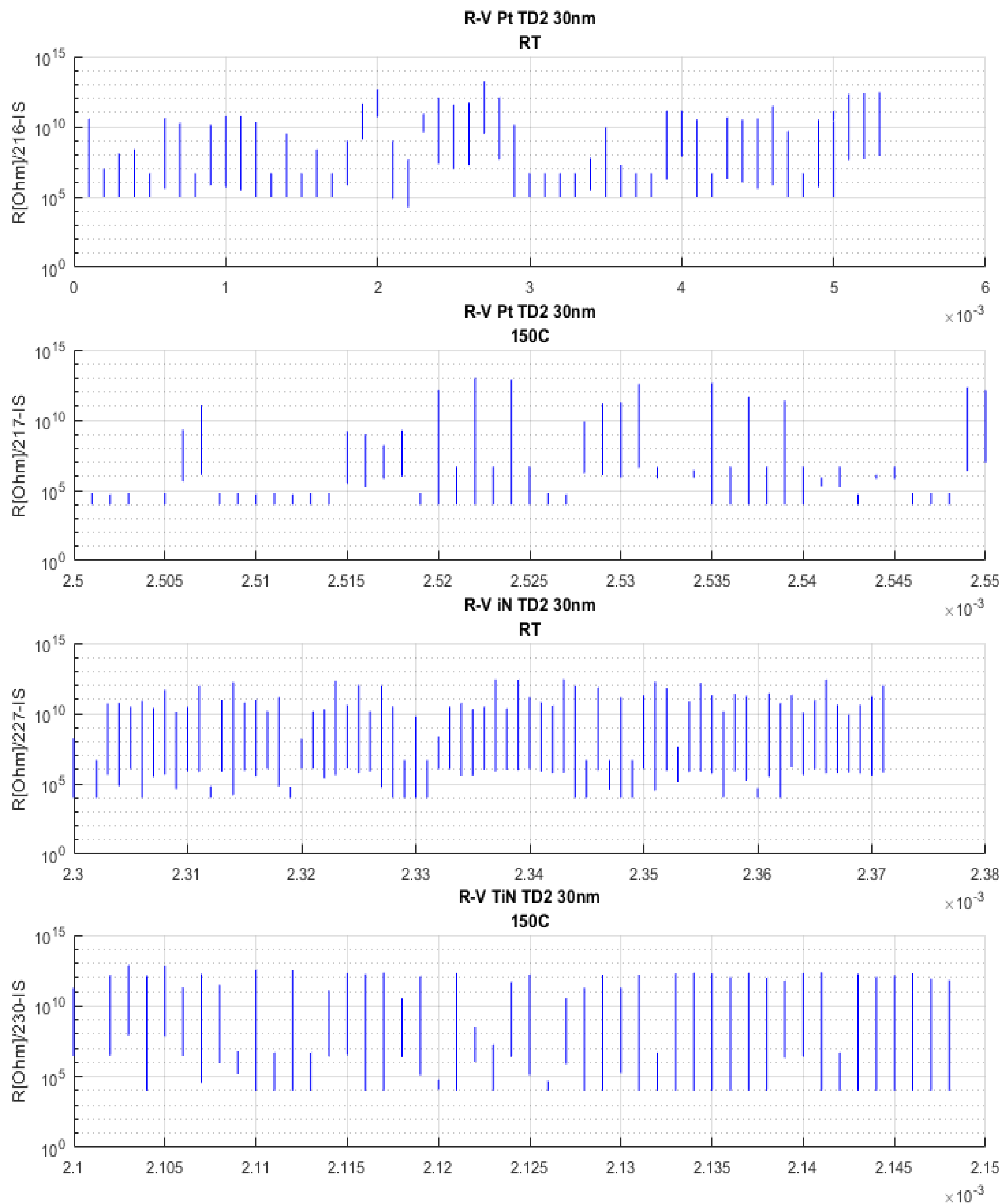

Figure 24. *The overview of the ON and the OFF resistance of the samples deposited using the TD2 target on the platinum and TiN substrates at RT and 150C (ZY view)*

Interpretation of results. When one describes the resistive switching, it is important to draw the resistance-voltage curve. When the curve has a specific shape in the semilogarithmic scale, it gives signposts what materials may participate in the switching. The variability in switching was extremely high. The curves have different shapes attributed to the different conduction mechanisms. Due to high variability as well as a large number of used parameters, it would make impossible to attribute the specific feature to the certain target.

The straight line in the semilogarithmic scale is associated with the doped targets as well as to the instability of the conductive filaments. This instability may be related to the presence of mechanical stress due to the introduction of the secondary phase, for example, due to oxidations. The unstable conductive filament causes rather the unipolar type than the bipolar type of switching.

The shape of the curve depends on the used parameters. However, the search of suitable parameters can be a very tedious task. Additionally, when the cell exhibits the threshold or metallic type of switching, such a cell does not change the switching type to another. Typically, the threshold-like and metallic types of switching require the different testing techniques. If one tried to change the switching type, such a cell would probably be short-circuited.

The threshold-like as well as memory (or metallic) switching was observed in samples deposited by all three targets. However, the most pronounced threshold-like switching behavior was observed in samples, deposited by TD0 target on the platinum substrate, which is explained separately in Appendix 9.

REFERENCES

Balakrishnan, M., Thermadam, S.C.P., Mitkova, M. & Kozicki, M.N. (2006). A low power non-volatile memory element based on copper in deposited silicon oxide, 2006 7th Annual Non-Volatile Memory Technology Symposium, IEEE, pp. 104-110.

Equations of straight lines on various graph papers

Lim, E.W. & Ismail, R. (2015). Conduction Mechanism of Valence Change Resistive Switching Memory: A Survey, Electronics, Vol. 4(3), pp. 586-613.

Mehonic, A., Vrajitoarea, A., Cueff, S., Hudziak, S., Howe, H., Labbe, C., Rizk, R., Pepper, M. & Kenyon, A. (2013). Quantum conductance in silicon oxide resistive memory devices, Scientific reports, Vol. 3pp. 2708.

Tomozeiu, N. (2011). Silicon oxide (SiOx, 0< x< 2): a challenging material for optoelectronics, Optoelectronics–Materials and Techniques.Ed.Predeep, P.

Wouters, D. (2012). Resistive switching materials and devices for future memory applications, Tutorial on 43 rd IEEE Semiconductor Interface Specialists Conference (SISC), San Diego.

APPENDIX 9

” THE THRESHOLD SWITCHING”

TO THE MASTER THESIS “CHARACTERIZATION OF THE DOPED SILICON DIOXIDE AND ITS IMPLICATION ON THE RESISTIVE SWITCHING PHENOMENA IN THE ELECTROCHEMICAL METALLIZATION CELLS”

LIST OF FIGURES

Figure 1. The overview of the current-voltage characteristics of the samples deposited using the TD0 target on the platinum substrate at RT showing the threshold-like switching behavior 2
Figure 2. The test for the Schottky emission: ln(J) – sqrt(E) of the sample deposited on the platinum substrate at RT. 3
Figure 3. The test for the Schottky emission: the ZY view of log(J)-sqrt(E) of the sample deposited on the platinum substrate at RT 4
Figure 4. The test for the Frenkel-Poole emission: the 3D view of log(J)-sqrt(E) of the sample deposited on the platinum substrate at RT 5
Figure 5. The test for the Frenkel-Poole emission: the 3D view of log(J)-sqrt(E) of the sample deposited on the platinum substrate at RT 5
Figure 6. The overview of the current-voltage characteristics of the samples deposited using the TD0 target on the platinum substrate at 150C showing the threshold-like switching behavior 6
Figure 7. The current-voltage characteristics of the samples deposited using the TD0 target on the platinum substrate at 150C showing the threshold-like switching behavior 7
Figure 8. The test for the Schottky emission: the ln(J) – sqrt(E) of the sample deposited using the TDO target on the platinum substrate at 150C. 8
Figure 9. The test for the Schottky emission: the ln(J) – sqrt(E) of the sample deposited using the TD0 target on the platinum substrate at 150C. 8
Figure 10. The test for the Frenkel-Poole emission: the 3D view of the log(J)-sqrt(E) of the sample deposited on the platinum substrate at 150C 9
Figure 11. The test for the Frenkel-Poole emission: the ZY view of the log(J)-sqrt(E) of the sample deposited on the platinum substrate at 150C 10

1.1.1 Threshold switching

1.1.1.1 *Room temperature*

1.1.1.1.1 The I-V curves

Figure 1 displays the overview of the I-V curves corresponding to the samples deposited using the TD0 target on the platinum substrate at RT displaying the threshold-like switching behavior. Three different types of the I-V curves can be observed; therefore, they are shown separately in the following figures.

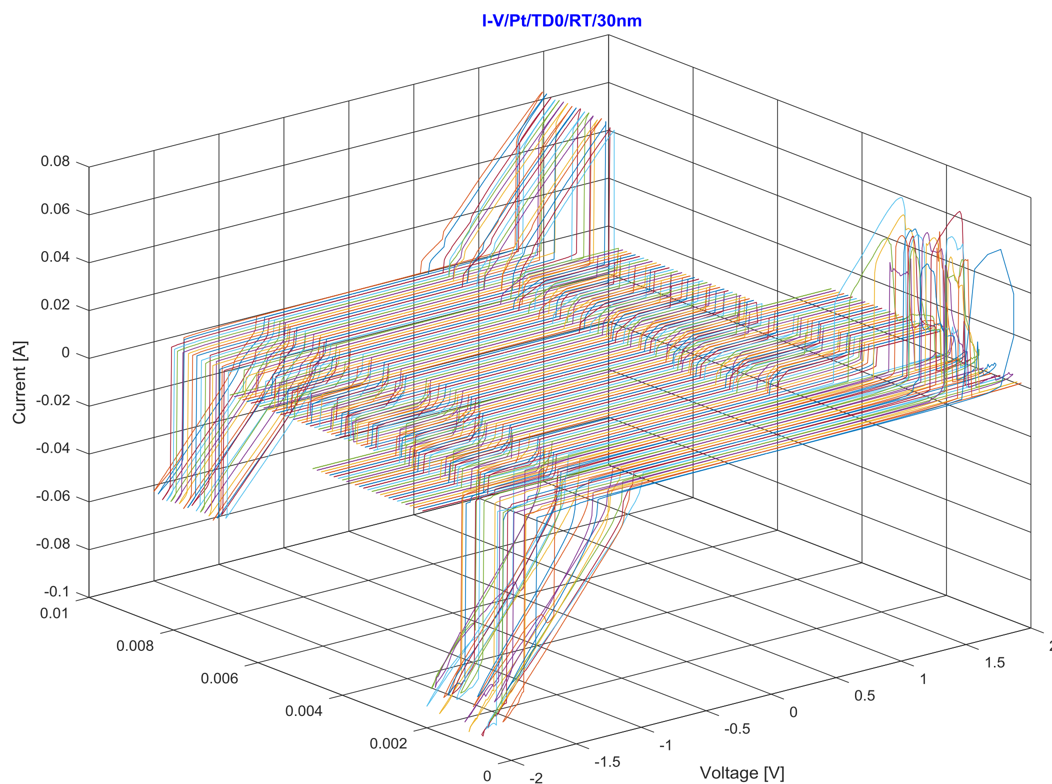

Figure 1. *The overview of the current-voltage characteristics of the samples deposited using the TD0 target on the platinum substrate at RT showing the threshold-like switching behavior*

1.1.1.1.2 The Schottky emission

Figure 2 shows the 3D data fitting of 100 curves for the identification of the Schottky emission as the conduction mechanism. One curve from the same data in ZY view is plotted separately in Figure 3.

A part of the curve as shown in Figure 3 may be seen as a straight line using the logarithmic scales in a region corresponding to the OFF state. However, the overall impression is that the Schottky emission as conduction mechanism is not the dominating type. Also, the shape variation in the curves corresponds to the change in the current compliance.

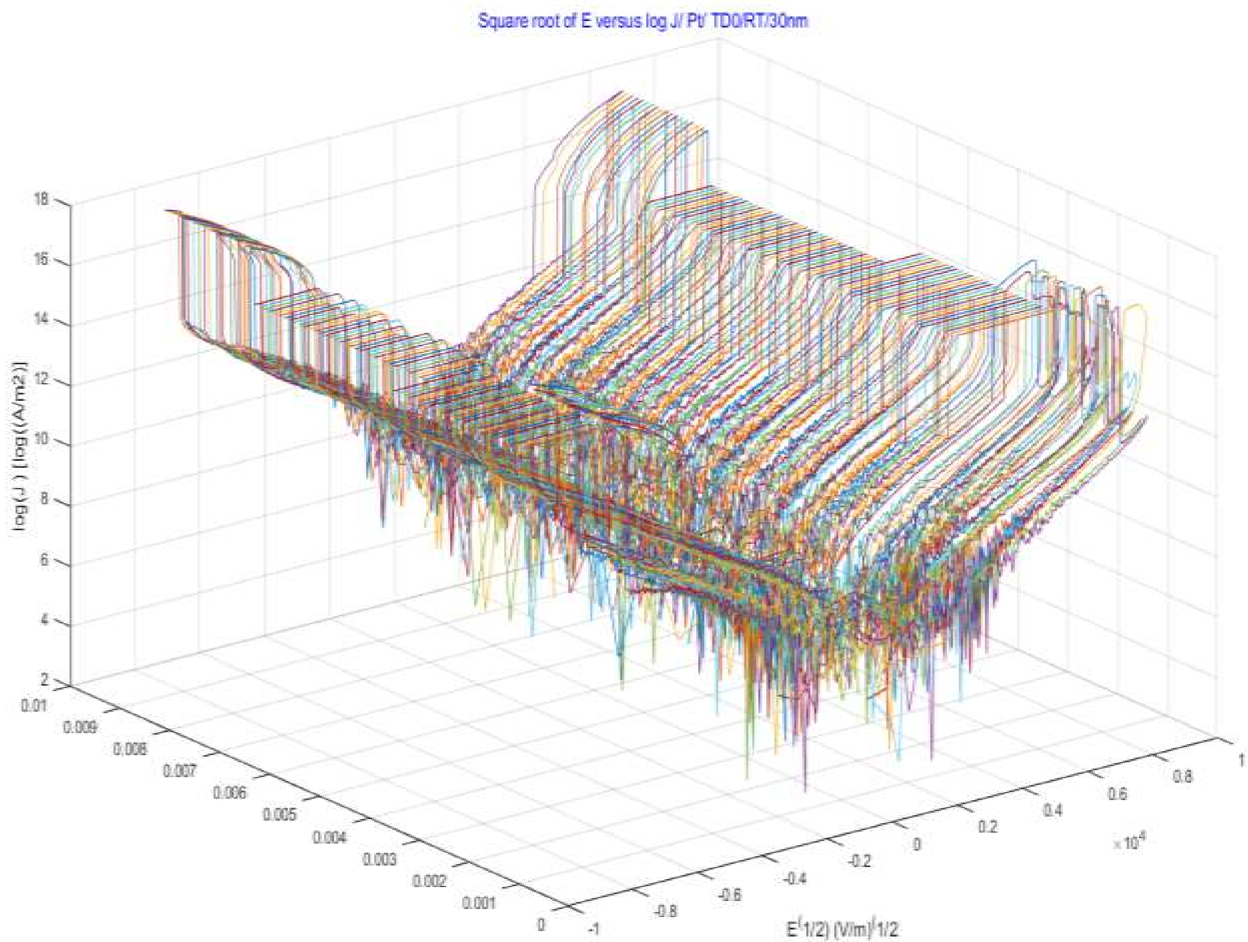

Figure 2. *The test for the Schottky emission: ln(J) – sqrt(E) of the sample deposited on the platinum substrate at RT.*

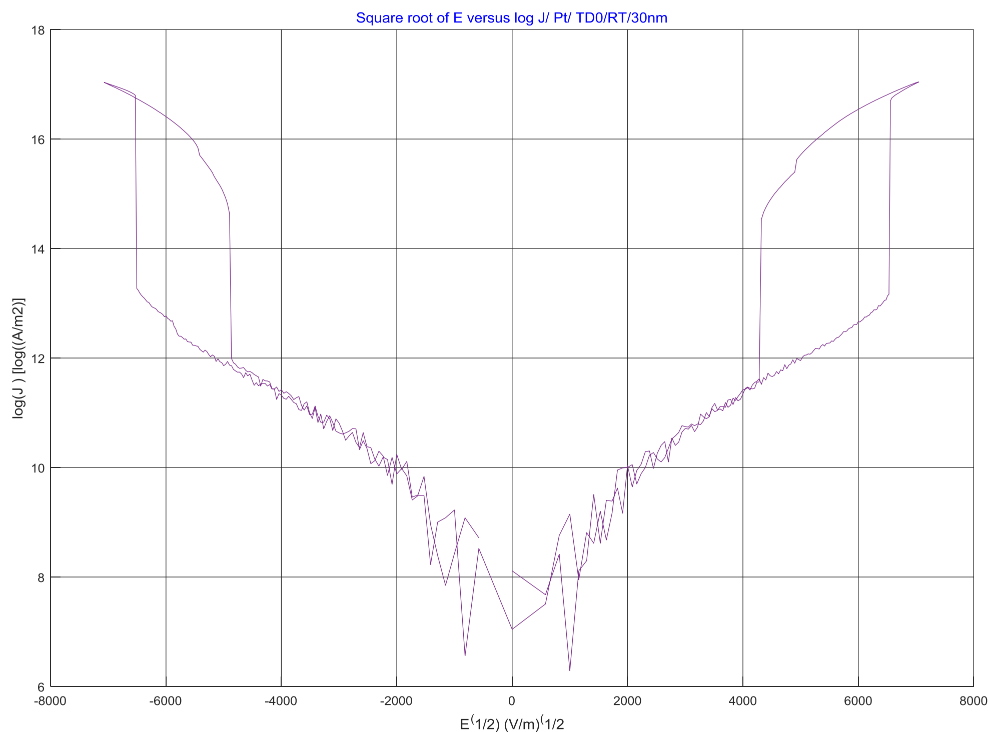

Figure 3. *The test for the Schottky emission: the ZY view of log(J)-sqrt(E) of the sample deposited on the platinum substrate at RT*

1.1.1.1.3 The Frenkel-Poole emission

Figure 4 shows the 3D data fitting of 100 curves for the identification of the Frenkel-Poole emission as the conduction mechanism. One curve from the 3D group was plotted separately in Figure 5.

It is worth noting from Figure 5 that only relatively small regions in the curves can be approximated as straight lines using this scale. Therefore, it can be stated that the Poole-Frenkel mechanism is not the dominant conduction mechanism.

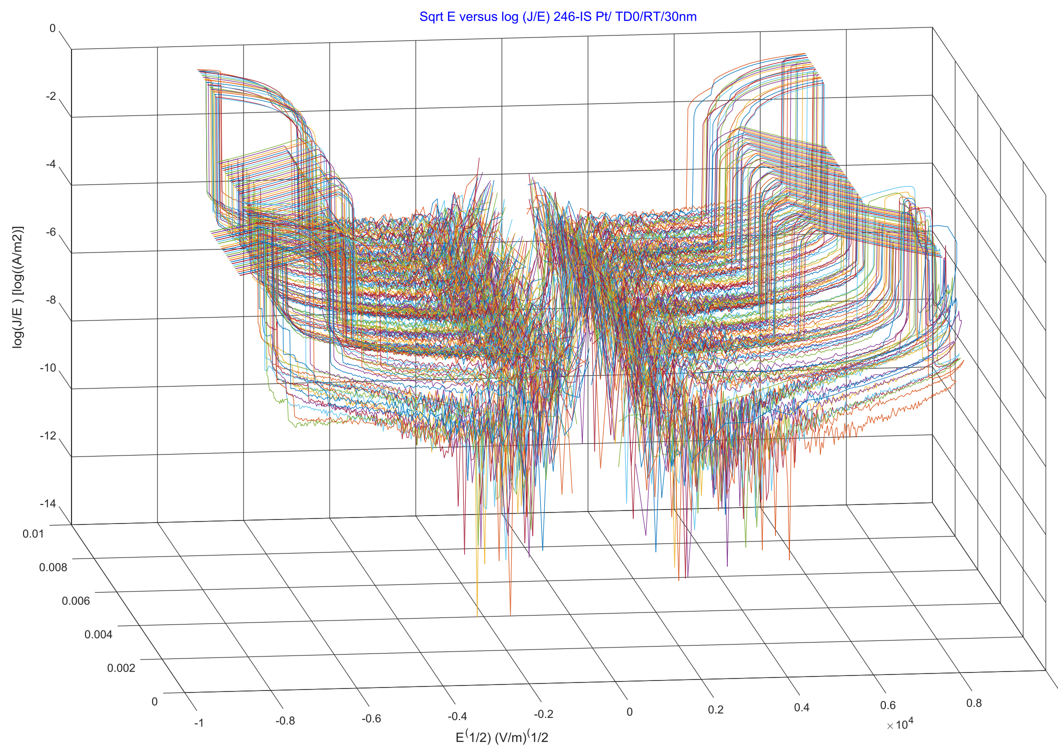

Figure 4. *The test for the Frenkel-Poole emission: the 3D view of log(J)-sqrt(E) of the sample deposited on the platinum substrate at RT*

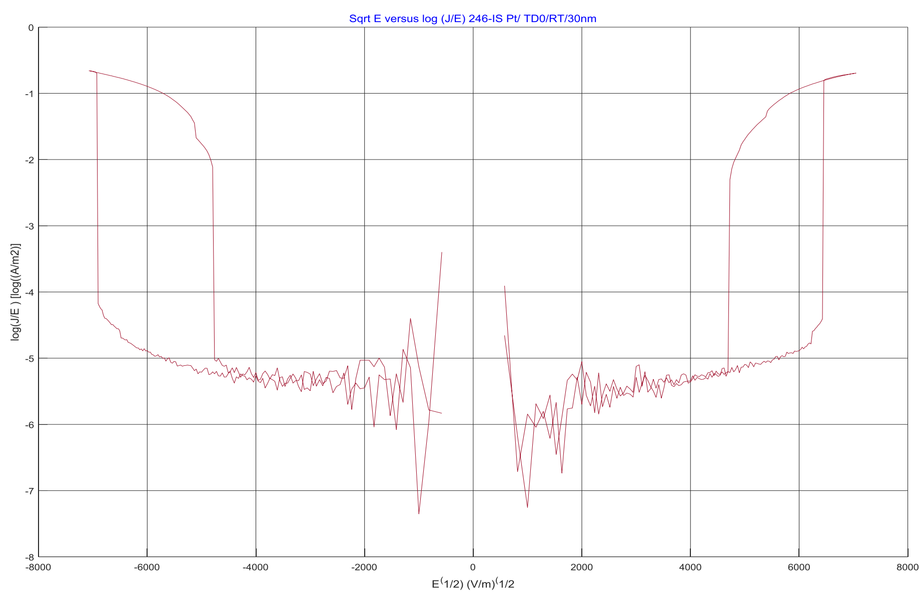

Figure 5. *The test for the Frenkel-Poole emission: the 3D view of log(J)-sqrt(E) of the sample deposited on the platinum substrate at RT*

1.1.1.2 *150C*

1.1.1.2.1 The I-V curves

Figure 6 shows a 3D view of the 103 current-voltage curves of the samples deposited using the TD0 target on the platinum substrate at 150C showing threshold-like switching behavior. In addition, the ZY view of the data is separately shown in the next figures.

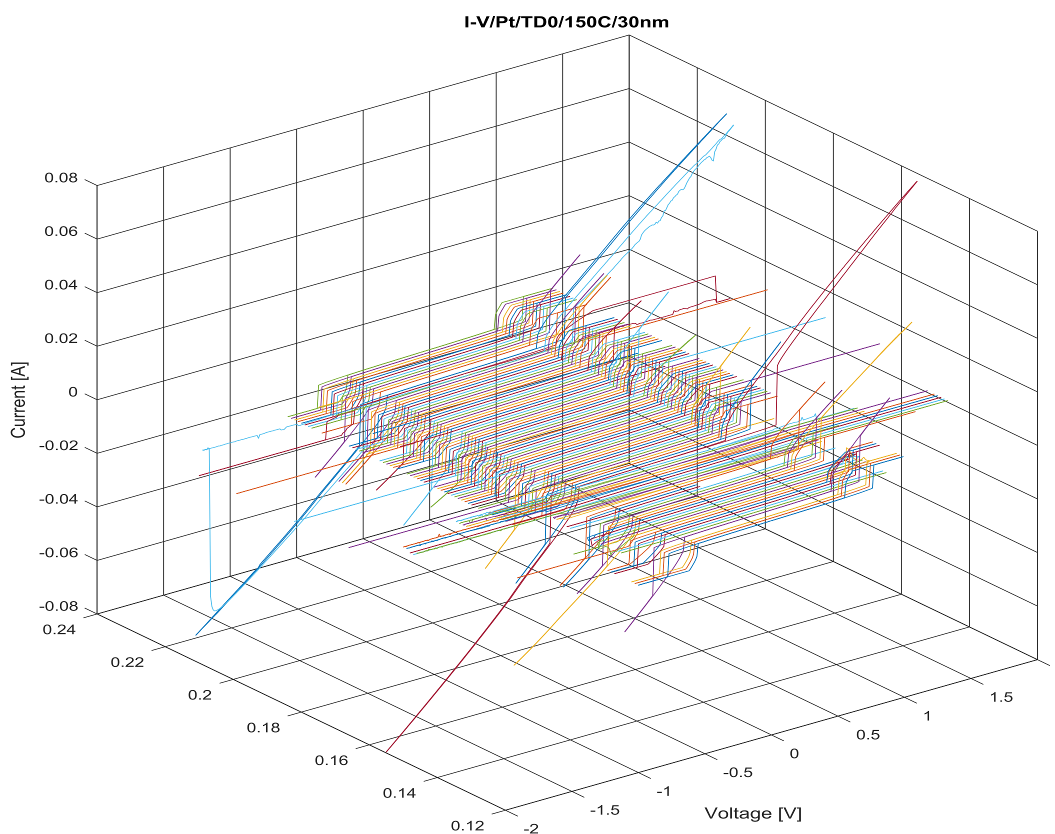

Figure 6. *The overview of the current-voltage characteristics of the samples deposited using the TD0 target on the platinum substrate at 150C showing the threshold-like switching behavior*

Figure 7 shows the example of the curves without overshooting peaks on the negative side. It means that opposite electrodes were connected first and then disconnected as a result of the electrochemical dissolving the metallic filament. However, the curve on the positive side has an overshooting peak, which means that the electrodes stayed connected during the forward and the backward sweep.

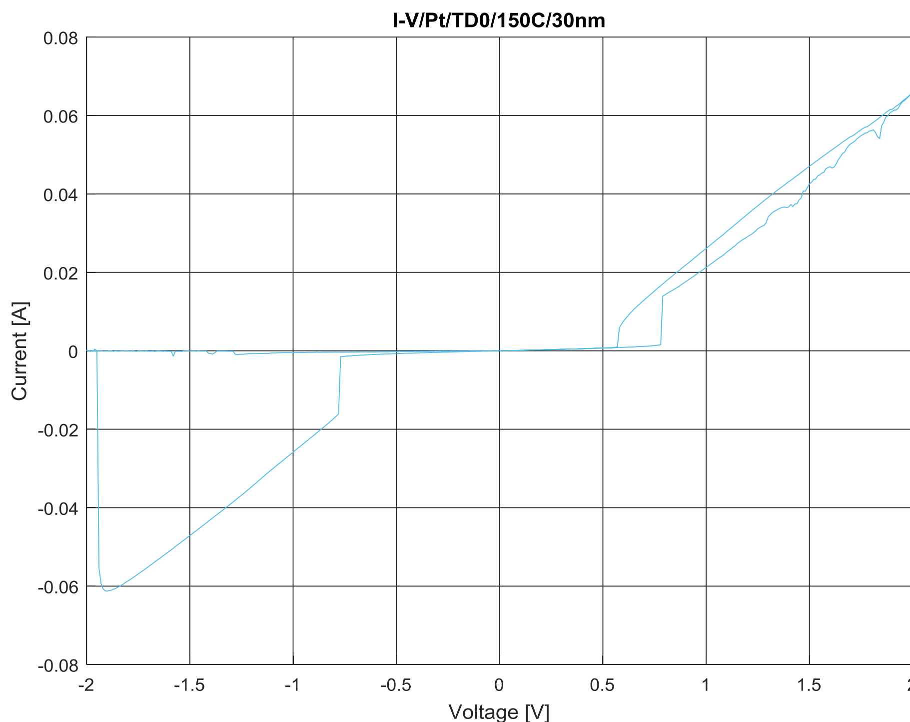

Figure 7. *The current-voltage characteristics of the samples deposited using the TD0 target on the platinum substrate at 150C showing the threshold-like switching behavior*

1.1.1.2.2 The Schottky emission

Figure 8 shows the 3D data fitting of 103 curves for identification of the Schottky emission as the conduction mechanism. One curve was plotted separately as it can be seen in Figure 9.

In Figure 9, a small part of the curve may be thought as an approximated straight line when the logarithmic scale in the OFF state is used. However, in general, it seems that in this sample the Schottky emission as conduction mechanism is not the dominating type.

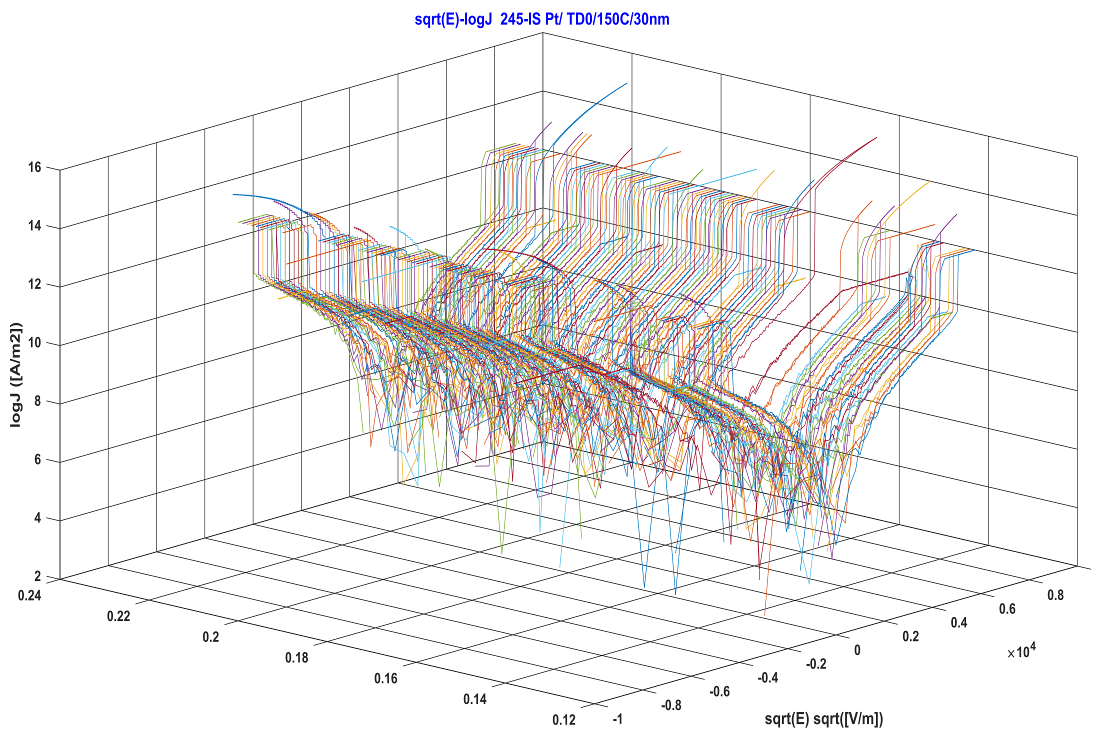

Figure 8. *The test for the Schottky emission: the ln(J) – sqrt(E) of the sample deposited using the TDO target on the platinum substrate at 150C.*

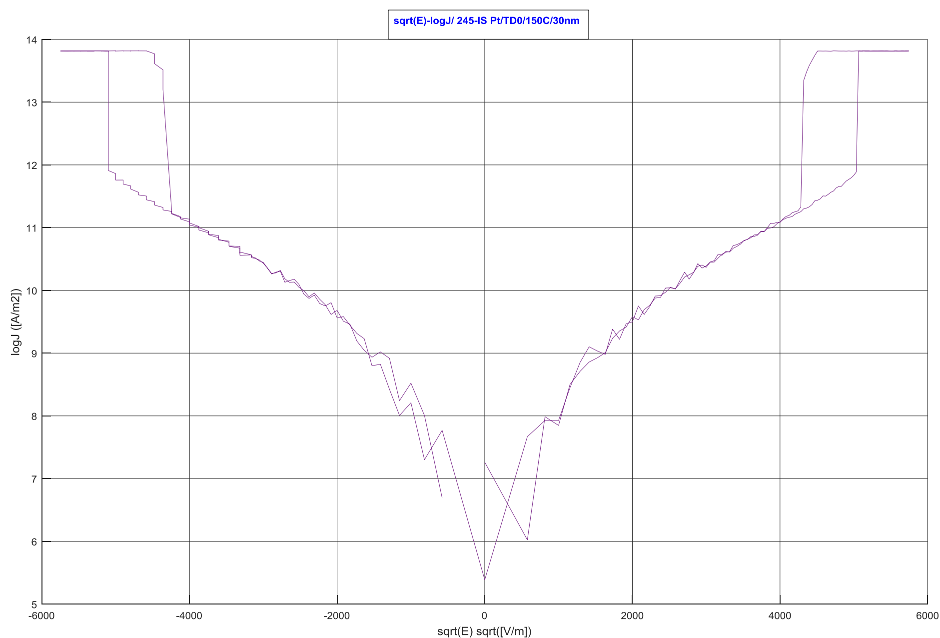

Figure 9. *The test for the Schottky emission: the ln(J) – sqrt(E) of the sample deposited using the TD0 target on the platinum substrate at 150C.*

1.1.1.2.3 The Frenkel-Poole emission

Figure 10 shows the 3D data fitting of 103 curves for the identification of the Frenkel-Poole emission as the conduction mechanism. One curve of the same data in ZY view is drawn in Figure 11.

In Figure 11, for example, only very small regions in the curves can be approximated as a straight line using this scale. Therefore, it can be stated that the Poole-Frenkel mechanism is not the dominant conduction mechanism.

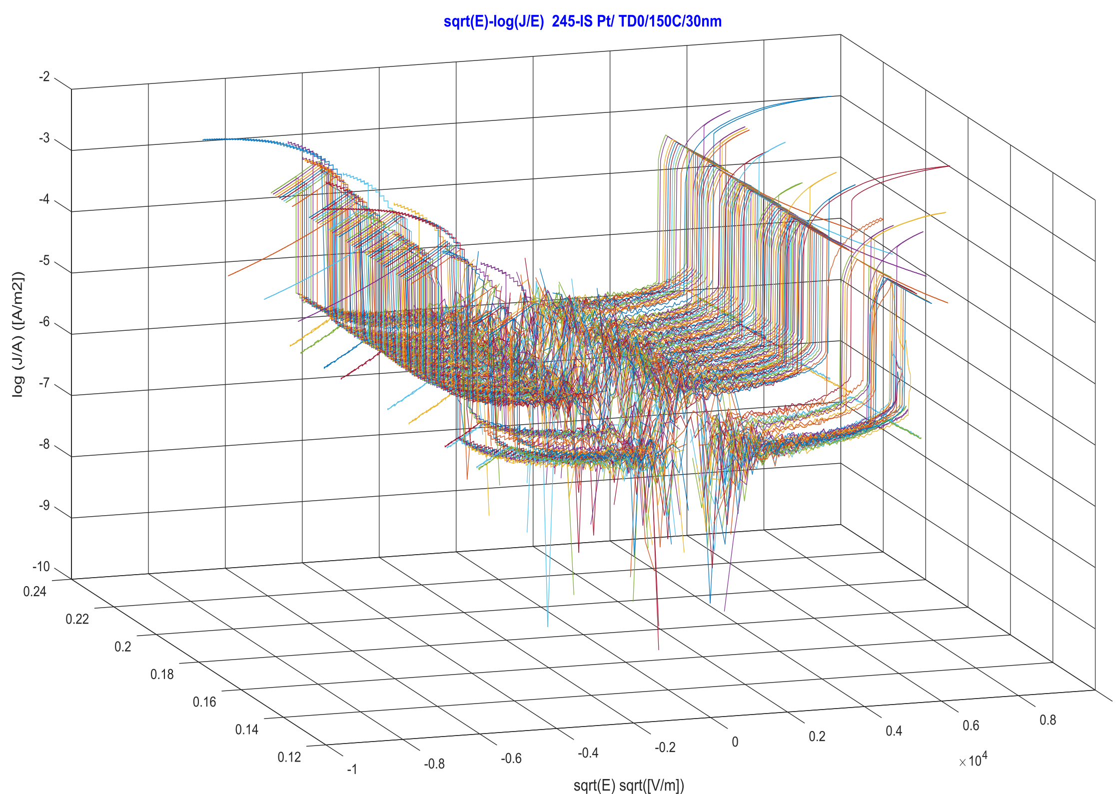

Figure 10. *The test for the Frenkel-Poole emission: the 3D view of the log(J)-sqrt(E) of the sample deposited on the platinum substrate at 150C*

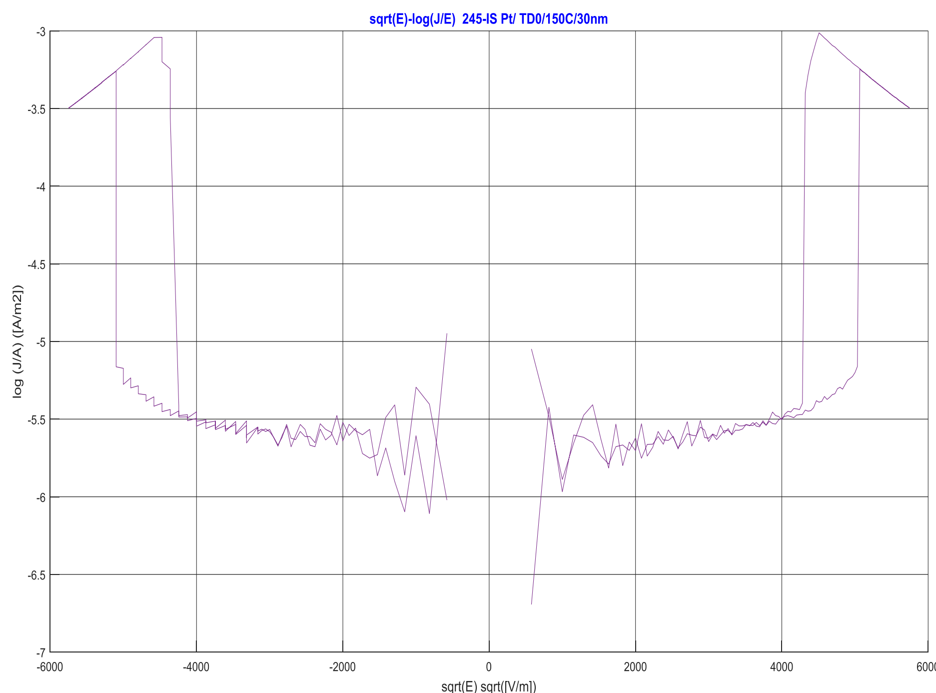

Figure 11. *The test for the Frenkel-Poole emission: the ZY view of the log(J)-sqrt(E) of the sample deposited on the platinum substrate at 150C*

Interpretation of obtained results. Two 30nm-thick samples deposited on the platinum substrate at RT (246-IS) and 150C (245-IS) exhibit the threshold-like behavior. The current-voltage characteristics of sample N245-IS (150C) are shown Figures 24-26 and Figures 38-39 of Master thesis. The current-voltage characteristics of sample N246-IS (RT) are shown in Figures 33-35 of Master thesis. The overview of the resistance-voltage characteristics of both samples is shown in Figure 4 of Appendix 8 as well in Figure 12 of this Appendix 9. Altogether, 13 cells of size 100µmx100µm from sample N245-IS (103 curves) and 16 cells of size 50µmx50µm from sample 246-IS (100 curves) exhibited the threshold-like behavior.

Unlike all other samples, the variability of switching voltage, the used current compliance, as well as resistance, in these samples with threshold-like behavior was extremely low as shown in Figure 12 of this Appendix 9. With only a few exceptions, both these samples started to switch with the threshold-like type of behavior, when the current compliance was set at 0.01A or 0.1A. The shape of the curve was quadratic with the current compliance of 0.01V and triangular with the current compliance of 0.1V. However, when the current compliance was set at 0.001, the switch was always closed. In addition, the hysteresis has disappeared as shown in Figure 26 of Master thesis.

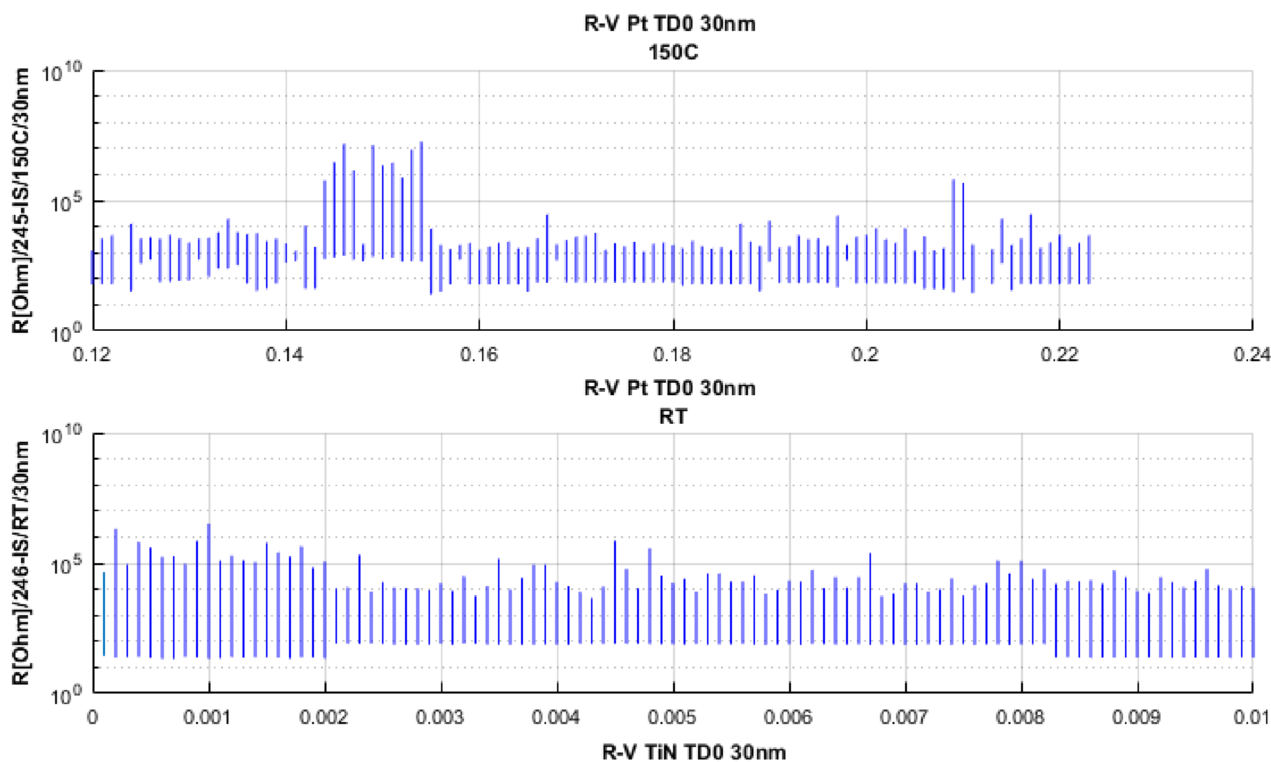

Figure 12. *The ZY view of the ON and the OFF resistance of the samples deposited using the TD0 target on the platinum substrate at RT (245-IS) and 150C (246-IS).*

The electrical measurement of both samples, which exhibited the threshold-like behavior, was performed 1st June 2016 in Aachen Germany. When the report about the threshold-like behavior was sent 27st June 2016, it was suggested that the reason and theoretical explanation of threshold-like behavior need to be investigated in more detail. However, after 1st June 2017, it was extremely difficult to reproduce such kind of behavior. The possible explanation can be due to the different moisture uptake. The possible influence of moisture on the type of switching is consistent with the explanation based on the Pourbaix diagram, wetting and dewetting of nanopores as well as the effect of pH on the electrochemical activity of metallic cations in oxide during resistive switching.

The relative humidity was between 94% and 100% on 1st June 2016. All day was frog, dizzle as well as sprinkles and light rain. After 1st June 2016, the relative humidity varied a lot but was the mostly much-much less than 94%. Unfortunately, the relative humidity, atmospheric pressure or temperature were not usually taken into account as the monitoring parameters during the normal electrical measurements without using a vacuum. However, when the relative humidity varied typically between 35% to 100% from day to day, it would have an influence on the electric performance of all electronic devices. It may have influence, especially on the nanoscale devices, which work in non-controllable atmospheric conditions.

The using Pourbaix diagram for the interpretation of results and influence of pH on the electrochemical activity of metallic cations in oxide during resistive switching are explained in more details in Appendix 2. The explanation of observed effects related to wetting and dewetting of nanopores and their influence on ionic transport together with ionic Column blockade and quantized conductance is explained separately in Appendix 10.

APPENDIX 10

” *Quantum size effect and ionic Coulomb blockade*”

TO THE MASTER THESIS “CHARACTERIZATION OF THE DOPED SILICON DIOXIDE AND ITS IMPLICATION ON THE RESISTIVE SWITCHING PHENOMENA IN THE ELECTROCHEMICAL METALLIZATION CELLS”

LIST OF FIGURES

Figure 1. The SEM images of the planar Ag/SiO2 /Pt -based device displaying the growth of the conductive filament at a different time (Sun et al. 2014).. 8
Figure 2. The TEM images of the creating and erasing of a conductive filament in two different Ag: SiO2-based planar devices with different spacing between electrodes (a-c and h-i) (Yang et al. 2012)... 9
Figure 3. The SEM image displaying the displacement reaction of Al with Cu at a different time (60 sec. and 70sec.) (Chin et al. 2014) 10
Figure 4. I-V curves through a 12 nm polymer nanopore at a different pH values (Pevarnik et al. 2012) 11
Figure 5. Schematic of a biological voltage-gated porous channel junction with ionic selectivity at a different pH (Pevarnik et al. 2012).. 12
Figure 6. The observation of quantum conductance steps with inset of height of G0 (Zhao et al. 2015). 14
Figure 7. The example of a curve with the stepwise change of resistance in the 30 nm-thick sample deposited using the TD1 target on the TiN substrate 15
Figure 8. The example of a curve with the stepwise change of resistance in the 30 nm-thick sample deposited using the TD1 target on the TiN substrate: two successive sweeps. 16

1.1 Ionic current in solid electrolyte

According to *electrical resistivity*, solids can be classified as metals, semiconductors, and insulators. The properties of ionic materials can be placed between metals and semiconductors. An increase in temperature causes the decrease in the electrical conductivity of metals, whereas in semiconductors it causes increasing in both electronic and ionic conductivity. In ionic solids, an increase in temperature causes increasing in the ionic conductivity (Sunandana 2015). Ionic conduction is usually thermally-activated and is small because the mobility of ions is small (Dearnaley et al. 1970).

The solid-state ionic materials are usually *ionic crystals*, in which lattice vacancies, interstitials, and impurities affect electric properties. The defects in ionic solids have an effective charge, which moves through solid under application of the external electric field (Sunandana 2015).

The ionic conductor could exhibit both ionic and electronic conductivities thus being MEIC (a mixed electronic–ionic conductor) due to intrinsic properties or due to doping. However, any material could exhibit non-zero ionic and electronic conductivities. The ionic permeation through the solid electrolyte requires the presence of a small electronic current. In addition, a small ionic current is needed for the transport of ions in an electronic conductor (Sunandana 2015).

An ion can be monoatomic or polyatomic. The cation and anion are the ions, which possess a net charge of positive (cation) or negative (anion) signs. The ions are free to move in gas, liquid or solid. Ionic diffusion through matter under the influence of the gradient (chemical potential or concentration) is responsible for *ionic or electrolytic conductivity*. The ionic movement is based on the jumps of ions from place to place (Sunandana 2015).

When neutral species diffuse through neutral matter, there would not be a noticeable interaction between species and matter. However, charged species cause *the polarization* of surrounding matter during the movement. In solids, the ionic diffusion depends on the structure of the crystal and therefore is mostly anisotropic. The Fick's law is used for the explanation of ionic diffusion whereas Ohm's law can explain ionic conductivity (Sunandana 2015).

In solid electrochemical devices, one ionic component is assumed to be *immobile* whereas another one is highly *mobile* (Maier 2005). In addition, either anions or cations are assumed to be more mobile in comparison to opposite charge carriers in ionic solids (Sunandana 2015).

In nanoscales, *electrostatic effects* confine a defect structure at the larger degree than in the ground state. The interaction between charged species in small spacings may also be more pronounced. In nanoscales, the charge carriers cannot escape each other, which causes excitonic (electron-hole) interactions (Maier 2009).

The ionic transport *alongside the dislocations and grain boundaries* is important in many technological applications. The calculations suggest that it is easier to create the vacancy in some specific sites than in the perfect lattice. The short-circuit diffusion mechanism seems to be much like the diffusion in the bulk. However, the mobility and concentration are greater in the core than in the bulk region (Atkinson 1984).

In the *nanoporous glasses* and thin films, the conductivity of protons increases with an increase in the *water absorption*, due to the presence of the hydroxyl groups. The amount of absorbed water depends on the pore size and structure (Daiko 2014).

1.2 Ionic transport in biological cells

Solid-state ionics is analogical to the biological cell, where the ions move through the open ionic channel. *The gating* (or opening and closing) *the ionic channel* enables the ion transport. The selectivity of ionic channels for specific ions is based on the size, valence, and hydration energy of ions. The ionic current depends on the direction of ion transport; therefore, the ionic current could be rectifying. The gating in ionic channels may be dependent on voltage or ligand or be mechanosensitive (Sunandana 2015).

The Monte Carlo simulations show that *the anion selectivity* inside nanopores is due to the screening of charges by monovalent, divalent and trivalent cations. At high pH, the junction with monovalent cations was OFF. At low pH, the junction was ON. The junction with divalent cations was always on ON. However, at high pH, the pore junction with trivalent cations was ON and at low pH was OFF again. In pores, ionic selectivity (cation or anion) can be reversed. The screening effects are sensitive to pH and electrostatic interaction between ions (Albesa et al. 2013).

In biological cells, ions moving through nanopores form *quasi-particles*. In one of these quasi-particles states, the hydrated ions are surrounded by semi-bound molecules of water. Many of such quasi-particles interact in *nanopores with finite capacitance*. This implies the existence of threshold concentration beyond which ions of the same sign could not enter the pore. In nanopores, ionic conductance is suggested as being *quantized.* It would also be a function of the radii of the hydrating layer and a pore radius. This is similar to the mesoscopic effect of *the Coulomb blockade of electrons* (Meyertholen & Di Ventra 2013).

1.3 Conductance in nano-scales

Rectification and selectivity of ionic transport. The conical nanopores show *the rectifying behavior* and *ionic selectivity*, which depends on the direction of the concentration gradient (Cervera et al. 2007). After applying the electric field, the silica nanopore in the electrolyte can

rectify the ionic current. *The rectification* implies a higher *ionic current* for one voltage polarity than for the other (Cruz-Chu et al. 2009a).

A charged polymer nanopore would have *a high ionic selectivity* due to the preferential flow of counter-ions and rejection of the ions of the same sign (Cruz-Chu et al. 2009b). The ionic selectivity of the charged nanopores is due to the small radius of pores and the relatively high surface potential and small radius. The conductance would decrease with the finite size of the ions. However, the *ionic selectivity* would increase when the ion size increases (Cervera et al. 2010). The conically shaped nanopore with the solid-state gel electrolyte rectifies the current and work sas an ionic diode (Plett et al. 2017).

Monte Carlo simulations show that *the anion selectivity* in the nanopores was due to a screening of the negative charges by the cations. Additionally, the conductive mode depends on the pH value. However, the monovalent, divalent, and trivalent cations show different behavior from each other (Albesa et al. 2013).

The dangling bonds in silica nanopores can be responsible for the asymmetric current-voltage characteristics with *rectificatio*n because the silica pores without the dangling bonds produce the symmetric current curve. *The rectification* can be suppressed by lowering the pH of the electrolyte, neutralizing the surface charge or coating by Al2O3 (Cruz-Chu et al. 2009a). The dangling bonds can dehydrate the ions and temporally bind the ion to the pore surface, whereas that without dangling bonds cannot dehydrate and retain the ions (Cruz-Chu et al. 2009a). The nanoporous network acts like an ionic diode that rectifies the direction of the current flow depending on the electrolyte's pH value (Pevarnik et al. 2012).

The study of the *ionic transport* via the solid-state nanopores as a function of the ionic strength and the pore size shows the presence of an anomalously large ionic conduction at the moderate and even small concentrations of ions. With the fixed aspect ratio of the pore, the smaller pores would conduct as well as the large ones do. It seems that the effective electric size is much bigger than the geometric size of the solid-state nanopore (Lee et al. 2012). In the hydrophobic pores, the transport of ions depends on the *pH of the electrolyte* (Pevarnik et al. 2012).

Gating of nanopores. Current- voltage characteristics confirm the presence of the reversible and voltage-induced *opening and closing of the pores* for the transport of the mobile ions. The non-conducting states were associated with water vapor, which creates a highly resistive bottleneck for the transport of ions inside the pore (Powell et al. 2011).

The hydrophobic nanopore can be wetted and dewetted due to the water evaporation and condensation inside the pores. The transition from the *conducting* to *the non-conducting mode* can be controlled by the electric potential. The non-conducting state of the pore corresponds to the

water vapor -filled pores, but the conducting state indicates the wetting along the entire length of the pores (Powell et al. 2011).

The hydrophobic layer can create *an extra barrier for water* and ion flow at the pore entrance with the consequent rectification of the ionic current. The conductive or open time of the pore can be prolonged if the voltage is increased. However, the decrease in voltage stops the ionic transport again (Pevarnik et al. 2012).

The multilevel switching. In resistive switching devices, the *stepwise* change of conductance with time was suggested to be due to *the quantized conductance* (Terabe et al. 2005; Miranda et al. 2012; Tappertzhofen 2014). The multilevel (or quantized or step-like) conductance was found in electroformed SiOx thin film (Dearnaley et al. 1970), in n-type poly-Si/SiOx/p-type poly-Si device (Mehonic et al. 2013), as well as in Ag/AgI/Pt and Ag/SiO2/Pt memory cells (Tappertzhofen 2014).

This stepwise behavior is assumed to be due to the constriction of the electron motion in the nanofilament of the size being comparable to the Fermi wavelength of the electron. The laterally confined charge carrier would be in the discrete sub-bands. The quantized steps would be present, if the biasing was larger than the sub-band energy as well as subband distance was larger than kBT (Mehonic et al. 2013). The variation of filament's diameter is not enough to explain the multilevel switching (Tappertzhofen 2014; van den Hurk 2016).

In nanoscales, a single (discrete) metallic atom can determine the resistance of the memory cell (Tappertzhofen 2014). The cell resistance can be partially determined by a tunneling effect in the filament tip, which does not contact the active electrode (Menzel et al. 2012; van den Hurk 2016).

The ionic quantized conductance. The ionic quantized conductance was investigated as a function of the effective radius of the pore in nanoporous films. In addition, the role of the dehydration at the ion transport via nanopores was the object of study too. The ions with a higher valence create a stronger hydration shell, and therefore they provide a larger decrease in the ionic current (Zwolak et al. 2010).

The quantized conductance or stepwise conductance depends on the width of the channel. The conductance may be expressed as $G = N\frac{2e^2}{h}$, where h is Planck's constant, e denotes the electron charge, as well as N is the number of modes allowed. N is dependent on size of the point contact size according to the equation $N \approx \frac{2W}{\lambda_F}$, where W is the width of point contact, and λ_F denotes the Fermi wavelength. The ionic conductance of *quasiparticles* cannot take on any size but instead it is quantized. In a nanopore, the behavior of the hydration layers is extremely dependent on the radius of the pore (Meyertholen & Di Ventra 2013).

In nanosize filaments, the electron motion is restricted, causing the conductance *quantization*. A diameter of the filament is comparable with the Fermi wavelength for the electron. In silicon-rich SiOx devices, the conductance is quantized at room temperature in such way that the value of conductance is the multiplication of the half-integer of G0. This suggests the ballistic transport of electrons through a filament. The model predicts an integer quantization for metallic ECM devices and half-integer quantization in a VCM memory cell (Mehonic et al. 2013).

A half-integer or integer multiplication of quantum conductance have been observed in the Ag/SiO2/indium tin oxide (ITO) devices. The quantized conductance was attributed to the ballistic electron transport in a lateral constriction of the filament. The size of the filament is comparable to the Fermi wavelength of the electrons. Nevertheless, the reproducibility of this effect was low (Gao et al. 2014).

Here, *the half-integer quantized conductance* with spontaneous filament decay was observed in Cu/SiO2/W memristive devices at room temperature (Nandakumar et al. 2016).

1.4 *The ionic Coulomb blockade*

The molecular dynamics simulations suggest that the ion-ion interaction in nanoporous films can cause *the ionic Coulomb blockade effect*. *The ionic Coulomb blockade* implies the nanoionic buildup, which blocks the ionic transport due to the electrostatic repulsion. The ionic Coulomb blockade resembles the electronic Coulomb blockade, where the electron experiences large resistance at the interface between a quantum dot and the electrode. The ionic Coulomb blockade seems to be dependent on the ion concentration. The blocking effect can be related to the much *larger ionic resistance at the entrance of the pore* than the ionic resistance without the pore (Krems & Di Ventra 2013).

The Coulomb blockade would occur as a result of *the ionic transport* through a channel with the size comparable to the size of the hydration layer around the ion. At a very low density of the ions, it would be possible to observe the step-like conductance for a single particle. Moreover, with a larger density of the ion-ion interactions, the ionic Coulomb blockade can occur if the pore channel has the small capacitance (Feng et al. 2016).

The ionic transport through the nanopores is usually ohmic. Nevertheless, the voltage-induced non-linear behavior was observed with the *ion dehydration* and *hydrophobic wetting*. It was found that the ionic transport was non-linear with a voltage gap at low applied bias. Both the dehydration and Coulomb blockade are suggested to be responsible for the ionic transport in the sub-nanometer pore (Feng et al. 2016).

The studied monovalent as well as divalent ions have the non-linear current-voltage characteristics. The nanopore junction has the resistance as well as the capacitance. The suppressing of the conductance is a result of the discrete energy, which is needed for adding the ion charge to the pore. It would be possible to observe the ionic Coulomb blockade at room temperature, while this charging energy would be larger than the energy of the thermal fluctuation at room temperature. Adjusting the chemical potential by applying a voltage to the electrode allows removing or adding charge to the pore. The ion flux can pass via the pore when the ion energy would be larger than the energy of the Coulomb gap. The negatively charged surface of the nanopore together with an increased pH would add the negative charges into the pore (Feng et al. 2016).

The decreasing of the size of the Coulomb gap occurs when the size of the pore is increased. The non-linearity of the current-voltage characteristics disappears when the pore size is near 1nm, which is a sign of the vanishing of the transport barrier to the ionic flow (Feng et al. 2016).

Theory of small current-biased tunnel junctions suggests that, at low temperature, *the Coulomb interaction between electrons* can block the current of a single electron. In addition, the current components of Cooper-pair (Josephson) and the quasiparticle (single-electron) may be quantized (Averin & Likharev 1986).

Coulomb blockade is a phenomenon where tunneling across a junction is either enhanced or suppressed for certain energies as a result of the quantization of charge and Coulomb effects. The transport is likely only if the used voltage is larger than the charging energy in the central region of the junction according to the equation $|V| \geq \frac{|q|}{2C}$. Otherwise, there would be no charge transport and Coulomb blockade occurs. In a nanopore, the build-up of ions can hinder *the flow of other ions*. An approaching ion will be blocked if its kinetic energy is less than that of the barrier. This blockade is analogous to the Coulomb blockade demonstrated in quantum dot systems coupled to two electrodes. The observation of *ionic Coulomb blockade* should be possible in any nanopore with a constriction small enough to interfere with hydration layers (Meyertholen & Di Ventra 2013).

Transport of discrete cations in SiO2. In the Cu- or Al-doped SiO2 memory cell, the filament in SiO2 is composed of *the Ag particles*, which *are discrete and dispersed in SiO2*. The granulation of Ag- filament may be explained to be due to the low redox reaction rate and low mobility of ions in the SiO2 (Chen et al. 2017a).

The SEM images of planar Ag/SiO2 /Pt planar device shown in Figure 1 (Sun et al. 2014) displays the growth of the conductive filament at a different time. It can be seen that, at earlier stages, *Ag particles* are *dispersed* through the volume of SiO2. The clustering in the larger conglomerates occurs later. The conductive path can be approximated as the metallic filament only at final stages.

In addition, the structure of the metallic filament is rather very discrete than the continuous and solid filament. In fact, this metallic filament consists of many discrete Ag clusters.

Perhaps, if the mass transport of Ag or transport of Ag ions, was disturbed or blocked as in the case of Coulomb blockade, threshold switching or stepwise resistance, then the opposite electrodes could not be connected and the cell would be OFF.

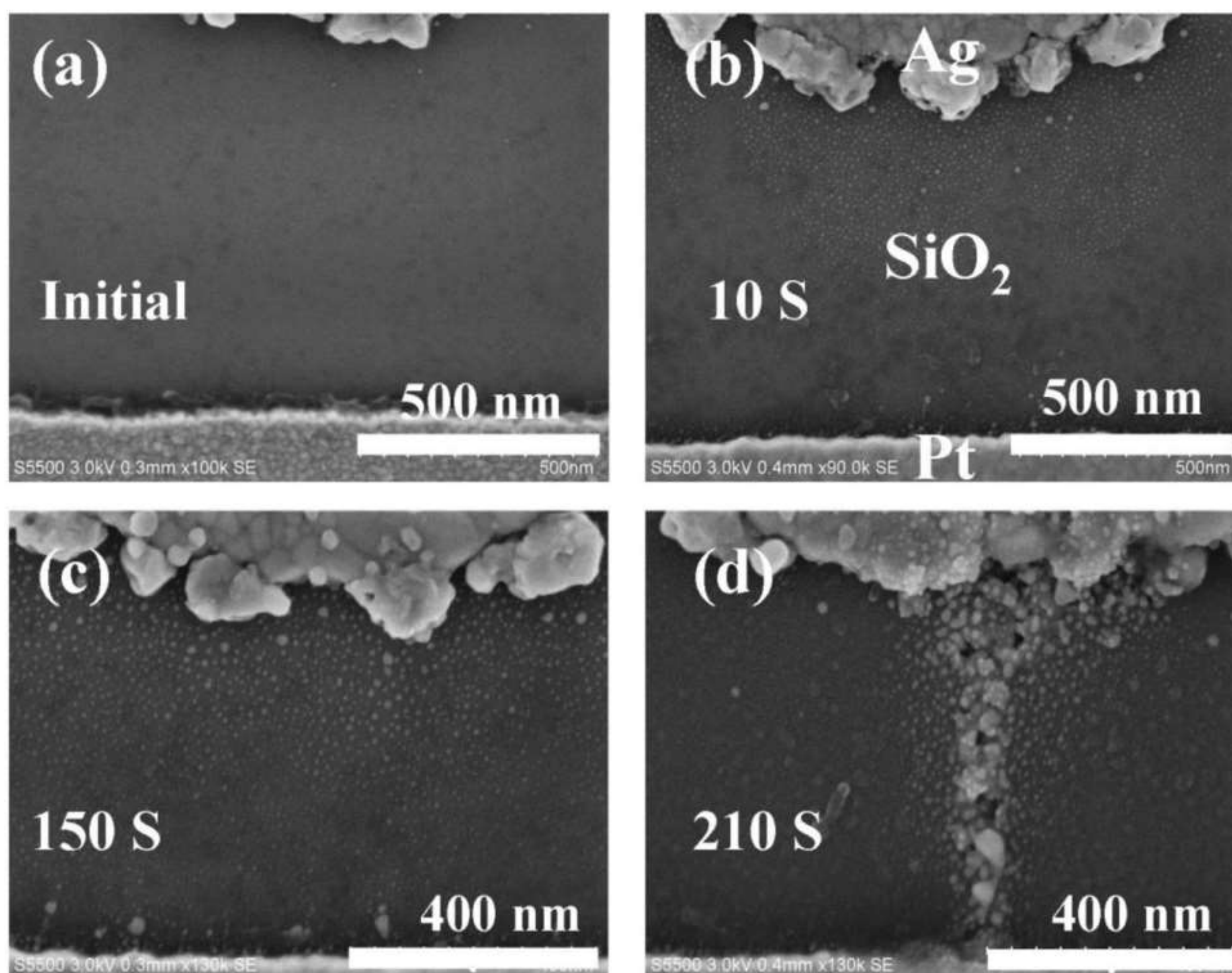

Figure 1. *The SEM images of the planar Ag/SiO2 /Pt -based device displaying the growth of the conductive filament at a different time (Sun et al. 2014).*

Figure 2 displays the TEM images, which show the creating and erasing of a conductive filament in two different Ag: SiO2-based planar devices with different spacing between electrodes (a-c and h-i). In this figure, the discrete structure of the conductive filament can be seen. Even when the opposite electrodes are connected, the conductive path consists of small discrete clusters rather than the solid continuous metallic filament.

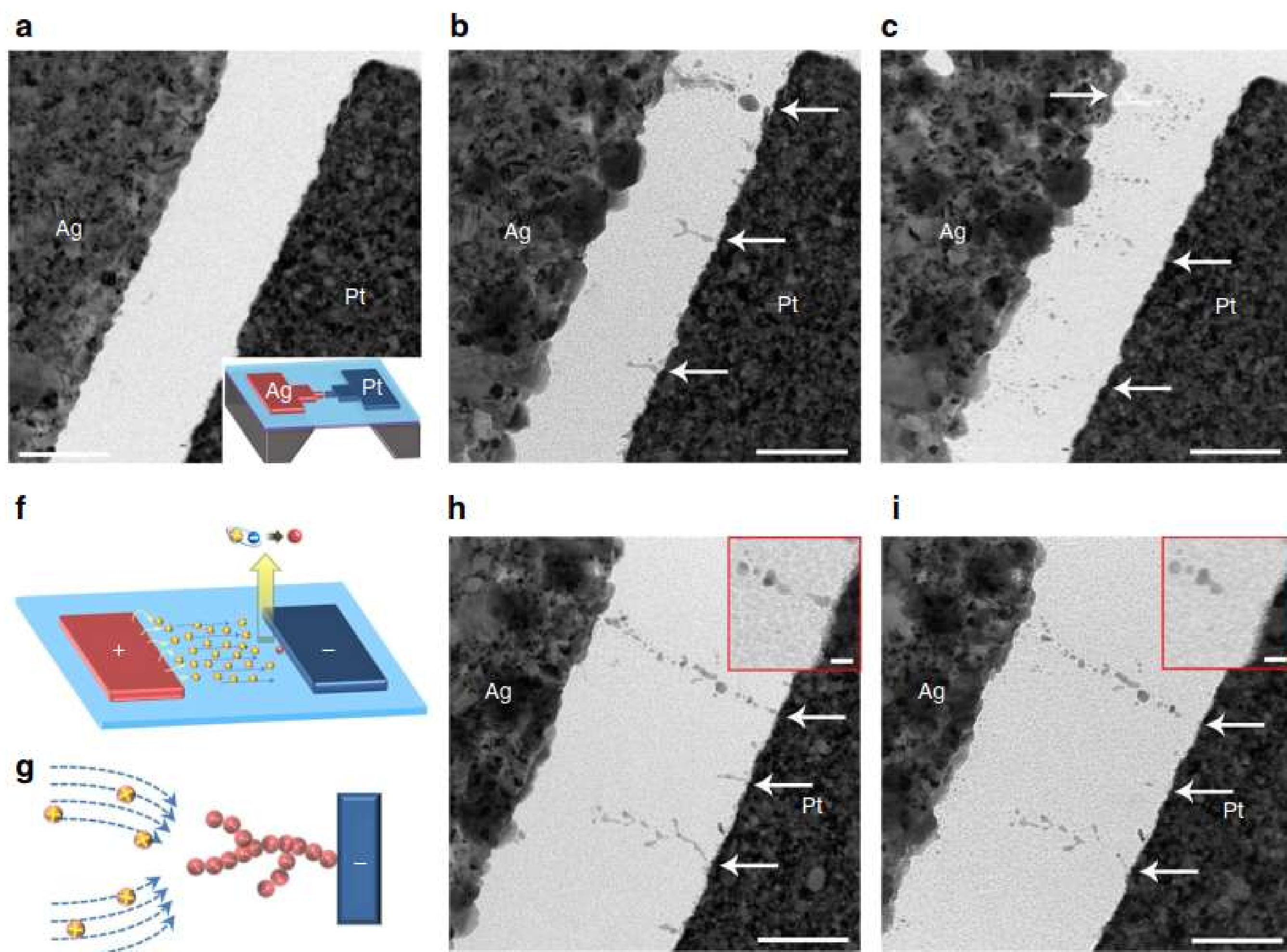

Figure 2. *The TEM images of the creating and erasing of a conductive filament in two different Ag: SiO2-based planar devices with different spacing between electrodes (a-c and h-i) (Yang et al. 2012).*

Figure 3 shows SEM image displaying the displacement reaction of Al with Cu at different times (Chin et al. 2014). It can be seen also, that mass transport of Cu also occurs through many discrete steps. In addition, the Cu is dispersed in a SiO2 matrix.

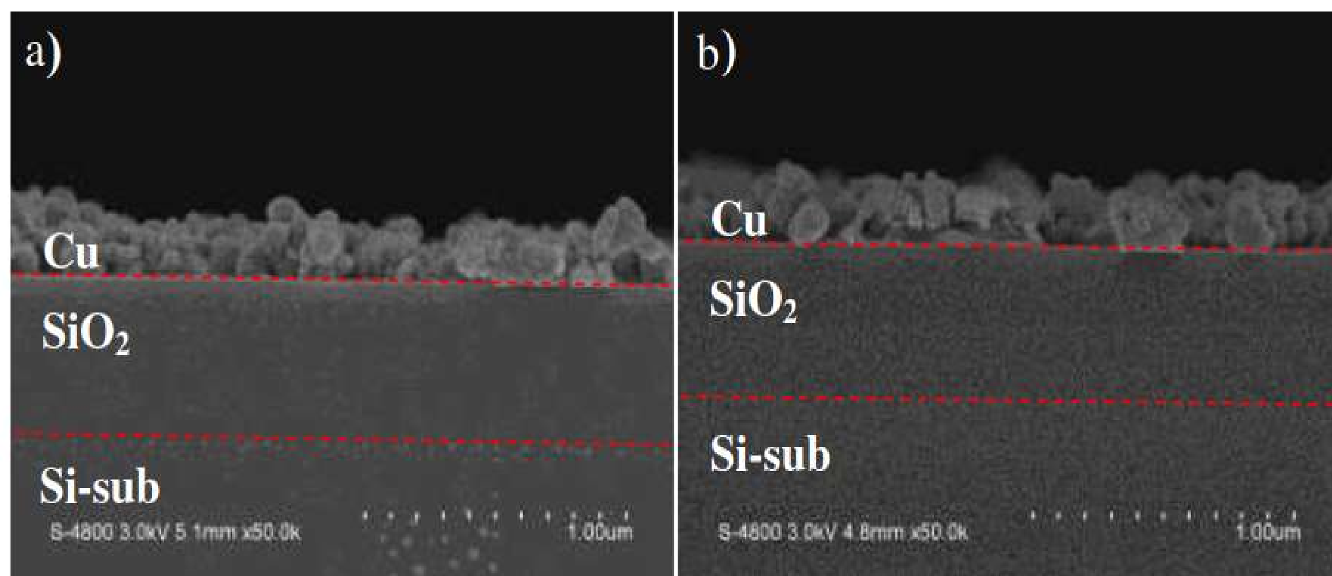

Figure 3. *The SEM image displaying the displacement reaction of Al with Cu at a different time (60 sec. and 70sec.) (Chin et al. 2014)*

Based on the Figures 1-3 of this Appendix 10, one can state that the mass transport of Cu, Ag, as well as other dopants, through SiO2 occurs through many discrete steps in all volume of SiO2. The mobile ions should propagate through nanopores in network of SiO2. If the ions cannot pass through the pore, they cannot agglomerate and form the metallic filament in later stages. Moreover, according to Figure 1 of this Appendix 10, the conductive path is not continuous but consists of the discrete clusters.

Figure 4 shows current-voltage curves through a 12 nm polymer nanopore at different pH values. In biological cells, the voltage-gated channels are responsible for ionic gating through hydrophobic cavities. These channels can rectify because ionic transport is more effective in one direction than in other direction. Therefore, these biological channels behave as ionic diodes in nanopores. The rectification in such a diode depends on the pH of the electrolyte. The conducting and non-conducting state of such a diode depends on wetting and dewetting of nanopores (Pevarnik et al. 2012).

In Figure 4, the current-voltage characteristics of polymer nanopore with liquid electrolyte resembles that with threshold-like switching curves biased with the current compliance of 0.1A shown in Appendix 9. The OFF state in the middle of the curves relates to a non-conducting state explained to be due to the water vapor in nanopores.

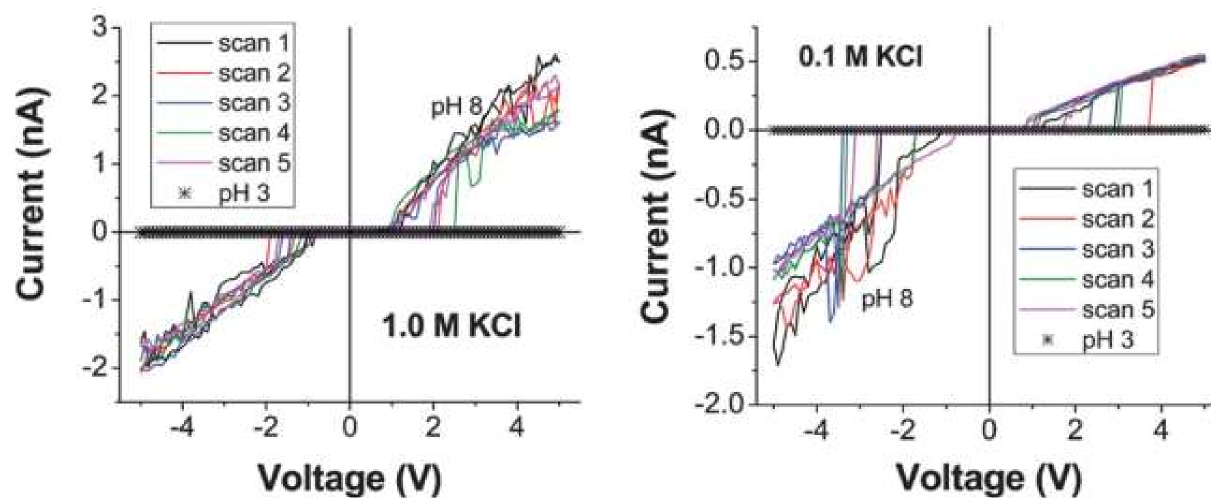

Figure 4. *I-V curves through a 12 nm polymer nanopore at a different pH values (Pevarnik et al. 2012)*

Figure 5 shows a schematic of a biological voltage-gated porous channel junction with ionic selectivity at a different pH (Pevarnik et al. 2012). Here, it is exemplified that wetting and deweting of pores depends on the pH value of electrolyte. The shape of pores in SiO2 could be, of course, completely different.

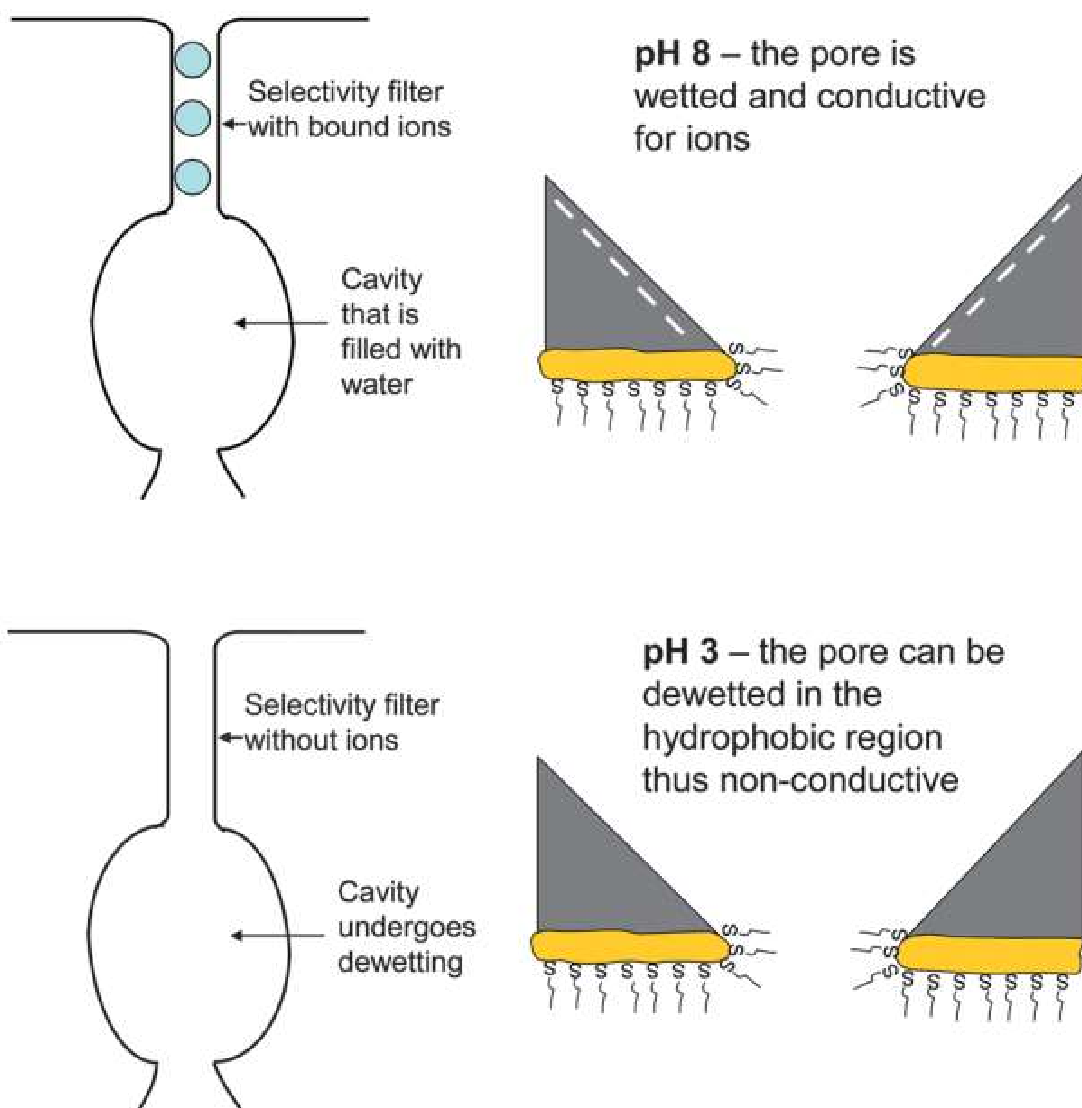

Figure 5. *Schematic of a biological voltage-gated porous channel junction with ionic selectivity at a different pH (Pevarnik et al. 2012).*

The explanation of threshold switching. It is suggested that the threshold-like switching behavior observed in SiO2-based ECM memory cell resembles the behavior of the electrolyte in the biological voltage-gated nanoporous channel. As shown in Appendix 9, the electrical measurements of both samples with the threshold-like switching behavior were performed on the same day, 1st June 2016. All day, the relative humidity in the air was extremely high (94%-100%). It was not possible to reproduce this kind of behavior in later days when the relative humidity was different. The working hypothesis relates the threshold-like switching to wetting and dewetting of nanopores in SiO2. The dewetting corresponds to the evaporation of water molecules and to the non-conductive OFF state. The wetting of nanopores relates to the conductive ON state.

The explanation of quantized conductance. The stepwise conductance, multistep conductance or quantized conductance is frequently reported in different types of resistive memory devices (Tappertzhofen et al. 2012; Tsuruoka et al. 2012; Mehonic et al. 2013; Zhao et al. 2015; Li et al. 2015; Nandakumar et al. 2016).

In Ag/Ta2O2/Pt memory device, the quantized conductance was observed. This effect is seen as the stepwise increase and decrease in conductance. The effect is explained to be due to creating and dissolving the metallic filament "with atomic contact of different integer multiplies" and the limiting supply of Ag ions, which participate in the formation of the filament (Tsuruoka et al. 2012).

The explanation of the quantized conductance is usually related to the restricted ballistic electronic transport in the nanoscale filament (Mehonic et al. 2013).

In Cu/amorphous C/Pt memory cell, the quantized conductance was observed. The effect is explained to be due to the limited number of available Cu ions. The effect is related to the relaxing of resistive states. Electron transport in the filament of atomic size is quantized and is a multiple of conductance $G_0 = 2e^2/h \approx 1/12{,}9kOhm$, where h is Planck's constant, as well as e is a charge of the electron. The effect is typically associated with point contacts comprising of a few atoms. The effect is explained to be due to the spontaneous, volatile and uncontrollable dissolving of the conductive filament (Zhao et al. 2015).

The presence of quantized conductance was overviewed for many different types of ECM and VCM cells. However, the step values were found to be G0 or 0.5G0, as well as the mixing of these both values, and even non-integer of G0. The effect should be observed when the conductive filament is of atomic size (Li et al. 2015).

In Cu/SiO2/W memory cell, the half-integer quantized conductance was observed. The effect is associated to nanoscale devices, where the conductive filament is comparable with the Fermi wavelength. The half-integer conductance level was observed during the spontaneous decays. Some quantized levels were missing (Nandakumar et al. 2016).

Example of a typically reported plot of conductance versus time can be seen in Figure 6. The observation of quantum conductance steps with inset of height of G0 (Zhao et al. 2015).

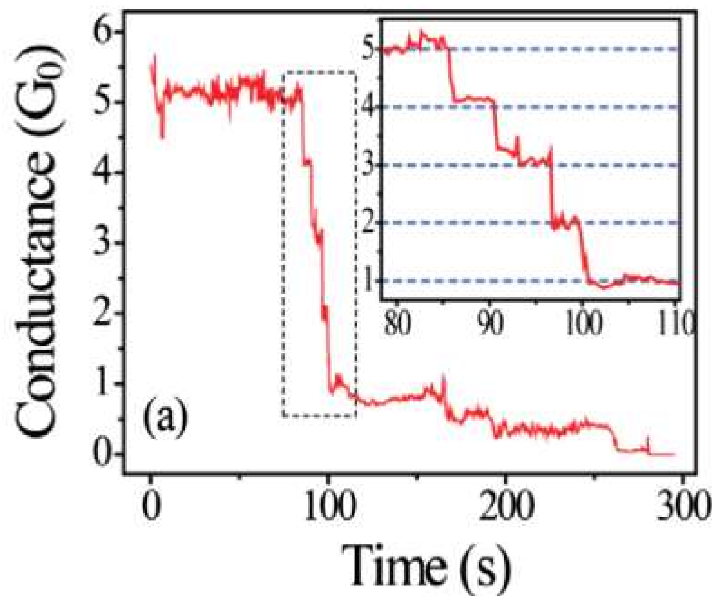

Figure 6. The observation of quantum conductance steps with inset of height of G0 (Zhao et al. 2015).

During our project, the stepwise type of conductance was observed also in sample 207-IS deposited using the TD1 target on the TiN substrate as shown in Figure 7 and Figure 8. These curves are only shown as two examples from many others. The shape of the curve with corresponding jumps varies a lot. However, the resistance in all the other curves is also changed in a stepwise manner.

Here, the stepwise conductance as well as the threshold switching is explained to be due to the restricted ionic transport in the nanopore during the creating and dissolving of the conductive filament. The conductive filament cannot only be metallic, but also can be partly or completely oxidized. This implies that the current may flow through a semiconductive oxide.

The transition between the resistance states during the switching is also informative because it can give signs if the created filament is metallic or not. Inclining line on a logarithmic scale indicates that the current and voltage are exponentially related to each other. In Figure 6 and Figure 7, resistance undergoes many different types of change. Not all of them are of ohmic type. This contradicts with the traditional explanation that the resistance change in a memory cell is only due to the creating and dissolving of the metallic filament.

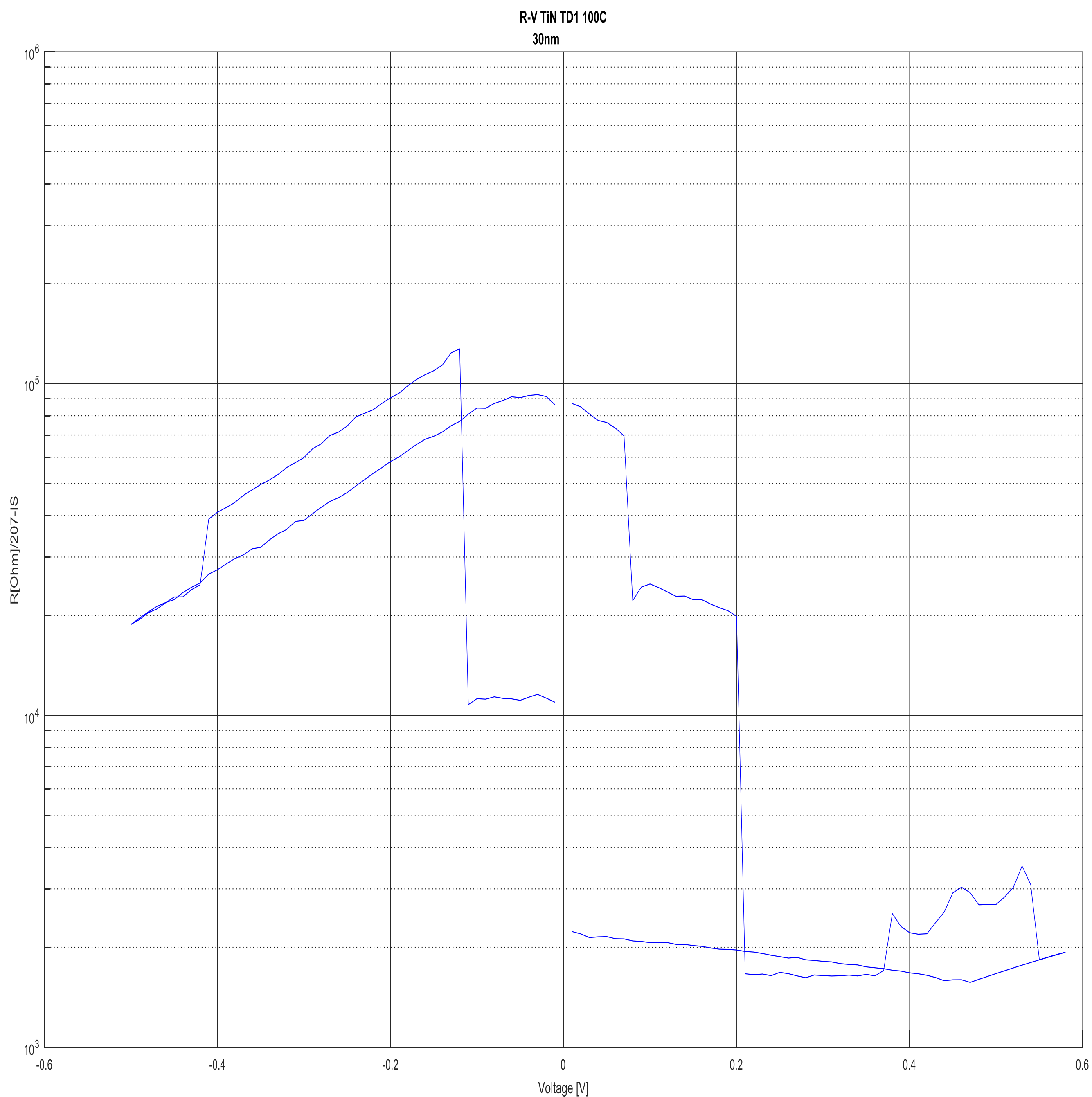

Figure 7. The example of a curve with the stepwise change of resistance in the 30 nm-thick sample deposited using the TD1 target on the TiN substrate

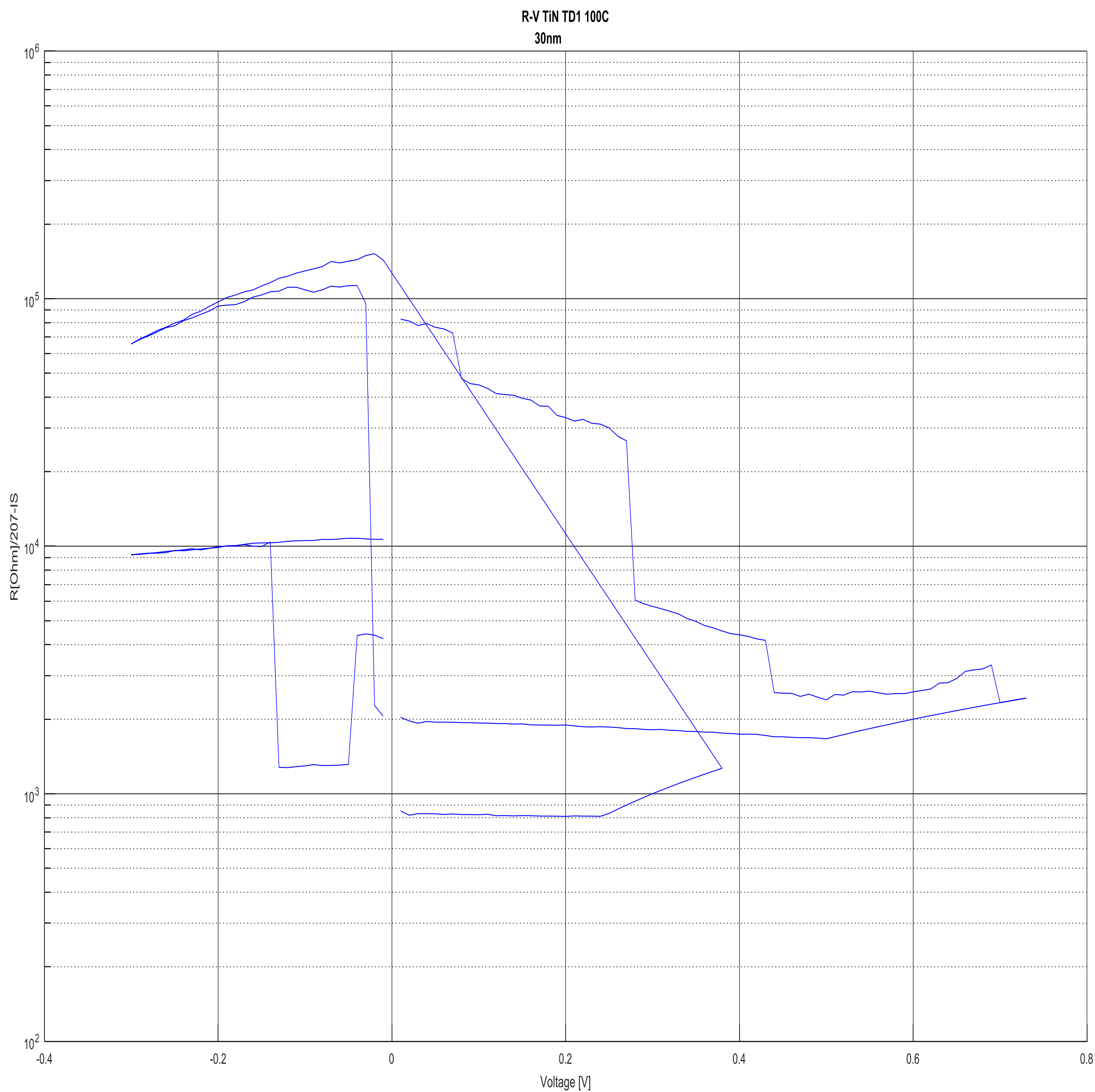

Figure 8. *The example of a curve with the stepwise change of resistance in the 30 nm-thick sample deposited using the TD1 target on the TiN substrate: two successive sweeps.*

The explanation of the ionic Coulomb blockade. The threshold-like switching can probably be explained in many different ways. However, here, all the observed effects are related to the specific ionic transport in nanopores, which was restricted. The restriction relates to the existence of the energy barrier. When the cations became mobile (see Appendix 2 Phourbaix diagram), they should overcome the existing barrier in the nanopore entrance.

In addition, the nanopores have the limited capacitance, which implies that when the mobile cations cannot enter the pore, their energy is less than the certain value. The pore region has the electrostatic energy ($E = \frac{1}{2}CV^2$), which ions need to overcome.

The existing energy barrier to cation flow can be written as $\Delta E = \frac{Q^2}{2C}$ (Meyertholen & Di Ventra 2013). Q is a charge consisting of the monovalent, divalent, as well as trivalent ions inside the nanopores. This Q value changes when the ion enters or flows away from the pores. The capacitance C cannot be easily changed because the size and shape of pores is rigid after fabrication. The less the capacitance is at constant Q, the higher the energy barrier is. The conductive filament is created, when the ionic transport through the nanopores is not restricted.

The cation can gain the additional energy to overcome the energy barrier ΔE when the voltage is increased. Therefore, the OFF state in the threshold-like switching curve is explained in such a way that the ionic transport was restricted because the mobile cations could not overcome the existing barrier until the threshold voltage value is exceeded.

In addition, the threshold-like switching behavior was related to the energy consideration, because the variability of the switching behavior of the memory cells was extremely low. These cells behaved in exactly the same way in a very narrow biasing window. However, the variability was extremely high in all other cases expect of threshold-like behavior. In addition, the threshold-like switching in ECM cell is explained to be due to the moisture uptake by the nanopores. The evaporated water molecules would create the highly resistive state inside nanopores.

The stepwise change in resistance may indicate that only portion of the ions can pass through the pore because of the restricted ionic transport. For example, another explanation can be related to the fact that not all of the ions were mobile, due to wrong pH value.

REFERENCES

Albesa, A.G., Rafti, M. & Vicente, J.L. (2013a). Trivalent cations switch the selectivity in nanopores, Journal of molecular modeling, Vol. 19(6), pp. 2183-2188.

Albesa, A.G., Rafti, M. & Vicente, J.L. (2013b). Trivalent cations switch the selectivity in nanopores, Journal of molecular modeling, Vol. 19(6), pp. 2183-2188.

Atkinson, A. (1984). Diffusion along grain boundaries and dislocations in oxides, alkali halides and carbides, Solid State Ionics, Vol. 12pp. 309-320.

Averin, D. & Likharev, K. (1986). Coulomb blockade of single-electron tunneling, and coherent oscillations in small tunnel junctions, Journal of Low Temperature Physics, Vol. 62(3-4), pp. 345-373.

Cervera, J., Ramírez, P., Manzanares, J.A. & Mafé, S. (2010). Incorporating ionic size in the transport equations for charged nanopores, Microfluidics and nanofluidics, Vol. 9(1), pp. 41-53.

Cervera, J., Alcaraz, A., Schiedt, B., Neumann, R. & Ramirez, P. (2007). Asymmetric selectivity of synthetic conical nanopores probed by reversal potential measurements, The Journal of Physical Chemistry C, Vol. 111(33), pp. 12265-12273.

Chen, W., Tappertzhofen, S., Barnaby, H.J. & Kozicki, M.N. (2017). SiO2 based conductive bridging random access memory, Journal of Electroceramics, pp. 1-23.

Chin, F., Lin, Y., You, H., Yang, W., Lin, L., Hsiao, Y., Ko, C. & Chao, T. (2014). Advanced Cu chemical displacement technique for SiO2-based electrochemical metallization ReRAM application, Nanoscale research letters, Vol. 9(1), pp. 592.

Cruz-Chu, E.R., Aksimentiev, A. & Schulten, K. (2009a). Ionic current rectification through silica nanopores, The Journal of Physical Chemistry C, Vol. 113(5), pp. 1850-1862.

Cruz-Chu, E.R., Ritz, T., Siwy, Z.S. & Schulten, K. (2009b). Molecular control of ionic conduction in polymer nanopores, Faraday discussions, Vol. 143pp. 47-62.

Daiko, Y. (2014). Proton conduction in nanopores of sol–gel-derived porous glasses and thin films, Journal of Sol-Gel Science and Technology, Vol. 70(2), pp. 172-179.

Dearnaley, G., Stoneham, A. & Morgan, D. (1970). Electrical phenomena in amorphous oxide films, Reports on Progress in Physics, Vol. 33(3), pp. 1129.

Feng, J., Liu, K., Graf, M., Dumcenco, D., Kis, A., Di Ventra, M. & Radenovic, A. (2016). Observation of ionic Coulomb blockade in nanopores, Nature materials, Vol. 15(8), pp. 850-855.

Gao, S., Chen, C., Zhai, Z., Liu, H., Lin, Y., Li, S., Lu, S., Wang, G., Song, C. & Zeng, F. (2014). Resistive switching and conductance quantization in Ag/SiO2/indium tin oxide resistive memories, Applied Physics Letters, Vol. 105(6), pp. 063504.

Krems, M. & Di Ventra, M. (2013). Ionic Coulomb blockade in nanopores, Journal of Physics: Condensed Matter, Vol. 25(6), pp. 065101.

Lee, C., Joly, L., Siria, A., Biance, A., Fulcrand, R. & Bocquet, L. (2012). Large apparent electric size of solid-state nanopores due to spatially extended surface conduction, Nano letters, Vol. 12(8), pp. 4037-4044.

Li, Y., Long, S., Liu, Y., Hu, C., Teng, J., Liu, Q., Lv, H., Suñé, J. & Liu, M. (2015). Conductance quantization in resistive random access memory, Nanoscale research letters, Vol. 10(1), pp. 420.

Maier, J. (2005). Nanoionics: ion transport and electrochemical storage in confined systems, Nature materials, Vol. 4(11), pp. 805-815.

Maier, J. (2009). Thermodynamics of nanosystems with a special view to charge carriers, Advanced Materials, Vol. 21(25-26), pp. 2571-2585.

Mehonic, A., Vrajitoarea, A., Cueff, S., Hudziak, S., Howe, H., Labbe, C., Rizk, R., Pepper, M. & Kenyon, A. (2013a). Quantum conductance in silicon oxide resistive memory devices, Scientific reports, Vol. 3pp. 2708.

Mehonic, A., Vrajitoarea, A., Cueff, S., Hudziak, S., Howe, H., Labbe, C., Rizk, R., Pepper, M. & Kenyon, A.J. (2013b). Quantum conductance in silicon oxide resistive memory devices, Scientific reports, Vol. 3pp. 2708.

Menzel, S., Böttger, U. & Waser, R. (2012). Simulation of multilevel switching in electrochemical metallization memory cells, Journal of Applied Physics, Vol. 111(1), pp. 014501.

Meyertholen, A. & Di Ventra, M. (2013). Quantum Analogies in Ionic Transport Through Nanopores, arXiv preprint arXiv:1305.7450, .

Miranda, E., Jimenez, D. & Suñé, J. (2012). The quantum point-contact memristor, IEEE Electron Device Letters, Vol. 33(10), pp. 1474-1476.

Nandakumar, S., Minvielle, M., Nagar, S., Dubourdieu, C. & Rajendran, B. (2016a). A 250 mV Cu/SiO2/W memristor with half-integer quantum conductance states, Nano letters, Vol. 16(3), pp. 1602-1608.

Nandakumar, S., Minvielle, M., Nagar, S., Dubourdieu, C. & Rajendran, B. (2016b). A 250 mV Cu/SiO2/W memristor with half-integer quantum conductance states, Nano letters, Vol. 16(3), pp. 1602-1608.

Pevarnik, M., Healy, K., Davenport, M., Yen, J. & Siwy, Z.S. (2012). A hydrophobic entrance enhances ion current rectification and induces dewetting in asymmetric nanopores, Analyst, Vol. 137(13), pp. 2944-2950.

Plett, T.S., Cai, W., Le Thai, M., Vlassiouk, I.V., Penner, R.M. & Siwy, Z.S. (2017). Solid-State Ionic Diodes Demonstrated in Conical Nanopores, The Journal of Physical Chemistry C, Vol. 121(11), pp. 6170-6176.

Powell, M.R., Cleary, L., Davenport, M., Shea, K.J. & Siwy, Z.S. (2011). Electric-field-induced wetting and dewetting in single hydrophobic nanopores, Nature Nanotechnology, Vol. 6(12), pp. 798-802.

Sun, H., Liu, Q., Li, C., Long, S., Lv, H., Bi, C., Huo, Z., Li, L. & Liu, M. (2014). Direct observation of conversion between threshold switching and memory switching induced by conductive filament morphology, Advanced Functional Materials, Vol. 24(36), pp. 5679-5686.

Sunandana, C. (2015). Introduction to solid state ionics: phenomenology and applications, CRC Press, .

Tappertzhofen, S. (2014). Redox and mass transport phenomena in resistively switching thin films, Universitätsbibliothek, .

Tappertzhofen, S., Valov, I. & Waser, R. (2012). Quantum conductance and switching kinetics of AgI-based microcrossbar cells, Nanotechnology, Vol. 23(14), pp. 145703-1-6.

Terabe, K., Hasegawa, T., Nakayama, T. & Aono, M. (2005). Quantized conductance atomic switch, Nature, Vol. 433(7021), pp. 47-50.

Tsuruoka, T., Hasegawa, T., Terabe, K. & Aono, M. (2012). Conductance quantization and synaptic behavior in a Ta2O5-based atomic switch, Nanotechnology, Vol. 23(43), pp. 435705.

van den Hurk, J. (2016). Germanium Sulphide Based Resistive Switching Devices, .

Yang, Y., Gao, P., Gaba, S., Chang, T., Pan, X. & Lu, W. (2012). Observation of conducting filament growth in nanoscale resistive memories, Nature communications, Vol. 3pp. 732.

Zhao, X., Xu, H., Wang, Z., Zhang, L., Ma, J. & Liu, Y. (2015). Nonvolatile/volatile behaviors and quantized conductance observed in resistive switching memory based on amorphous carbon, Carbon, Vol. 91pp. 38-44.

Zwolak, M., Wilson, J. & Di Ventra, M. (2010). Dehydration and ionic conductance quantization in nanopores, Journal of Physics: Condensed Matter, Vol. 22(45), pp. 454126.